

# **PROCEEDINGS**

## **PHOTOVOLTAIC SCIENCE APPLICATIONS AND TECHNOLOGY**

### **PVSAT-13**

Conference C99 of the SOLAR ENERGY Society  
Bangor University, Bangor, UK  
5 - 7 April 2017



the **SOLAR ENERGY** society  
UK Section of the  
**INTERNATIONAL SOLAR ENERGY SOCIETY**

# **Photovoltaic Science, Applications and Technology (PVSAT-13)**

5-7 April 2017, Bangor University, Bangor, UK

Proceedings Editors: Michael Hutchins, Rob Treharne and Alex Cole

## **Sponsors:**

IET Journals, The Institution of Engineering and Technology  
Royal Society of Chemistry Energy Sector  
Sêr Solar  
M SPARC  
Engineering Research Network Wales (NRN AEM)  
IQE plc  
Compound Semiconductor Centre, Cardiff  
EPSRC Centre for Doctoral Training, Photovoltaics, University of Liverpool  
EPSRC SUPERGEN SuperSolar, Loughborough University  
Bangor University  
The Institute of Physics Materials and Characterisation Group

## **Conference Chairs:**

Nigel Mason, PV Consulting Ltd, Conference Chair  
Alex Cole, The Centre for Process Innovation, Programme Chair  
Jeff Kettle, Bangor University, Local Organiser

## **Organising Committee:**

Nigel Mason, PV Consulting Ltd  
Alex Cole, The Centre for Process Innovation  
Rolf Crook, University of Leeds  
Ken Durose, University of Liverpool  
Ralph Gottschalg, Loughborough University  
Michael Hutchins, The Solar Energy Society (UK-ISES)  
Stuart Irvine, Swansea University  
Jeff Kettle, Bangor University  
Nicola Pearsall, Northumbria University  
Steve Ransome, Steve Ransome Consulting  
Hari Reehal, London South Bank University  
Rob Treharne, University of Liverpool  
Trystan Watson, SPECIFIC, Swansea University

*Published by:*

The Solar Energy Society  
PO Box 489  
Abingdon  
OX14 4WY  
United Kingdom  
Tel +44 (0)7760 163559  
Fax +44 (0)1235 848684  
Email [info@uk-isес.org](mailto:info@uk-isес.org)  
[www.uk-isес.org](http://www.uk-isес.org)  
[www.pvsat.org.uk](http://www.pvsat.org.uk)

Copyright: The Solar Energy Society, 2017

ISBN 0 904963 83 7

No part of this publication may be reproduced, stored in a retrieval system or transmitted in any form without the prior written permission of the Publishers. The Publishers are not responsible for the accuracy of the claims and statements made by the authors in the text printed in this publication



## The Solar Energy Society

UK National Section of the  
International Solar Energy Society (UK-ISES)



[www.pvsat.org.uk](http://www.pvsat.org.uk)  
[www.uk-ises.org](http://www.uk-ises.org)

13th Photovoltaic Science, Applications and Technology Conference

# PVSAT-13

Bangor University  
Bangor, UK

Wednesday 5<sup>th</sup> –Friday 7<sup>th</sup> April 2017

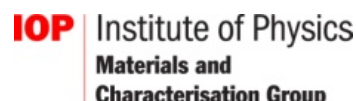
## CONFERENCE PROCEEDINGS C99

M. G. Hutchins, R. Treharne, A. Cole, Editors

*Sponsored and supported by*



EPSRC CENTRE FOR DOCTORAL TRAINING  
NEW AND SUSTAINABLE  
PHOTOVOLTAICS







## PVSAT-13 CONTENTS

Novel Deposition Method to Print Binder-Free Inks on Large Scale Carbon Perovskite Solar Cells S. M. P. Meroni, F. De Rossi, A. Pockett, T. De Brito Melo, R. Escalante, J. Searle, J. Baker, Y. Mouhamad, M. J. Carnie, E. Jewell, G. Oskam and T. Watson	1
Understanding the Photoelectron Spectroscopy of Perovskites for Photovoltaics James D McGettrick, Katherine Hooper, Adam Pockett, Jenny Baker, Matthew Carnie and Trystan Watson	5
Thermo-Mechanical Stresses of Silicon Photovoltaic Modules Michael Owen-Bellini, Jiang Zhu, Thomas R. Betts, Ralph Gottschalg	9
Perovskite-Silicon Tandem Cells Utilizing a Semi-Transparent Silver Nanowire Composite Electrode Adam Pockett, Sultan Zhantuarov, Harry Lakhiani, Joel Troughton, Trystan Watson, Nurlan Tokmoldin, Matthew Carnie	13
Optimization of PV-PCM system for South-West UK climate Sourav Khanna, K S Reddy and Tapas K Mallick	17
New mechanism in proton irradiated CdTe solar cells revealed by SCAPS modelling S. J. C. Irvine, D. A. Lamb, C. I. Underwood and V. Barrioz	21
Gold Nanorods for application in Plasmonic Luminescent Solar Concentrators A. Sethi, S. Chandra , H. Ahmed and S. J. McCormack	25
First Flight Test of a Thin Film Cadmium Telluride Solar Cell on Cover Glass in Space D. A. Lamb, C. I. Underwood, A. Dyer, J. Hall and S. J. C. Irvine	29
Optimum use of the Loss Factors Model (LFM) for improved PV performance modelling Steve Ransome and Juergen Sutterlueti	33
Highly Effective $TiO_{2-x}$ Electron Transport Layers via Atmospheric Pressure Plasma Enhanced CVD John L. Hodgkinson, Heather M. Yates, Arnaud Walter, Sylvain Nicolay	39
Characterisation and optimisation of processing time for perovskite solar cells Katherine Hooper, Joel Troughton, James McGettrick, Francesca De Rossi, Michael Newman, Wing Chung Tsoi, and Trystan Watson	43



## PVSAT-13 CONTENTS

Understanding and controlling electron transfer between sensitizer and electrolyte Peter J. Holliman, Christopher Kershaw, Arthur Connell, Eurig W. Jones, Robert Hobbs, Rosie Anthony, Leo Furnell, James McGettrick, Dawn Geatches and Sebastien Metz	49
SiGeSn as a 1.0eV component sub-cell in III-V multi-junction solar cells Phoebe Pearce, Tom Wilson, Andrew Johnson, Radeck Rouck, Andrew Clark, Tomos Thomas, Markus Führer, Nicholas Ekins-Daukes, Rick Hoffman Jr, David Begarney	53
Impact of stratospheric aerosol geoengineering on PV and CPV output CJ Smith, JA Crook, R Crook, LS Jackson, SM Osprey, PM Forster	57
Uncertainty Contributions in Photocurrent Linearity Measurements of PV Devices using a Flash Solar Simulator M. Bliss, B.V. Mihaylov, G. Koutsourakis, T.R. Betts, R. Gottschalg	61
Flexible Cu <sub>2</sub> ZnSn(S,Se) <sub>4</sub> solar cells made from nanoparticle inks Xinya Xu, Guillaume Zoppi, Yongtao Qu, Vincent Barrioz and Neil S. Beattie	65
Remote monitoring and failure detection for distributed small-scale PV systems E. Koubli, D. Palmer, Paul Rowley and R. Gottschalg	69
Very high humidity fabrication of perovskite solar cells Joel Troughton, Katherine Hooper and Trystan Watson	73
Satellite or Ground-based Irradiation Data: which is closer to reality? Diane Palmer, Elena.Koubli, Ian Cole, Tom Betts and Ralph Gottschalg	77
Agent-based modelling of the effect of government policy on the adoption of domestic photovoltaic systems in Great Britain Phoebe Pearce and Raphael Slade	81
Development of ZnO/CdS/CdTe core-shell nanorod-based solar cells with an extremely thin absorber G. Kartopu, S. Yerci, H.E. Ünal, V. Barrioz, P. Aurang, W. Hadibrata, Y. Qu, C. Özcan, L. Bowen, A.K. Gürlek, P. Maiello, R. Turan, and S.J.C. Irvine	85
Enhanced Stability in CsSnI <sub>3</sub> Perovskite Photovoltaics K. P. Marshall, M. Walker, R. I. Walton, and R. A. Hatton	89
MOCVD of SnS with large grains and stoichiometry control for thin film photovoltaics Andrew J. Clayton, Stuart J. C. Irvine, Peter Siderfin and Cecile M. E. Charbonneau	93



## PVSAT-13 CONTENTS

A Simple Optical Setup for Current Mapping of Small Area PV Devices Using Different Sampling Strategies G. Koutsourakis, S. R. G. Hall, M. Bliss, T.R. Betts and R. Gottschalg	97
A comparison of different selenisation approaches for solution-processed Cu(In,Ga)(S,Se) <sub>2</sub> solar cells S. Uličná, P. Arnou, C.S. Cooper, L.D.Wright, A.V. Malkov, J.M. Walls and J.W. Bowers	101
Accelerated weathering test for evaluating “transparent encapsulants on steel substrate” and prediction of lifetime improvement of solar cell Sanjay Ghosh, Vasil Stoickov, Luke Haponow, Jeff Kettle, Ana L. Martínez, David Gómez, Pascal Sánchez	105
Sr <sub>4</sub> Al <sub>14</sub> O <sub>25</sub> : Eu, Dy as a potential downconverter for crystalline-silicon solar cells Joseph Day, S. Senthilarasu, Tapas K. Mallick	109
Water Vapour Transmission Rate of Ethylene Vinyl Acetate (EVA) Encapsulant with different Curing Levels Jiang Zhu, Christina Ng, Daniel Montiel-Chicharro, Thomas R. Betts, Ralph Gottschalg	113
Outdoor degradation, performance analysis and software modelling of Organic Photovoltaics (OPVs) fixed to a building prototype Vasil Stoichkov, Noel Bristow, Dr Tracy Sweet, Dr Jeff Kettle	117
Functionalised Schottky Barriers on Steel N E Ryall, R. Crook and J A Weinstein	121
Evaluation of Effective Carrier Lifetime of CdTe Solar Cells Using Transient Photovoltage Decay Measurements Vincent Tsai, George Koutsourakis, Martin Bliss, Thomas R. Betts, Ralph Gottschalg	125
Analysis of Luminescent Solar Concentrator Performance Using a Ray Tracing Algorithm: Modelling, Optimization and Validation M. Rafiee, S. Chandra, H. Ahmed and S. J. McCormack	129
Triple-Junction Concentrator Photovoltaic-Thermoelectric Hybrid Receivers: Robustness, Validation and Preliminary Reliability Studies Matthew Rolley, Tracy Sweet, Vasil Stoichkov, Noel Bristow, Jeff Kettle, Gao Min	133
Influence of sulfur loading during sulfurization of Cu <sub>2</sub> ZnSnS <sub>4</sub> absorber layers for thin film solar cells S. Mazzamuto, S. Dale, L.M. Peter, N.M. Pearsall, I. Forbes	137



## PVSAT-13 CONTENTS

Metrology of Dye-sensitized Solar Cells Leo Furnell, Peter J. Holliman, Rosie Anthony, Arthur Connell, Eurig W. Jones, Christopher P. Kershaw	141
U-value calculation of CdTe thin film PV glazing using indoor characterization Hameed Alrashidi, Aritra Ghosh, Walid Issa, Nazmi Sellami, Sundaram Senthilarasu, Townley Stuart, Mallick Tapas	145
Large Area Deposition of $\text{CH}_3\text{NH}_3\text{PbI}_3$ Films Using Aerosol-Assisted Chemical Vapour Deposition Heather M. Yates and Mohammad Afzaal	149
Process Development of Sublimated Cu-free CdTe Solar Cells C. Potamialis, F. Lisco, B. Maniscalco, M. Togay, J. W. Bowers and J. M. Walls	153

## **PVSAT-13 PAPERS**



## Novel Deposition Method to Print Binder-Free Inks on Large Scale Carbon Perovskite Solar Cells

S. M. P. Meroni,<sup>†</sup> F. De Rossi,<sup>†</sup> A. Pockett,<sup>†</sup> T. De Brito Melo,<sup>†</sup> R. Escalante,<sup>‡</sup> J. Searle,<sup>†</sup> J. Baker,<sup>†</sup> Y. Mouhamad,<sup>†</sup> M. J. Carnie,<sup>†</sup> E. Jewell,<sup>†</sup> G. Oskam<sup>‡</sup> and T. Watson<sup>\*†</sup>

<sup>†</sup> SPECIFIC, Bay Campus, SA1 8EN, Swansea, UK.

<sup>‡</sup> CINVESTAV—IPN, Unidad Mérida. C.P. 97310, Mérida, Yuc., México.

\* Corresponding Author T.M.Watson@Swansea.ac.uk

### Introduction

Organic-inorganic halide perovskite is a class of material that allows the preparation of efficient thin film solar cells via solution phase deposition. Since the first application in photovoltaic cells, astonishing results have been achieved with different architectures on both rigid [1, 2] and flexible [3] substrates. The high performance and ease of processing make perovskite solar cells (PrSCs) promising for future application and commercialization. However, some issues need to be addressed, in particular the high cost of materials, the stability, and issues related to the technology up-scaling.

Han and co-workers have developed a fully printable architecture based on a mesoporous stack (mStack) which includes a titanium dioxide ( $\text{TiO}_2$ ) film, zirconium dioxide ( $\text{ZrO}_2$ ) as insulating spacer and conductive carbon as top contact. The perovskite solution can be dropped on the top layer and infiltrates through the mStack of the carbon PrSC (CPrSC) [4]. The CPrSC architecture is characterized to be fully printable, stable over 1000 hours under continuous 1 sun illumination [5], and does not contain unstable and expensive organic materials such as Spiro-OMeTAD. A crucial issue is the deposition and subsequent infiltration of perovskite precursor solutions, which needs to be as homogeneous as possible to give efficient modules. The infiltration occurs usually by drop deposition [5] and, very recently, by inkjet printing [6]. Drop deposition does not allow a controlled deposition and is only suitable for small scale devices. Inkjet printing allows controlled and uniform depositions but the droplets of solution are deposited one-by-one and it requires a large number of nozzles to print over a large area in a reasonable time scale [7]. Other printing techniques, such as screen and flexographic printing, requires inks with binders to tune the rheological properties of the solution. However, binders may effect the electrical properties of the final layer and are often removed by heating above 400°C, which is too high for perovskite films [7, 8].

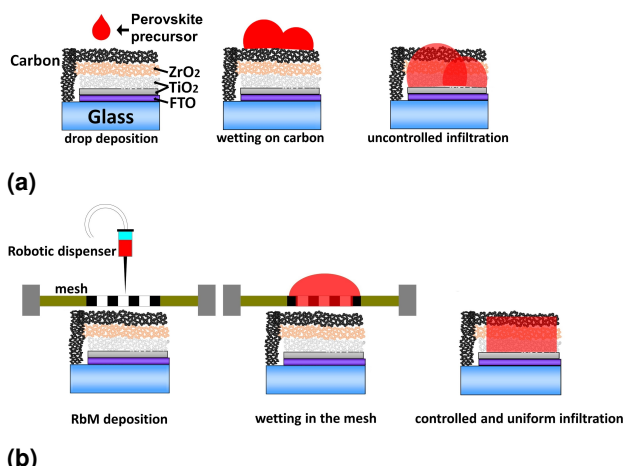


**Figure 1** Schematic representation of (a) the drop process and (b) the RbM deposition of perovskite precursor solutions on carbon perovskite solar cells (CPrSCs).

In this work, we present a novel deposition method, which involves the use of a robotic dispenser and a mesh to easily and quickly deposit binder-free inks, such as perovskite solutions, homogeneously on a large area (Fig 1). In this robotic mesh (RbM) deposition technique, the automated dispenser controls the amount of solution to be deposited, whereas the mesh spreads the liquid on a selected area by generating many little droplets, as in inkjet printing but all simultaneously. The effectiveness of the RbM technique was compared to the optimized drop deposition in terms of performance and stability on 1 cm<sup>2</sup> device. A 2-step deposition method, where  $\text{PbI}_2$  is dropped into the film and converted by immersion of the whole film in a methylammonium iodide (MAI) solution to form methylamine lead iodide ( $\text{CH}_3\text{NH}_3\text{PbI}_3$ ) perovskite, was adopted. In fact, the infiltration of  $\text{PbI}_2$ , bright yellow, allows a visual monitoring of its infiltration in the mStack. Devices prepared by RbM were compared to control cells in terms of performance and stability. Measurements of external quantum efficiency (EQE) and electrical impedance spectroscopy (EIS) were carried out to confirm the results.

## Experimental

FTO conductive glass ( $7 \Omega_{sq}$ ) was patterned with a Nb: YVO<sub>4</sub> laser before cleaning. After plasma etching treatment, a compact TiO<sub>2</sub> layer was deposited by spray pyrolysis and heated at 550°C. Mesoporous layers of TiO<sub>2</sub>, ZrO<sub>2</sub> and carbon were screen printed and annealed at 550°C (TiO<sub>2</sub>) or 400°C (ZrO<sub>2</sub> and carbon). For the drop method, a drop of saturated (460 mg/mL) PbI<sub>2</sub> in N,N-Dimethylformamide (DMF), kept at 70°C to avoid crystallization, was deposited on the active area of the cells. For the RbM method, the needle dispenser continuously delivered the PbI<sub>2</sub> solution to the mesh surface as it progressed across the sample in a single line. The mesh then allows the PbI<sub>2</sub> to directly descend in small droplet form into the mesoporous stack. A less concentrated (350 mg/mL) PbI<sub>2</sub> solution was used to avoid clogging the needle during the deposition. In both cases, PbI<sub>2</sub> was dried at 70°C in the oven after infiltration, then cells were dipped in a 10 mg/mL MAI solution in 2-propanol (IPA). When the perovskite conversion is completed, the cells were rinsed in anhydrous IPA. Current-voltage (JV) measurement was carried out under Xe lamp calibrated using silicon reference cell and KG5 filter, and using a Keithley 2400 source meter at a scan rate of 20 mV/s between -0.1 V and 1.1 V in forward and reverse scan. The active area was defined through an aperture mask with an area of 9 mm<sup>2</sup>. Stability tests were performed under continuous irradiation from white LEDs in ambient condition (25–30°C, around 50% RH) at both 1 and 0.5 equivalent sun recording a complete JV curve every 15 min in the first 5 hours and every 60 min for remainder of the test. EQE measurements were collected using a QE X10 spectral response machine in the wavelength range between 300 nm and 850 nm in direct current (DC) mode with a light spot of less than 10 mm<sup>2</sup>. EIS measurements were performed on unmasked devices using a Gamry potentiostat and scanning from 1 MHz to 0.1 Hz at open circuit under illumination from LED at 530 nm at 1 equivalent sun. Light intensity was modulated by using neutral light filters.

## Results and Discussion

**Perovskite infiltration** Contact angle measurement of a PbI<sub>2</sub> solution in DMF on carbon (Fig 2) shows that the liquid is absorbed in the mStack in only 0.3 sec, with an initial angle of only 8°. This suggests that the surface energy of mesoporous carbon is high enough to rapidly absorb the solution and facilitate infiltration in the mStack. Still, the deposition of single droplets and the dispensing of a continuous liquid line causes the DMF solutions to infiltrate but

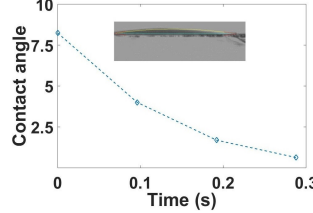


**Figure 2** Contact angle dropping over time of a PbI<sub>2</sub> solution in DMF on a carbon layer due to infiltration. Inset, a droplet at time 0.

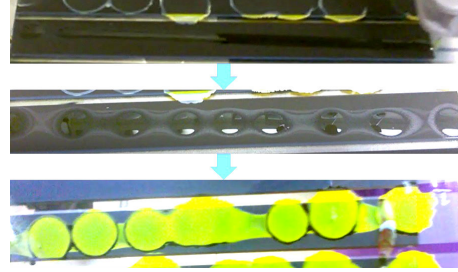


**Figure 3** Deposition of PbI<sub>2</sub> solution on mesoporous stack. A PbI<sub>2</sub> solution is deposited as continuous line over a carbon stripe; the liquid reorganizes in drops; the characteristic dot-like pattern is evident from the back side through the glass.

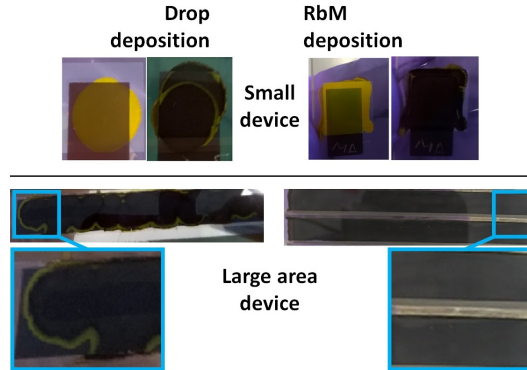


**Figure 4** Devices prepared by drop (LEFT) or RbM (RIGHT) deposition. On the top, small devices (1 cm<sup>2</sup>) before and after conversion of PbI<sub>2</sub>; at the bottom, long stripes (10 cm<sup>2</sup>) after conversion with a blow-up of a selected area.

without spreading across the entire surface (Fig 3). The result is a dot-like pattern of material, as shown in our previous work [9] (Fig 3 and 4), which leads to a relevant portion of the mStack not filling with perovskite, thus not active in light absorption and photocurrent generation.

Moreover, a PbI<sub>2</sub> solution infiltrates in the mStack with a characteristic coffee stain pattern [10], where a high amount of PbI<sub>2</sub> can accumulate at the edges of the ring. At this edge area, the PbI<sub>2</sub> crystals may saturate the pores and do not let the MAI precursor

reach those pores and convert into  $\text{CH}_3\text{NH}_3\text{PbI}_3$ . This is a possible scenario that explains the typical yellow ring that we observe in our devices after drop deposition. By contrast, the RbM method allows greater control over the infiltration by depositing a uniform layer across the surface. Perovskite films deposited by RbM are, in fact, characterized by a controlled geometry and a homogeneous infiltration and improved conversion to  $\text{CH}_3\text{NH}_3\text{PbI}_3$  (Fig 4).

**Cell characterization** Cells made by the RbM method were compared to control (Ctrl) cells obtained using drop deposition. Cells were masked on a dark active area during JV test, thus the effect of the characteristic yellow rings in Ctrl cells cannot be seen in the cell performance.

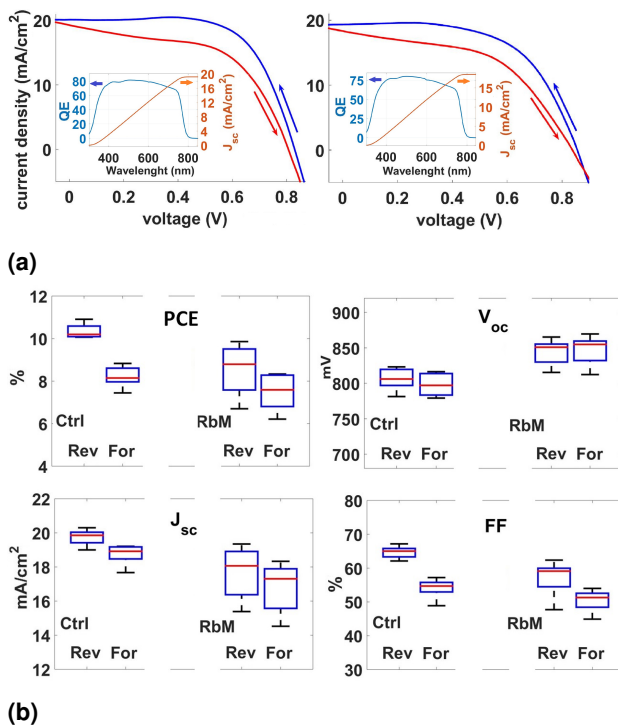


**Figure 5** (a) JV curves of champion devices for RbM (PCE 10.9%) and drop (9.9%) deposition in forward (from low to high voltage) and reverse scan. Inset, EQE spectra of the devices. (b) Statistical analysis of JV data comparing Ctrl and RbM cells.

The JV curves of the champion devices for both methods are comparable (Fig 5a) in terms of both performance and hysteresis. On average,  $J_{sc}$  and FF for RbM are slightly lower than for Ctrl cells, probably because of the lower concentrated  $\text{PbI}_2$  solution that was used. In fact, Ctrl cells were prepared with

a saturated solution of  $\text{PbI}_2$  to enhance the crystal formation. However, saturated solutions of  $\text{PbI}_2$  are prepared at 70°C and re-crystallize at room temperature. Since the temperature of the needle could not be controlled in the experiment, a low concentrated  $\text{PbI}_2$  was used to allow the deposition by RbM. The need of an optimization of the RbM method is also confirmed by the larger standard deviation of cell performance compared to Ctrl cells (Fig 5b). Important parameters to optimize are the dispensing pressure, the amount of liquid to deposit and the needle temperature during the deposition. The temperature of the needle, in particular, can allow the deposition of concentrated solutions, changes in viscosity of the liquid and modification of the evaporation rate of the solvent.

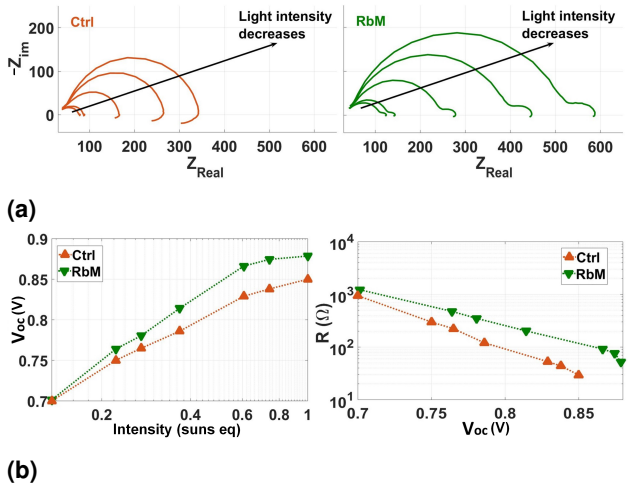


**Figure 6** (a) EIS Nyquist plot at different light intensity of a representative cell per each deposition method. (b) Intensity dependence of the  $V_{oc}$  (LEFT); recombination resistance dependence of the applied voltage,  $V_{oc}$  (RIGHT).

Interestingly, the  $V_{oc}$  of RbM cells is higher than Ctrl ones, likely due to a higher recombination resistance, as confirmed by EIS (Fig 6). The diameter of the arcs determines the resistive elements, which can be related to the recombination resistance due to the linear trend observable with the light intensity [11]. It should be noted that the recombination rate, which is the inverse of the recombination resistance [12], is always faster in Ctrl cells than in RbM for a given voltage (Fig 6b). This effect may be explained considering that RbM allows a more uniform  $\text{PbI}_2$  infiltration and, thus, better pore filling, but more investigation is needed to understand the effect of the RbM deposition.

The EIS present negative loops in Ctrl cells but not in RbM cells (Fig 6a). Although it is not clear how to in-

terpret this effect, the phenomenon can be correlated to the degradation of perovskite [13]. A degradation product of  $\text{CH}_3\text{NH}_3\text{PbI}_3$  is  $\text{PbI}_2$  [14], which is present in the Ctrl cells due to the incomplete conversion.

The negative loops can also be related to the poor charge injection due to the presence of multiple interface layers [15]. The  $\text{PbI}_2$  phase might be seen as further barrier layer in the Ctrl cells.

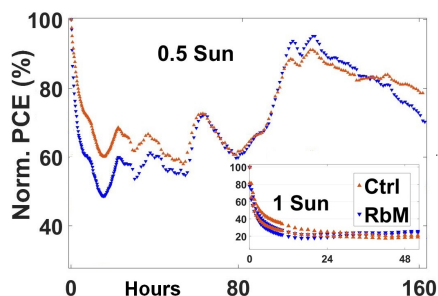


**Figure 7** Normalized PCE of both Ctrl and RbM cells over time during continuous illumination from white LED, at 0.5 and 1 equivalent sun. At 0.5 sun, the drop in PCE is not as severe as under 1 sun and a nearly complete recovery is observed after few days.

Stability tests under LED light soaker were performed with both Ctrl and RbM non-encapsulated cells. Although they degrade in a matter of hours under 1 equivalent sun due to the instability of  $\text{CH}_3\text{NH}_3\text{PbI}_3$  under light in air [14], both types of cells are stable under 0.5 sun for over 160 h (Fig 7). Interestingly, the performance decreases dramatically in the first few hours but an unexpected recovery occurs after a day of continuous exposition. Even a complete recovery is observed after few days of testing.

## Conclusions

RbM is a new deposition technique based on the combined use of a robotic dispenser and a mesh. The liquid can be deposited and allows homogeneous and controlled deposition even over a large area.

RbM was successfully used to prepare CPrSC devices with over 9% PCE, comparable with the control cell performance. JV measurement, stability tests, EQE and EIS were used to compare devices prepared by RbM and a more optimized method, i.e. drop deposition, and confirm the RbM to be effective and reliable.

A further optimization of the method and comparison with other deposition techniques is currently ongoing. The optimized RbM method will then be tested on large scale devices and series connected modules.

## References

- [1] M. Liu, M. B. Johnston and H. J. Snaith, *Nature*, 2013, **501**, 395–8.
- [2] M. Saliba, T. Matsui, J.-Y. Seo, K. Domanski, J.-P. Correa-Baena, M. K. Nazeeruddin, S. M. Zakeeruddin, W. Tress, A. Abate, A. Hagfeldt and M. Grätzel, *Energy Environ. Sci.*, 2016, **9**, 1989–1997.
- [3] J. Troughton, D. Bryant, K. Wojciechowski, M. J. Carnie, H. Snaith, D. A. Worsley and T. M. Watson, *J. Mater. Chem. A*, 2015, **3**, 9141–9145.
- [4] Z. Ku, Y. Rong, M. Xu, T. Liu and H. Han, *Sci. Rep.*, 2013, **3**, 3132.
- [5] A. Mei, X. Li, L. Liu, Z. Ku, T. Liu, Y. Rong, M. Xu, M. Hu, J. Chen, Y. Yang, M. Grätzel and H. Han, *Science*, 2014, **345**, 295–298.
- [6] S. G. Hashmi, D. Martineau, X. Li, M. Ozkan, A. Tiihonen, M. I. Dar, T. Sarikka, S. M. Zakeeruddin, J. Paltakari, P. D. Lund and M. Grätzel, *Adv. Mater. Technol.*, 2016, **4**, 1600183.
- [7] F. C. Krebs, *Sol. Energ. Mat. Sol. Cells*, 2009, **93**, 394–412.
- [8] J. Baker, D. Deganello, D. T. Gethin and T. M. Watson, 2014, **18**, 86–90.
- [9] K. E. A. Hooper, H. K. H. Lee, M. J. Newman, S. Meroni, J. Baker, T. M. Watson and W. C. Tsoi, *Phys. Chem. Chem. Phys.*, 2017, **131**, 6050–6051.
- [10] L. Malfatti, Y. Tokudome, K. Okada, S. Yagi, M. Takahashi and P. Innocenzi, *Micropor. Mesopor. Mat.*, 2012, **163**, 356–362.
- [11] A. Pockett, G. Eperon, N. Sakai, H. Snaith, L. M. Peter and P. J. Cameron, *Phys. Chem. Chem. Phys.*, 2017, **19**, 5959–5970.
- [12] A. Pockett, G. E. Eperon, T. Peltola, H. J. Snaith, A. Walker, L. M. Peter and P. J. Cameron, *J. Phys. Chem. C*, 2015, **119**, 3456–3465.
- [13] Q. Tai, P. You, H. Sang, Z. Liu, C. Hu and L. W. Helen, *Nat. Commun.*, 2016, **6**, 1–8.
- [14] D. Wang, M. Wright, N. K. Elumalai and A. Uddin, *Sol. Energ. Mat. Sol. Cells*, 2016, **147**, 255–275.
- [15] M. Anaya, W. Zhang, B. C. Hames, Y. Li, F. Fabregat-Santiago, M. E. Calvo, H. J. Snaith, H. Míguez and I. Mora-Sero, *J. Mater. Chem. C*, 2017, **5**, 634–644.

# Understanding the Photoelectron Spectroscopy of Perovskites for Photovoltaics

James D McGettrick, Katherine Hooper, Adam Pockett, Jenny Baker, Matthew Carnie and Trystan Watson\*

SPECIFIC, Swansea University, College of Engineering, Bay Campus, Swansea SA1 8EN

\* Corresponding Author: [t.m.watson@swansea.ac.uk](mailto:t.m.watson@swansea.ac.uk)

## Introduction

The emergence of perovskite solar cells based on methyl ammonium lead trihalides ( $\text{MAPX}_3$ ) structures has created a research explosion[1–3]. This group of materials ticks many of the boxes for a new generation of solar cells as they offer substantial power conversion efficiencies in combination with the opportunity for high-throughput reel-to-reel solution processing and the associated potential for low cost manufacture.  $\text{MAPX}_3$  perovskite solar cells also offer other potential benefits such as colour variation and low temperature processing routes. Options remain open for the material choices and structures for  $\text{MAPX}_3$ , which gives a broad and vibrant research field.

Whilst x-ray photoelectron spectroscopy (XPS) has been used previously for studying  $\text{MAPX}_3$  materials, many of the analyses could potentially provide non-specialist surface science groups with considerable insight. This work highlights three aspects of perovskite materials in which XPS analyses offer more information than is currently typically utilised. Understanding the following phenomena will allow greater scope for process optimization, materials optimization and failure modes of such perovskites.

In this work we will focus on three main areas of interest: 1) Quantitative stoichiometry, 2) Importance of peak position, 3) Aging and controlled evolution of inconsistently observed  $\text{Pb}(0)$  peaks[4–8].

## Experimental

All perovskite films were freshly produced in ambient laboratory conditions. FTO glass ( $7 \Omega/\text{sq}$ , Solaronix) was cleaned in 2% hellmanex(aq.), DI water, acetone, isopropyl alcohol (IPA), and a 10 min air plasma clean. A 50 nm layer of  $\text{TiO}_2$  was deposited at by spray pyrolysis ( $300^\circ\text{C}$ ) of titanium diisopropoxide bis(acetylacetone), in IPA (10% v/v).

Mesoporous  $\text{TiO}_2$  layers were obtained by spin coating Dyesol 30NR-D in ethanol (2:7 w/w) at 4500 rpm for 30 s and sintering for 30 min at  $550^\circ\text{C}$ .

Several different cell architectures are discussed within this paper. A brief outline is given below for control hot-plate (HP) samples[9]:

“MAPI”, Methyl Ammonium Lead Iodide, via the sequential deposition route[10]. 1 M  $\text{PbI}_2$  in dimethyl formamide (DMF) was spin coated at 6500 rpm for 1 min, dried at  $70^\circ\text{C}$  for 10 min. The film was then submerged in a solution of 10 mg/ml MAI in IPA, rinsed in IPA and dried/annealed at  $70^\circ\text{C}$  for 30 min.

“MAPIC”, Methyl Ammonium Lead Iodide/Chloride, layers were made from a mixed MAI(Dyesol)/ $\text{PbCl}_2$ (Sigma) precursors solution deposited in a single spin coating step (3:1 molar ratio at 40% w/w in DMF)[2]. After coating at 2000 rpm over 30s, the film is annealed at RT for 10 min and  $100^\circ\text{C}$  for 90 min.

“Triple Cation” layers are deposited via the published method for films of  $\text{Cs}_{0.05}(\text{MA}_{0.17}\text{FA}_{0.83})_{(1-0.05)}\text{Pb}(\text{I}_{0.83}\text{Br}_{0.17})_3$  via the introduction of chlorobenzene anti solvent with 10 s remaining of the precursor spin coating at 1000 rpm for 10 s, 4000 rpm for 20 s. Obtained films were annealed at  $100^\circ\text{C}$  for 60 min.

“Triple Mesoporous Carbon” layers are based on sequential deposition of MAPI in the triple mesoporous  $\text{TiO}_2/\text{ZrO}_2/\text{Carbon}$  architecture utilised by Han *et al*[11]. They utilise radically different film thicknesses and screen printing deposition. Their preparation is outlined in detail elsewhere[9].

Where utilised, near infrared (nIR) heating replaced the final heating step in each case. Typical dwell times in the 24 kW AdPhos nIR/IR Coil Lab LV2 were 2-5 s with lamp intensities optimised in each case.

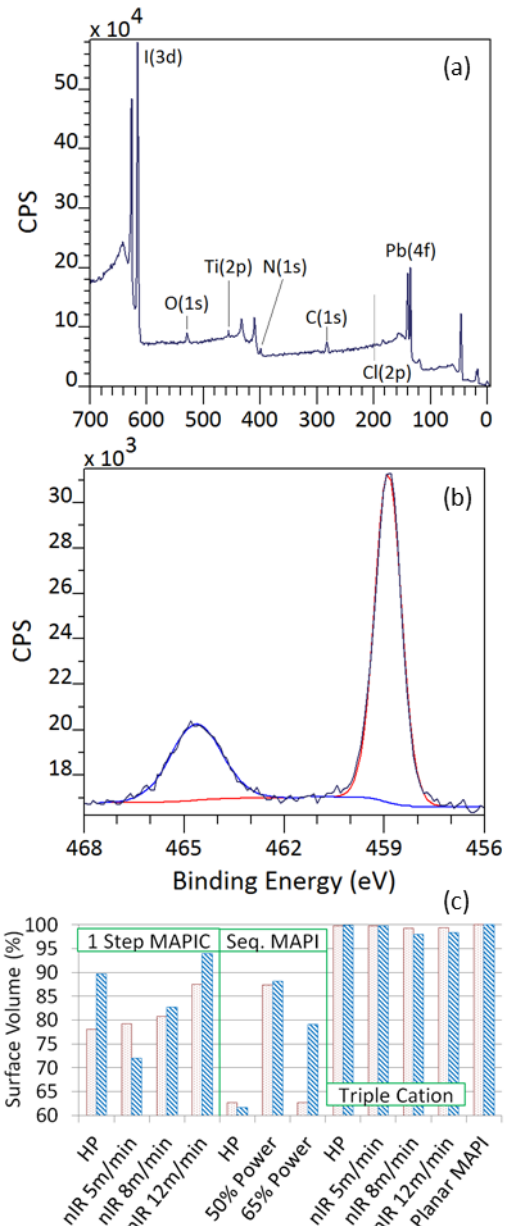


Figure 1. (a) MAPIC HP wide scan & (b) Ti(2p) high resolution. (c) Quantification of perovskite surface volume coverage. Data from centre (red spots) and edge (blue stripes).

XPS was recorded on a Kratos Axis Supra instrument (Kratos Analytical, Manchester, UK) using a 15 mA (225 W) monochromated Al K $\alpha$  source. Typical analytical spot sizes were  $\sim$ 300 x 700  $\mu\text{m}$ . All spectra were recorded using the Kratos charge neutraliser (18.0 mA current, 1.30 V bias & 4.20 V balance). A pass energy of 20 eV was used for high resolution spectroscopy, with 160 eV for wide scans.

Data was quantified using CasaXPS (version 2.3.17dev6.4k) with 0.3:0.7 Gaussian:Lorentzian lineshapes, and Shirley backgrounds, with charge

compensation to the C-C component at 284.8 eV.

### 1. Quantitative Stoichiometry

One area often overlooked is the importance of the wide or survey scan, that should highlight the presence of any element (other than H, He). For MAPIC (Fig 1a), as well as the expected intense Pb & I peaks and contributions from N, C (perovskite & contaminant), signals from the underlying TiO<sub>2</sub> layer are also observed. Cl is not observed.

Indeed these undesired signals such as the Ti(2p) (Fig. 1b), can give insight into the film coating consistency over a large area ( $\sim$ 700 x 300  $\mu\text{m}$  in this case). As XPS samples  $<$ 10 nm, any signal from the underlying TiO<sub>2</sub> is a strong indicator of an incomplete capping layer. Quantifying the amount of Ti and hence TiO<sub>2</sub> present allows for a quantitative estimate of coating quality (Fig. 1c). In this case there is a clear variability in coverage between processing routes with Triple Cation & Planar MAPI films showing excellent coverage, whilst MAPIC and Seq. MAPI give relatively large routes for contact between TiO<sub>2</sub> and the subsequent HTM.

Of particular note is that for MAPIC, the coverage appears to be sensitive to nIR line speeds, with coverage at 12 m/min higher than the HP control.

In addition the 3:1:1 stoichiometric ratio between halide:MA:Pb (or the Triple Cation Equivalent) can offer considerable insight into the quality of the perovskite material itself when combined with the quantitative nature of XPS, and study of peak positions.

### 2. Importance of Peak Position

The importance of peak position can be illustrated with the N(1s) spectra for this set. Two peak positions are typical for the nitrogen species in perovskites such as MAPIC (Fig. 2a). The predominant peak at 402.1 eV is attributed to charged N $^+$  in the methyl amines in the perovskite structure. Quantification of the N $^+$  gives a 1:1 N $^+$ :Pb ratio. The smaller peak at 400.0 eV is less commonly observed, but is typical for an uncharged organic nitrogen and has previously been observed for adsorbed methyl amine on Pt[12]. Its presence is a strong indicator that the MAI present in the precursor was sufficient to react all the PbX<sub>2</sub>.

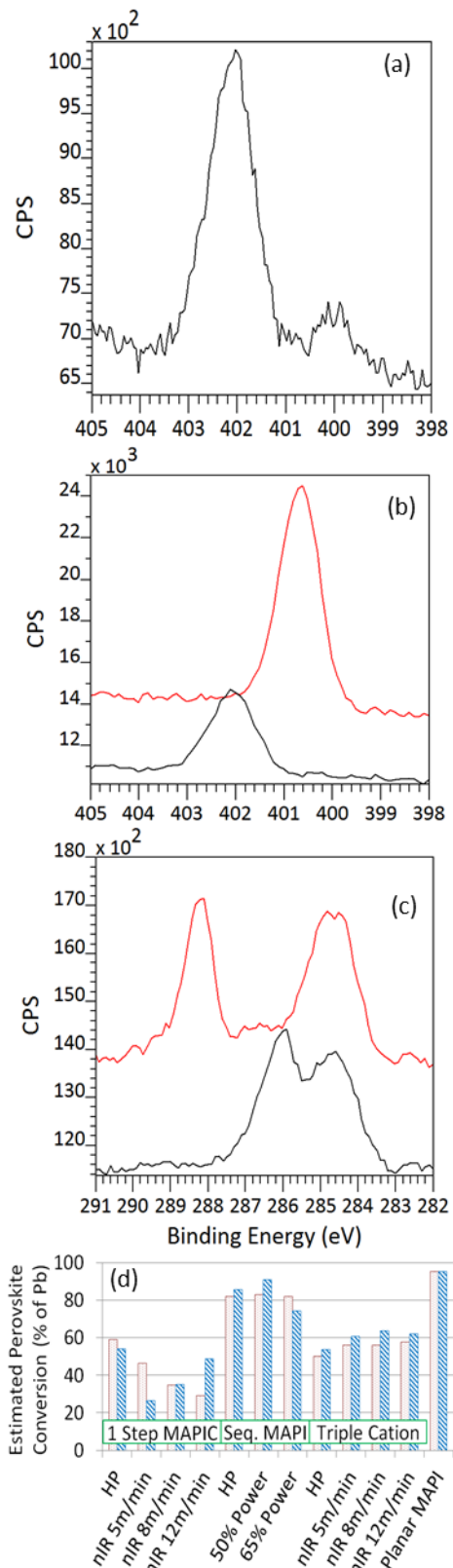


Figure 2. (a) Typical MAPI film with an MAI excess. (b) Variability between MA (black) and FA (red). (c) Variability in carbon peak shifts for MA (black) and FA (red). (d) Utilising measured nitrogen and perovskite stoichiometry to estimate perovskite conversion. Data from film centre (red spots) and edge (blue stripes).

It should be noted that nitrogen peak position is sensitive to local charge (Fig. 2b) and that in the case of formadimium species used in the Triple Cation cells the peak is at 400.4 eV. There is a similar shift in the C(1s) envelope for these materials, with the peak at 286.3 characteristic of MAPIC/MAPI[8] shifting to 288.4 eV for the Triple Cation. These peak shifts highlight that charge is localised on the nitrogen atom in the case of methyl amine and the carbon atom in the case of formadimium. Again the relative stoichiometry of these peaks (C:N) is as expected given the precursor materials.

The N:Pb can be used to generate an estimate of conversion to perovskite across the whole set of process variations (Fig 2d). In all cases beyond the planar MAPIC control, the films are nitrogen deficient. Seq. MAPI shows a high conversion rate at the top surface, with the Triple Cation and 1 Step MAPIC slightly lower. For the entire data set, the residuals after perovskite are accounted for are consistent with a Pb:I ratio of 1:2 or residual  $\text{PbI}_2$  present on the top surface.

### 3. Aging Samples and Pb(0) Evolution.

Treatments similar to those in sections 1 & 2 were carried out on the planar MAPI sample after storage in a dessicator cabinet in the dark for 4 months. 7 points are examined from EME of the 28 mm sample, with points 1-4 notably yellowing and points 5-7 apparently still brown.

Surface coverage drops from 100% to ~98% in the yellowed areas, with only very mild drops on the brown areas (Fig 3a). Using Pb, N & I ratios it is possible to estimate the retained perovskite at this time as only ~25% of the lead on the surface. In the case of the brown area (locations 5-7) the residual is again consistent with  $\text{PbI}_2$ . The yellow region (locations 1-4) is both nitrogen and iodine deficient, which is typical of aging under ambient conditions. Pb here is retained mainly in the Pb(II) oxidation state, and is probably a complex mix of various oxidised lead compounds[13].

Interestingly a strong Pb(0) signal is observed at 136.5 eV, alongside the more pronounced Pb(II) peak at 138.1 eV. The Pb(0) peak is particularly pronounced for the partly degraded brown region. Some examples of degrading perovskites that are clearly more prone to evolution of Pb(0) have already been reported[14].

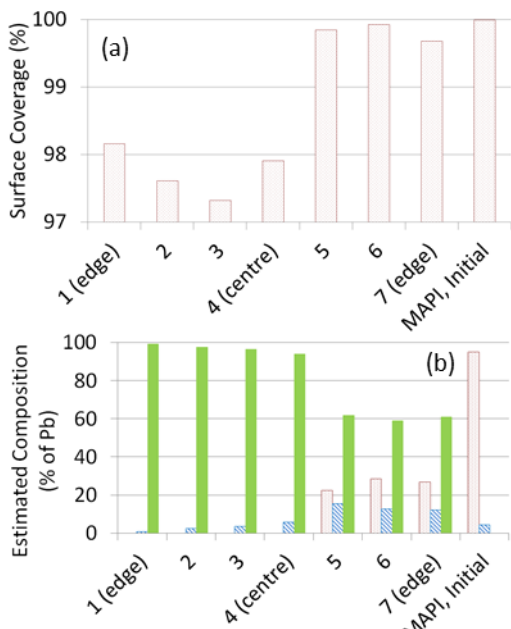


Figure 3. Aging of MAPI (a) Perovskite surface volume coverage, (b) Estimated proportion of MAPI (red spots), Pb(0) (blue stripes), other Pb(II) compounds (green).

Pb(0) signals are intermittently observed in the literature. Most reports suggest that perovskite is stable under conditions used for spectroscopy, but other reports suggest beam damage as a likely cause. The presence of these peaks is expected to result in stoichiometric errors and cause evolution of electron density to Fermi level. We have observed that stresses can be applied that will cause evolution of the Pb(0) peak over time on otherwise pristine perovskite films (Fig 4.) and conversely do not observe this peak under typical controlled analysis conditions for fresh films.

#### Conclusions

The use of XPS to quantitatively assess the quality of a range of perovskite films is presented. Surface coverage defects can be identified and quantified. The overall conversion of the precursors can also be estimated and it is clear that in most cases the surfaces are methyl amine or formamidium deficient, leaving  $\text{PbI}_2$  on the surface. Analysis of peak positions indicates differences in bonding between the methyl amine and formamidium ions. Finally, aged MAPI samples show methyl amine deficiencies and a tendency to form Pb(0).

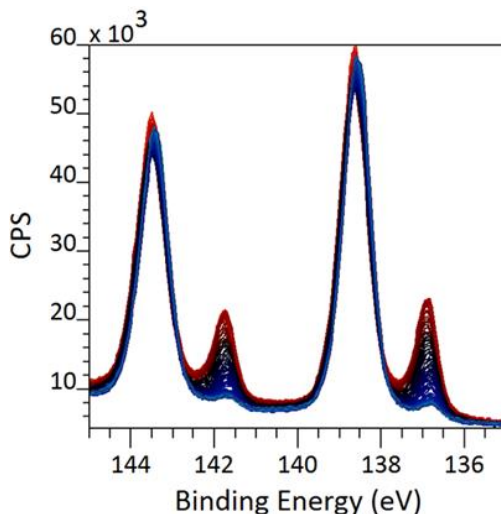


Figure 4. Controlled evolution of Pb(0) peaks on Triple Mesoporous Carbon cells.

1. A. Kojima, K. Teshima, Y. Shirai, and T. Miyasaka, *J. Am. Chem. Soc.*, 2009, **131**, 6050–1.
2. M. M. Lee, J. Teuscher, T. Miyasaka, T. N. Murakami, and H. J. Snaith, *Science*, 2012, **338**, 643–7.
3. H.-S. Kim et al, *Nature*, 2012, **591**, 1–7.
4. B. Conings et al, *Adv. Mater.*, 2013, **26**, 2041–6.
5. R. Lindblad et al, *J. Phys. Chem. Lett.*, 2014, **4**, 3–8.
6. A. Calloni et al, *J. Phys. Chem. C*, 2015, **119**, 21329–21335.
7. H. Xie, X. Liu, L. Lyu, D. Niu, Q. Wang, J. Huang, and Y. Gao, *J. Phys. Chem. C*, 2015, **120**, 215–220.
8. S. R. Raga, M. C. Jung, M. V. Lee, M. R. Leyden, Y. Kato, and Y. Qi, *Chem. Mater.*, 2015, **27**, 1597–1603.
9. K. E. A. Hooper et al, *Phys. Chem. Chem. Phys.*, 2017, **131**, 6050–6051.
10. J. Burschka, N. Pellet, S.-J. Moon, R. Humphry-Baker, P. Gao, M. K. Nazeeruddin, and M. Grätzel, *Nature*, 2013, **499**, 316–9.
11. A. Mei, X. Li, L. Liu, Z. Ku, T. Liu, Y. Rong, M. Xu, M. Hu, J. Chen, Y. Yang, M. Grätzel, and H. Han, *Science*, 2014, **345**, 295–8.
12. J. J. Chen and N. Winograd, *Surf. Sci.*, 1995, **326**, 285–300.
13. W. Huang, J. S. Manser, P. V. Kamat, and S. Ptasinska, *Chem. Mater.*, 2016, **28**, 303–311.
14. B. Conings et al, *Adv. Energy Mater.*, 2015, **5**, 1–8.

# Thermo-Mechanical Stresses of Silicon Photovoltaic Modules

Michael Owen-Bellini\*, Jiang Zhu, Thomas R. Betts, Ralph Gottschalg

Centre for Renewable Energy Systems Technology, Wolfson School of Mechanical, Electrical and Manufacturing Engineering, Loughborough University, Loughborough, Leicestershire, LE11 3TU

\* Corresponding Author: M.Owen-Bellini@lboro.ac.uk

## Abstract

Modelling and analysis of the thermo-mechanical behaviour of silicon photovoltaic (PV) modules has been conducted using finite-element numerical methods (FEM). Experimentally determined material properties have been implemented in the model to represent the 6-cell mini-modules fabricated at the Centre for Renewable Energy Systems Technology (CREST). The stresses generated during indoor accelerated ageing tests and real outdoor conditions have been compared. It is found that the thermo-mechanical stresses are highest at the extreme temperatures during indoor testing. The outdoor accumulated stress generated within the interconnecting ribbons is greater than the stress generated during indoor thermal cycling programs for the same amount of temperature travelled. The results shed light on the relevance of indoor accelerated ageing programs to real outdoor conditions.

## Introduction

Solder bond failures, cell cracks and encapsulant delamination are mechanisms which contribute significantly to the degradation of modules. Such mechanisms can be attributed to the unavoidable thermo-mechanical strains which are induced during normal operation of the devices [1-2]. Mismatches in material properties, most notably the coefficient of thermal expansion, results in the generation of compressive and shear stresses within the module components. Thermo-mechanical degradation mechanisms have previously been identified as critical. They are tested for in type approval tests [3]. The tests are largely empirical in nature and whilst they are useful in identifying critical issues with module designs, they are no predictor of service life. The complexities of the outdoor environments and a lack of understanding of the mechanical behaviour of modules

are some of the reasons why such tests have not been improved upon.

The complex nature of PV module assemblies makes it difficult to measure the internal stresses. In this work, the finite-element method is employed to estimate the stresses and strains which are generated during indoor accelerated test conditions and in outdoor conditions at Loughborough. The results presented highlights the relevance of indoor accelerated ageing to long-term fatigue and service life estimations for field deployed modules.

## Finite-Element Model

### Geometry

A finite-element model has been developed to reflect the mini modules which are produced at CREST. The modules contain six mono crystalline silicon cells connected in series via solder-coated copper-based ribbons. The active circuit is encapsulated in ethylene vinyl-acetate (EVA) which binds together a float glass front cover and polymeric backsheet. The dimensions for each component have been summarised in Table 1.

Component	Length	Width	Height
Cell	156	156	0.22
Glass	538	359	2.9
EVA	538	359	0.62
Backsheet	538	359	0.41
Ribbons	Var.	1.5	0.13
Solder	Var.	1.5	0.02

Table 1: Dimensions of the elements in the modules, mm

Symmetry boundary conditions have been applied which effectively halves the model and reduces the computational requirements without compromising the accuracy of the results. The screen capture

in Figure 1 demonstrates a cross-sectional view of the model, focusing on the interconnection between two cells.

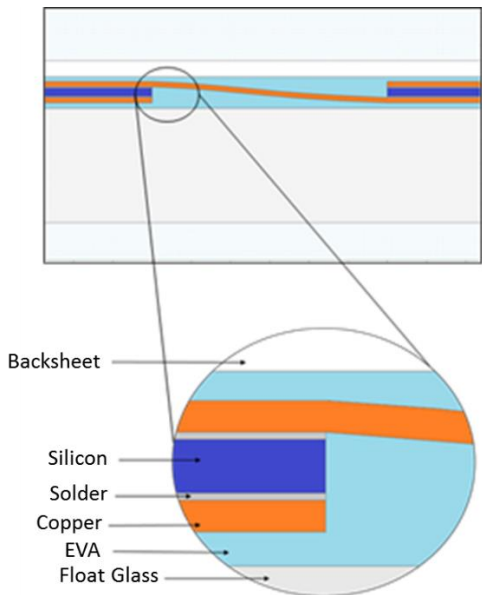


**Figure 1: Cross-sectional screen capture for the FEM model**

### Material Properties

User-inputted material properties are required for FEM simulations. The relevant properties in this model are the coefficient of thermal expansion (CTE), Young's Modulus (or Shear Modulus) and Poisson's ratio. To get the most accurate results, it is important to provide the model with accurate material property values. These have been obtained experimentally for the materials used in the modules produced at CREST. The glass, ribbons and backsheets all exhibit linear material properties, such that determining their values is relatively simple. For CTE and Young's modulus, a TA Instruments Q400 thermomechanical analyser is used. EVA is a complex polymer with viscoelastic properties and as such requires a more complex modelling approach to capture its behaviour.

### Viscoelasticity of EVA

Viscoelasticity describes materials which exhibit both elastic and viscous characteristics. For an applied strain, the generated stress is dependent on both temperature and time. This kind of behaviour can be significant when considering the range of operating temperatures and the rate of change of temperature experienced by PV modules.

According to the Generalised Maxwell Model, the viscoelastic behaviour of a material can be represented as a number of spring-dashpot elements combined in parallel. The springs and dashpots represent the elastic and viscous portions of a single Maxwell element, respectively. The model requires that the elasticity and viscosity of each Maxwell branch be quantified. The necessary values can be determined experimentally using a TA Hybrid-2 rheometer. Storage (or shear) modulus is measured over a range of oscillatory frequencies at multiple isotherms ranging from -40 to 150°C in steps of 10°C. The measurements can then be fit to the Generalised Maxwell model to determine the number of Maxwell elements required, and the Maxwell element parameter values.

Stress relaxation is indicative of viscoelastic behaviour and can be used to validate the model. A rapid step deformation is applied to a small sample of EVA, and the stress required to hold that deformation is measured over time such that relaxation can be observed. The experiment is conducted with the same rheometer at isotherms of -20, 0, 40 and 80°C. The same experiment is then modelled in COMSOL Multiphysics, with the Generalised Maxwell Model parameters applied to the material properties of EVA. Figure 2 below demonstrates the model's suitability to capturing the relaxation behaviour (and therefore viscoelastic behaviour) of the EVA, with an observed root mean squared error of 0.12.

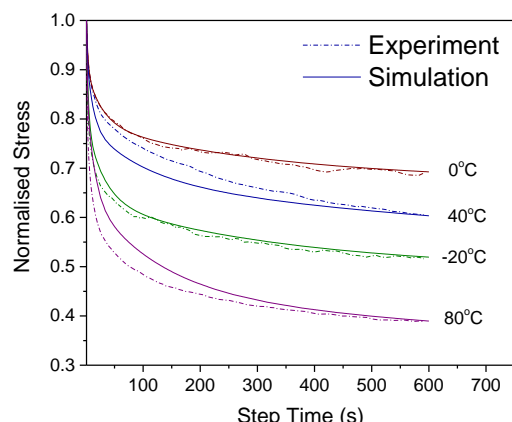


**Figure 2: Simulated and measured stress relaxation test used as a means of validating viscoelastic model**

The material properties for all components have been summarised in Table 2.

Component	CTE ( $10^{-6}/K$ )	Young's Modulus (GPa)	Poisson Ratio
Cell	2.6	170	0.28
Glass	9	73.1	0.17
EVA	Viscoelastic		0.49
Backsheet	150	3.2	0.4
Ribbons	17	110	0.35
Solder	10	10	0.4

**Table II: Summary of material properties used in the simulations**

### Loading Conditions

Loading conditions are required to simulate the effect that external forces have on the model. In this case, module operating temperatures are applied to simulate the thermally-induced mechanical strains. Two thermal profiles are used. Case A is the indoor accelerated temperature profile which are applied during accelerated ageing testing procedures. Case B is module temperature measurement data taken directly from the rear surface of modules installed at the outdoor monitoring facility at CREST for a typical day in June. For simplicity, module temperature is assumed to be homogenous through all components. Total temperature travelled is the absolute sum of the temperature changes during a period of time. Here it is used as a means of normalising the thermal profiles used. One cycle from Case A is equivalent to 250°C travelled. For 1 day of real data in case B, the total temperature travelled is 501°C, approximately equivalent to 2 thermal cycles.

### Mechanical Behaviour

Applying case A allows the mechanical behaviour to be observed at the extreme temperatures. The stresses observed in the glass and backsheet (Figure 3) reveals more about the behaviour at low temperatures and the reasons for mechanical deformation. The colour bar represents the Von Mises stresses which are highest in the backsheet and inner surface of the glass. The arrows represent the 3rd principal stresses, and are effectively a representation of the type of stress, with red and blue arrows

representing tensile and compressive stresses, respectively.

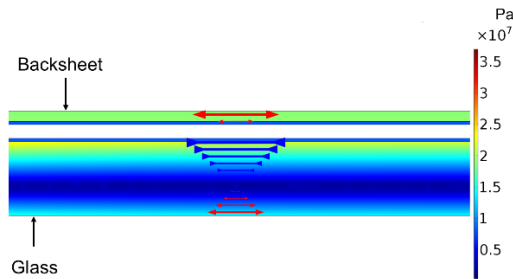


**Figure 3: Stresses on the backsheet and glass at -40°C. Colour bar represents Von Mises stress and arrows indicate 3rd Principal Stress**

The 3rd principal stress indicates that the backsheet and front surface of the glass are in high tension, whereas the inner surface of the glass is in compression. This behaviour can be attributed to the mismatch in coefficient of thermal expansion, which is much greater in the backsheet than the glass. As the module temperature decreases, the backsheet tries to shrink faster than the other components. Without the freedom to shrink as required, the backsheet is pulled in tension. The contraction of the backsheet and EVA pulls on the glass, which does not contract as rapidly. This causes the module to bend and applies stresses on the cells and interconnects. The negative values for 3rd principal stresses on the cells, as shown in Figure 4, reveals that they are under high compressive stress due to the contraction and deformation of the other components. Such stresses can be responsible for the initiation and propagation of cracks. The maximum compressive stress on the cell for case A was found to be 145MPa, whereas for case B it was found to be much less at 94.7MPa.

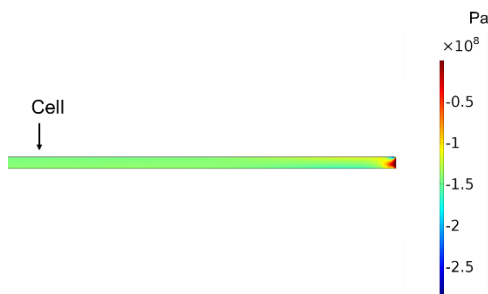


**Figure 4: 3rd Principal stress observed on the silicon cells**

Contraction of the assembly forces the cells to move closer together. This displacement generates shear stresses on the interconnecting ribbons and solder bonds.

The stress tensor in the x-direction for the interconnections are shown in Figure 5. It is seen that the stress is lower on the ribbon bend between the cells due to its flexibility and freedom to move as the cells move closer.

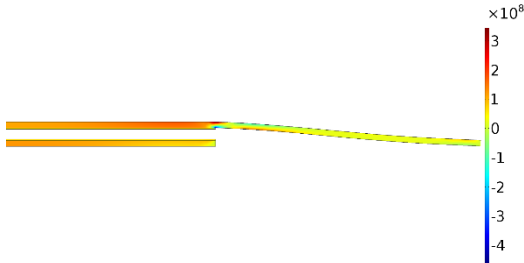


**Figure 5: Stress tensor in the x-direction on the interconnecting ribbon and solder**

### Stress Accumulation of Solder Bonds

Degradation of solder bonds is the critical failure mechanism attributed to thermomechanical degradation. For each thermal profile case, the accumulated stress on the solder bonds is calculated. It is shown in Figure 6 that the accumulated stress on the solder bonds is highest in the outdoor environment.

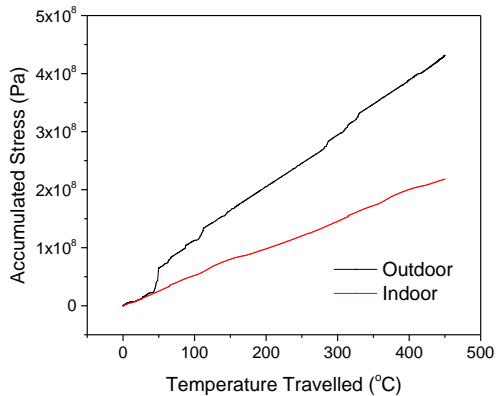


**Figure 6: Accumulated stresses on solder bonds for indoor and typical outdoor conditions in June over the same temperature travelled**

Even though the maximum stress observed during indoor thermal cycling is higher, the continual fluctuation and cycling of temperatures in the outdoors results in an increased accumulation of stress on the solder bonds. It is this accumulation of stresses and continuous cycling that results in the fatiguing and degradation of the solder bonds, leading to increased series resistance and power loss until the bonds

become completely disconnected and total failure of the device occurs.

### Conclusions

Simulations of the thermomechanical behaviour of monocrystalline silicon mini modules during indoor and outdoor thermal cycling have been conducted. It is found that mismatched material properties cause the backsheet and glass front cover to experience high tensile stress as the components contract at low temperatures resulting in a deformation of the module assembly. Because of the deformation, the cells are under high compressive stresses, whilst the displacement of the cells causes the interconnecting ribbons and solder bonds to experience shear stresses. Whilst the maximum observed stress is highest during indoor accelerated testing, the accumulation of stresses on the solder bonds are greater in outdoor conditions. This is likely a result of the continual fluctuation of temperature experienced in outdoor climates. These results could indicate that the stresses which are generated during accelerated testing are too extreme, and whilst they are useful for testing modules for their susceptibility to high levels of stress, they may not be so useful in quantifying long-term fatigue mechanisms and effective service life.

### References

- [1] J.-S. Jeong, N. Park, and C. Han, "Field failure mechanism study of solder interconnection for crystalline silicon photovoltaic module," *Microelectron. Reliab.*, vol. 52, no. 9–10, pp. 2326–2330, Sep. 2012.
- [2] W. Herrmann, N. Bogdanski, F. Reil, M. Köhl, K. –. Weiss, M. Assmus, and M. Heck, "PV module degradation caused by thermomechanical stress: real impacts of outdoor weathering versus accelerated testing in the laboratory," *Proc. SPIE*, vol. 7773, no. 1, p. 77730I–77730I–9, 2010.
- [3] "61215. Crystalline Silicon Terrestrial Photovoltaic (PV) Modules—Design Qualification and Type Approval," *International Electrotechnical Committee*, vol. 3, 2005

# Perovskite-Silicon Tandem Cells Utilizing a Semi-Transparent Silver Nanowire Composite Electrode

Adam Pockett<sup>1</sup>, Sultan Zhantuarov<sup>2</sup>, Harry Lakhiani<sup>1</sup>, Joel Troughton<sup>1</sup>, Trystan Watson<sup>1</sup>, Nurlan Tokmoldin<sup>2</sup>, Matthew Carnie <sup>\*1</sup>

1. SPECIFIC, College of Engineering, Swansea University, Bay Campus, Fabian Way, Swansea, SA1 8EN

2. Institute of Physics and Technology, Almaty, Kazakhstan

\* corresponding author e-mail: m.j.carnie@swansea.ac.uk

## Abstract

We have utilised a semi-transparent composite silver nanowire electrode which can be deposited using a spray or spin coating technique. The layer has a sheet resistance of  $40 \Omega/\square$  with broad spectral transmission exceeding 70%. This was employed as the top contact in a meso-TiO<sub>2</sub>/Perovskite/Spiro-OMeTAD architecture cell. The bandgap of the perovskite layer was tuned using Br substitution to give a slightly wider, more optimal bandgap for silicon tandem cell application. This has allowed us to produce semi-transparent perovskite cells with a PCE of 12% for a 1 cm<sup>2</sup> active area. A series connected 4-terminal tandem has a  $V_{oc}$  of over 1.5 V.

## Introduction

Prior to reaching commercialisation for wide scale electricity generation, any emerging solar cell technology must inevitably be compared to the current industry standard of silicon photovoltaic devices. Lab based silicon cells have reached efficiencies exceeding 26%, with commercial module efficiencies approaching 20% [1]. The low-cost of producing silicon modules, around \$0.50 per watt, presents a challenging barrier for the commercialisation of emerging technologies [2]. Thin-film devices, predominantly cadmium telluride (CdTe), have attained a respectable market share but do not seem likely to displace silicon PV on a large scale.

One potential route to commercialisation therefore could be to use a complimentary emerging technology to enhance existing silicon module performance in a tandem device architecture. This process would be in addition to the existing silicon PV manufacturing route, where a low-cost top cell could result in a significant efficiency improvement without the need for a completely new manufacturing facility. In order to make this approach viable, the

processing of the top cell needs to be inexpensive and fast.

Whilst silicon PV devices are capable of achieving high efficiencies, the relatively small bandgap (~1.1 eV) is below the optimum for a single junction solar cell [3]. The narrow bandgap gives silicon a broad spectral absorption range, but higher energy photons are not exploited. The excess energy of shorter wavelength photons is lost as photo-generated carriers are thermalised to the band edges. This leads to silicon solar cells having lower open-circuit voltages compared to a material in which higher energy carriers can be extracted, although the broad absorption range does lead to high current densities.

In a tandem device a material with a larger bandgap is placed on top of the silicon cell. This higher bandgap material will absorb most of the shorter wavelength light ( $hv > E_{g,top}$ ), being able to generate a high photovoltage. The top cell needs to be transparent for longer wavelengths ( $hv < E_{g,top}$ ), allowing the silicon device to absorb the red to NIR light as illustrated in Figure 1.

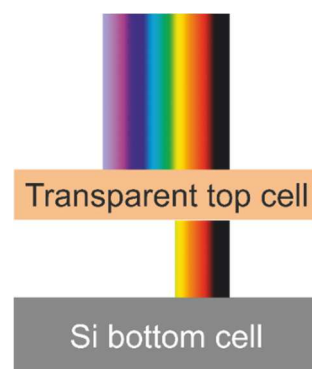


Figure 1: Tandem cell configuration showing absorption of shorter wavelength light by a wider bandgap top cell, allowing longer wavelengths to pass through to be absorbed by the silicon cell.

There are two main approaches to making tandem cell devices. The two sub cells can be mechanically stacked, thus having 4

terminals which can be used to connect the device in series or parallel (or potentially operated individually). Alternatively, the top cell can be deposited directly on to the bottom sub cell resulting in a monolithic device with 2 terminal connections.

The ratio of light that is absorbed in the top and bottom cells is critical to optimising the tandem device. It has been calculated that the optimum bandgap for a silicon based tandem top cell is around 1.75 V, with a theoretical device efficiency limit of around 40% [4, 5]. The bandgap of the perovskite material, methylammonium lead triiodide ( $\text{CH}_3\text{NH}_3\text{PbI}_3$ ), is approximately 1.6 eV which is close to the optimum value for a tandem top cell [6]. It has been shown that the bandgap of the perovskite materials depends on their chemical composition. Changing the methylammonium cation or adjusting the halide can result in materials with different bandgaps [7, 8]. Most commonly the bandgap of the perovskite is increased by the addition of bromide ions. Tuning the iodide to bromide ratio can give materials with bandgaps in the range 1.6 to 2.3 eV [7]. This flexibility of the perovskite has led to reports of several high efficiency tandem devices [9-11].

For a tandem device the current output from both sub cells must be matched in order to achieve high efficiencies. If connected in series (or as part of a monolithic 2 terminal tandem) the current output will be limited by the lower current sub cell. This current matching can be improved by tuning the bandgap and/or optimising the transparency of the top cell (e.g. layer thicknesses).

In this work, a semi-transparent mesoscopic perovskite device was fabricated using a silver nanowire electrode. This device was then connected in series with a silicon solar cell and mechanically stacked on top to create a 4 terminal device.

## Experimental

**Perovskite cell fabrication:** FTO substrates were patterned using Zn powder and 4M HCl acid. Substrates were then cleaned using Hellmanex before rinsing with DI water, acetone and IPA. A compact  $\text{TiO}_2$  blocking layer was deposited using spray pyrolysis at 500°C of a 0.2 M Titanium diisopropoxide bis(acetylacetone) solution in IPA. A mesoporous  $\text{TiO}_2$  layer was deposited by spin coating a solution of diluted titania paste (Dyesol 30 NR-D, 2:7 weight ratio in IPA) at 4000 rpm for 30

seconds. The mesoporous layer was annealed at 550 °C for 30 minutes. The perovskite layer was deposited by spin coating a 1.25M solution of  $\text{CH}_3\text{NH}_3\text{I}$  (Dyesol) and  $\text{PbI}_2$  (Sigma) in a 4:1 (v:v) mixture of DMF and DMSO, at 4000 rpm for 30 seconds. This included the addition of 100  $\mu\text{L}$  of ethyl acetate after 15 seconds to assist in the crystallisation of the perovskite. The films were dried on a hotplate at 100 °C for 10 mins. A hole transport layer of 90 mg  $\text{ml}^{-1}$  spiro-OMeTAD in chlorobenzene (additives: 30  $\mu\text{l ml}^{-1}$  tBP, 20  $\mu\text{l ml}^{-1}$  Li-TFSI solution: 0.6 M in acetonitrile) was spin coated at 4000 rpm for 30 seconds before allowing to dry at room temperature. A solution containing silver nanowires in IPA (Sigma) was sprayed onto the devices which were preheated to 50 °C on a hotplate.

**Characterisation:** Masked devices (1  $\text{cm}^2$ ) were tested under a class AAA solar simulator (Newport Oriel Sol3A) at AM1.5 and 100  $\text{mW cm}^{-2}$  illumination conditions using a Keithley 2400 source meter. EQE measurements were carried out using a PV Measurements QEX10 system. UV-Vis measurements were performed using a Perkin-Elmer Lambda 750 spectrophotometer.

## Results and Discussion

The silver nanowire electrode had a sheet resistance of 40  $\Omega/\square$  with an optical transparency of around 70% at wavelengths between 500 and 1400 nm as shown in Figure 2. This does not include the scattered light component, which may be beneficial to device operation.

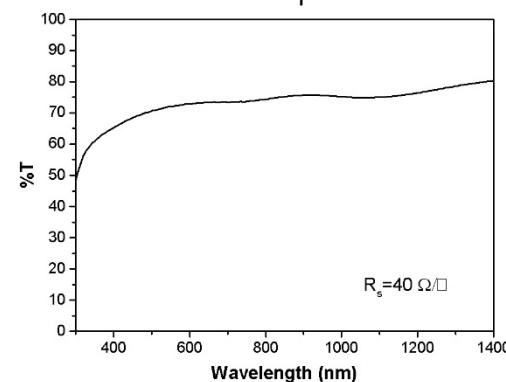
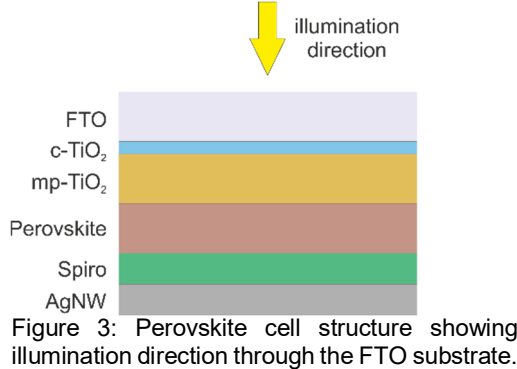


Figure 2: Optical transmission of the silver nanowire electrode.

As the perovskite cell is illuminated through the FTO substrate (Figure 3) only the long wavelength transparency of the nanowire electrode is important as the perovskite layer should absorb most light at shorter wavelengths.



The semi-transparent perovskite devices had a champion cell efficiency of 12.9%. The cells showed minimal hysteresis in the JV curve as shown in Figure 4, as is consistent with devices containing a mesoporous  $\text{TiO}_2$  scaffold. High open-circuit voltages of around 1 V and fill factors in excess of 65% show that the cells were of good quality and that the addition of the sprayed top contact did not cause significant shunting pathways. The devices also had an active area of  $1 \text{ cm}^2$  which is reasonably large compared to many of the perovskite cell record efficiency devices in literature. These larger area devices often suffer from reduced fill factors (and therefore efficiency) due to the increase in series resistance from the larger area.

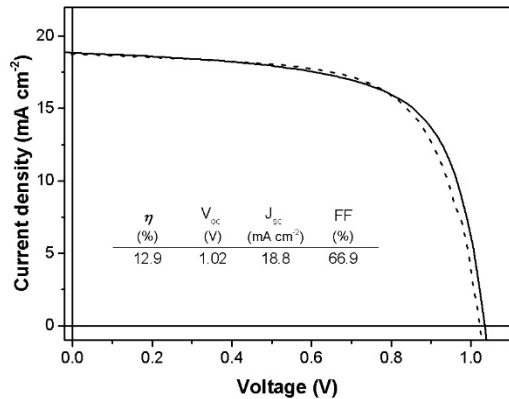


Figure 4: Current-voltage curve for a  $1 \text{ cm}^2$  semi-transparent perovskite cell. The devices show negligible hysteresis.

The transparent perovskite device was then connected in series and placed on top of a silicon PN junction solar cell. The silicon device was also masked to  $1 \text{ cm}^2$ , from a device area of approximately  $2.5 \text{ cm}^2$ . This masking led to a reduction in  $V_{oc}$  from 0.61V to 0.57V, which is relatively low for a silicon solar cell. Figure 5 shows the current-voltage characteristics of the series connected device and the two devices measured separately (the silicon

device was measured with the perovskite device on top).

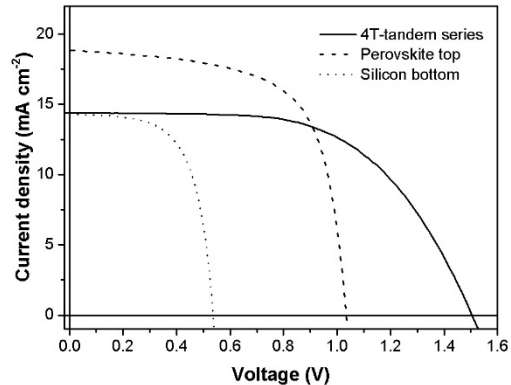


Figure 5: Current-voltage curves of the perovskite top cell, silicon cell with the perovskite cell placed on top to filter out shorter wavelength light, and the two stacked cells connected in series.

The series connected tandem device has an efficiency of 12.7%, which is below that of the unfiltered standalone silicon device (see Table 1). However, the tandem device does generate an open-circuit voltage of 1.5 V which is an important target for applications such as water splitting [12]. It is clear that the two sub-cells are not current matched, with a difference of approximately  $4 \text{ mA cm}^{-2}$  between them. The tandem device is therefore limited by the silicon sub-cell.

Cell	$\eta$ (%)	$V_{oc}$ (V)	$J_{sc}$ ( $\text{mA cm}^{-2}$ )	FF (%)
Perovskite top cell	12.9	1.02	18.8	66.9
Silicon bottom cell	4.9	0.52	14.3	66.5
Silicon standalone	14.9	0.57	36.7	72.0
4T Tandem (series)	12.7	1.50	14.4	58.7

Table 1: J-V device parameters for the individual cells and series connected tandem.

The split in photocurrent generation between the two sub-cells is shown clearly in the external quantum efficiency spectra in Figure 6. It is clear from the difference in integrated area of the two spectra that the silicon device is generating substantially less current. To improve this the transmittance of the top cell at longer wavelengths needs to be enhanced. Either the bandgap of the perovskite layer or the NIR transmittance of the top cell needs to be improved.

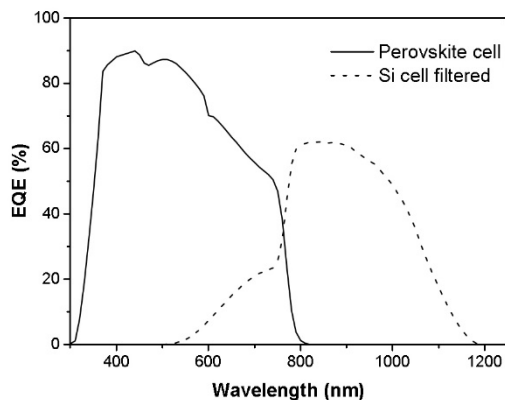


Figure 6: External quantum efficiency spectra of the two sub cells (Si cell filtered by perovskite top cell).

## Conclusion

A 4 terminal series connected tandem solar cell has been constructed from a perovskite solar cell top cell and silicon solar cell bottom cell. The semi-transparent top cell was fabricated using a silver nanowire composite electrode to allow longer wavelength light to pass through to the silicon cell.

The perovskite top cell can be optimised further by tuning the bandgap of the material, as well as improving the transparency of the device to longer wavelength light. Additionally, the use of a higher quality HIT silicon solar cell, with reduced masking, would lead to a much higher performing tandem device.

Whilst the results here do not represent a record perovskite tandem device efficiency, the emphasis here has been placed on using a low-cost, solution processable manufacturing route as opposed to expensive vapour deposition processes [13]. Further optimisation should allow the tandem device performance to exceed that of the standalone silicon device. Indeed, one approach would be to use separate control circuits for each sub-cell which would enable each one to be operated at its own maximum power point [11]. In this way the total tandem efficiency is the sum of the sub-cell efficiencies. In this case it would represent a tandem device efficiency of 17.8%. Of course, the increase in BOS costs should be accounted for before considering this a legitimate approach.

## Acknowledgements

A.P., S.Z., N.T, and M.C. thank the British Council Newton Al-Farabi Partnership Program for funding. J.T. and T.W. thank the EPSRC for funding: SPACE Modules (EP/M015254/1) and SPECIFIC IKC (EP/N020863/1).

## References

- Green, M.A., et al., *Solar cell efficiency tables (version 49)*. Progress in Photovoltaics: Research and Applications, 2017. **25**(1): p. 3-13.
- Green, M.A., *Commercial progress and challenges for photovoltaics*. Nature Energy, 2016. **1**: p. 15015.
- Rühle, S., *Tabulated values of the Shockley–Queisser limit for single junction solar cells*. Solar Energy, 2016. **130**: p. 139-147.
- Martí, A. and G.L. Araújo, *Limiting efficiencies for photovoltaic energy conversion in multigap systems*. Solar Energy Materials and Solar Cells, 1996. **43**(2): p. 203-222.
- Meillaud, F., et al., *Efficiency limits for single-junction and tandem solar cells*. Solar Energy Materials and Solar Cells, 2006. **90**(18–19): p. 2952-2959.
- Umari, P., E. Mosconi, and F. De Angelis, *Relativistic GW calculations on CH<sub>3</sub>NH<sub>3</sub>PbI<sub>3</sub> and CH<sub>3</sub>NH<sub>3</sub>SnI<sub>3</sub> Perovskites for Solar Cell Applications*. Scientific Reports, 2014. **4**: p. 4467.
- Noh, J.H., et al., *Chemical Management for Colorful, Efficient, and Stable Inorganic–Organic Hybrid Nanostructured Solar Cells*. Nano Letters, 2013. **13**(4): p. 1764-1769.
- Eperon, G.E., et al., *Formamidinium lead trihalide: a broadly tunable perovskite for efficient planar heterojunction solar cells*. Energy & Environmental Science, 2014. **7**(3): p. 982-988.
- Bailie, C.D., et al., *Semi-transparent perovskite solar cells for tandems with silicon and CIGS*. Energy & Environmental Science, 2015. **8**(3): p. 956-963.
- Eperon, G.E., et al., *Perovskite-perovskite tandem photovoltaics with optimized bandgaps*. Science, 2016.
- Fu, F., et al., *Low-temperature-processed efficient semi-transparent planar perovskite solar cells for bifacial and tandem applications*. Nature Communications, 2015. **6**: p. 8932.
- Kageshima, Y., et al., *A miniature solar device for overall water splitting consisting of series-connected spherical silicon solar cells*. Scientific Reports, 2016. **6**: p. 24633.
- Bush, K.A., et al., *23.6%-efficient monolithic perovskite/silicon tandem solar cells with improved stability*. Nature Energy, 2017. **2**: p. 17009.

# Optimization of PV-PCM system for South-West UK climate

Sourav Khanna<sup>\*•</sup>, K S Reddy<sup>\*\*</sup> and Tapas K Mallick<sup>\*</sup>

<sup>\*</sup>Environment and Sustainability Institute, Penryn Campus, University of Exeter, Cornwall TR10 9FE, United Kingdom

<sup>\*\*</sup>Department of Mechanical Engineering, Indian Institute of Technology Madras, Chennai 600 036, India

<sup>\*</sup> Corresponding Author [s.khanna@exeter.ac.uk](mailto:s.khanna@exeter.ac.uk)

## Abstract

The conventional silicon photovoltaic (PV) cell manages to convert only a small fraction of the incident solar radiation into electricity. The rest becomes heat which raises the temperature of the PV and decreases its efficiency. The heat generated in the PV can be extracted by attaching a box filled with phase change material (PCM). Due to large latent heat capacity of PCM, it can extract heat from PV without rise in temperature which will lower down the PV temperature and will increase its efficiency. Once the PCM reaches its completely molten state, the incident solar radiation will increase the temperature of the system. Thus, in the current work, the optimum quantity of PCM is calculated to maintain the PV at low temperature for a given amount of solar radiation in a day at Cornwall, UK ( $50.17^{\circ}\text{N}$ ,  $5.12^{\circ}\text{W}$ ). An in-house developed model is used to predict the thermal performance of the inclined PV-PCM system.

## Introduction

The exposure of PV in solar radiation leads to rise in PV temperature which results in decrease in the electrical efficiency [1]. PCM has been used by some researchers to extract the heat from PV. Huang et al. [2-7] have presented the two-dimensional and three-dimensional numerical models and experimental measurements for analysing the thermal performance of PV-PCM system. Hasan et al. [8-9] have analysed the performance by using different types of PCM under different climates. Browne et al. [10-11] have utilized the stored heat in PCM to heat up the water. Sharma et al. [12] have coupled the building integrated concentrated PV with PCM. Brano et al. [13], Smith et al. [14], Aelenei et al. [15], Park et al. [16], Atkin and Farid [17], Kibria et al. [18] and Mahamudul et al. [19] have presented the one-dimensional numerical models to analyse the thermal performance of PV-PCM system. In the current work, the optimum quantity of PCM (i.e. the depth of PCM container) has been found out for Cornwall, UK ( $50.17^{\circ}\text{N}$ ,  $5.12^{\circ}\text{W}$ ) to maintain the PV at low temperature.

## Methodology

In the chosen PV-PCM system, a box filled with PCM is attached at the back of PV panel as shown in Fig. 1. The system is inclined at an angle  $\beta$ . PV panel is considered to be made up of five layers. 1<sup>st</sup> layer (4mm thick) is glass, 2<sup>nd</sup> layer (0.5mm thick) is ethylene vinyl acetate (EVA), 3<sup>rd</sup> layer (0.3mm thick) is silicon, 4<sup>th</sup> layer (0.5mm thick) is EVA and 5<sup>th</sup> layer (0.1mm thick) is teflon. The depth of PCM container is  $\delta$ . The incident solar radiation is considered to be uniformly distributed over the surface of the PV and the contact resistances are not considered in the current work. The bottom and side walls of PCM container are insulated and top wall (4mm thick) of container is made up of aluminium. The convective and radiative heat losses from the top surface of system are considered and can be calculated as follows

$$Q_L = h[T_{at\ y=0} - T_a] + \sigma \varepsilon_t F_{t,s} [T_{at\ y=0}^4 - T_s^4] + \sigma \varepsilon_t F_{t,g} [T_{at\ y=0}^4 - T_g^4] \quad (1)$$

where,  $h$  is the convective heat transfer coefficient of the top surface which is combination of natural and forced convection and can be calculated using the study of Kaplani and Kaplanis [20].  $T_a$  is the ambient temperature.  $\sigma$  is Stefan-Boltzmann constant.  $\varepsilon_t$  is the emissivity for long wavelength radiation of the top surface.  $F_{t,s}$  and  $F_{t,g}$  are the view factors of top surface with respect to sky and ground respectively.  $T_s$  and  $T_g$  are the sky and ground temperature respectively.

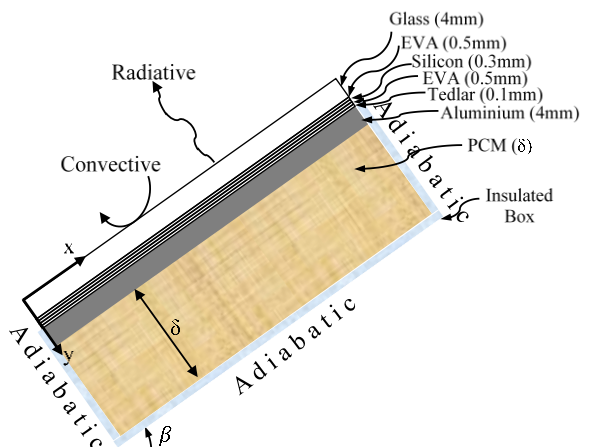


Fig. 1 PV-PCM system

The temperature of the system and velocities in  $x$  and  $y$  directions can be found out by solving below equations

$$\rho C_p \frac{\partial T}{\partial t} = \frac{\partial}{\partial x} \left( k \frac{\partial T}{\partial x} - \rho C_p u_x T \right) + \frac{\partial}{\partial y} \left( k \frac{\partial T}{\partial y} - \rho C_p u_y T \right) + G \quad (2)$$

$$\rho \left( \frac{\partial u_x}{\partial t} + u_x \frac{\partial u_x}{\partial x} + u_y \frac{\partial u_x}{\partial y} \right) = -\frac{\partial p}{\partial x} + \mu \left( \frac{\partial^2 u_x}{\partial x^2} + \frac{\partial^2 u_x}{\partial y^2} \right) + \rho g_x \quad (3)$$

$$\rho \left( \frac{\partial u_y}{\partial t} + u_x \frac{\partial u_y}{\partial x} + u_y \frac{\partial u_y}{\partial y} \right) = -\frac{\partial p}{\partial y} + \mu \left( \frac{\partial^2 u_y}{\partial x^2} + \frac{\partial^2 u_y}{\partial y^2} \right) + \rho g_y \quad (4)$$

$$\frac{\partial u_x}{\partial x} + \frac{\partial u_y}{\partial y} = 0 \quad (5)$$

where  $\rho$  is density,  $C_p$  is specific heat capacity,  $T$  is temperature,  $t$  is time,  $k$  is thermal conductivity and  $u_x$  and  $u_y$  are velocities in  $x$  and  $y$  directions respectively which are 0m/s for solid regions of the system.  $G$  is heat generation in the silicon layer,  $p$  is pressure,  $\mu$  is dynamic viscosity and  $g_x$  and  $g_y$  are accelerations due to gravity in  $x$  and  $y$  directions respectively. The latent heat of PCM has been captured as rise in  $C_p$  during phase change region. The solid-liquid phase change has been taken care of by using very high viscosity for the portion of PCM where temperature is below solidification temperature and low viscosity where temperature is above liquidification temperature.

## Results and Discussion

In the current work, the variations in the temperature of PV-PCM system with time have been computed for various depths ( $\delta$ ) of PCM container for June month at Cornwall, UK ( $50.17^\circ\text{N}$ ,  $5.12^\circ\text{W}$ ). Optimum depth has been calculated to maintain the PV at low temperature. The values of the parameters used for the calculations are presented in Table 1 and 2. The tilt angle of the system is taken as  $45^\circ$  and the PV electrical efficiency at standard test conditions is taken as 20%.

	1 <sup>st</sup> layer	2 <sup>nd</sup> layer	3 <sup>rd</sup> layer	4 <sup>th</sup> layer	5 <sup>th</sup> layer
$C_p$ (kJ/kg-K)	0.50	2.09	0.68	2.09	1.25
$k$ (W/m-K)	1.8	0.35	148	0.35	0.2
$\rho$ (kg/m <sup>3</sup> )	3000	960	2330	960	1200

Table 1 Thermal properties of PV

$C_p$	1.8 kJ/kg-K if $T < 26.1^\circ\text{C}$ 232 kJ/kg-K if $26.1^\circ\text{C} \leq T \leq 27.1^\circ\text{C}$ 2.4 kJ/kg-K if $T > 27.1^\circ\text{C}$
$k$	0.19 W/m-K if $T < 26.1^\circ\text{C}$ 0.18 W/m-K if $T > 27.1^\circ\text{C}$
$\mu$	$10^5$ kg/m-s if $T < 26.1^\circ\text{C}$ 0.001798 kg/m-s if $T > 27.1^\circ\text{C}$
$\rho$	785 kg/m <sup>3</sup>

Table 2 Thermal properties of RT25 PCM

The incident solar radiation on tilted surface and ambient temperature for the chosen month have been plotted in Fig. 2.

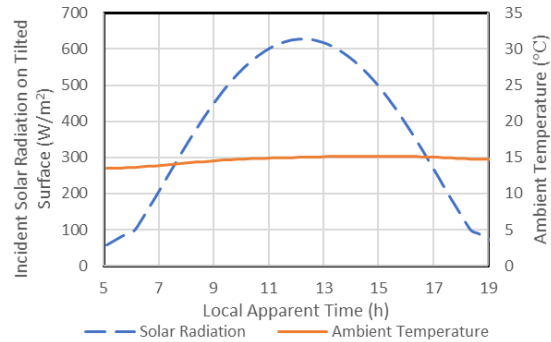


Fig. 2 Variation in the incident solar radiation and ambient temperature with time in June at Cornwall, UK ( $50.17^\circ\text{N}$ ,  $5.12^\circ\text{W}$ )

The variations in the temperature of PV with time have been plotted in Fig. 3 for various depths ( $\delta$ ) of PCM container and the corresponding melting of PCM with time has been shown in Fig. 4 for  $\delta = 2\text{cm}$ . The results show that from local apparent time (LAT) = 0600h to LAT = 0900h, the PV temperature increases rapidly because PCM in the container is in solid phase and its rate of heat extraction is very less due to low thermal conductivity. Beyond LAT = 0900h, the rate of increase in PV temperature slows down because PCM starts melting and extracting heat from PV as latent heat. Beyond LAT = 1300h (for  $\delta = 2\text{cm}$ ), the PV temperature starts increasing rapidly because PCM gets almost fully melted resulting in decrease in the rate of heat extraction and increase in PV temperature.

The results also show that as depth of PCM container increases, the duration increases for which the PV can be maintained at low temperature. However, for a fixed total daily solar radiation, beyond a certain depth, further increase in depth of container does not lead to significant decrease in PV temperature. The results show that, for June month at Cornwall, UK ( $50.17^\circ\text{N}$ ,  $5.12^\circ\text{W}$ ), PCM container with depth as 3cm is the optimum one.

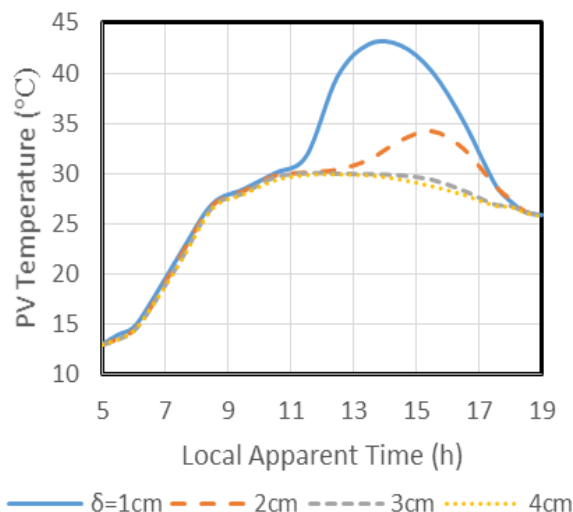
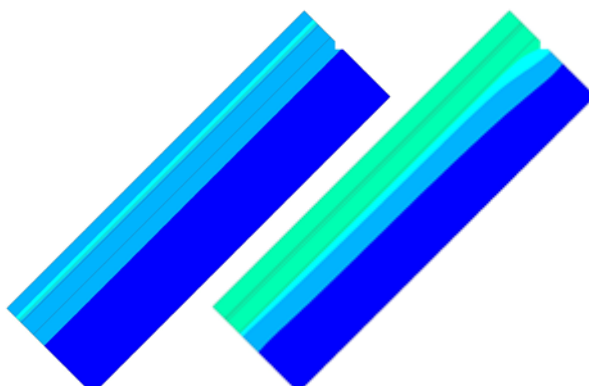
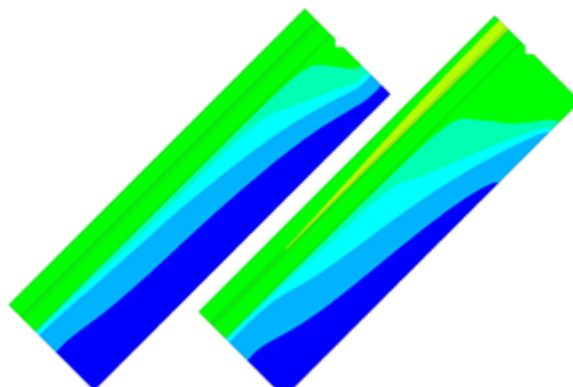


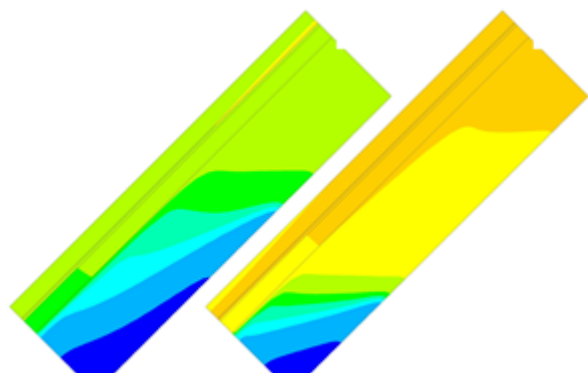
Fig. 3 Variation in the temperature of PV (in PV-PCM system) with time for various values of depth ( $\delta$ ) of PCM container



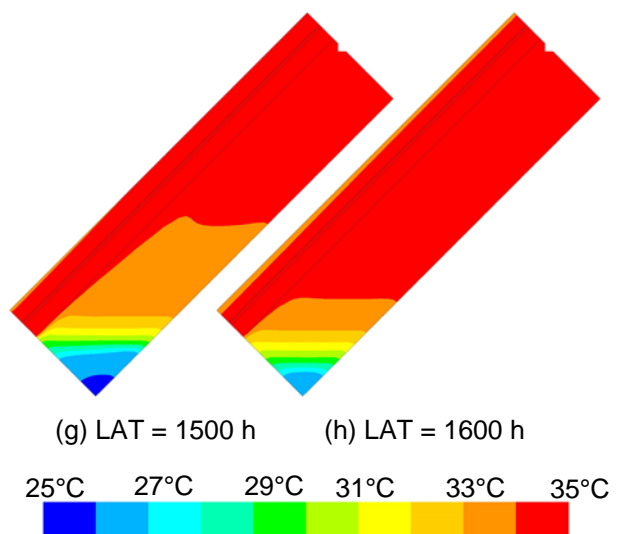
(a) LAT = 0900 h      (b) LAT = 1000 h



(c) LAT = 1100 h      (d) LAT = 1200 h



(e) LAT = 1300 h      (f) LAT = 1400 h



(g) LAT = 1500 h      (h) LAT = 1600 h

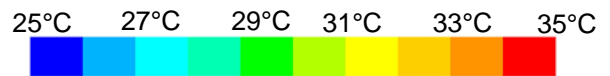


Fig. 4 Variation in the temperature of PV-PCM system with time for depth ( $\delta$ ) of PCM container as 2cm

## Conclusions

In the current work, the variations in the temperature of PV-PCM system with time have been computed for various depths of PCM container for June month at Cornwall, UK ( $50.17^{\circ}\text{N}$ ,  $5.12^{\circ}\text{W}$ ). It has been found that PCM extracts heat from PV as latent heat and lowers down the PV temperature. However, once the PCM reaches its completely molten state, the incident solar radiation increases the temperature of the system. Thus, in the current work, the optimum depth of PCM container is calculated to maintain the PV at low temperature and it is found that 3cm depth of PCM container is the optimum one.

## Acknowledgment

The authors gratefully acknowledge the financial support from EPSRC-DST funded Reliable and Efficient System for Community Energy Solution - RESCUES project (EP/K03619X/1).

## References

- [1] Skoplaki E., Palyvos J.A., 2009. On the temperature dependence of photovoltaic module electrical performance: A review of efficiency/power correlations. *Solar Energy* 83, 614–624.
- [2] Huang M.J., Eames P.C., Norton B., 2004. Thermal regulation of building-integrated photovoltaics using phase change materials. *International Journal of Heat and Mass Transfer* 47, 2715–2733.
- [3] Huang M.J., Eames P.C., Norton B., 2006. Phase change materials for limiting temperature rise in building integrated photovoltaics. *Solar Energy* 80, 1121–1130.
- [4] Huang M.J., Eames P.C., Norton B., 2006. Comparison of a small-scale 3D PCM thermal control model with a validated 2D PCM thermal control model. *Solar Energy Materials & Solar Cells* 90, 1961–1972.
- [5] Huang M.J., Eames P.C., Norton B., 2007. Comparison of predictions made using a new 3D phase change material thermal control model with experimental measurements and predictions made using a validated 2D model. *Heat Transfer Engineering* 28, 31–37.
- [6] Huang M.J., Eames P.C., Norton B., Hewitt N.J., 2011. Natural convection in an internally finned phase change material heat sink for the thermal management of photovoltaics. *Solar Energy Materials & Solar Cells* 95, 1598–1603.
- [7] Huang M.J., 2011. The effect of using two PCMs on the thermal regulation performance of BIPV systems. *Solar Energy Materials & Solar Cells* 95, 957–963.
- [8] Hasan A., McCormack S.J., Huang M.J., Norton B., 2010. Evaluation of phase change materials for thermal regulation enhancement of building integrated photovoltaics. *Solar Energy* 84, 1601–1612.
- [9] Hasan A., McCormack S.J., Huang M.J., Sarwar J., Norton B., 2015. Increased photovoltaic performance through temperature regulation by phase change materials: Materials comparison in different climates. *Solar Energy* 115, 264–276.
- [10] Browne M.C., Lawlor K., Kelly A., Norton B., McCormack S.J., 2015. Indoor characterisation of a photovoltaic/ thermal phase change material system. *Energy Procedia* 70, 163–171.
- [11] Browne M.C., Quigley D., Hard H.R., Gilligan S., Ribeiro N.C.C., Almeida N., McCormack S.J., 2016. Assessing the thermal performance of phase change material in a photovoltaic/thermal system. *Energy Procedia* 91, 113–121.
- [12] Sharma S., Tahir A., Reddy K.S., Mallick T.K., 2016. Performance enhancement of a Building-Integrated Concentrating Photovoltaic system using phase change material. *Solar Energy Materials & Solar Cells* 149, 29–39.
- [13] Brano V.L., Ciulla G., Piacentino A., Cardona F., 2014. Finite difference thermal model of a latent heat storage system coupled with a photovoltaic device: Description and experimental validation. *Renewable Energy* 68, 181–193.
- [14] Smith C.J., Forster P.M., Crook R., 2014. Global analysis of photovoltaic energy output enhanced by phase change material cooling. *Applied Energy* 126, 21–28.
- [15] Aelenei L., Pereira R., Gonçalves H., Athienitis A., 2014. Thermal performance of a hybrid BIPV-PCM: modeling, design and experimental investigation. *Energy Procedia* 48, 474–483.
- [16] Park J., Kim T., Leigh S.B., 2014. Application of a phase-change material to improve the electrical performance of vertical-building-added photovoltaics considering the annual weather conditions. *Solar Energy* 105, 561–674.
- [17] Atkin P., Farid M.M., 2015. Improving the efficiency of photovoltaic cells using PCM infused graphite and aluminium fins. *Solar Energy* 114, 217–228.
- [18] Kibria M.A., Saidur R., Al-Sulaiman F.A., Aziz M.M.A., 2016. Development of a thermal model for a hybrid photovoltaic module and phase change materials storage integrated in buildings. *Solar Energy* 124, 114–123.
- [19] Mahamudul H., Rahman M.M., Metselaar H.S.C., Mekhilef S., Shezan S.A., Sohel R., Karim S.B.A., Badiuzaman W.N.I., 2016. Temperature regulation of photovoltaic module using phase change material: a numerical analysis and experimental investigation. *International Journal of Photoenergy* 5917028, 1–8.
- [20] Kaplani E., Kaplanis S., 2014. Thermal modelling and experimental assessment of the dependence of PV module temperature on wind velocity and direction, module orientation and inclination. *Solar Energy* 107, 443–460.

## New mechanism in proton irradiated CdTe solar cells revealed by SCAPS modelling

\*S. J. C. Irvine<sup>1</sup>, D. A. Lamb<sup>1</sup>, C. I. Underwood<sup>2</sup> and V. Barrioz<sup>3</sup>

<sup>1</sup>Centre for Solar Energy Research, College of Engineering, OpTIC Centre, Swansea University, St Asaph, LL17 0JD, UK

<sup>2</sup>Surrey Space Centre, University of Surrey, Guildford, GU2 7XH, UK

<sup>3</sup>Department of Mathematics, Physics & Electrical Engineering, Northumbria University, NE1 8ST

Corresponding author: [s.j.c.irvine@swansea.ac.uk](mailto:s.j.c.irvine@swansea.ac.uk)

### Introduction

The successful demonstration of high performance CdTe solar cells onto space qualified ultra-thin (100  $\mu\text{m}$ ) glass (UTG) has enabled intense proton radiation tests, simulating the effects of irradiation in space, to be carried out under laboratory conditions [1]. Previous reports of proton irradiation have not had the benefit of the cerium doped radiation hardened glass substrates with inevitable optical loss under higher proton fluences [2]. For the first time, it is possible to model the EQE,  $J_{\text{sc}}$ ,  $V_{\text{oc}}$  and FF of solar cells irradiated with different proton fluences without the parasitic effects of transmission loss in the glass superstrate.

This paper reports on the interpretation of the intense proton induced degradation and partial recovery under low temperature annealing conditions using Solar Cell Capacitance Simulator (SCAPS) modeling [3]. The chosen proton energy was 0.5 MeV to create maximum absorption and therefore maximum damage in the CdTe solar cell. A simulation of the 0.5 MeV proton irradiation through the CdTe face of the solar cell on UTG is shown in Fig. 1. A series of solar cell arrays were measured before and after irradiation with doses ranging from  $1 \times 10^{12} \text{ cm}^{-2}$  to  $1 \times 10^{15} \text{ cm}^{-2}$  with the lowest dose causing negligible degradation and the highest dose reducing the photo-response to zero [4].

The CdTe solar cells were deposited onto space qualified cover glass supplied by Qioptiq Space Technology. All the layers were deposited using Metal-organic Chemical Vapour Deposition (MOCVD) using the process described in [1].

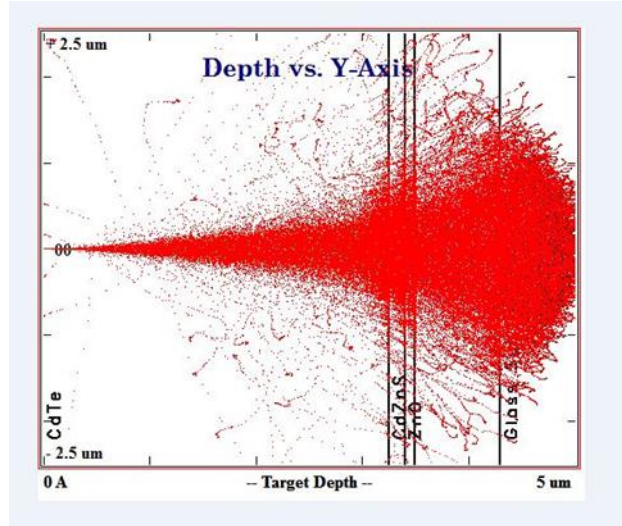


Fig. 1 Simulation of 0.5 MeV proton tracks in CdTe PV structure showing maximum absorption of the protons in the device structure.

### SCAPS Model

The SCAPS model for the un-irradiated PV cells was based on a window layer of  $\text{Cd}_{1-x}\text{Zn}_x\text{S}$ , with bandgap of 2.7 eV and thickness 0.16  $\mu\text{m}$  to give the correct short wavelength EQE response. The modeling of the CdTe layer was based on a reduced bandgap  $\text{Cd}(\text{Te},\text{S}):As$  interface layer of 1.39 eV followed by 1.85  $\mu\text{m}$  thick CdTe:As layer with  $N_a=1 \times 10^{16} \text{ cm}^{-3}$  and a contact layer of CdTe:As. The intermediate low bandgap S diffused layer is based on work by Taylor et al. [5]. This structure for the baseline structure is shown in Fig. 2. For this baseline structure the acceptor doping in the interfacial alloy and the bulk of the CdTe absorber was confirmed by C-V depth profiling of the PV device. A deep level trap, set at 0.7 eV above the VB, was introduced, based on the work of Proskuryakov et al. [6]. The fitted trap density was  $1.5 \times 10^{15} \text{ cm}^{-3}$ . The model fit to the EQE spectrum is shown in Fig. 3 and the J-V parameters in Table 1.

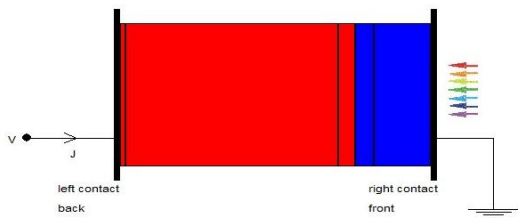


Fig. 2 SCAPS model showing the p-type CdTe layers in red and the n-type window and AZO layers in blue.

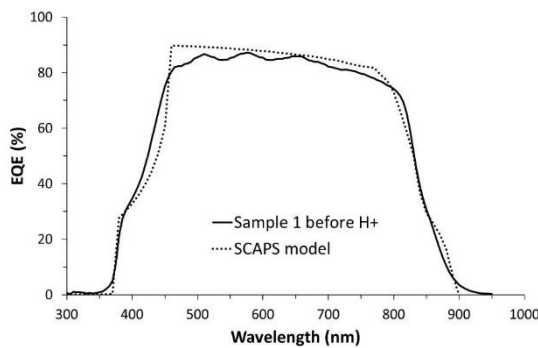


Fig. 3 The measured EQE spectrum for an un-irradiated PV cell (solid line) with the SCAPS model fit (dotted line).

	$\eta$ (%)	$V_{oc}$ (mV)	$J_{sc}$ (mA/cm <sup>2</sup> )	FF
Data	15.5	786	25.1	78.8
SCAPS	13.7	779	23.6	74.4

Table 1 Comparison of the J-V parameters for the un-irradiated PV, between the measured values and the fitted SCAPS model.

### Modeling of $1 \times 10^{13}$ cm<sup>-2</sup> proton irradiated devices

The approach taken with the irradiated solar cells was to keep these baseline parameters the same, as far as possible, and see if the changes in EQE and J-V parameters could be reproduced by just changing a combination of the absorber layer acceptor density or trap density ( $N_a$  or  $N_t$ ) in the CdTe:S and CdTe absorber layers. The values in both layers were kept the same. The irradiation of  $1 \times 10^{13}$  cm<sup>-2</sup> caused a small decrease in average cell efficiency from 12.9 to 11.0 % with most of the decrease occurring in the  $V_{oc}$  and FF. The SCAPS model fit can be seen in the EQE spectrum in Fig. 4 and the J-V parameters in Table 2. An excellent fit is obtained and was achieved with only changing the  $N_a$  value and keeping the trap density the same. The value of  $N_a$  was reduced from  $1 \times 10^{16}$  cm<sup>-3</sup> to  $1.5 \times 10^{15}$  cm<sup>-3</sup>. Attempts at changing the trap density did not improve the fit.

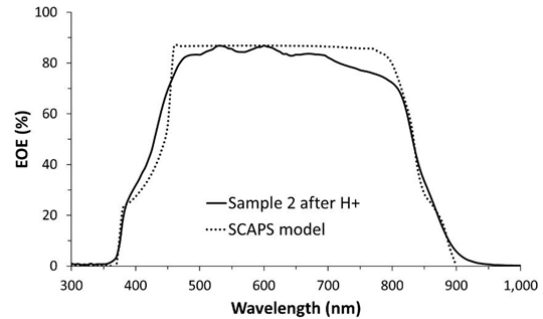


Fig. 4 Comparison of EQE for Sample 2 following  $1 \times 10^{13}$  cm<sup>-2</sup> proton irradiation and the SCAPS model with  $N_a = 1.5 \times 10^{15}$  cm<sup>-3</sup>.

	$\eta$ (%)	$V_{oc}$ (mV)	$J_{sc}$ (mA/cm <sup>2</sup> )	FF
Data	11.0	716	24.2	63.5
SCAPS	10.7	731	23.0	63.4

Table 2 Comparison of J-V parameters following  $1 \times 10^{13}$  cm<sup>-2</sup> proton irradiation between measured values and SCAPS modelling.

### Modeling of $1 \times 10^{14}$ cm<sup>-2</sup> proton irradiated devices

The higher proton dose caused a large decrease in the efficiency from an average of 13.2% to 1%. An inspection of the EQE spectrum, shown in Fig. 5, indicates that the a buried junction had formed with a spike in the EQE close to the band edge. The fitting of the buried junction was more difficult than for the lighter proton dose but the general features of the EQE were obtained with adjusting the carrier concentrations on the n-type and p-type side of the junctions and the junction depth. The trap density was also changed and settled at a slightly lower value of  $7 \times 10^{14}$  cm<sup>-3</sup> although this was similar to the starting value of  $1 \times 10^{15}$  cm<sup>-3</sup> and no great significance can be drawn from this. The main change is in the conversion from p-type to n-type for a depth of 2.2  $\mu$ m. The SCAPS  $V_{oc}$  decreased to 514 mV compared with the measured value of 515 mV. The other parameters had a much poorer fit due to an increase in shunting and reverse bias breakdown in the SCAPS model.

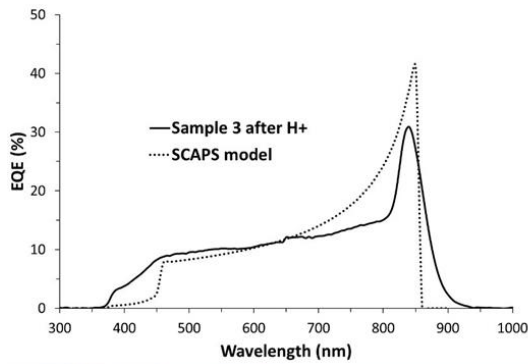


Fig. 5 Comparison of EQE for Sample 3 following  $1 \times 10^{14} \text{ cm}^{-2}$  proton irradiation and the SCAPS model with  $N_a = 9 \times 10^{14} \text{ cm}^{-3}$ ,  $0.3 \mu\text{m}$  thick. For the n-type layer the thickness was  $2.2 \mu\text{m}$ ,  $N_d = 9 \times 10^{14} \text{ cm}^{-3}$ ,  $N_t = 7 \times 10^{14} \text{ cm}^{-3}$ .

#### Low temperature anneal of $1 \times 10^{14} \text{ cm}^{-2}$ proton irradiated devices

A post-proton irradiation anneal was carried out on Sample 3, which experienced a fluence of  $1 \times 10^{14} \text{ cm}^{-2}$  and Sample 5, the control. Using a Carbolite™ tube furnace, under a nitrogen atmosphere and at atmospheric pressure, the samples were held at  $100^\circ\text{C}$  for 168 hours. This test closely simulates MIL-883 – method 1019.8 and is typical of thermal conditions that could be expected in Earth orbit.

Both the sample proton irradiated at  $1 \times 10^{14} \text{ cm}^{-2}$  proton fluence, and an un-irradiated control PV device, were subject to the same inert atmosphere anneal. Figure 6 shows how this simple and a relatively low temperature anneal had a dramatic effect on recovery of the EQE. No significant change was observed in the control PV cell. The efficiency was increased from 4% to 73% of its original performance with no evidence of the buried junction remaining. Relative mean  $J_{sc}$ , which had taken the most significant hit from the proton irradiation, was increased to above the initial mean  $J_{sc}$ , from 22.0 to  $23.0 \text{ mA/cm}^2$ . Figure 7 shows that this is due to an increase in the long wavelength EQE which is similar to the post irradiated EQE for the  $1 \times 10^{13} \text{ cm}^{-2}$  proton dose device. The EQE fit was obtained by adjustment of only the  $N_a$  compared with the baseline device parameters. The fitted  $N_a$  was  $8 \times 10^{14} \text{ cm}^{-3}$ , somewhat lower than the un-irradiate  $N_a$  but with removal of the buried junction, consistent with restoration of the p-type CdTe absorber layer.

The corresponding J-V parameters for the annealed device are shown in Table 3. This shows an excellent fit for all the J-V parameters which is remarkable considering the gross

degradation in performance of the irradiated cell, before anneal.

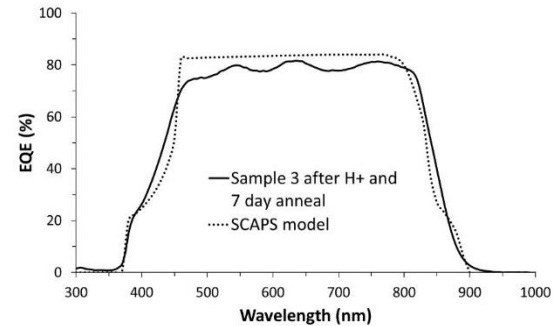


Fig. 6 A comparison of EQE for the  $1 \times 10^{14} \text{ cm}^{-2}$  proton irradiated device, following a low temperature anneal, with the fitted SCAPS EQE curve.

	$\eta$ (%)	$V_{oc}$ (mV)	$J_{sc}$ (mA/cm $^2$ )	FF (%)
Data	9.4	723	23.0	56.5
SCAPS	8.0	723	21.1	52.2

Table 3. Comparison of the measured and SCAPS J-V parameters following the low temperature anneal of the  $1 \times 10^{14} \text{ cm}^{-2}$  irradiated PV devices.

#### Discussion

The SCAPS modelling of the EQE spectra and the J-V parameters shows that the changes that occur during intense proton irradiation can be explained by a change in the acceptor concentration ( $N_a$ ) in the CdTe absorber layer with no significant change in the trap density ( $N_t$ ). This was a surprising result considering that strongly ionising nature of high energy protons. The change in  $N_a$  for the  $1 \times 10^{13} \text{ cm}^{-2}$  proton irradiated devices was confirmed by C-V profiling that gave a bulk  $N_a$  of  $1 \times 10^{15} \text{ cm}^{-3}$  where the unirradiated C-V profile gave a bulk  $N_a$  of  $1 \times 10^{16} \text{ cm}^{-3}$ . This provides excellent corroboration of the SCAPS model fit of  $1.5 \times 10^{15} \text{ cm}^{-3}$ . The formation of a buried junction with the higher radiation dose of  $1 \times 10^{14} \text{ cm}^{-2}$  can be seen as further decrease in  $N_a$  to the extent that donors become dominant for a thickness of  $2.2 \mu\text{m}$ .

The partial recovery after a 7-day low temperature anneal indicated that the compensation was reversible and the C-V profile gave bulk values for  $N_a$  in the range of  $1 \times 10^{14}$  to  $1 \times 10^{15} \text{ cm}^{-3}$ , consistent with the recovery in the SCAPS model. These results can be explained by the proton irradiation creating interstitial hydrogen forming a shallow donor. The proton irradiation is sufficiently high to create up to  $5 \times 10^{17} \text{ cm}^{-3}$  donors if all the protons were absorbed in the CdTe layer, more

than enough to compensate the active As acceptors. This is also consistent with the recovery following a low temperature anneal in nitrogen, considering that hydrogen is a fast diffuser in CdTe. The absence of any residual damage, causing an increase in the trap density, requires a more extensive study with other species of ionizing radiation. The quality of the SCAPS model fit to the EQE spectra and agreement with the J-V parameters cannot be obtained by changing the trap density, which was the original intention.

### Conclusions

A SCAPS model was developed to replicate the device performance of thin film CdTe solar cells on UTG. Independently measured parameters were used as far as possible. The baseline (unirradiated device) fixed the thickness and bandgap of the (Cd,Zn)S and CdTe:S layers. The value of  $N_t$  was also varied but remained similar to the baseline figure and was consistent with literature reports. The modelling considered two different 0.5 MeV proton doses that covered the range of doses where significant solar cell degradation occurred. The recovery of the higher proton dose devices, following a 100 °C anneal, was remarkable in only having to change the  $N_a$  from the baseline value to obtain a good fit. The modelling has provided new and unexpected insights to the behaviour of these thin film PV devices under intense proton irradiation.

### Acknowledgements

The authors acknowledge financial support from the Engineering and Physical Science Research Council (EPSRC, Grant Ref. EP/K019597/1 and EP/K01935X/1). Qioptiq Space Technology is thanked for the supply of space qualified cerium-doped cover glass. The authors also would like to acknowledge the European Regional Development Fund (ERDF) and the Welsh European Funding Office (WEFO) for funding the 2<sup>nd</sup> Solar Photovoltaic Academic Research Consortium (SPARC II) which supported the modelling. The authors would like to thank professor Marc Burgelman for providing the SCAPS model.

### References

- [1] S.J.C. Irvine, D.A. Lamb, A.J. Clayton, G. Kartopu and V. Barrioz, "Cadmium telluride solar cells on ultrathin glass for space applications", *Journal of Electronic Materials*, 43, (2014), pp. 2818-2823.
- [2] G. Yang, E. W. Cho, Y. J. Hwang, B. K. Min, Y. Kang, D. Kim and J. Kim "Radiation hard and ultra-lightweight polycrystalline CdTe thin film solar cells for space applications", *Energy Technology*, (2016), 10.1002/ente.201600346
- [3] M. Burgelman, P. Nollet and S. Degrave, "Modelling polycrystalline semiconductor solar cells", *Thin Solid Films*, 361-362, (2000), pp. 527-532
- [4] D. A. Lamb, S. J. C. Irvine, C. I. Underwood, V. Barrioz, R. Gwilliam, J. Hall and M. A. Baker "Proton Irradiation of CdTe Thin Film Photovoltaics Deposited on Cerium-Doped Space Glass", (submitted to Progress in Photovoltaics, March, 2017)
- [5] A. A. Taylor, J. D. Major, G. Kartopu, D. Lamb, J. Duenow, R. G. Dhere, X. Maeder, S. J. C. Irvine, K. Durose, B. G. Mendis, "A Comparative Study of Microstructural Stability and Sulfur Diffusion in CdS/CdTe Photovoltaic Devices", SOLMAT, Volume 141, (2015), pp. 341–349.
- [6] Y. Y. Proskuryakov, K. Durose, J. D. Major, M. K. Alturkestani, V. Barrioz, S. J. C. Irvine, E. W. Jones, "Doping levels, trap density of states and the performance of co-doped CdTe(As,Cl) photovoltaic devices", *Solar Energy Materials and Solar Cells* 93, (2009), pp. 1572-1581

# Gold Nanorods for application in Plasmonic Luminescent Solar Concentrators

A. Sethi<sup>a,\*</sup>, S. Chandra<sup>a</sup>, H. Ahmed<sup>a</sup> and S. J. McCormack<sup>a</sup>

<sup>a</sup>Dept. of Civil, Structural and Environmental Engineering. Trinity College Dublin, Dublin, Ireland.

\*Corresponding author Email: [sethia@tcd.ie](mailto:sethia@tcd.ie) Tel: + 353 1 896 2671

**Keywords:** Plasmonic coupling, luminescent solar concentrators, gold nanorods

## Abstract

Luminescent solar concentrator (LSC) device is based on energy down shifting phenomenon with a primary goal of trapping, and concentrating solar radiation. The trapped light is guided to the photovoltaic cell through total internal reflection where it is absorbed and converted to electricity. LSC with its flexible design have the potential to find extensive use in the building integrated photovoltaics [1]. However, the optical efficiency of LSCs is limited by the properties of doped fluorescent materials. Plasmonic properties of metal nanoparticles (MNP) such as Gold (Au) and nanorods can be used for the enhancement of fluorescence of quantum dots (QDs), rare earth complexes and organic dyes in LSC devices [2]. The fluorescence enhancement of the luminescent species placed in the vicinity of MNP is dependent on spacing between the fluorophore- MNP, surface plasmon resonance (SPR) spectral overlap, and orientation. To maximize plasmonic coupling it is required to control spacing with the fluorophores and that can be achieved through concentration distribution of MNPs. The MNP-fluorophore composite in a polymer matrix material is required to have soluble and dispersion compatibility in this matrix material. Since, the wide range of MNPs synthesised using wet chemistry are functionalized with CTAB (hexadecyltrimethylammonium bromide) [3, 4, 5], that is insoluble in organic solvent hence in the polymer. This requires functionalizing MNPs and to make them soluble in organic solvent and polymer. Nanorods (NRs) were synthesized using the seed mediated wet chemical process, with the capping agent. The colloidal solution obtained has a high shape yield for the NRs as is evident by UV-VIS and SEM characterisation. The NRs were successfully separated from the by-products such as spheres and cubes.

## Introduction

The ever-increasing global energy demands

can be met by the photovoltaic conversion of energy. Since 2008 there has been a huge decrease in the cost of the solar cell systems but for photovoltaics to become economic further cost reductions have to be achieved. Luminescent solar concentrators (LSCs) can concentrate both the direct and diffused sunlight [6] without the need of expensive solar tracking systems. This makes it easier for the LSCs to be integrated in the urban environment [7]. Silicon based PV cells remain relatively expensive (0.62 €/W for highly efficient crystalline module) [8] and limited in coloration and shape. LSCs consist of a slab of transparent plastic (PMMA) or glass in which luminescent species, originally organic dyes and now even quantum dots and rare earth complexes are dispersed. Light is absorbed by these fluorophores and is re-emitted at a longer wavelength. If the re-emitted light falls outside the escape cone it is trapped within the waveguide due to total internal reflection and is guided to the edge of the slab for conversion into electricity by the solar cells. The low conversion efficiency of the LSC design causes them to be uneconomic. The main deficiencies are: The non-unity quantum yield of the fluorophores results in non-radiative relaxation of the absorbed photon in the form of heat. The isotropic emission of photons by the fluorophores results in the loss of the light through the front surface of the waveguide. Re-absorption of the photons due to an overlap of the absorption and emission spectra of the fluorophores aggravates the escape cone and non-unity quantum yield losses for the LSC. Due to the limited spectral response of the fluorophores it is difficult to utilize the entire AM1.5 solar spectrum. Plasmonic interaction between metal nanoparticles (MNPs) and the fluorophores can help reduce these losses thus enhancing the optical efficiency of LSC. MNPs (Au, Ag) exhibit localized surface plasmon resonance (LSPR) with SPR wavelengths falling in the visible region. The LSPR results in a strong electric field enhancement that decays exponentially from the surface of the MNP. A

fluorophore placed in the vicinity of the MNP is excited due to dipole–dipole interactions. The spacing between the fluorophore and the MNP can dramatically affect the fluorescence rate [9] and consequently the fluorescence quantum yield (FQY) [10], lifetime and Photoluminescence (PL) intensity. The plasmonic coupling depends on the orientation of the MNP with respect to the fluorophore, the enhancement is higher when the fluorophore dipole is along the main axis of the anisotropic NP [11]. Coherent excitation of surface plasmon takes place when Surface plasmon resonance (SPR) frequency overlaps with the frequency of the fluorophore and the spacing between them is greater or equal to 5 nm [12]. The MNP acts as a nanoantenna enhancing the strength of the dipole oscillator and thus enhancing fluorescence [13]. The SPR frequency is primarily the function of the size and shape of the Au NR. For this work, a precise control over the size of the NRs to match their wavelength with that of the fluorophores. Au NRs are crucial to align our fluorophores in the matrix to reduce the escape cone losses in the LSC design. In the past few years many Au NR synthetic strategies have been developed to achieve decent yields and monodispersity. This work focuses on the synthesis, purification and extraction of Au NR from the parent solution for a successful dispersion of the rods in organic solvent. CTAB was used as the capping agent for the seeds and the rods; CTAB capped seeds lead to the formation of single crystalline NRs as opposed to pentatwinned rods from citrate capped seeds. It is important to note that citrate capped seeds though more stable lead to the formation of various crystallographic habits and that is the main reason for a lower shape yield ~30% in the synthesis of pentatwinned rods. Despite the relatively higher yield of CTAB-Au NRs spheres and cubes are present as the by-product in the colloidal solution. Purification and shape separation was carried out using centrifugation by optimizing the centrifugal force and time for different aspect ratio (AR) NRs. The limitations imposed by the environment and the host material in a LSC require the NRs to be dispersed in a solvent that is compatible with the host material and does not change the shape of the NRs. QDs available in the market are usually dispersed in organic solvent such as toluene, to make the composite of the MNP with the QD need the NRs to be dispersed in toluene as well. Removal of excess CTAB is therefore imperative to ensure a successful phase transfer of the NRs from an aqueous to organic solution. Finding the amount of Gold Nanorods in the solution is important to optimize the

concentration of the MNPs in the MNP-fluorophore composite. An organic salt such as CTAB can hamper the results obtained for Au concentration from the inductively coupled plasma spectrometer (ICP-MS). This work will mainly focus on the synthesis, characterization, purification and shape separation of Au NRs.

### Experimental section & Methodology

**Au NR synthesis:** An optimized seed mediated method was carried out to prepare an aqueous colloidal solution of Au NRs of aspect ratio ~4 and ~3.5. The seed solution was prepared by mixing 600  $\mu$ l of ice cold 0.01M NaBH<sub>4</sub> to the solution of 0.1M CTAB and 50mM HAuCl<sub>4</sub>. It is important for an instantaneous addition of the reductant to the solution to achieve simultaneous production of all nuclei. CTAB capped seeds are relatively less stable than citrate capped seeds. Growth solution of NRs was prepared by mixing the gold precursor with CTAB at 27–30°C to form a complex between the Au salt and CTAB. After the addition of mild reducing agent AA the growth solution changed from dark yellow to colourless due to the reduction of Au(III) to Au(I). 40 $\mu$ l and 80 $\mu$ l of 5mM AgNO<sub>3</sub> was added to this growth solution. The presence of Ag<sup>+</sup> ions is crucial for the formation of single crystalline rods as it hinders the formation of pentatwinned rods. Finally, 120 $\mu$ l of seed solution was added to the growth solution to complete the reduction of Au(I) to Au (0). The final NR solution was kept in the water bath at 27°C for 30 min to ensure the complete reduction of Au.

**Optical characterisation:** UV-Vis-NIR spectroscopy is one of the main tools required for the characterisation of the NRs. The full width at half maximum (FWHM), shape of the longitudinal LSPR band in the optical spectrum are a good indication about the size dispersion in the NR solution. The position of the plasmon band can give us an estimate of the average aspect ratio of the NRs. Presence of a shoulder in the transverse peak and the ratio between the transverse and longitudinal peak are an indication of by-products present in the solution.

**Microscopic characterisation:** Scanning Electron Microscope (SEM) Carl Zeiss Ultra was used to image the NRs. It can give good approximation of the size of the NRs. In lens detector is used to see the Au NR dispersed on a Si wafer. It is important to optimise the electron acceleration voltage as a higher EV can cause carbon deposition and damage the NRs while the image is being taken, a lower EV decreases the resolution of the image. TEM is

a better tool if a precise knowledge about the structure and dimension of the NRs is necessary.

### Purification of Au NRs

Shape yield obtained after the seeded growth mechanism is usually very low to be sufficient for the targeted application. Wet chemical synthesis of the gold NRs inevitably contains spheres and cubes as the by-product. Therefore, post synthesis purification and separation is important to maximize the yield of monodisperse samples. Purification methods [14] including centrifugation [15], electrophoresis [16], depletion interaction forces [17] have been proposed in the separation of metal nanoparticles.

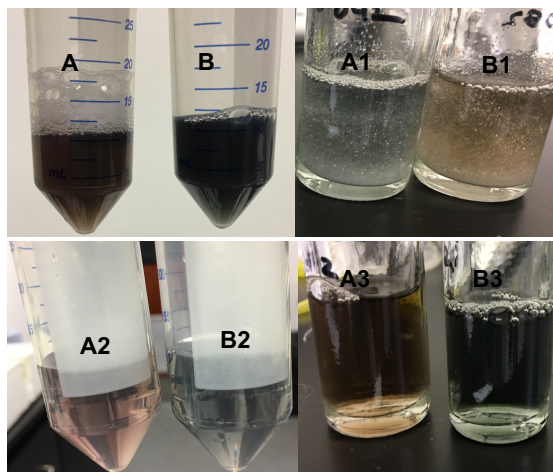


**Figure 1:** A, B (top left): Au NPs containing 80 $\mu$ l and 40 $\mu$ l respectively re-dispersed in DI water after the first centrifugation cycle at 12,000g/30min. A1, B1 (top right): Supernatant after the first centrifugation cycle, it mainly consists extra CTAB as is evident by the crystallization of the CTAB within a few hours. A2, B2 (bottom left): Au NPs left in the pellet after the second centrifugation cycle re-dispersed in DI water. A3, B3 (bottom right): Supernatant after the second centrifugation cycle, containing mainly the NRs.

Centrifugation was used to separate the NRs from the spheres and cubes. Although there are scattered reports in literature to use centrifugation-assisted sedimentation but there was difficulty to achieve efficient separation reproducibly. Small differences in concentrations, centrifugation parameters and size of the NRs can lead the NRs to either sediment out or remain in the solution after centrifugation. It is difficult to separate Au NRS with low AR<4. We perform two-step centrifugation; the first step involves the

isolation and purification of all the Au nanoparticles from the excess CTAB. Excess CTAB can affect the phase transfer of the NRs into an organic solution, and centrifugation temperature below 20°C causes the crystallization of CTAB and hinders the purification of the NR solution as can be seen in Figure 1.

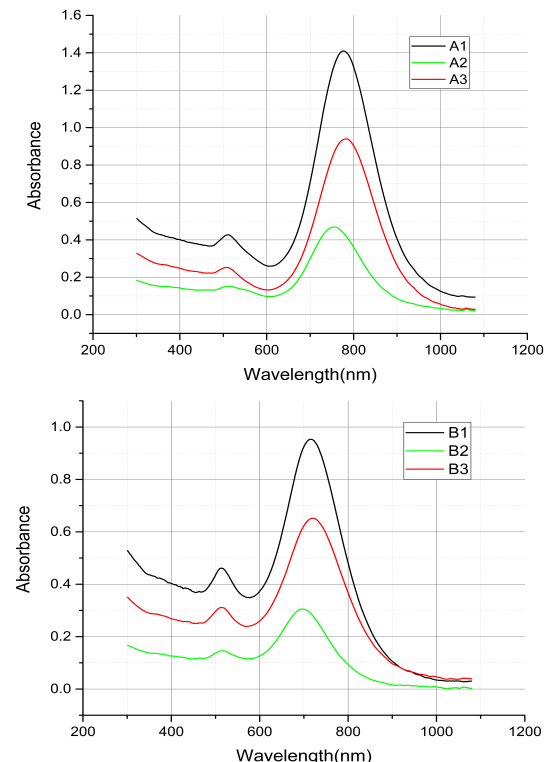


**Figure 2:** (top): UV-Vis spectra of aforementioned (Figure 1) solution of NRs containing 80 $\mu$ l of AgNO<sub>3</sub>. (bottom): Absorption spectra of Au NRs containing 40 $\mu$ l of AgNO<sub>3</sub> thus lower AR NRs.

### Results and Discussion

Au NRs were synthesised of different AR by changing the no. of Ag<sup>+</sup> ions in the growth solution. For single crystal rods higher concentration of Ag<sup>+</sup> ions will increase the AR of the rods [18].

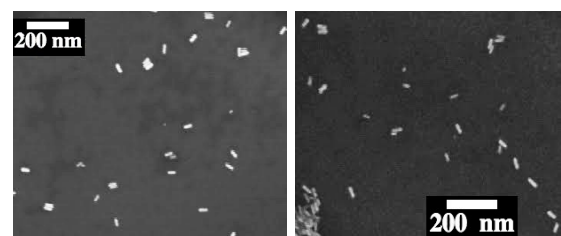


**Figure 3:** SEM images of A3 NR solution, containing NRs with L~40nm and W~10nm.

Figure 1 shows the apparent colour change of the NR solution after the second centrifugation cycle. A2, B2 and A3, B3 are the pellet and supernatant, the latter containing longer NRs and the former containing mainly the spheres, cubes and the shorter NRs. This is confirmed by the UV-vis spectra in Figure 2. There is a blue shift in the longitudinal peak for A2, B2 (green) spectrum indicating the presence of smaller NPs than the supernatant. Figure 3 shows the SEM image of the NRs having an AR ~4 for the 790 nm longitudinal peak. A successful synthesis, purification (removal of excess CTAB), shape separation of the NRs have been achieved. The NRs are stable for long periods of time. The next step is to extract the NRs from aqueous to organic solvent for research in PLSC.

### Acknowledgement

This work was supported and funded by the European Research Council (PEDAL Project Number 639760).

### References and Links

- [1] Debije, Michael G., and Paul PC Verbunt "Thirty years of luminescent solar concentrator research: solar energy for the built environment." *Advanced Energy Materials* 2.1 (2012): 12-35.
- [2] Chandra, Subhash, et al. "Enhanced quantum dot emission for luminescent solar concentrators using plasmonic interaction." *Solar Energy Materials and Solar Cells* 98 (2012): 385-390
- [3] Nikoobakht, Babak, and Mostafa A. El-Sayed. "Preparation and growth mechanism of gold nanorods (NRs) using seed-mediated growth method." *Chemistry of Materials* 15.10 (2003): 1957-1962.
- [4] Scarabelli, Leonardo, et al. "A "tips and tricks" practical guide to the synthesis of gold nanorods." (2015): 4270-4279.
- [5] Jana, Nikhil R., Latha Gearheart, and Catherine J. Murphy. "Wet chemical synthesis of high aspect ratio cylindrical gold nanorods." *The Journal of Physical Chemistry B* 105.19 (2001): 4065-4067.
- [6] A. Goetzberger, "Fluorescent solar energy collectors: Operating conditions with diffuse light," *Appl. Phys. A*, vol. 16, no. 4, pp. 399–404, 1978.
- [7] D. Chemisana, "Building integrated concentrating photovoltaics: a review," *Renew. Sustain. Energy Rev.* 15(1), 603–611 (2011)
- [8] For example, see [www.Solarbuzz.com](http://www.Solarbuzz.com), which provides a regular survey of photovoltaic module and solar electricity generation costs.
- [9] Chen, Y., Munechika, K., Plante, I.J., Munro, A.M., Skrabalak, S.E., Xia, Y., Ginger, D.S., (2008). Excitation enhancement of CdSe quantum dots by single metal Nanoparticles. *Applied Physical Letters*, 93, 5, 053106-3.
- [10] Musken, O.L., Giannini, V., Sanchez, J.A., Rivas, J.G., (2007). Strong enhancement of the radiative decay rate of emitter by single plasmonic nanoantennas. *Nano Letters*, 7, 9, 2871-2875.
- [11] Thomas, M., Greffet, J.J., Carminati, R., Arias-Gonzalez, J.R., (2004). Single molecule spontaneous emission close to absorbing nanostructures. *Applied Physics Letters*, 85, 17, 3863-3.
- [12] Shalaev, V.M., Sarichev, A.K., (1998). Nonlinear optics of random metal-dielectric films. *Physical Review B*, 57, 13265–13288.
- [13] Drachev, V.P., Khaliullin, E.N., Kim, W., Alzoubi, F., Rautian, S.G., Safonov, V.P., Armstrong, R.L., Shalaev, V.M., (2004). Quantum size effect in two-photon excited luminescence from silver nanoparticles. *Physical Review B*, 69, 035318-5.
- [14] Kowalczyk, B.; Lagzi, I.; Grzybowski, B. A. Nanoseparations: Strategies for Size And/or Shape-Selective Purification of Nanoparticles. *Curr. Opin. Colloid Interface Sci.* 2011, 16, 135–148.
- [15] Xiong, B.; Cheng, J.; Qiao, Y.; Zhou, R.; He, Y.; Yeung, E. S. Separation of Nanorods by Density Gradient Centrifugation. *J. Chromatogr. A* 2011, 1218, 3823–3829
- [16] Xu, X.; Caswell, K. K.; Tucker, E.; Kabisatpathy, S.; Brodhacker, K. L.; Scrivens, W. A. Size and Shape Separation of Gold Nanoparticles with Preparative Gel Electrophoresis. *J. Chromatogr. A* 2007, 1167, 35–41.
- [17] Mao, Y.; Cates, M. E.; Lekkerkerker, H. N. W. Depletion Force in Colloidal Systems. *Phys. A* 1995, 222, 10–24.
- [18] Perez-Juste, J.; Pastoriza-Santos, I.; Liz-Marzá n, L. M.; Mulvaney, P. Gold Nanorods: Synthesis, Characterization and Applications. *Coord. Chem. Rev.* 2005, 249, 1870–1901.

# First Flight Test of a Thin Film Cadmium Telluride Solar Cell on Cover Glass in Space

\*D. A. Lamb<sup>1</sup>, C. I. Underwood<sup>2</sup>, A. Dyer<sup>2</sup>, J. Hall<sup>3</sup> and S. J. C. Irvine<sup>1</sup>

<sup>1</sup>Centre for Solar Energy Research, College of Engineering, Swansea University, OpTIC Centre, St Asaph, LL17 0JD, UK

<sup>2</sup>Surrey Space Centre, University of Surrey, Guildford GU2 7XH, UK

<sup>3</sup>Qioptiq Space Technology Ltd, Glascoed Road, St Asaph, Denbighshire, UK, LL17 0LL

## Abstract

The world's first thin film solar cell on cover glass flight test has been demonstrated by CSER, Swansea University and the University of Surrey through the UK and Algerian Space Agencies AISat Nano CubeSat mission. Two separate measurements of the thin film solar cell payload have been made to date. Initial results are promising with each of the  $4 \times 1\text{cm}^2$  CdTe cells producing a current voltage curve and beaming the data back to mission control. Cell performance surpassed that of the terrestrial measurements with  $V_{oc}$  increasing by almost 25%. The improvement in  $V_{oc}$  is attributed in part to lower cell temperature measurement and extended light soaking. However, additional work is required to corroborate the in-flight data and provide further insight into this significant  $V_{oc}$  improvement.

## 1. Introduction

Photovoltaics (PV) make up a small but increasing fraction of the terrestrial electricity supply. However, for extra-terrestrial applications PV is essential; providing power for onboard operations of satellites, space craft and Lunar and Martian rovers. Commercial PV for space is focused around multi-junction gallium arsenide compounds on germanium wafers. These solar cells have excellent efficiencies of >30% AM0 and therefore offer very high power density, but this performance comes at a cost; the multi-junction cells are expensive, rigid and the bulk of their weight is made up of the germanium wafer and ubiquitous radiation protection cover glass. Emerging applications in space such as; Solar Electric Propulsion, Space Based Solar Power and Lunar and Martian Bases will require a much higher power-to-weight ratio than is currently available and at a fraction of the cost. To meet these demands the Centre for Solar Energy Research (CSER), Swansea University have developed an innovative solution. By depositing thin film cadmium telluride directly onto the radiation hard cover glass the research team have shown that the power-to-weight ratio for the solar cell can be increased two-fold over the multi-junction technology [1]. Two further benefits of using the ultra-thin cover glass, as the substrate, are that its inherent flexibility can be maintained, leading to novel stowage and

deployment options, and the materials cost of the process is reduced.

An opportunity to flight test the thin film solar cell structure arose with the joint UK and Algerian Space Agencies AISat-Nano technology demonstration CubeSat. A successful bid, in collaboration with the University of Surrey, was made to fly a payload capable of characterising the thin film solar cells in orbit, via an automated current-voltage (I-V) measurement circuit. For the Thin Film Solar Cell (TFSC) payload to be included aboard the satellite, 3 fully working flight models needed to be delivered to the satellite manufacturers within 9 months. The team designed an encapsulated space robust solar cell, the measurement electronics and the measurement software [2]. Once completed, a TFSC payload flight model, comprising four test cells, was successfully integrated onto the satellite at the Surrey Space Centre (SSC), and launched from Southern India into a  $661\text{km} \times 700\text{km}$ ,  $98.2^\circ$  Sun Synchronous orbit on 26<sup>th</sup> September 2016 [3]. The spacecraft was commissioned and the TFSC payload operated. The initial flight data showed that the payload was operating well producing 4 good I-V curves for each of the cells. This paper describes the new cell technology, the flight payload, the measurement design and the first flight results of thin film CdTe solar cells in Earth orbit.

## 2. Experimental

An atmospheric-pressure metal organic chemical vapour deposition (MOCVD) process was used to produce all the semiconductor layers. The PV device structure, was achieved by depositing; an aluminium-doped zinc oxide (AZO) transparent conducting oxide (TCO), n-type cadmium zinc sulfide window and p-type cadmium telluride absorber layers directly onto the cover glass.

Figure 1 shows one of the 3 fully encapsulated CdTe TFSC flight models designed to be sufficiently robust to survive the mission and to provide in-flight I-V measurements [2]. The gold strips either side make contact to the common TCO while the four gold fingers in the middle allow back contact to the  $4 \times 1\text{cm}^2$  rectangular cells. The encapsulated structure was exposed

to environmental testing including temperature profiling over -40 °C to + 70 °C. It was also subjected to vibrational testing as part of the satellite manufacturers pre-flight procedure.

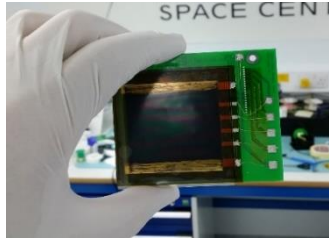


Figure 1. The flight model has  $4 \times 1\text{cm}^2$  defined solar cells. The gold tracks allow remote measurement of the cells current-voltage characteristics.

### 3. Results and Discussion

The encapsulated flight models were measured using an AM0 calibrated ABET solar simulator [1]. Table 1 shows data for the best performing model, CSER817, which was the one finally chosen for flight. The modest efficiencies were limited by the high series resistance and low fill factors that arose from the design of the encapsulation and a higher than ideal contact resistance. This was the result of using a conductive silver epoxy between the gold fingers and the  $1\text{ cm}^2$  gold back contacts that was a compromise between minimizing the series resistance and achieving mechanical robustness. The  $J_{sc}$  values were in the region of  $28\text{ mA cm}^{-2}$  for AM0 ( $136.6\text{ mA cm}^{-2}$ ) compared to  $23.5\text{ mA cm}^{-2}$  when measured under AM1.5G.  $V_{oc}$  was between 745 and 761 mV, not unusual for the device structure. Typically, CdTe devices on AZO/cover glass substrates have  $V_{oc}$  ranging between 700 and 830 mV depending upon growth and post growth treatment.

Cell's	0	1	2	3
$\eta\%$	9.5	8.6	9.2	8.4
$J_{sc}\text{ (mA/cm}^2)$	27.6	28.2	27.8	27.4
$V_{oc}\text{ (mV)}$	761	760	756	745
FF %	61.0	54.1	60.6	55.7
$R_s\text{ (\Omega cm}^2)$	6.8	11.2	7.2	8.4

Table 1. J-V parameters for CSER817,  $4 \times 1\text{cm}^2$  encapsulated solar cells. Measured under an AM0 calibrated solar simulator.

Figure 2 shows the flight model CSER817 mounted to the outside of the 3-unit CubeSat and ready to be shipped to the launch site in Southern India. Body mounted multi-junction gallium arsenide based solar cells can be seen in figure 2. These provide the satellites electrical power. An internally mounted printed

circuit board prepared by the University of Surrey enabled measurement of the  $4 \times 1\text{cm}^2$  CdTe solar cells. When commanded, the non-linear current-voltage response of each of the  $4 \times 1\text{cm}^2$  cells in orbit are measured with the solar illumination independently calibrated by an attitude sensor. It also measures the ambient temperature and sends all data to the AlSat Nano's on-board computer. The measurement electronics make 256 readings per cell, starting from  $V_{oc}$  (current demand = 0 mA), up to a maximum of ~51 mA current demand. The maximum anticipated current demand for the  $1\text{cm}^2$  cells is < 30 mA however, if current demand exceeds the cell's capability, a diode bypass kicks in to protect the cell. Each reading takes 1ms, each cell is surveyed in ~256 ms with a survey of all four cells in just over 1 second.

The programmed current demand from the precision current sink and the measured current (as measured as a voltage over a precision 10-ohm resistor) matched, both on the ground and in-flight. This test provides a calibration of the analogue-to-digital converter. The ground and in-flight data as measured by the electronics were smooth and did not indicate any noise or interference. The results from the in-flight measurements were consistent from run to run, with  $V_{oc}$  nearly independent of light intensity and  $I_{sc}$  varying as expected. As a further controlled test the TFSC payload engineering model was measured at CSER. The I-V parameters matched those as measured using CSER's Kiehley 2400 to within 1.5 %.

As the CubeSat passes within range of the ground station in Oran, Algeria the on-board computer data is downloaded and then distributed to the various end users including the TFSC payload team.



Figure 2. AlSat Nano at Surrey Space Centre ready to be shipped for launch. The TFSC Payload is mounted below multi-junction solar cells.

Figure 3 shows the launch of the Polar Satellite Launch Vehicle (PSLV) that deployed 7

satellites into two different orbits. The AISat Nano being deployed into a 690km orbit. A series of spacecraft health checks and in orbit commissioning procedures were performed by SSC before operations were then transitioned to Algeria's newly developed AISat Nano ground station in Oran. A few weeks later the first data was received from the TFSC payload signifying a world first in the measurement, in space, of a solar cell deposited onto cover glass.



Figure 3. Launch of PSLV-C35 inserting AISat Nano into 690 km orbit, 26<sup>th</sup> Sep. 2016. Image courtesy of Department of Space Indian Space Research Organisation

Figure 4 shows data from the second batch of TFSC payload measurements where, due to gradual rotation of the satellite, the illumination intensity was approximately 70% of 1 sun. The TFSC payload temperature was 4 °C and notably the  $V_{oc}$  was significantly higher than measured in the laboratory. All 4 cells were operational. The robustness and design of the encapsulation, measurement electronics and software was a success.

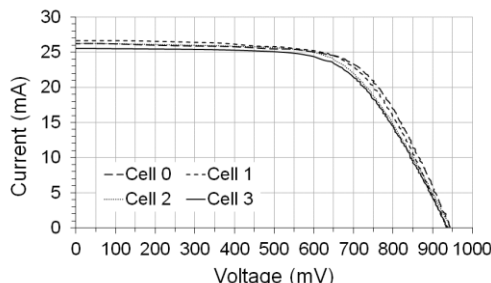


Figure 4. Current (mA) versus voltage (mV) remote measurement of the 4×1 cm<sup>2</sup> CdTe solar cells. TFSC Payload temperature = 4 °C.

Table 2 shows the J-V parameters for the in-flight measurements. Fill factor and series resistance were close to those measured in the laboratory.  $J_{sc}$  was lower than measured terrestrially and is attributed to the less than 1 sun illumination due to the angle of sun to satellite at time of measurement.  $V_{oc}$  however is significantly higher than measured in the laboratory. The in-flight cells measured 25 % higher  $V_{oc}$  which, along with the less than 1 sun

illumination, yielded solar cell efficiencies between 16 and 17 %.

Cells	0	1	2	3
$\eta$ %	17.0*	16.9*	16.4*	16.0*
$J_{sc}$ (mA/cm <sup>2</sup> )	26.2	26.7	26.3	25.6
$V_{oc}$ (mV)	945	938	946	938
FF %	66	64	63	64
$R_s$ ( $\Omega$ cm <sup>2</sup> )	8.4	8.6	10.2	10.0

Table 2. J-V parameters for 4×1 cm<sup>2</sup> encapsulated solar cells. Measured in-flight under approximately 70% of 1 sun and at 4 °C. \*high efficiencies are due to very high  $V_{oc}$  and further work is required to explain the increase over the laboratory based measurements.

To investigate the significant increase in  $V_{oc}$  two possible factors were investigated, using one of the spare flight models.

- $V_{oc}$  increases with decreasing cell temperature
- $V_{oc}$  increases with increased exposure to direct sun light

It should be noted that the solar simulator AM0 measured  $V_{oc}$  for the spare flight model was between 40-50 mV lower than that of the TFSC payload. It is standard procedure to light soak CdTe solar cells before measuring their I-V. A typical 10-minute soak being employed for the CSER laboratory measured cells shown in table 1. Studies of other non-MOCVD CdTe cells have shown  $V_{oc}$  to improve by ~4% when light soaked due to depopulation or filling of trap states in the absorber [4]. With the MOCVD deposited CdTe, figure 5 shows the  $V_{oc}$  increasing with extended light soaking beyond the standard 10 minutes and not clearly saturating after 270 minutes. Interestingly, the average increase of  $V_{oc}$  over the 270 minutes was also 4%.

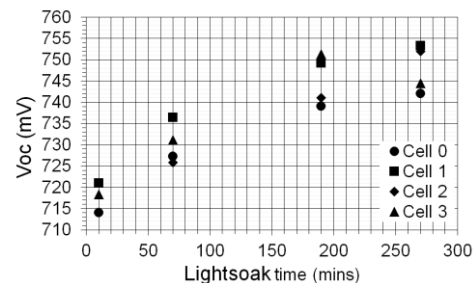


Figure 5. Measurement of  $V_{oc}$  (mV) versus light soak time (minutes) of the spare flight model under AM0 solar simulator. Temperature of cells during each measurement ~ 30 °C

The same spare flight model was then subject to measurement under AM0 solar simulation but at a reduced temperature shown in figure 6. Accurate temperature control proved difficult. The measurements will be repeated in future work with a custom-built stage that can achieve a stable temperature down to the 4 °C experienced by the in-flight cells. Figure 6 indicates that the expected trend of increasing  $V_{oc}$  with reduced temperature will come into play for the cells in space. Virtuani et al. measured the temperature coefficient for CdTe solar cell  $V_{oc}$  to be 0.24 (%/°C) [5] where the very approximated data in figure 6 shows a reasonable agreement with a temperature coefficient of 0.28 (%/°C).

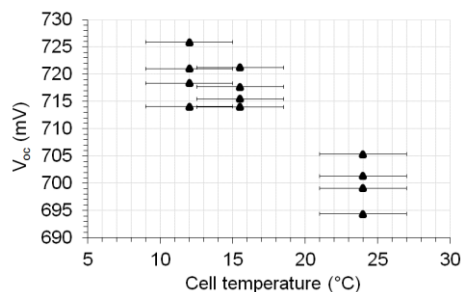


Figure 6. Measurement of  $V_{oc}$  (mV) versus cell temperature (°C) of spare flight model under AM0 solar simulator.

If both suggested pathways to improved  $V_{oc}$  are additive, then table 3 shows; actual laboratory  $V_{oc}$  measurements taken at 30 °C (AM0 with a 10-minute light soak), then applying the nominal 4% improvement to  $V_{oc}$  due to the extended light soaking the cells received in space, then further applying 0.28 %, to this new  $V_{oc}$ , per °C temperature drop (a 26 °C reduction) and finally the in-flight measured  $V_{oc}$  at a cell temperature of 4 °C.

Cells	0	1	2	3
$V_{oc}$ (mV) Lab.	761	760	756	745
* $V_{oc}$ (mV) +4%	794	793	786	775
* $V_{oc}$ (mV) @4 °C	851	850	846	833
$V_{oc}$ (mV) In-flight	945	938	946	938

Table 3. Laboratory measured  $V_{oc}$  then applying the coefficients for both light soaking and decrease in temperature experienced by the in-flight cells. Finally, the in-flight measured  $V_{oc}$ .

The factors of light soaking for 270 minutes and the temperature coefficient of  $V_{oc}$  still falls some 12% short of the in-flight measurements. Further work is planned to corroborate the in-flight data by looking at further light soaking and thermal treatment to provide further insight into the significant  $V_{oc}$  improvement.

#### 4. Conclusion

The world's first thin film solar cell on cover glass has been flight tested and its photovoltaic properties measured. All 4×1cm<sup>2</sup> cells produced I-V curves with parameters very similar to those shown in the laboratory with the exception of  $V_{oc}$ .  $V_{oc}$  was found to be 25% higher than that of the laboratory measured AM0 value. The in-flight cells were however, 26 °C lower in temperature and had experienced AM0 light exposure for a period exceeding 1000 hours. The effects of these two potential  $V_{oc}$  enhancers were investigated using an equivalent flight model. At least half of the  $V_{oc}$  increase could be reasonably be attributed to the in-flight cell's temperature and modest exposure to light. However, more data captures from the in-flight cells and further analysis is required to fully understand this significant increase of  $V_{oc}$ . The results of this study could have significance for  $V_{oc}$  improvement of terrestrial solar cells. The performance will be plotted over the lifetime of this mission to test the resilience of these thin film cells to radiation and thermal stressing experienced in low Earth orbit.

#### Acknowledgements

The authors acknowledge the UK and Algerian Space Agencies for the opportunity to take part in the AlSat Nano mission. The financial support from the Engineering and Physical Science Research Council (EPSRC, Grant Ref. EP/K019597/1 and EP/K01935X/1). Qioptiq Space Technology is thanked for the supply of space qualified cerium-doped cover glass.

#### References

- [1] D. A. Lamb *et al.* "Characterization of MOCVD Thin-Film CdTe Photovoltaics on Space-Qualified Cover Glass" IEEE Journal of Photovoltaics Volume:6, Issue: 2, (2016) pp.557 - 561
- [2] D. A. Lamb *et al.* "Preparation of CdTe PV on Ultra-thin Space Cover Glass for Flight Testing on the AlSat-Nano Satellite Mission", PVSAT-12, 6-8<sup>th</sup> April (2016) conference proceedings
- [3] <https://www.gov.uk/government/news/launcl-success>
- [4] M. Gostein and L. Dunn "Light soaking effects on photovoltaic modules: Overview and literature review", Photovoltaic Specialists Conference, (2011) 37th IEEE pp. 003126- 003131
- [5] A. Virtuani *et al.* "Overview of Temperature Coefficients of Different Thin Film Photovoltaic Technologies", 25th EUPVSEC, , Valencia, Spain, 6-10 Sep. (2010) pp.4248-4252

# OPTIMUM USE OF THE LOSS FACTORS MODEL (LFM)

## FOR IMPROVED PV PERFORMANCE MODELLING

<sup>1</sup>Steve Ransome (SRCL Kingston on Thames, UK) and

<sup>2</sup>Juergen Sutterlueti Gantner Instruments, AT)

<sup>1</sup> [steve@steveransome.com](mailto:steve@steveransome.com) and <sup>2</sup>[J.Sutterlueti@gantner-instruments.com](mailto:J.Sutterlueti@gantner-instruments.com)

### 1) What is the Loss Factors Model?

The LFM is a PV performance model where the coefficients are based on the shape of measured IV curves under different irradiance and temperature conditions (either indoor or outdoor).

The relative efficiency ("Eff.measured" / "Eff.nameplate") otherwise known as the Module Performance Ratio DC (PR<sub>DC</sub> or MPR) is the product of the LFM's 6 independent and normalised physically significant loss parameters.

The LFM can be used to analyse all existing PV technologies (e.g. standard and "high efficiency" c-Si; Thin Film such as CdTe, CIGS; OPV ) at all sites and at all orientations (e.g. fixed tilt, tracked and CPV).

### 2) What the LFM can do

- Optimisation of PV manufacture by quantifying limiting losses (e.g. how much of the potential P<sub>MAX</sub> is lost due to the parasitic R<sub>SERIES</sub>?)
- Identify module variability, atypical behaviour and under performance.
- Generate coefficients for modelling such as P<sub>MAX</sub> thermal coefficient (gamma γ %P<sub>MAX</sub>/K ) and Low light efficiency (η 0.2kW/m<sup>2</sup> / η 1.0kW/m<sup>2</sup>)
- Validate online measurements, characterise and quantify any degradation identifying the causes.
- Commissioning getting fast values for P<sub>MAX.MEASURED</sub> / P<sub>MAX.NOMINAL</sub>
- Once coefficients are established it can be used to predict site energy yield and can check systems on line for optimized Levelized cost of Energy (LCoE) and effective risk mitigation.

### 3) How the LFM differs from other models

The 1-diode (and similar models)[4] fit their coefficients (e.g. I<sub>SC0</sub>, R<sub>SHUNT</sub>, R<sub>SERIES</sub>,

I<sub>O</sub> and Ideality Factor n) to model an entire IV curve.

It is not always possible to find a perfect fit to the whole curve simultaneously particularly when there are non-uniformities in the module, shading, degradation, non ohmic back contacts or properties such as bias dependent current.

Any "imperfections" in the curve such as current mismatch steps or rollover due to non-ohmic back contact behaviour cause the model fit to depend on how the algorithms minimise the RMS error which may be dependent on the IV point distribution or possibly weighted towards V<sub>MP</sub>, I<sub>MP</sub> where it is most important.

Models such as the SAPM [4] need up to 29 parameters to fit the I<sub>SC</sub>, I<sub>MP</sub>, V<sub>MP</sub> and V<sub>OC</sub> (and their temperature coefficients). R<sub>SC</sub> and R<sub>OC</sub> are not modelled explicitly but these matter when coming to investigate degradation modes. Their parameters are not normalised and many tend to have a non-physical meaning making understanding them difficult.

The LFM has been developed to extract the maximum amount of physically significant information from just 6 normalised (and for the most part independent) parameters with two check parameters.

LFM coefficients are derived from fitting points to the IV curve such as I<sub>SC</sub>, I<sub>MP</sub>, V<sub>MP</sub> and V<sub>OC</sub> as shown in figure 1.

It then fits gradients for R<sub>SC</sub> and R<sub>OC</sub> and quantifies how much loss is associated with each of these 6 values rather than the measured Amps, Ohms or Voltage which are module area and design specific.

The 6 LFM Values are all "normalised losses" because they are scaled by measurements at reference conditions (e.g. I<sub>SC,STC</sub>) meaning values are area independent and work from cm<sup>2</sup> cells through modules to strings, combiner boxes, inverters, stations and multi MWp arrays [5].

Normalised values can be used to study the reproducibility of modules. For example as the normalised V<sub>OC</sub> is given by

$$nV_{oc} = V_{oc, \text{MEASURED}} / V_{oc, \text{REFERENCE}}$$

then its distribution is likely to be a Gaussian like spread with a peak and Std Dev which quantify the mode module tolerance and spread as percentages of reference values rather than fixed voltages which would be number of series cell dependent.

#### 4) Deriving coefficients for the LFM from an IV measurement

Measure the IV curve(s) of a module with date+time, plane of array irradiance of the closest match reference cell (to minimise AOI and spectral corrections) and  $T_{\text{AMBIENT}}$  and  $T_{\text{MODULE}}$ .

Also record Windspeed WS, Air Mass AM, Angle of Incidence AOI, Beam Fraction BF (= 1 - Diffuse Fraction) for further corrections where needed.

Figure 1 illustrates how the LFM's 6 Loss Factors ( $n_{lsc}$ ,  $n_{Rsc}$ ,  $n_{lmp}$ ,  $n_{Vmp}$ ,  $n_{Roc}$  and  $n_{Voc}$ ) are derived from the measured IV curve.

(The MMF is Module Mismatch factor which affects the  $I_{sc}$  of the module but for a well-matched reference cell this can be ignored and isn't considered further in this paper). Spectral corrections will be introduced later to the LFM.

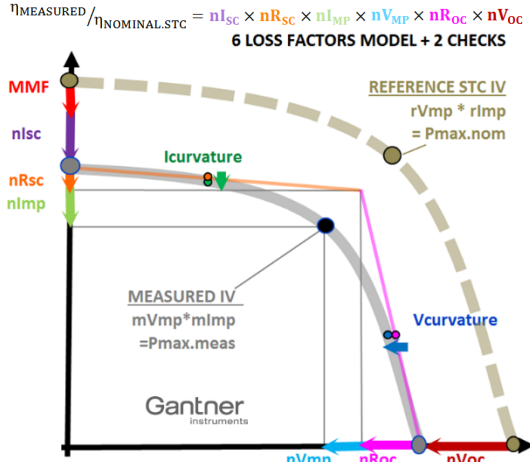


**Fig 1:** 6 Derived LFM parameters  $n^{***}$  from measured vs. reference IV values with 2 curvature check values ( $n_{lc}$  and  $n_{Vc}$ )

#### 5) Monitoring LFM Values with time and data smoothing

Figure 2 illustrates weather parameters irradiance (\*100  $\text{kW/m}^2$  green), module(red) and ambient(orange) temperatures (C) and 6 derived LFM values (bottom) over a typical morning from sunrise to just after noon with mostly

clear but some intermittent cloud events in September in Arizona.

Before 07:00 (A) the sun was below the horizon so there was only a little diffuse irradiance meaning some unusual values particularly for  $n_{lsc}$  and  $n_{Voc}$ .

From 07:00 to 13:00 the LFM values for steady irradiance were all smooth and between 85% and 115% as expected.

When there were sharp changes in irradiance (B) there are sometimes some glitches in LFM parameters away from the steady state values. Note that as everything is normalised it is easy to remove glitches when deriving modelled performance as is shown in the sanitised data A' and B'.

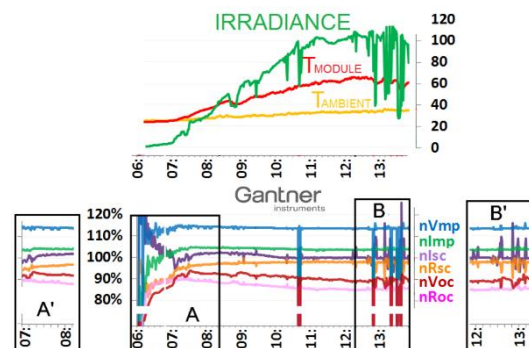


**Fig 2:** Raw Weather parameters (top) and LFM values(bottom) for a mostly clear morning. A' and B' are sanity checked (good, non-transient measurements) data.

#### 6) Which LFM parameters cause efficiency to vary with irradiance?

Figure 3 illustrates how the 6 parameters vary vs. irradiance for measurements of a typical well behaved TF module. These shapes are typical for all well-behaved PV modules. Because  $n_{Voc}$  depends heavily on  $T_{\text{MOD}}$  it is best to show it as temperature corrected  $n_{Voc,T}$ .

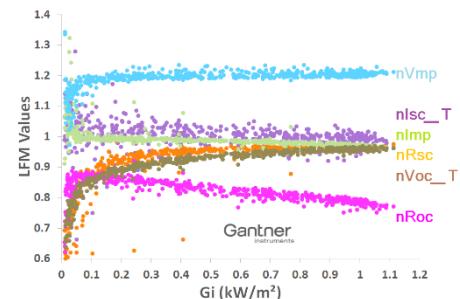


**Fig 3.** LFM parameters vs. irradiance for a typical well behaved CdTe module

The 6 LFM parameters depend on the following effects

$nI_{SC\_T}$	Soiling, Air Mass, Angle of incidence and reflectivity. It will usually have the largest scatter of the LFM parameters.
$nV_{OC\_T}$	~ logarithmically dependent vs $G_i$ , dependent on $T$ by the factor $\beta_{VOC}$
$nR_{SC}$	Rising with $G_i$ (has a worse loss at low light levels) $R_{SHUNT}$
$nR_{OC}$	Falls with $G_i$ (has a worse loss at high light levels) $R_{SERIES}$
$nI_{MP}$	Quite flat vs $G_i$
$nV_{MP}$	Quite flat vs $G_i$

Figure 4 plots the two curvature parameters  $n_{LC}$  (identifies IV curve steps due to mismatch cracking shading) and  $n_{VC}$  (identifies  $R_s$  problems e.g. due to Schottky contact rollover).

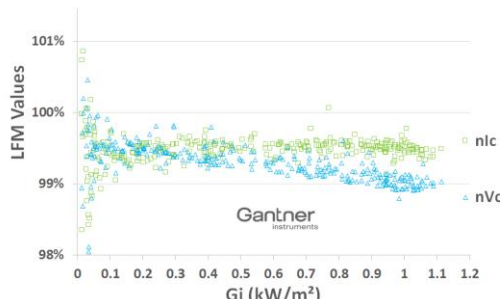


**Fig 4:** LFM curvature parameters vs. irradiance for a well behaved CdTe module.

Note the change in y-scale from fig 3 as these values are much closer to 100%. Absolute values will depend somewhat on the module technology but for a good measurement on an undegraded and unshaded module they should be smooth and quite flat from around 0.1 to 1.0kW/m<sup>2</sup>. Any changes in cell cracking or shading will cause the  $n_{LC}$  to fall at high light level. Incidences of rollover or increasing series resistances will cause  $n_{VC}$  to change.

Because the  $P_{RD}$  depends on the product of all 6 parameters then Low light efficiency performance depends mostly on which parameters fall there i.e.

$nV_{OC\_T}$  - ~log dependent, falls at low light

$nR_{SC}$  - As  $I_{SC} \sim I_{SC,STC} * G$  then  $R_{SHUNT}$  has a higher effect at lower light levels.  $R_{SHUNT}$  usually rises near exponentially at low light but its loss effect is usually greater at low light)

The High light performance depends mostly on

$nR_{OC}$  (which depends on  $\sim I^2 R_{SERIES}$ )

Most of the differences between the low and high light efficiency of different technologies can be understood by characterising these three parameters.

## 7) Characterising the module temperature dependency with LFM parameters

Plot all of the 6 LFM parameters vs. temperature as in figure 5. Preferably select clear sky conditions with low angle of incidence and reasonably high  $T_{MOD}$  to get a better fit.

The apparent temperature coefficient is the gradient of each of the parameters below.

Gradient = $d/dT_{MOD}$	Coeff
$nV_{OC\_U}$	$bV_{OC}$
$nI_{SC\_U}$	$aI_{SC}$
$(nI_{SC\_U} * nR_{SC} * nI_{MP})$	$aI_{MP}$
$(nV_{OC\_U} * nR_{OC} * nV_{MP})$	$bV_{MP}$
<b>Note :</b>	
$aI_{MP} + bV_{MP} =$	<b>Gamma</b>

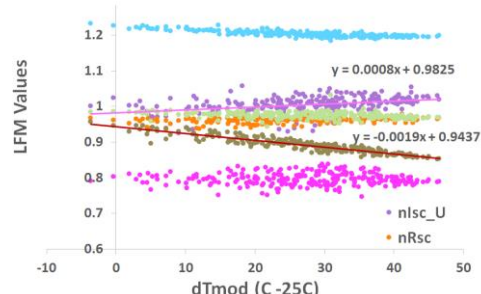


**Fig 5:** LFM parameters vs. module temperature with coefficients  $a_{Isc}$  and  $b_{Voc}$  for a well behaved CdTe module [Gantner instruments data]

## 8) LFM coefficients vs. PV technologies - c-Si, Thin Film

Some of the 6 LFM coefficients can be seen to differ by PV technology

- c-Si usually has lower  $R_{SERIES}$  (as it's due to tabbing related rather than TCO) meaning a better  $n_{ROC}$  particularly at high light levels when current is high
- Some thin films appear to have "better low light response" because they have "High light  $R_{SERIES}$  loss" meaning their  $n_{ROC}$  fall faster at high light level
- The efficiency of some thin films can collapse at low light levels and these can be characterised by the amount of  $n_{VOC}$  or  $n_{RSC}$  drops.

## 9) Quantifying Degradation at different conditions due to different LFM parameters

LFM can show which of the 6 parameters is causing any changes rather than just "Eff vs time" e.g. changes in nRsc or nRoc may indicate RSHUNT or RSERIES (respectively) related problems

The LFM can determine if the efficiency drop depends on conditions e.g. low light efficiency might drop at different rates than at high light levels

Figure 6 plots the changes in two LFM parameters nRsc and nRoc over time (years 2010 – 2016 are marked by different colours) for an abnormally bad TF module which is falling at ~3%/year.

The nRoc appears to be degrading about 1%/y at all light levels, the nRsc is degrading faster at low light levels (-2%/y) than at high light levels (-0.5%/y) indicating a non ohmic component of RSHUNT.

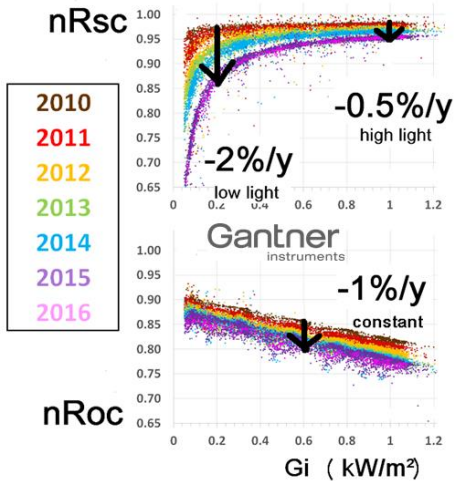


**Fig 6:** A degrading module shown by plots of changing nRsc and nRoc vs. irradiance (x – axis) vs. time (year)

Seasonal annealing (which can occur in some devices) would appear as an oscillation in one or more of the LFM parameters with time.

The magnitude and phase of the change with respect to season or recent weather conditions (e.g. average module temperature for the previous month) can be used to identify and quantify the effect.

## 10) Curve fitting

Several different methods (to be described) can be used to fit LFM curves depending on their shape as in figures 3. These include the following dependencies

Linear	$y = m * GI + c$
Logarithmic	$y = a * \log(GI)$
Power series	$y = 1 - GI^n$

Combinations with empirical parameters can be fitted as in [4] and are shown in fig 7.

$$nLFM = C_0 + C_1 * \log(GI) - C_2 * GI^2$$

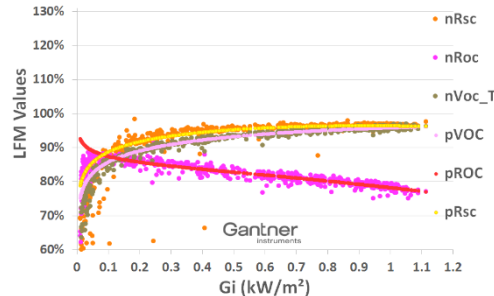


**Fig 7:** nLFM fits using a constant, log and power term.

These are then used for Fault diagnostics (if the performance differs from expected) and Energy Yield prediction (using expected climate data).

**Appendix A** gives Python Format code and definitions with links to measurement data from GI. This model is being added to PVLIB.

## 11) References

- [1] Gantner Instruments Web portal
- [2] PVPMC [www.pvpmc.org](http://www.pvpmc.org)
- [3] Sutterlueti et al "Improved PV Performance Modelling by Combining the PV\_LIB Toolbox with the Loss Factors Model (LFM)" 42nd PVSC 2015
- [4] Stein et al 28<sup>th</sup> PVSEC Paris 2013
- [5] Sellner et al 27<sup>th</sup> PVSEC Frankfurt 2012

## Appendix A) LFM Equations (in Python code format)

```

# GLOSSARY OF PARAMETER NAMES AND EQUATIONS TO BE USED FOR PVPMC/PVLIB
# SRCL and Gantner Instruments
# Ver : 170407t17_1 yyymmddhh_tz
# Nomenclature *default if missing)
# Prefixes
#   m* measurement
#   r* reference
#   n* normalised
#   a* alpha current temperature coefficient
#   b* beta voltage temperature coefficient
# Suffixes (if more than one use in alphabetical order e.g. _AST)
#   _U uncorrected (default if missing)
#   _T corrected for Tmodule
#   _A corrected for angle of incidence
#   _S corrected for spectrum
#
# Variable names
# Gi = Plane of array irradiance kW/m2
# PRDC = DC Performance ratio or MPR = Efficiency.measured/Efficiency/nominal
# POA = Plane of array
# LLEC = Low light efficiency coefficient
# mTAMB = measured Ambient temperature
# mTMOD = measured Module temperature
# YA = dc Energy yield "kWh.DC/kWp"

# DEFINITIONS AT STC
TSTC = 25 # C
GSTC = 1 # kW/m2
WSSTC = 1 # ms^-1
# GET THE PV DATASHEET REFERENCE VALUES r* AND TEMPERATURE COEFFICIENTS
# rIsc, rImp, rVmp, rVoc
# aIsc_Ref, bVoc_Ref, Gamma_Ref
#
# MEASURE THE CONDITIONS AND IV CURVE(S), DERIVE THE FOLLOWING #
# dt                                # DATE+TIMES
# Gi                                # POA irradiance kW/m2
# mTamb                            # Ambient temperature
# mTmod                            # module temperature

# mIsc, mRsc                         # from curve fit near V=0
# mImp, mVmp                          # from curve fit near max(I * V)
# mRoc, mVoc                          # from curve fit near I=0
#
# mI2 = I @ Vmp/2                     # cell mismatch, shading ?
# mV2 = V @ Imp/2                     # rollover from non ohmic back contact?
#
#                                         Colour      #RGB
# DERIVE CURVATURE PARAMS
nIc = mI2/(mIsc-mVmp/2/mRsc)        # I@Vmp/2           LightGreen EAF5DC
nVc = mV2/(mVoc-mImp/2*mRoc)         # V@Imp/2           LightBlue C8F0FF

# CALCULATE (mIr, mVr) WHERE RSC and ROC LINES CROSS to make maths easier
mIr=(mIsc*mRsc-mVoc)/(mRsc-mRoc)    # calc I @ Rsc-Roc intercept
mVr=mRsc*(mVoc-mIsc*mRoc)/(mRsc-mRoc) # calc V @ Rsc-Roc intercept

# now calculate normalised LFM parameters unit %
nIsc_U = mIsc/rIsc/Gi               # U=Un temp corr Purple      #AB73D5
nRsc   = mIr/mIsc                  # Orange      #FF8409
nImp   = mImp/mIr*rIsc/rImp       # Green       #BEE296
nVmp   = mVmp/mVr*rVoc/rVmp       # Blue        #5BD2FF
nRoc   = mVr/mVoc                  # Pink        #CC00CC
nVoc_U = mVoc/rVoc                 # U=Un temp corr Brown     #948A54

nIdc_U = mImp/rImp/Gi              # MidGreen   #D3ECB9
nVdc_U = mVmp/rVmp                # MidBlue   #93E1FF

# can also correct by temperature _T
nVoc_T = nVoc_U * (1-bVoc_Ref*(mTmod-Tstc)) # Temp correct by bVoc
nIsc_T = nIsc_U * (1-aIsc_Ref*(mTmod-Tstc)) # Temp correct by aIsc

```



# Highly Effective $\text{TiO}_{2-x}$ Electron Transport Layers via Atmospheric Pressure Plasma Enhanced CVD

John L. Hodgkinson<sup>\*a</sup>, Heather M. Yates<sup>a</sup>, Arnaud Walter<sup>b</sup>, Sylvain Nicolay<sup>b</sup>

<sup>a</sup>Materials and Physics Research Centre, University of Salford, Cockcroft Building, Manchester, M5 4WT  
<sup>b</sup>Centre Suisse d'Electronique et de Microtechnique (CSEM), PV-Center, Jaquet-Droz 1, 2002 Neuchâtel, Switzerland.

\* Corresponding Author J.L.Hodgkinson@salford.ac.uk

## Abstract

Perovskite solar cells have shown considerable promise as architecture for the next generation of solar modules, attracting extensive research across the globe. However, one of the remaining challenges is the cost effective large scale production of the component layers, typically produced via spin coating or vacuum based deposition technologies. In this work we demonstrate the use of an atmospheric pressure, plasma enhanced, CVD (AP PECVD) process to produce  $\text{TiO}_{2-x}$  films for use as electron transport layers (ETL), compatible with existing online transparent conductive oxide (TCO) production. The film must be sufficiently thin in order to provide effective electron transport, yet suitably dense and defect free to provide a hole blocking function in order to avoid recombination with electrons from the TCO electrode. Operating a PECVD system at atmospheric pressure presents a significant challenge, often resulting in compromised film properties compared to vacuum processes. We show that by careful design and control of plasma parameters,  $\text{TiO}_{2-x}$  ETL can be deposited over a 10 x 10 cm substrate in a continuous manner.  $\text{TiO}_{2-x}$  was deposited on commercial TCO (Solaronix TCO22-15) and used to construct mesoscopic perovskite cells ( $1 \text{ cm}^2$ ). The cells showed overall efficiencies exceeding those achieved by the reference cells which used a sputtered  $\text{TiO}_{2-x}$  ETL. This work demonstrates a new capability for AP PECVD, with our demonstrator unit clearly showing the potential for scale up whilst offering a route to enhance ETL, and hence overall cell performance.

## Introduction

The electron transport layer (ETL) plays a critical role in the performance of most perovskite PV architectures, extracting photogenerated electrons from the perovskite and transporting these charges

to the electrode [1]. The ETL also serves as a hole blocking layer, preventing recombination of holes generated in the perovskite with electrons in the TCO electrode. The ETL layer, typically  $\text{TiO}_2$ , needs to be compact, defect free and conformal to avoid poor cell performance.

This layer is usually produced by spin coating [2] which is limited to small areas, or vacuum processes such as ALD [3] or magnetron sputtering. Which although scalable, incur high start-up and running costs, with additional issues associated with batch processing. In this work we demonstrate the feasibility of a continuous, large area atmospheric pressure CVD process which utilises plasma activation to provide growth at near ambient temperatures (AP PECVD). This approach combines control of film properties with uniform, large area deposition, potentially reducing costs and providing new scope for optimisation and in-line integration [4, 5].

## Experimental

The  $\text{TiO}_{2-x}$  films were deposited at ambient temperature using the laboratory scale reactor shown in figure 1. The roll to roll system may be used to convey solid substrates up to 20 x 20 cm to provide dynamic coating and simulate a continuous production process. In this work, 10 cm x 10 cm substrates were used to suit the cell fabrication process.  $\text{TiO}_{2-x}$  films were deposited on 3mm float glass and a commercial F:SnO<sub>2</sub> (FTO), TCO22-15 supplied by Solaronix. Titanium (IV) isopropoxide (TTIP) ( $\geq 97\%$  Aldrich) was delivered via a conventional bubbler at a rate of  $5 \times 10^{-5} \text{ mol} \cdot \text{min}^{-1}$  with a total process gas flow of  $14.6 \text{ L} \cdot \text{min}^{-1}$ . Film thickness was controlled by the number of passes under the coating head. Argon (99.998% BOC) was used throughout with plasma activation being provided by an audio frequency system. This unit operates at a resonant frequency in the order of 3.2 kHz and features high

frequency suppression to attenuate the current spikes associated with a filamentary discharge [6], helping to maintain a diffuse discharge.



**Figure 1:** Photograph showing the roll to roll AP PECVD system

The AP PECVD  $\text{TiO}_{2-x}$  films were characterised via X-ray photoelectron spectroscopy (Kratos Axis Nova), with experimental data processed using the ‘Casa XPS’ software package. The scans were calibrated using the C1s binding energy of 285 eV. The crystallographic structure was assessed by both X-ray Diffraction (Siemens D5000) and Raman spectroscopy using a 532 nm laser [7]. Film thicknesses were measured by masking the substrate with ‘Kapton’ polyimide tape and measuring the resultant step using a ‘Dektak 3ST’ surface profiler. The sheet resistance of the films was measured using a Jandel Universal four point probe. Reflection and transmission values were measured simultaneously between 400 and 800 nm using a visible/near IR fiber optic spectrophotometer (Ocean Optics, USB 2000+) and the associate ‘SpectraSuite’ software. Haze measurements were taken using lab built spectrometer consisting of a 75 W xenon lamp, integrating sphere and four broadband filters centring on four wavelengths (800, 650, 531, and 450 nm).

The AP PECVD films were used to construct  $1 \text{ cm}^2$  mesoporous perovskite cells alongside reference cells using a previously optimised sputtered ETL. The method, along with dark conductivity and cell performance evaluation, has been described in previous work by the authors [8].

## Results & Discussion

The process was capable of producing uniform and adherent  $\text{TiO}_{2-x}$  layers on the TCO22-15 substrate (Fig 2.). The image shows a film deposited on TCO after initial masking. The intense uniform purple reflection at the positions of  $\text{TiO}_{2-x}$  deposition confirms the film uniformity.

XPS analysis showed the films to be sub-stoichiometric, determined by the deconvolution of the high resolution O 1s and Ti 2p spectra, with  $2\text{p}_{3/2}$  at 458.8 eV and  $2\text{p}_{1/2}$  at 464.5 eV showing spin orbital splitting in the order of 5.7 eV, indicative of  $\text{Ti}^{4+}$  attached to  $\text{O}^{2-}$  [9]. A minor third component at 457.4 eV was assigned to the presence of  $\text{Ti}^{3+}$  [10], confirming the sub-stoichiometry and highlighted in the example spectra given in figure 3.

It was found that the stoichiometry of the film could be varied with applied voltage and hence plasma intensity as shown in figure 4. An applied voltage of 1.6 kV was chosen for the test samples as a low level of activation would minimise the risk of powder formation and particle inclusion within the hole blocking layer. XRD and Raman measurements showed the films to be amorphous in each case due to the room temperature deposition. Films were deposited at a line speed of  $10.69 \text{ m.hr}^{-1}$ , for 4, 6 and 10 passes under the AP PECVD head, resulting in film thicknesses of 40, 55 and 85 nm respectively.

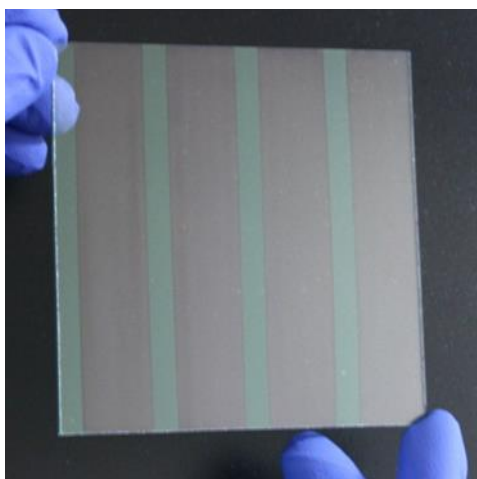


**Figure 2:** Photograph showing the AP PECVD  $\text{TiO}_{2-x}$  film on the  $10 \times 10 \text{ cm}$  TCO22-15 substrate prior to cell construction.

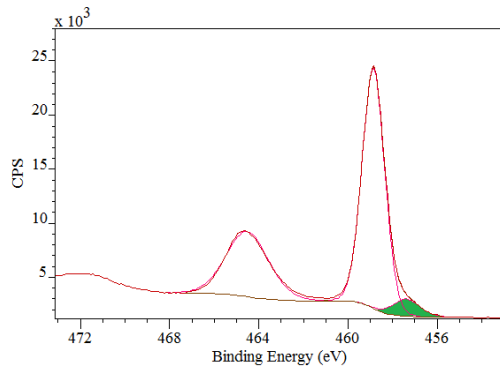


**Figure 3:** High resolution Ti 2p spectrum showing the significant  $\text{Ti}^{3+}$  contribution.

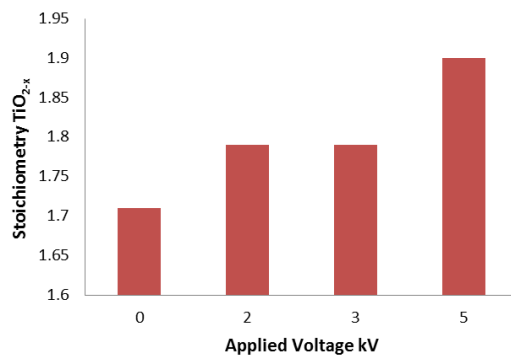


**Figure 4:** Plot showing the increase in stoichiometry with applied voltage.

The addition of the  $\text{TiO}_{2-x}$  layer resulted in an increase in mean reflection (400-800 nm) between 1.1 and 3.8% and an increase in transmission from 77.7 to  $81 \pm 1\%$ . Usually, one would expect a decrease in transmission on increasing reflection. However, this can be explained by the reduced haze ( $\sim 1\%$  reduction) due to the smoother surface provided by the  $\text{TiO}_{2-x}$  layer. The AFM images given in figure 5 show the significant reduction in rms roughness provided by the amorphous  $\text{TiO}_{2-x}$ , with the roughness dropping from 14 nm for the uncoated TCO surface to 4 nm after  $\text{TiO}_{2-x}$  coating. This suggests that the  $\text{TiO}_{2-x}$  does not coat conformally, but gradually fills the surface troughs. The films allowed conductivity in the horizontal plane comparable to the uncoated TCO, as measured by four point probe with values ranging from 12.4 to 13.4  $\Omega/\square$ . However, dark conductivity measurements showed increased resistance compared to the sputtered reference film which appeared to be related to the increased thickness of the AP PECVD films.

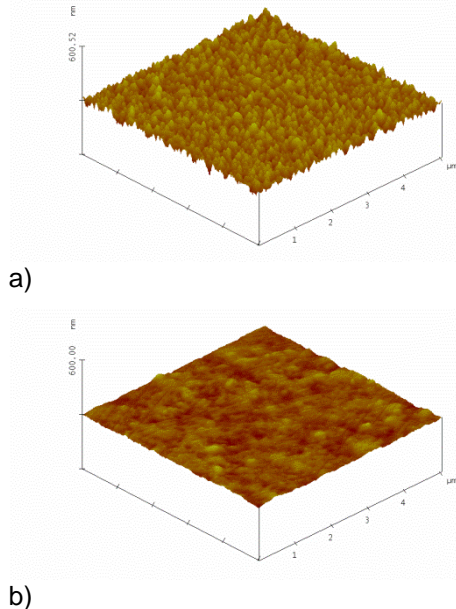


**Figure 5:** 5  $\mu\text{m}$  AFM images showing a) the 14 nm rms TCO22-15 surface and b) coated with 40 nm  $\text{TiO}_{2-x}$  resulting in 4 nm rms.

The AP PECVD films on TCO22-15 were used to construct mesoporous perovskite cells and tested alongside reference cells using a 23 nm sputtered  $\text{TiO}_{2-x}$ . The results were highly encouraging, showing efficiencies greater than the optimised reference samples, as summarised in figure 6. This observation was reflected in the Maximum Power Point tracking (MPP) with the cell fabricated from the 40 nm film achieving 13.57% after 5 minutes with the reference stabilising at 13.15%. J-V plots for the 40 nm film showed improved fill factor in the forward and reverse direction of 59.44 / 67.08% compared to the sputtered reference  $\text{TiO}_{2-x}$  57.07 / 65.42%.

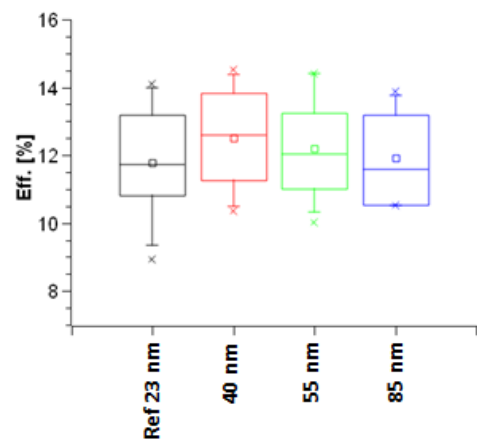


**Figure 6:** Cell efficiency distribution for the AP PECVD  $\text{TiO}_{2-x}$  and sputtered reference film.

## Conclusion

The AP PECVD process proved capable of producing highly effective  $TiO_{2-x}$  ETL on TCO22-15 substrates achieving an efficiency of 14.53% (13.57% MPP) within a  $1\text{ cm}^2$  mesoporous perovskite cell. This exceeded the efficiency of 14.11% (13.15% MPP) resulting from the previously optimised sputtered ETL, and is particularly notable in the context of the greater thickness ( $\geq 40\text{ nm}$  vs  $23\text{ nm}$ ).

Dark conductivity values indicated significantly reducing conductivity and increasing activation energy with thickness, suggesting further advantage for a thinner film. This will be the subject of further work, with ongoing optimisation of growth conditions offering significant scope for further improvements, combined with a highly scalable atmospheric pressure process.

## Acknowledgements

This work was financed by Framework 7 grant FP7 NMP.2012.1.4-1 309530 PLIANT “Process line implementation for applied surface nanotechnologies”. XPS analysis was provided by the NEXUS national facility, with Raman analysis kindly provided by J.E. Proctor and Malik Hakeen at the University of Salford

## References

1. Yang, G., et al., *Recent progress in electron transport layers for efficient perovskite solar cells*. Journal of Materials Chemistry A, 2016. **4**(11): p. 3970-3990.
2. Zhang, C.X., et al., *Influence of different  $TiO_2$  blocking films on the photovoltaic performance of perovskite solar cells*. Applied Surface Science, 2016. **388**: p. 82-88.
3. Chen, L., et al., *Compact layer influence on hysteresis effect in organic-inorganic hybrid perovskite solar cells*. Electrochemistry Communications, 2016. **68**: p. 40-44.
4. McCurdy, R.J., *Successful implementation methods of atmospheric CVD on a glass manufacturing line*. Thin Solid Films, 1999. **351**(1–2): p. 66-72.
5. Nelson, D.M., M.M. Radtke, and S.E. Phillips, *Chemical Vapor Deposition Process for Depositing a Silica Coating on a Glass Substrate*. 2016, Pilkington Group Limited: USA.
6. Bogaerts, A., et al., *Gas discharge plasmas and their applications*. Spectrochimica Acta Part B: Atomic Spectroscopy, 2002. **57**(4): p. 609-658.
7. Smith, D., et al., *Hydrogenation of Graphene by Reaction at High Pressure and High Temperature*. ACS nano, 2015. **9**(8): p. 8279-8283.
8. Yates, H.M., et al., *Progression towards high efficiency perovskite solar cells via optimisation of the front electrode and blocking layer*. Journal of Materials Chemistry C, 2016.
9. Simonsen, M.E., et al., *Surface properties and photocatalytic activity of nanocrystalline titania films*. Journal of Photochemistry and Photobiology A: Chemistry, 2008. **200**(2–3): p. 192-200.
10. Kumar, P.M., S. Badrinarayanan, and M. Sastry, *Nanocrystalline  $TiO_2$  studied by optical, FTIR and X-ray photoelectron spectroscopy: correlation to presence of surface states*. Thin Solid Films, 2000. **358**(1–2): p. 122-130.

## Characterisation and optimisation of processing time for perovskite solar cells

Katherine Hooper, Joel Troughton, James McGettrick, Francesca De Rossi, Michael

Newman, Wing Chung Tsoi, and Trystan Watson\*

SPECIFIC, College of Engineering, Swansea University, Bay Campus, Swansea, SA1 8EN

\* Corresponding Author T.M.Watson@swansea.ac.uk

### Introduction

Since their inception in 2009 [1] and solid state breakthroughs in 2012 [2,3] perovskite solar cells (PSCs) have become a promising candidate for low cost thin film photovoltaics with rapid improvements in performance and a large variety of different architectures. Now with a certified efficiency over 22% in 2016 [4] they are starting to rival conventional thin film technologies. However in order to become commercially viable there are two main challenges for PSCs; stability and large scale processability.

It is critical to focus research on the potential bottlenecks to large scale industrial manufacture such as the deposition and heating processes. Some architectures are particularly energy and time intensive such as the fully printable mesoscopic stack [5] which requires over 2 hours 400°C+ heating, and those based on mesoporous TiO<sub>2</sub> [3] which require 1 hour at 550°C. In addition there is the annealing of the perovskite from solution which can take between 30 and 90 min for most perovskite films. Antisolvent methods [6] can help induce crystallisation to reduce annealing time [7] but some, such as for triple cation perovskite films [8], still greatly benefit heating for 60 min at 100°C to grow uniform large grains after they have been seeded. Triple cation perovskite is one of the most desirable to adapt for scaling up because it has achieved over 20% efficiency and the mixture of cations make it more stable than methylammonium lead halide perovskite alone [8].

Alternative heating techniques have been used to rapidly heat perovskite films in seconds and milliseconds via near infrared (NIR) [9], rapid thermal annealing [10], and visible light based pulses [11,12]. Reducing the high temperature processing time for the sintering of TiO<sub>2</sub> in PSCs has not yet been addressed although it has been demonstrated in dye-sensitised solar cells also using NIR radiation [13]. Here we expand upon previous work using NIR to rapidly sinter compact and mesoporous TiO<sub>2</sub> layers simultaneously for a PSC

device. We also study the NIR annealing of both methylammonium and mixed cation based perovskite films to produce efficiencies of over 12%.

### Experimental

#### Preparation of films and devices

Both samples and devices were fabricated in an identical manner up to the layer of interest. FTO coated glass ( $7 \Omega/\square$ , Solaronix) was sonicated in a solution of 2% hellmanex in DI water, followed by DI water, acetone and IPA before 10 minutes of oxygen plasma cleaning. 50 nm of compact TiO<sub>2</sub> (c-TiO<sub>2</sub>) was deposited at 300°C by spray pyrolysis of titanium diisopropoxide bis(acetylacetone), in a 1:9 volume solution of IPA. It was sintered for 30 min at 550°C. In the case of devices it was cooled after spraying and sintered the same time as the subsequent mesoporous TiO<sub>2</sub> layer. Mesoporous TiO<sub>2</sub> (m-TiO<sub>2</sub>) was obtained by spin coating a suspension of TiO<sub>2</sub> nanoparticles (Dyesol 30NR-D:ethanol 2:7 wt) at 4500 rpm for 30 s and sintered for 30 min at 550°C.

Two different perovskites were studied; methylammonium based (CH<sub>3</sub>NH<sub>3</sub>, MA), and mixed cation containing MA, formamidinium (CH<sub>3</sub>(NH<sub>2</sub>)<sub>2</sub>, FA) and caesium. They were prepared onto m-TiO<sub>2</sub>/c-TiO<sub>2</sub>/FTO glass substrates. MAPbI<sub>3-x</sub>Cl<sub>x</sub> films were spin coated at 2000 rpm for 30 s from a 3:1 molar solution of MAI and PbCl<sub>2</sub> at 40 wt% in DMF. They were held at room temperature for 10 min and then annealed on a hot plate at 100°C for 90 min. Triple cation perovskite films, Cs<sub>0.05</sub>(MA<sub>0.17</sub>FA<sub>0.83</sub>)<sub>(1-0.05)</sub>Pb(I<sub>0.83</sub>Br<sub>0.17</sub>)<sub>3</sub> [8], were spin coated with a profile of 1000 rpm for 10 s, then 4000 rpm for 20 s where chlorobenzene antisolvent was dripped onto the spinning substrate with 10 s remaining. They were then annealed on a hot plate for 60 min at 100°C.

For the fabrication of solar cell devices a spiro-OMeTAD film was spin coated at 3000 rpm for 30 s from a solution of 75 mg/ml in chlorobenzene with additives of 30 µl/ml 4-tert-butylpyridine, and 20 µl/ml

bis(trifluoromethane) sulfonamide lithium salt solution (520 mg/ml in acetonitrile). Gold electrodes were evaporated at  $10^{-4}$  torr using an Edwards 306 thermal evaporator. The final device structure is shown in figure 1.

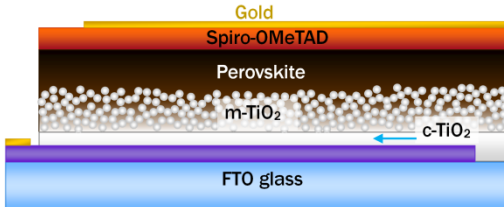


Figure 1: Schematic of device structure

All NIR heating was performed using a 24 kW NIR oven (AdPhos NIR/IR Coil lab LV2), previously described in detail elsewhere [9, 13]. Compact and mesoporous  $\text{TiO}_2$  films were sintered simultaneously using a lamp intensity of 100% and NIR exposure time of 12.5 s. Perovskite films were exposed to between 5 and 2 s of NIR radiation with lamp intensities between 50 and 90%.

#### Characterisation of films and devices

The c- $\text{TiO}_2$  hole blocking layers (BL) were characterised by cyclic voltammetry, Raman spectroscopy and x-ray diffraction (XRD) as detailed below. Cyclic voltammetry (CV) was performed on a Solartron potentiostat with a Calomel reference electrode and Pt counter electrode in an electrolyte of  $\text{K}_3[\text{Fe}(\text{CN})_6] + \text{K}_4[\text{Fe}(\text{CN})_6]$  in 0.5M KCl. Raman spectroscopy was carried out on a Renishaw Invia Raman system in backscattering configuration with a laser excitation of 532 nm. XRD data was obtained using a Bruker D8 Discover instrument with a  $\text{CuK}_\alpha$  beam at 40 kV and 40 mA, using 0.5 s at 0.5  $2\theta$  step size scan for  $\text{TiO}_2$  and 0.1 s at 0.01  $2\theta$  step size scan for perovskite. Scanning electron microscopy (SEM) images of films were collected using a Jeol JSM-7800F field emission gun electron microscope with a 5 kV beam, and 6-10 mm working distance.

For current-voltage measurements of solar cells, devices were masked to  $0.1 \text{ cm}^2$  and tested under a class AAA solar simulator (Newport Oriel Sol3A) at AM1.5 and  $100 \text{ mW cm}^{-2}$  illumination conditions calibrated against a KG5 filtered silicon reference cell (Newport Oriel 91150-KG5) using a Keithley 2400 source meter. IV sweeps were performed from both  $V_{\text{OC}}$ -to- $J_{\text{SC}}$  and vice versa at a rate of  $0.1 \text{ V s}^{-1}$ .

## Results and Discussion

### Characterisation of NIR sintered $\text{TiO}_2$

The role of the c- $\text{TiO}_2$  blocking layer is to prevent recombination of electrons and holes at the FTO interface. It still needs to be conductive enough to allow transport of electrons so that charge can be transferred to the FTO contact. Cyclic voltammetry was used to determine the integrity of this layer.  $\text{TiO}_2$  acts as dielectric to the  $\text{Fe}(\text{CN})_6^{3-/4-}$  redox couple [14]. However, charge transfer does occur in contact with bare FTO as is shown in figure 2. Any anodic currents formed for the c- $\text{TiO}_2$  samples should be due to oxidisation of ferricyanide at the FTO surface, indicating pinholes in the  $\text{TiO}_2$ . Figure 2 shows the current is greatly suppressed by the oven (sprayed at 300°C, sintered at 550°C) and NIR (sprayed at 300°C, heated for 12.5 s with 90% lamp intensity) sintered  $\text{TiO}_2$  layers which suggests they should work well as a blocking layer. Interestingly c- $\text{TiO}_2$  which was only sprayed at 300°C but not subsequently sintered, displays the strongest blocking effect. This could be due to the low conductivity of the layer which without high temperature heating (to convert the amorphous  $\text{TiO}_x$  precursor to crystalline  $\text{TiO}_2$ ) is an order of magnitude lower than that of sprayed  $\text{TiO}_2$  after sintering [15].

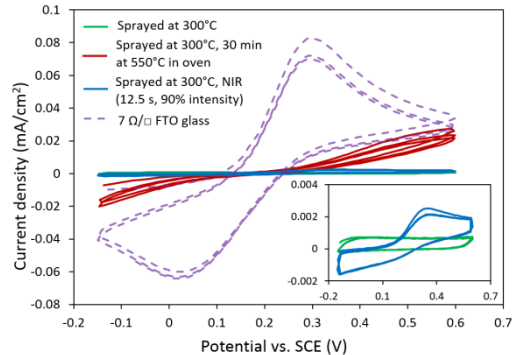


Figure 2: Cyclic voltammogram of FTO and c- $\text{TiO}_2$  BLs in  $\text{Fe}(\text{CN})_6^{3-/4-}$  electrolyte

CV was also performed on substrates of m- $\text{TiO}_2$  and c- $\text{TiO}_2$  sintered simultaneously to confirm that saving time by heating the layers together has no detrimental effect on the formation of an effective blocking layer. The mesoporous layer alone has no ability to block charge transfer to FTO so the it can be assumed that blocking effects observed on the m- $\text{TiO}_2$ /c- $\text{TiO}_2$ /FTO substrates are due to the conformity of the c- $\text{TiO}_2$ . In the case of both the oven and NIR heated samples

the blocking ability was identical to their c-TiO<sub>2</sub> only counterparts, suggesting there is no disadvantage to sintering simultaneously.

The crystallinity of the c-TiO<sub>2</sub> BLs was characterised using XRD and Raman spectroscopy (figure 3). Figure 3.a shows a peak at 25.3° for the NIR and hot plate sintered samples which corresponds to the (101) plane of anatase TiO<sub>2</sub>. No anatase peaks are present for the sprayed at 300°C only c-TiO<sub>2</sub> indicating it is still in its amorphous precursor state. Highly crystalline TiO<sub>2</sub> greatly aids electron transfer and it has been shown without the high temperature heating step to convert it to anatase the performance is poor in devices [15]. Raman spectroscopy in figure 3.b shows a strong peak observed at 144 cm<sup>-1</sup> which can be attributed to the E<sub>g</sub> vibrational mode of anatase TiO<sub>2</sub>. It is not present in the case of the sprayed at 300°C only or 12.5 s of 50%-60% intensity NIR exposure after spraying, again showing these films are amorphous. It also suggests that there was insufficient heat from the NIR at 50-60% intensity improve the crystallinity of the sprayed BL. Between 80-100% NIR the 144 cm<sup>-1</sup> peak increases as there is sufficient heat to convert the TiO<sub>2</sub> to the anatase phase.

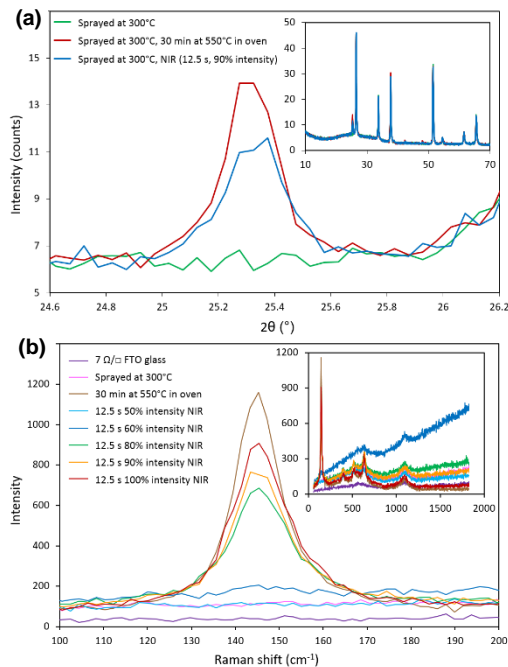


Figure 3: (a) XRD (b) and Raman of sprayed at 300°C and subsequently oven and NIR sintered c-TiO<sub>2</sub> BLs showing the region associated with crystalline anatase TiO<sub>2</sub> and full range measured (inset)

### Characterisation and optimisation of NIR annealed perovskite films

In previous work MAPbI<sub>3-x</sub>Cl<sub>x</sub> films (containing alumina nanoparticles) were annealed using NIR and fabricated into devices of equivalent performance to the hot plate annealed controls [9]. Here we reoptimised the NIR settings for MAPbI<sub>3-x</sub>Cl<sub>x</sub> on a mesoporous TiO<sub>2</sub> scaffold. With NIR heating both the exposure time and lamp intensity can be varied, and it is possible to achieve the same temperature for different combinations. Three different NIR exposure time and intensity combinations were chosen which avoid over and underexposure, leading to a dark brown film similar in appearance to a film annealed conventionally on a hot plate for 90 min at 100°C. SEM (figure 4) of the fastest, 2.08 s 90% intensity, and slowest, 5 s 50% intensity, NIR annealed films shows uniform round grains which appear flat and marked on the surface. In contrast the 90 min hot plate annealed MAPbI<sub>3-x</sub>Cl<sub>x</sub> produced a random distribution in grain shape and size.

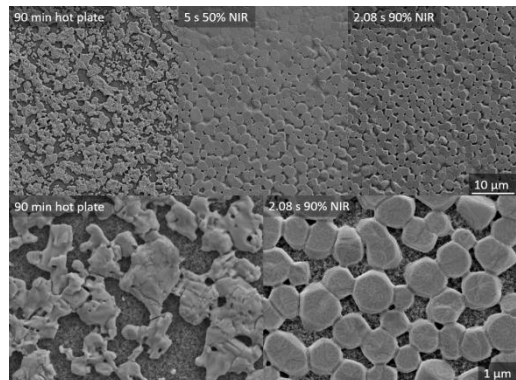


Figure 4: SEM images of MAPbI<sub>3-x</sub>Cl<sub>x</sub> films annealed by two different combinations of NIR time and intensity vs. by hot plate

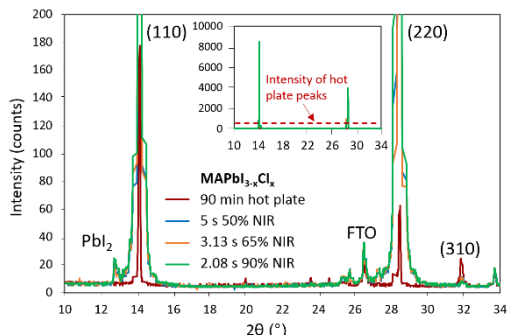


Figure 5: XRD of NIR and hot plate annealed MAPbI<sub>3-x</sub>Cl<sub>x</sub> films

The preferred orientation for the NIR annealed perovskite grains is reflected in the XRD (figure 5) where the intensity of the (110) and (220) perovskite are

respectively 48 and 61 times higher than those of the film annealed by hot plate. The height of the FTO peak is identical for all. The same NIR settings optimised for  $\text{MAPbI}_{3-x}\text{Cl}_x$  films were then used to anneal films of triple cation perovskite,  $\text{Cs}_{0.05}(\text{MA}_{0.17}\text{FA}_{0.83})_{(1-0.05)}\text{Pb}(\text{I}_{0.83}\text{Br}_{0.17})_3$ . After spin coating of the antisolvent the films already appear dark and glassy (similar to after annealing) so it is difficult to visually judge the effectiveness of annealing. The total energy input required to anneal both types of perovskite is assumed to be comparable because the conventional heating of both is over 1 hour at 100°C on a hot plate, suggesting the same NIR settings would be compatible.

There was little distinction between the XRD patterns of different NIR and hot plate annealed triple cation perovskite films, and they matched well with literature [8]. SEM images (figure 6) show the films are all smooth and have good coverage. The 5 s NIR heated film has similarly sized grains to the hot plate but the 2.08 s NIR sample appears to have marginally larger grains. There also appears to be surface defects on the NIR annealed films.

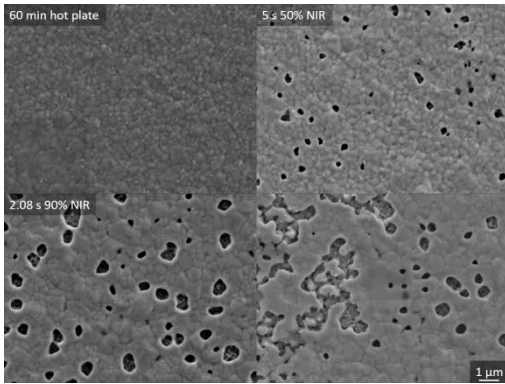


Figure 6: SEM images of NIR and hot plate annealed triple cation perovskite

#### **Reduction of processing time and fabrication of perovskite solar cells**

NIR heating has been used to significantly reduce the heating times of  $\text{TiO}_2$  and perovskite as illustrated in figure 7. Hot plate annealed triple cation PSCs were fabricated to compare oven vs. NIR sintered  $\text{c-TiO}_2/\text{m-TiO}_2$  layers. An interesting observation which provided some challenges was that etched FTO glass was prone to cracking during NIR processing. There is a large difference in NIR absorption between the glass and FTO [13] so the difference in temperature reached causes it to crack. To enable the

fabrication of devices the FTO was isolated after  $\text{TiO}_2$  sintering (for both oven and NIR heated layers) using a  $\text{CO}_2$  laser. This process slightly affected the performance but maximum efficiencies of 12.3% for the 12.5 s NIR sintered  $\text{TiO}_2$  and 12.5% for the 30 min oven sintered  $\text{TiO}_2$  were obtained.

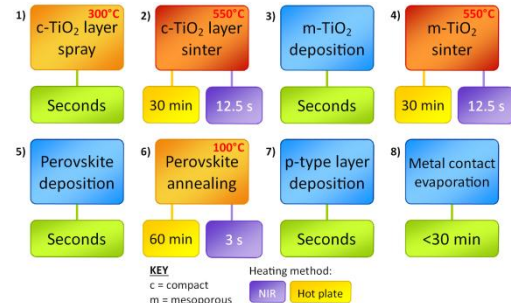


Figure 7: Schematic showing fabrication steps and associated times for a PSC with heating times for both hot plate and NIR methods

Figure 8 shows the efficiency of NIR annealed triple cation PSCs. They were fabricated on oven sintered  $\text{TiO}_2$  so that etched substrates could be used. The performance of 2.08 s NIR annealed cells was slightly better than the slower ones, due to an increase in  $J_{\text{SC}}$  and  $V_{\text{OC}}$ . The hot plate cells were the best with the highest FF and  $V_{\text{OC}}$ .

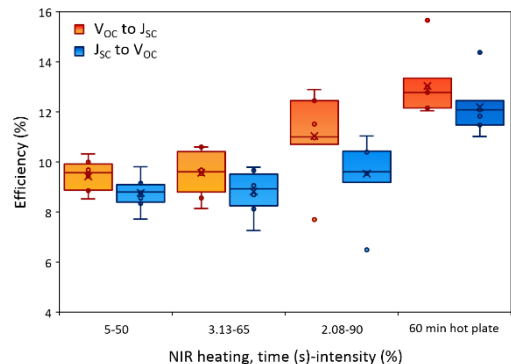


Figure 8: Box whisker plot of efficiency distribution (8 cells for each) in both scan directions for 3 different NIR settings and standard 60 min hot plate annealed triple cation PSCs

#### **Conclusions**

It is very promising that perovskite can be annealed in seconds with almost equal performance to films conventionally annealed on a hot plate for 60 min (average for 2.08 s NIR was about 91.4% of average for 60 min hot plate). Triple cation perovskite is one of the best performing in literature and has good stability [8] so reducing the annealing time

should be more commercially relevant than for MAPbI<sub>3-x</sub>Cl<sub>x</sub> films which have poor stability. Further study is needed to optimise the NIR heating (avoid surface defects) and also to determine if the optimal grain structure is being obtained with a cross sections since long columnar grains are desirable. In the case of 12.5 s NIR annealed c-TiO<sub>2</sub>/m-TiO<sub>2</sub> the performance is equal to that of the 30 min oven equivalent. There were issues using NIR to heat etched FTO glass substrates due to the temperature difference between FTO and glass causing cracks. However it has been found that using finely etched (~1 mm thick) lines it is possible to expose the FTO glass to the settings required for TiO<sub>2</sub> sintering without any damage to the substrate. Therefore it is possible to fabricate fully NIR heating perovskite devices with heating steps <30 s compared to 1.5 hours for conventional devices.

## References

- [1] A. Kojima, K. Teshima, Y. Shirai, T. Miyasaka, *J. Am. Chem. Soc.* **2009**, 131, 6050
- [2] M.M. Lee, J. Teuscher, T. Miyasaka, T.N. Murakami, H.J. Snaith, *Science* **2012**, 338, 643
- [3] H.-S. Kim, C.-R. Lee, J.-H. Im, K.-B. Lee, T. Moehl, A. Marchioro, S.-J. Moon, R. Humphry-Baker, J.-H. Yum, J. E. Moser, M. Grätzel, N.-G. Park, *Sci. Rep.* **2012**, 591
- [4] <https://www.nrel.gov/pv/assets/images/efficiency-chart.png>
- [5] A. Mei, X. Li, L. Liu, Z. Ku, T. Liu, Y. Rong, M. Xu, M. Hu, J. Chen, Y. Tang, M. Grätzel, H. Han, *Science* **2014**, July, 295
- [6] N.J. Jeon, J.H. Noh, Y.C. Kim, W.S. Yang, S. Ryu, S. Il Seok, *Nat. Mater.* **2014**, 13 897
- [7] M. Yin, F. Xie, H. Chen, X. Yang, F. Ye, E. Bi, Y. Wu, M. Cai, L. Han, *J. Mater. Chem. A* **2016**, 4, 8548
- [8] M. Saliba, T. Matsui, J.-Y. Seo, K. Domanski, J.-P. Correa-Baena, M. K. Nazeeruddin, S. M. Zakeeruddin, W. Tress, A. Abate, A. Hagfeldt, M. Grätzel, *Energy Environ. Sci.* **2016**, 9, 1989
- [9] J. Troughton, C. Charbonneau, M.J. Carnie, M.L. Davies, D.A. Worsley, T.M. Watson, *J. Mater. Chem. A* **2015**, 3, 9123
- [10] V.L. Pool, B. Dou, D.G. Van Campen, T.R. Klein-Stockert, F.S. Barnes, S.E. Shaheen, M.I. Ahmed, M.F.A.M. van Hest, M.F. Toney, *Nature Communications* **2017**, 8:14075
- [11] B.W. Lavery, S. Kumari, H. Konermann, G.L. Draper, J. Spurgeon, T. Druffel, *ACS Appl. Mater. Interfaces* **2016**, 8, 8419
- [12] J. Troughton, M.J. Carnie, M.L. Davies, C. Charbonneau, E.H. Jewel, D.A. Worsley, T.M. Watson, *J. Mater. Chem. A* **2016**, 4, 3471
- [13] K. Hooper, M. Carnie, C. Charbonneau, T. Watson, *Int. J. Photoenergy* **2014**, 1-8
- [14] L. Kavan, N. Tétreault, T. Moehl, M. Grätzel, *J. Phys. Chem. C* **2014**, 118, 16408
- [15] K. Wojciechowski, M. Saliba, T. Leijtens, A. Abate, H.J. Snaith, *Energy Environ. Sci.* **2014**, 7, 1142



# UNDERSTANDING AND CONTROLLING ELECTRON TRANSFER BETWEEN SENSITIZER AND ELECTROLYTE

Peter J. Holliman<sup>a\*</sup>, Christopher Kershaw<sup>a,b</sup>, Arthur Connell<sup>a</sup>, Eurig W. Jones<sup>a</sup>, Robert Hobbs<sup>a</sup>, Rosie Anthony<sup>a</sup>, Leo Furnell<sup>a</sup>, James McGettrick<sup>a</sup>, Dawn Geatches<sup>c</sup> and Sébastien Metz<sup>c</sup>

<sup>a</sup> College of Engineering, Swansea University, Bay Campus, Crymlyn Burrows, Swansea SA1 8EN UK

<sup>b</sup> School of Chemistry, Bangor University, Bangor, Gwynedd LL57 2UW

<sup>c</sup> STFC, Daresbury, Warrington, Cheshire

Corresponding Author: p.j.holliman@swansea.ac.uk

## Introduction

Since their discovery in the early 1970's dye-sensitized solar cells (DSC's) have gone on to be one of the most promising forms of solar PV technology. They are environmentally safe, cheap to produce and have recently hit efficiencies of greater than 14 %. [1] DSC's are made up of a dye/sensitizer chemically adsorbed onto a semi-conducting metal oxide, sandwiched between two electrodes all connected by a liquid electrolyte. Photoexcitation of the

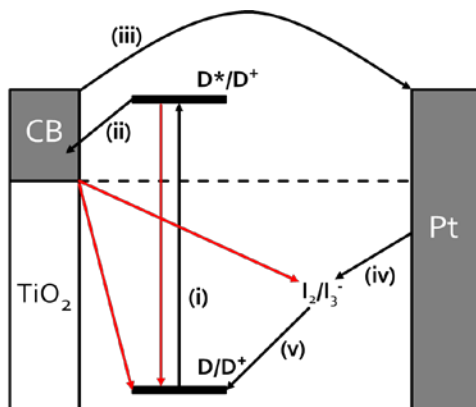


Figure 1: Schematic of DSC device

sensitizer promotes an electron from the HOMO to the LUMO leaving the sensitizer in an oxidised state. The sensitizer is regenerated by electron transfer from the electrolyte. The oxidised electrolyte is regenerated by recapturing the promoted electron via the counter (platinum) electrode. In DSC's, the sensitizer is one of the key components for high power conversion efficiencies. Extending spectral response of the sensitizer has been a focus point when trying to increase device performance. Attempts have been made in increasing the spectral response of panchromatic dyes such as "black dye" or "squaraines", however any increase in  $J_{sc}$  achieved comes at the expense of  $V_{oc}$ .[2] Ruthenium-bipyridyl (Ru-bipy) are currently the most widely used sensitizer in DSC devices. Since their first introduction in 1991, Ru-bipy sensitizers have been the

fore-runners in high-efficiency DSC devices with examples including C106 [3], N719 [4] and C101.[5,6] Ru-bipy dyes are highly efficient at ca. 550 nm but their response falls away dramatically between 650 and 700 nm.[7] Despite relatively simple synthesis, their purification Ru-bipy dyes is complex and Ru is costly so that these dyes are very expensive and challenging to upscale making them less desirable for industry production of DSC's [8] These problems have led to the development of many new organic dyes including triarylamines, [9-11] coumarins,[12] cyanines [13], indolines, [14,15] squaraines,[16-18] quinoxalines [19] and natural dyes.[20] These organic dyes are designed with a donor-pi linker-acceptor (D- $\pi$ -A) structural arrangement to maximise their efficiency. [21] These dyes absorb in the same region as Ru-bipy dyes, they are easier to synthesise, easier to purify and much cheaper. [7] Organic dyes often have higher  $\epsilon$  than their inorganic counterparts which can be extremely useful. Dyes with higher  $\epsilon$  can be used in smaller/thinner devices whilst absorbing just as much light. These thinner means reduced recombination losses and improved  $V_{oc}$ . [22] One of the most recent and promising chromophores to be published is the half-squaraine dyes. Originally discovered as an intermediate during the synthesis of squaraine dyes, these unsymmetrical or half squaraines are synthetically versatile, fluorescent with a high  $\epsilon$  and  $\lambda_{max}$  around 650 nm where Ru-bipy dyes are less sensitive. [23] Half-squaraines have been tested in ZnO devices giving  $\eta = 0.27\%$  [24] and 0.53% [25] and 3.54 % [26] in TiO<sub>2</sub> devices. Unlike other dyes half-squaraines are easily modified. This feature has led to the publication of half-squaraines absorbing all over the AM 1.5 solar spectrum, many of these being in the NIR. This makes them an ideal candidate for co-sensitization. Durrant et al. first reported a step-wise approach to co-sensitization by first sorbing a Ru-bipyridyl dye onto TiO<sub>2</sub>,

then treating with aluminium isopropoxide to deposit an Al<sub>2</sub>O<sub>3</sub> layer before sorbing a Ru-phthalocyanine dye. [27] This technique has led to the highest ever performing DSC device  $\eta = 14.7\%$ . [1] Up until recently the timescale for this technique was far too long. The process needed to be sped up massively in order to push down costs and make DSC's a truly low-cost photovoltaic technology. In 2010, Holliman et al. reported the first ultrafast co-sensitization, with the process taking < 5 min [28a] with ultra-fast sensitization reported in 2012 [28b]. As NIR sensitizers, half-squaraines could be used in conjunction with Ru-by dyes in order to harvest more light and therefore improve device efficiency. [29] As HFSQ's are easily modified they can be used as sensitizers not only in their own right but also as a model chromophore to study similar effects in other dyes. This allows us to study the effects of different modifications to the chromophore and what those effects do to device performance. A paper published in 2014 by Holliman et al. looked at using a HFSQ chromophore to study the effects of the anchoring group position on DSC performance. It is generally believed for the best performing dyes that a donor- $\pi$ -bridge-acceptor-anchor system must be chemisorbed with the acceptor unit situated closest to the metal oxide surface. Therefore, in the case of the half-squaraines the best performing device should have an anchor on the squaric acid unit as this is the acceptor. Several dyes were made each with the

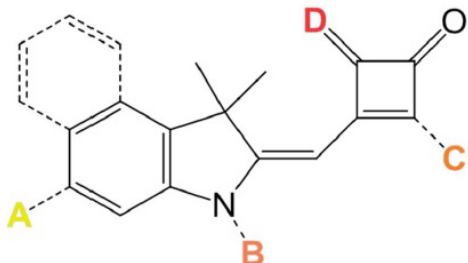


Figure 2: Dye anchoring points A, B and C on half-squaraine chromophore.  
Taken from [30]

carboxylic anchoring group on a different segment of the dye. One dye linked via the squaric acid (Acceptor/LUMO), another had its anchor on the Indole (Donor/HOMO) and the third dye had a linker coming off the nitrogen of the indole (between HOMO and LUMO). As expected the best performing dye linked via the squaric acid unit. The increase in performance was down to an increase in

$V_{oc}$ . [30] A follow up paper by Holliman et al. looked at how dyes orientated themselves on a TiO<sub>2</sub> as more than one anchoring group was introduced into the structure of the dye. As expected when dyes with a singular anchoring group were introduced to the TiO<sub>2</sub> they would have no choice but to bind at the only site available to them. However, it was when multiple anchoring groups were incorporated into the dye, interesting results occurred. As shown from the first paper the best

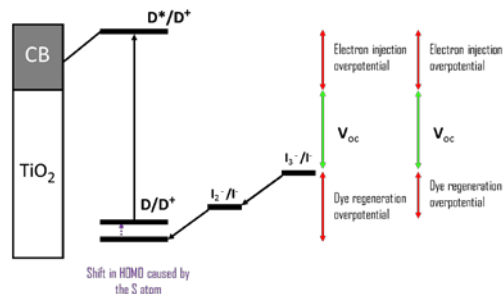


Figure 3: Shift in HOMO caused by the addition of sulfur to half-squaraine sensitizer

anchoring group came from the squaric acid moiety. When a second anchoring group was introduced (off the N of the indole), little effect was seen on the band gap. However, a significant increase of dye stability was recognised. Devices could be measured over days rather than minutes indicating that the dye was bonded to the titania via two anchoring groups. The next dye introduced an anchoring group bound to the indole benzene. When this dye was adsorbed onto titania a large bathochromic shift was observed. This alongside no significant change in performance suggested, the dye bonded through the anchoring group on the squaric acid unit rather than through the benzene indole. Finally, a dye with three anchoring groups was used. A significant decrease in  $\epsilon$  was observed. As expected this led to a drop-in device performance. Overall the paper suggests that though two linkers can improve device stability, the dyes themselves preferentially bind through the acceptor unit (donor- $\pi$  bridge-acceptor-anchor). Therefore, if the second anchor isn't close to the preferential binding site it takes little to no part in the bonding of the dye and therefore isn't involved in the process of electron injection. Holliman et al offer an interesting insight into the behaviour of the sensitizers and their self-assembly onto the TiO<sub>2</sub>. [31] The papers also give some evidence on the preferential

binding site of the dyes and indicate their orientation on the TiO<sub>2</sub> surface. It also describes how these affect device performance however, only three anchoring groups were investigated (carboxylic acid, vinyl dicyano and acyloin). Other anchoring groups such as hydroxamic acids, boronic acids, phosphonic acids and sulfonic acids have all been published and have varying effects on device performance. [32] A possible future study could incorporate all these anchoring groups into the same chromophore to gain a deeper understanding of electron injection dynamics. Another study could incorporate sulphur atoms in these dyes. Sulfur could be used as an atomic probe to study dye orientation at TiO<sub>2</sub> surfaces using angle-resolved X-ray photoelectron spectroscopy (AR-XPS). Using these data in conjunction with density functional theory (DFT) calculations of dye energy levels (e.g. HOMO and LUMO) and preferred dye orientations on model TiO<sub>2</sub> surfaces. Placing a sulfur atom within the dye could also give a deeper understanding of the electron transfer processes between the electrolyte and sensitizer. It has been suggested in multiple papers that sulfur can play an important role in the electron transfer between the dye and the electrolyte. Some papers claim a sulfur in the outermost region of the dye (HOMO), has its orbitals exposed to the I<sup>-</sup>/I<sub>3</sub><sup>-</sup> electrolyte which should aid regeneration of the oxidised dye by the electrolyte redox couple. There are other papers that claim a sulfur can have a negative influence on the performance of a device. They state, if the sulfur atom is in the LUMO of the dye it can provide binding sites for oxidised species in the redox shuffle (I<sub>2</sub> or I<sub>3</sub><sup>-</sup>), increasing their concentration close to the TiO<sub>2</sub> surface and thus accelerating the recombination process. [33-35]

## Conclusions

Combining the synthetic versatility of half-squaraine dyes with detailed surface analysis and modelling can yield insights into dye orientation on metal oxide surfaces and how this affects device performance.

## Acknowledgements

We gratefully acknowledge funding provided by from the Welsh Government

for NRN (CPK) and Sêr Cymru (PJH), the European Union and Welsh Government for Sparc II (LF, RA), and from EPSRC EP/M015254/1 (AC, EWJ), the EPSRC UK National Mass Spectrometry Facility at Swansea University and Pilkington-NSG for TEC™ glass.

## References

- K. Kakiage, Y. Aoyama, T. Yano, K. Oya, J. Fujisawa and M. Hanaya, *Chem. Commun.*, 2015, **51**, 15894–15897.
- M. K. Nazeeruddin, P. Péchy and M. Grätzel, *Chem. Commun.*, 1997, **1**, 1705–1706.
- Y. Cao, Y. Bai, Q. Yu, Y. Cheng, S. Liu, D. Shi, F. Gao and P. Wang, *J. Phys. Chem. C*, 2009, **113**, 6290–6297.
- M. K. Nazeeruddin, F. De Angelis, S. Fantacci, A. Selloni, G. Viscardi, P. Liska, S. Ito, B. Takeru and M. Grätzel, *J. Am. Chem. Soc.*, 2005, **127**, 16835–47.
- Y. Cao, Y. Bai, Q. Yu, Y. Cheng, S. Liu, D. Shi, F. Gao and P. Wang, *J. Phys. Chem. C*, 2009, **113**, 6290–6297.
- Nat. Publ. Gr.*, 1991, **353**, 737–740.
- P. J. Holliman, K. J. Al-Salihi, A. Connell, M. L. Davies, E. W. Jones and D. A. Worsley, *RSC Adv.*, 2014, **4**, 2515–2522.
- T. Bessho, E. Yoneda, J. Yum, M. Guglielmi, I. Tavernelli, H. Imai, U. Rothlisberger, M. H. Nazeeruddin and M. Grätzel, *J. Am. Chem. Soc.*, 2009, **131**, 5930–5934.
- H. Im, S. Kim, C. Park, S.-H. Jang, C.-J. Kim, K. Kim, N.-G. Park and C. Kim, *Chem. Commun. (Camb.)*, 2010, **46**, 1335–7.
- M. Liang and J. Chen, *Arylamine organic dyes for dye-sensitized solar cells.*, 2013, vol. 42.
- N. Mohammadi, P. J. Mahon and F. Wang, *J. Mol. Graph. Model.*, 2013, **40**, 64–71.
- K. Hara, Z. S. Wang, T. Sato, A. Furube, R. Katoh, H. Sugihara, Y. Dan-Oh, C. Kasada, A. Shinpo and S. Suga, *J. Phys. Chem. B*, 2005, **109**, 15476–15482.
- G. Pepe, J. M. Cole, P. G. Waddell and S. McKechnie, *Mol. Syst. Des. Eng.*, 2016, **1**, 86–98.
- S. Ito, S. M. Zakeeruddin, R. Humphry-Baker, P. Liska, R. Charvet,

- P. Comte, M. K. Nazeeruddin, P. Péchy, M. Takata, H. Miura, S. Uchida and M. Grätzel, *Adv. Mater.*, 2006, **18**, 1202–1205.
- 15 Y. Wu, M. Marszalek, S. M. Zakeeruddin, Q. Zhang, H. Tian, M. Grätzel and W. Zhu, *Energy Environ. Sci.*, 2012, **5**, 8261.
- 16 J. J. McEwen and K. J. Wallace, *Chem. Commun. (Camb.)*, 2009, 6339–6351.
- 17 M. Tian, M. Furuki, I. Iwasa, Y. Sato, L. S. Pu and S. Tatsuura, *J. Phys. Chem. B*, 2002, **106**, 4370–4376.
- 18 D. Lynch, *Metals (Basel)*, 2015, **5**, 1349–1370.
- 19 X. Lu, Q. Feng, T. Lan, G. Zhou and Z. S. Wang, *Chem. Mater.*, 2012, **24**, 3179–3187.
- 20 G. Calogero, A. Bartolotta, G. Di Marco, A. Di Carlo and F. Bonaccorso, *Chem. Soc. Rev.*, 2015, **44**, 3244–3294.
- 21 C.-P. Lee, R. Y.-Y. Lin, L.-Y. Lin, C.-T. Li, T.-C. Chu, S.-S. Sun, J. T. Lin and K.-C. Ho, *RSC Adv.*, 2015, **5**, 23810–23825.
- 22 A. Connell, P. J. Holliman, E. W. Jones, S. Ghosh, L. Furnell, R. J. Hobbs and M. L. Davies, *Mater. Res. Innov.*, 2015, **19**, 494–496.
- 23 H. -E Sprenger and W. Ziegenbein, *Angew. Chemie Int. Ed. English*, 1966, **5**, 894–894.
- 24 M. Matsui, H. Mase, J. Y. Jin, K. Funabiki, T. Yoshida and H. Minoura, *Dye. Pigment.*, 2006, **70**, 48–53.
- 25 N. Shahzad, F. Risplendi, D. Pugliese, S. Bianco, A. Sacco, A. Lamberti, R. Gazia, E. Tresso and G. Cicero, *J. Phys. Chem. C*, 2013, **117**, 22778–22783.
- 26 G. Cicero, G. Musso, A. Lamberti, B. Camino, S. Bianco, D. Pugliese, F. Risplendi, A. Sacco, N. Shahzad, A. M. Ferrari, B. Ballarin, C. Barolo, E. Tresso and G. Caputo, *Phys. Chem. Chem. Phys.*, 2013, **15**, 7198–7203.
- 27 J. N. Clifford, E. Palomares, M. K. Nazeeruddin, R. Thampi, M. Grätzel and J. R. Durrant, *J. Am. Chem. Soc.*, 2004, **126**, 5670–5671.
- 28 (a) P. J. Holliman, M. L. Davies, A. Connell, B. Vaca Velasco, T. M. Watson, *Chemical Commun.*, 2010, 46, 7256–7258. (b) P. J. Holliman, M. Mohsen, A. Connell, M. L. Davies, K. Al-Salihi, M. B. Pitak, G. J. Tizzard, S. J. Coles, R. W. Harrington, W. Clegg, C. Serpa, O. H. Fontes, C. Charbonneau and M. J. Carnie, *J. Mater. Chem.*, 2012, **22**, 13318.
- 29 Y. Ootani, K. Sodeyama, L. Han and Y. Tateyama, *Surf. Sci.*, 2016, **649**, 66–71.
- 30 A. Connell, P. J. Holliman, M. L. Davies, C. D. Gwenin, S. Weiss, M. B. Pitak, P. N. Horton, S. J. Coles and G. Cooke, *J. Mater. Chem. A*, 2014, **2**, 4055.
- 31 A. Connell, P. J. Holliman, E. W. Jones, L. Furnell, C. Kershaw, M. L. Davies, C. D. Gwenin, M. B. Pitak, S. J. Coles and G. Cooke, *J. Mater. Chem. A*, 2015, **3**, 2883–2894.
- 32 L. Zhang and J. M. Cole, *ACS Appl. Mater. Interfaces*, 2015, **7**, 3427–3455.
- 33 J. Teuscher, A. Marchioro, J. Andrès, L. M. Roch, M. Xu, S. M. Zakeeruddin, P. Wang, M. Grätzel and J. E. Moser, *J. Phys. Chem. C*, 2014, **118**, 17108–17115.
- 34 M. Planells, L. Pellejà, J. N. Clifford, M. Pastore, F. De Angelis, N. López, S. R. Marder and E. Palomares, *Energy Environ. Sci.*, 2011, **4**, 1820.
- 35 B. C. O'Regan, K. Walley, M. Juozapavicius, A. Anderson, F. Matar, T. Ghaddar, S. M. Zakeeruddin, C. Klein and J. R. Durrant, *J. Am. Chem. Soc.*, 2009, **131**, 3541–3548.

# **SiGeSn as a 1.0eV component sub-cell in III-V multi-junction solar cells**

Phoebe Pearce<sup>1\*</sup>, Tom Wilson<sup>1</sup>, Andrew Johnson<sup>2</sup>, Radeck Roucka<sup>3</sup>, Andrew Clark<sup>3</sup>, Tomos Thomas<sup>1</sup>, Markus Führer<sup>1</sup>, Nicholas Ekins-Daukes<sup>1</sup>, Rick Hoffman Jr.<sup>2</sup>, David Begarney<sup>2</sup>

<sup>1</sup> The Blackett Laboratory, Department of Physics, Imperial College London, SW7 2AZ, U.K.

<sup>2</sup> IQE PLC, Pascal Close, St. Mellons, Cardiff. CF3 0LW, U.K.

<sup>3</sup> Transluminate Inc., Palo Alto, CA, 94303, USA

\* Corresponding Author: phoebe.pearce15@imperial.ac.uk

## **Abstract**

Optimally efficient four-junction (4J) solar cells require a sub-cell with a bandgap close to 1 eV as the second-lowest energy sub-cell. Current high-efficiency 4J devices must incorporate some lattice mismatch between sub-cells to achieve an optimal combination of bandgaps, complicating the fabrication process; thus, novel materials which can achieve ~1eV bandgaps while remaining lattice-matched to Ge are required. Group IV Ge-rich SiGeSn alloys are a promising material, with functional single and triple junction devices incorporating SiGeSn having already been demonstrated. However, further investigation of the fundamental properties of relevant SiGeSn alloys is key to fabricating an efficient 4J device. We present optical measurements including photoluminescence, spectroscopic ellipsometry, and device characterisation of single and triple junction devices containing SiGeSn sub-cells. Initial results indicate the expected blueshift of the fundamental indirect gap and lowest direct gaps in SiGeSn relative to Ge with the addition of small amounts of Si and Sn. Device measurements indicate good EQE performance in both devices, while the open-circuit voltage is lower than expected based on absorption around 1 eV, indicating the lower indirect edge in SiGeSn limits the voltage.

## **Introduction**

An optimally efficient four-junction (4J) solar cell requires a sub-cell with a bandgap around 1.0 eV. Currently, the most efficient 4J cells incorporate lattice-mismatched 1 eV sub-cells, necessitating the use of inverted metamorphic (IMM) growth [1] or a wafer-bonding process [2], complicating the growth mechanism and driving up production costs. These processes could be avoided by using a 1.0 eV bandgap material lattice-matched to the other junctions.

Group IV silicon-germanium-tin (SiGeSn) alloys are one such promising material. Alloying Ge with both Si and Sn allows both the lattice parameter and the bandgaps to be tuned [3], so a material which remains lattice-matched to Ge with a direct bandgap close to 1.0 eV can be grown epitaxially onto Ge, making a fully lattice-matched 4J structure possible (see Fig. 1). In addition, 1.0 eV bandgap materials are useful

for use in tandem (2J) cells [4]. However, fundamental knowledge of the optical, electronic and material properties of SiGeSn at different lattice-matched compositions is scarce, and many investigations so far have been modelling-based rather than experimental. Investigation of properties such as optical constant and absorption data, carrier transport properties and energy of interband transitions, as well as the behaviour of SiGeSn-containing devices, will form an essential contribution to the literature. The overall aim is to understand how SiGeSn sub-cells function in solar cell devices, and optimise the SiGeSn sub-cell in both 2J and 4J devices.

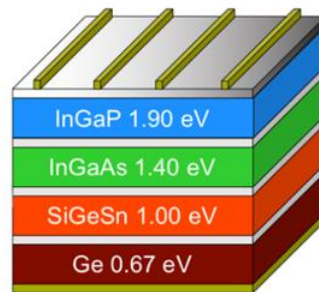


Figure 1. 4J device architecture using SiGeSn. From [5].

## **Experimental methods**

Optical measurements, including spectroscopic ellipsometry and steady-state photoluminescence measurements, are used to characterise unprocessed epitaxial samples. Ellipsometry was performed on a J.A. Woollam VASE ellipsometer with incident wavelength range 300-1700nm. Ellipsometric data can be used to extract critical point energies in the SiGeSn band structure through fitting a critical point parabolic band (CPPB) model (e.g. [6,7]). Direct transitions contribute much more strongly in ellipsometry data, and thus combining these measurements with photoluminescence measurements is necessary to fully investigate the fundamental indirect bandgap expected to lie around 0.7-0.8 eV. These measurements were performed using a 532nm Nd:YVO<sub>4</sub> laser for incident excitation, with low-temperature measurement performed with samples in a closed-cycle helium cryostat. An LN<sub>2</sub> cooled, extended InGaAs diode detector was used to measure the luminescence.

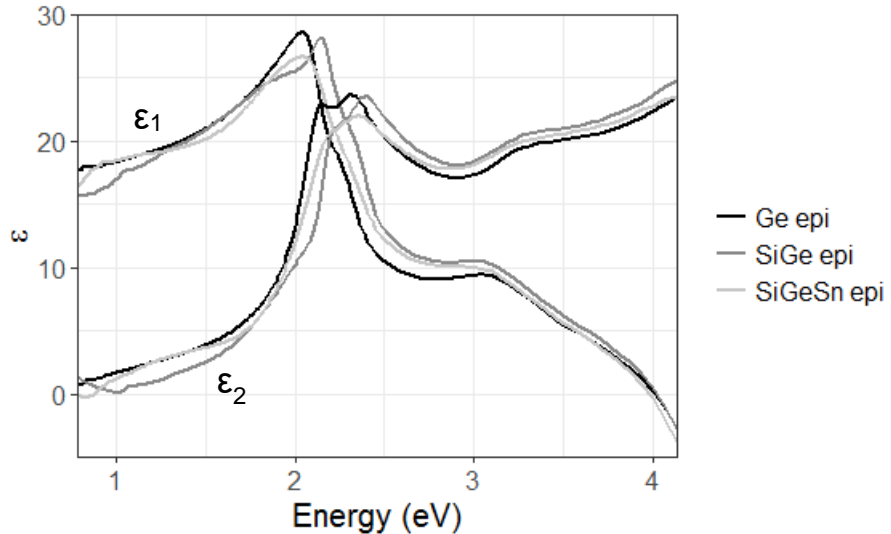


Figure 2. Pseudo-dielectric function ( $\epsilon = \epsilon_1 + i\epsilon_2$ ) of  $\approx 500$  nm epitaxial layers of Ge, SiGe and SiGeSn grown on a Ge substrate.

The feasibility of using Ge-rich SiGeSn as a sub-cell has been demonstrated in a single-junction device and a triple-junction InGaP/InGaAs/SiGeSn cell [8]. These devices have been characterised using external quantum efficiency (EQE) and current-voltage measurements (I-V). The EQE was measured with a quartz-halogen light source dispersed through a 0.3-m spectrometer. The photocurrent was recorded using a standard lock-in technique. Light I-V characteristics were measured under single-sun illumination conditions using a dual-source TS-Space Systems Class-A solar simulator, which uses both metal halide and quartz halogen lamps to provide a close match to the terrestrial AM1.5G spectrum in the wavelength range 320–2200 nm.

Transition (Symmetry point)	Energy (eV)		
	Ge	Si	SiGeSn
$E_{gap}$ (indirect)	0.66	1.12	0.8
$E_0$ ( $\Gamma$ )	0.80	4.2	1.06
$E_0 + \Delta_0$ ( $\Gamma$ )	1.09	n/a*	1.29
$E_1$ ( $L/\Lambda$ )	2.05	3.38	2.10
$E_1 + \Delta_1$ ( $L/\Lambda$ )	2.25	n/a*	2.30
$E'_0$ ( $\Gamma$ )	$\approx 3.1$	$\approx 3.3$	Not fitted
$E'_0 + \Delta'_0$ ( $\Gamma$ )	$\approx 3.2$	n/a*	Not fitted
$E'_0 + \Delta'_0 + \Delta_0$ ( $\Gamma$ )	$\approx 3.5$	n/a*	Not fitted
$E_2$ ( $X/\Delta$ )	4.35	4.27	Not fitted

\* = the spin-orbit splitting ( $\Delta$  energies) in Si is extremely small, so  $\Delta_1 = \Delta'_0 = \Delta_0 \approx 0$ .

Table 1. Transition energies for pure Ge and Si at room temperature. The symmetry point refers to the point in the Brillouin zone where the transition takes place, and  $\Delta$  are the spin-orbit splitting energies. Data from [9]. The SiGeSn column shows the results of fitting a CPPB model to the ellipsometric data (Figure 4).

## Results

The direct transition energies expected in pure Ge and Si are shown in Table 1. Ellipsometry measurements of bulk Ge and SiGe/SiGeSn grown on Ge substrates through metal-organic vapour-phase epitaxy (MOVPE) shows that the SiGe and SiGeSn critical point energies blueshift relative to Ge for the direct transitions around 2 eV (the  $E_1$  energy), as expected. The pseudo-dielectric function of the Ge substrate and epitaxial samples, calculated from ellipsometric data, is shown in Figure 2. The SiGe is blueshifted more than the SiGeSn; this is because the addition of Sn reduces  $E_1$ , while the addition of Si increases  $E_1$ . The samples used in ellipsometry and PL were both Ge-rich, with a higher fraction of Si than Sn, so an overall blueshift relative to Ge is still expected. The lowest direct transition in Ge (the  $E_0$  energy) lies around 0.8 eV, and thus at lower incident photon energies the substrate becomes transparent, complicating data analysis. However, since the addition of Si increases  $E_0$ , features around 1 eV are visible in both the SiGeSn and SiGe, likely from the transitions at  $E_0$  or  $E_0 + \Delta_0$ .

Fitting the SiGeSn ellipsometry data from Figure 2 with a CPPB model including an energy-dependent broadening parameter [7] also reproduces this blueshift in the critical point energies; the resulting fit is shown in Figure 4, with the fitted critical point energies for SiGeSn shown in Table 1. The model takes into account the layered structure of the material; the oscillations in the calculated fit to the SiGeSn data are due to interface reflections of a perfectly coherent monochromatic source as assumed in the model. These oscillations are not observed in the Ge fit as this is modelled as

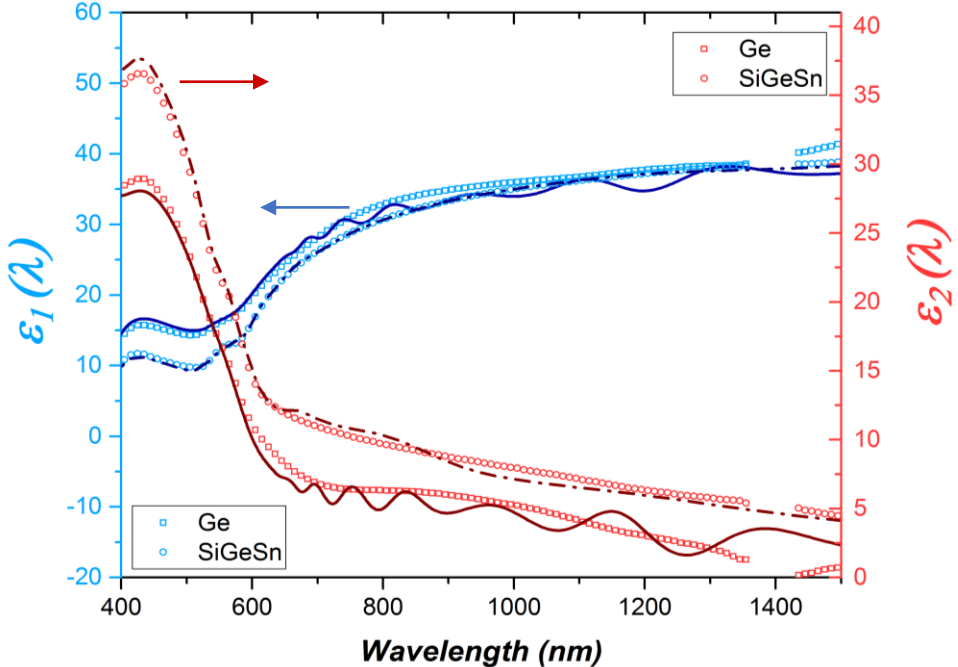


Figure 4. Pseudo-dielectric function data (points) and fit (lines) to an extended CPPB model as described in [7]. Fabry-Perot oscillations are seen in the model fits but not experimentally observed.

a single layer, and are not observed experimentally.

Figure 3 shows the results of photoluminescence measurements on both bulk Ge and epitaxial SiGeSn on Ge. Although the use of high-energy incident laser power means that > 99% of incident laser power is absorbed in the SiGeSn layer (assuming Ge-like absorption at high energies), for a simple SiGeSn on Ge structure, carriers are able to diffuse into the lower-bandgap substrate and only PL from the Ge is observed at both room and low temperature (30K). This indicates relatively long carrier diffusion lengths (> 500 nm at low temperature), an observation supported by the minority carrier diffusion length estimated from EQE modelling [8]. In order to observe PL from the epitaxial layer, it was necessary to grow a higher-bandgap barrier material between the SiGeSn and Ge substrate. In this SiGeSn/SiGe/Ge sample, a large contribution to the PL from the substrate is still visible; however, there is also an additional peak at 0.78eV. This corresponds to the expected location of the fundamental indirect bandgap for this SiGeSn alloy.

The EQE of the single and triple-junction cells were found to reach maxima of 80% and 70% respectively. The open-circuit voltage  $V_{OC}$  in the triple-junction cell was lower than expected (see Figure 5). While the absorption and thus EQE in the SiGeSn in both devices is dominated by transitions across the direct gap around 1eV, carrier thermalisation to the lowest available

conduction band states will mean  $V_{OC}$  is limited by the indirect gap. This effect, possibly in combination with high non-radiative recombination, will lower the  $V_{OC}$ . While this is not ideal, using the direct absorption edge allows a thin layer of SiGeSn to be used. A lower bound of 5μm on the minority carrier diffusions length was established through EQE modelling [8].

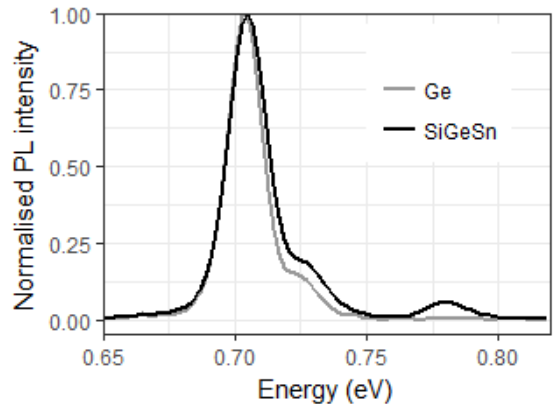


Figure 3. Low temperature (30K) PL of bulk Ge and the epitaxially-grown SiGeSn/SiGe barrier/Ge substrate structure. The ~0.7 eV peak is due to Ge in both cases, but the addition higher-energy peak at 0.78 eV is only observed in the SiGeSn sample.

## Conclusions

Ellipsometry and photoluminescence spectroscopy were used to confirm the expected shifts in SiGeSn energy transitions

relative to Ge for both the fundamental indirect bandgap and the two lowest-energy direct transitions in Ge-rich materials. This energy shift is confirmed through fitting a CPPB-type model to the SiGeSn ellipsometry data. The feasibility of utilising SiGeSn junctions in both single and multi-junction cells has been demonstrated. High EQE in both devices indicates that even with III-V growth onto SiGeSn, the material quality remains adequate, which is essential for producing an efficient 4J device. The main issue relating to SiGeSn sub-cells is the voltage penalty incurred through using the direct absorption edge, while the  $V_{oc}$  will be limited by the fundamental indirect bandgap.

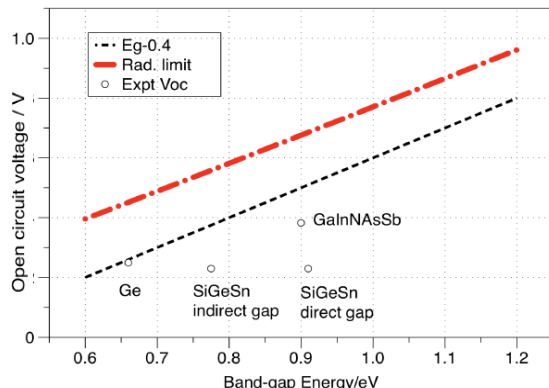


Figure 5.  $V_{oc}$  as a function of bandgap energy for various sub-cell materials ( $\circ$ ). The two lines show the radiative voltage limit as and an empirical  $V_{oc} - 0.4V$  line as proposed in [10]. Plot from [11].

## Acknowledgements

P. Pearce would like to acknowledge EPSRC CASE sponsorship from IQE plc.

## References

- [1] Stan M, Aiken D, Cho B, Cornfeld A, Ley V, Patel P, et al. High-efficiency quadruple junction solar cells using OMVPE with inverted metamorphic device structures. *J Cryst Growth* 2010;312:1370–4. doi:10.1016/j.jcrysgro.2009.10.059.
- [2] Tibbits TND, Beutel P, Grave M, Karcher C, Oliva E, Siefer G, et al. New Efficiency Frontiers With Wafer-Bonded Multi-Junction Solar Cells. 29th Eur PV Sol Energy Conf 2014:4. doi:10.4229/EUPVSEC20142014-4CP.2.1.
- [3] Moontragoon P, Soref RA, Ikonic Z. The direct and indirect bandgaps of unstrained Si $x$ Ge $1-x$ Sn $y$  and their photonic device applications. *J Appl Phys* 2012;112. doi:10.1063/1.4757414.
- [4] De Vos A. Detailed balance limit of the efficiency of tandem solar cells. *J Phys D Appl Phys* 1980;13:839–46. doi:10.1088/0022-3727/13/5/018.
- [5] Wilson T, Thomas T, Führer M, Ekins-Daukes NJ, Roucka R, Clark A, et al. Single and multi-junction solar cells utilizing a 1.0 eV SiGeSn junction. *AIP Conf Proc* 2016;1766:60006. doi:10.1063/1.4962096.
- [6] Adachi S. Optical dispersion relations for Si and Ge. *J Appl Phys* 1989;66:3224–31. doi:10.1063/1.344140.
- [7] Kim CC, Garland JW, Abad H, Raccah PM. Modeling the optical dielectric function of semiconductors: Extension of the critical-point parabolic-band approximation. *Phys Rev B* 1992;45:11749–67. doi:10.1103/PhysRevB.45.11749.
- [8] Roucka R, Clark A, Wilson T, Thomas T, Führer M, Ekins-Daukes N, et al. Demonstrating Dilute-Tin Alloy SiGeSn for Use in Multijunction Photovoltaics: Single- and Multijunction Solar Cells with a 1.0-eV SiGeSn Junction. *IEEE J Photovoltaics* 2016;6:1025–30. doi:10.1109/JPHOTOV.2016.2559785.
- [9] Adachi S. Model dielectric constants of Si and Ge. *Phys Rev B* 1988;38:12966–76. doi:10.1103/PhysRevB.38.12966.
- [10] King RR, Bhusari D, Boca A, Larrabee D, Liu X-Q, Hong W, et al. Band gap-voltage offset and energy production in next-generation multijunction solar cells. *Prog Photovoltaics Res Appl* 2011;19:797–812. doi:10.1002/pip.1044.
- [11] Roucka R, Clark A, Wilson T, Thomas T, Führer M, Ekins-Daukes N, et al. 3J Solar Cells Comprising a Lattice Matched Epitaxial SiGeSn SubCell. 12th Int. Conf. Conc. Photovolt. Syst., 2016.

# Impact of stratospheric aerosol geoengineering on PV and CPV output

CJ Smith<sup>a,b</sup>, JA Crook<sup>b</sup>, R Crook<sup>a</sup>, LS Jackson<sup>b</sup>, SM Osprey<sup>c</sup>, PM Forster<sup>b</sup>

<sup>a</sup>School of Chemical and Process Engineering, University of Leeds, Leeds, LS2 9JT, UK

<sup>b</sup>School of Earth and Environment, University of Leeds, Leeds, LS2 9JT, UK

<sup>c</sup>Department of Physics, University of Oxford, Oxford, UK

Corresponding author: R.Crook@leeds.ac.uk

## Introduction

Pumping sulphide gases into our upper atmosphere, the stratosphere, is considered a last-resort fix for climate change [1,2]. The sulphide molecules oxidise and condense to form droplets, or aerosols, of sulphuric acid. These aerosols are effective at scattering visible light, so reflecting a fraction of solar radiation back into space that would otherwise warm the earth's surface and lower atmosphere. However, with reduced visible radiation reaching the earth's surface, will the output of PV and concentrating PV (CPV) decrease?

The eruption of Mount Pinatubo in 1991 injected 20 Tg of SO<sub>2</sub> into the stratosphere, and this event is often used as an analog and inspiration for geoengineering. A reduction in global average temperatures of 0.5°C for 3 years can be attributed to this eruption, and the peak output of SEGS, a CSP generator in California, reduced by 20% [3].

## Method

This study used a global climate model called HadGEM2-CCS [4], provided by the Met Office Hadley Centre. The average climate from 1986 – 2005 was used as a baseline, and the average climate from 2040 – 2059 used for analysis, which is within the projected lifetime of newly installed solar power plant. Future climates were calculated under the RCP4.5 emissions scenario, which is considered to be a moderate scenario with concentrations of greenhouse gases continuing throughout the 21<sup>st</sup> century.

Geoengineering was simulated by the injection of 10×10<sup>12</sup> g of SO<sub>2</sub> per year from 2020

onwards [5]. The injection takes place between 16 km and 25 km altitude from a single point on the equator, at Ecuador, perhaps from a modified high altitude aircraft. Equatorial emissions are rapidly dispersed in a band close to the equator, driven by the rotation of the earth. The emissions are dispersed more slowly to high latitudes, driven by the Brewer-Dobson atmospheric circulation. Such emissions are projected to reduce global temperature rise by about 1°C.

Three systems were considered: fixed-angle PV, two-axis tracking PV, and two-axis tracking CPV. For the fixed-angle PV, the tilt angle was equal to the latitude, although this could be optimise further [6]. For PV, the cells are assumed to be manufactured from c-Si, with module efficiency equal to

$$\eta_{\text{PV}} = \eta_{\text{ref}}(1 - \beta(T_c - 25) + \gamma \log_{10} G_T) \quad (1)$$

where  $\eta_{\text{ref}} = 15\%$  giving a module efficiency of 19.5% under standard conditions,  $\beta = 0.0045 \text{ K}^{-1}$ , and  $\gamma = 0.1$  [7]. The total radiation incident on the tilted plane  $G_T$  is calculated from geometry, being the sum of direct and diffuse radiation, taking into account tracking with a 3-hour resolution.

CPV focuses sunlight using mirrors or lenses to massively reduce the cell area. This permits the use of more efficient, but more expensive, multi-junction cells. 2-axis tracking is essential so that the focal point stays aligned on the cells. Diffuse radiation cannot be extensively focussed, so CPV can only utilise direct irradiance.

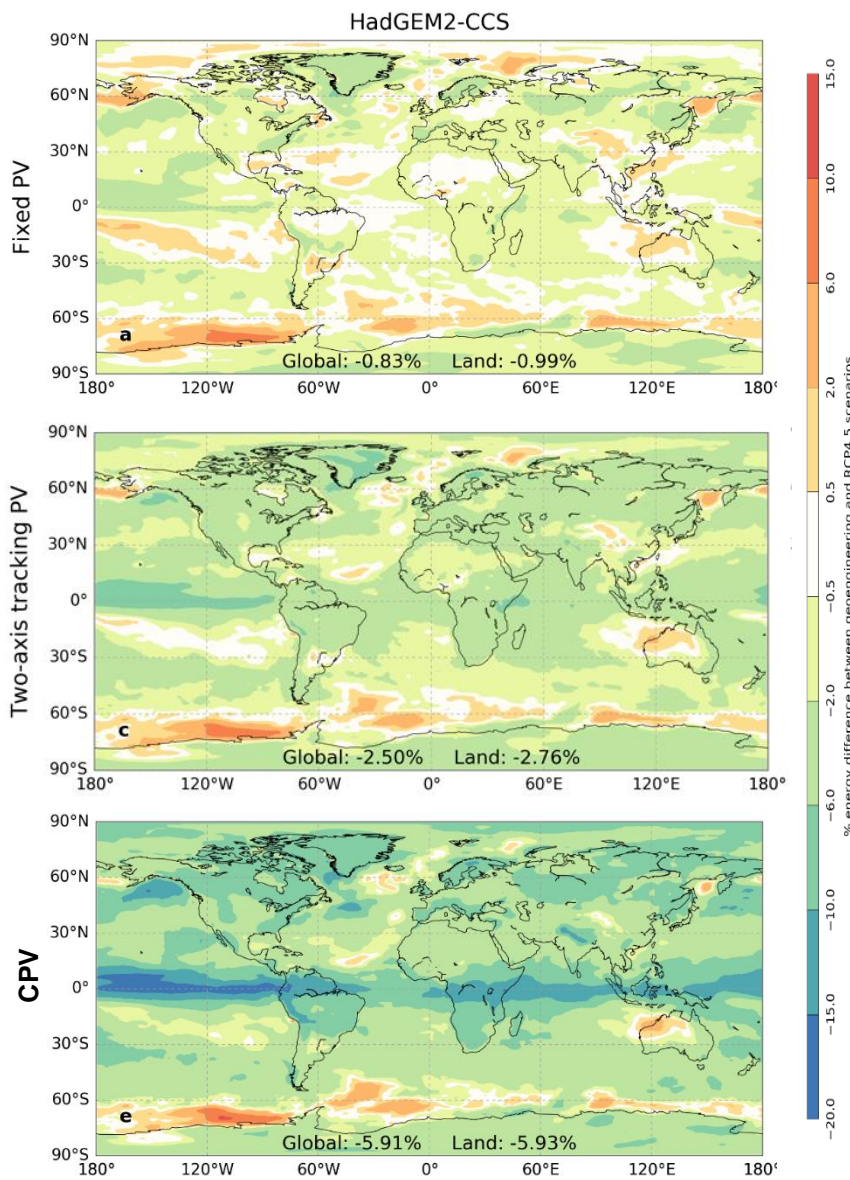


**Figure 1.** Change in output from PV (top), tracking PV (middle), and CPV (bottom) attributable to geoengineering.

Change from 1986-2005 to 2040-2059, %			Fixed PV		Tracking PV		CPV	
Region	Longitude	Latitude	SSI	RCP4.5	SSI	RCP4.5	SSI	RCP4.5
Algeria	0°-10° E	30°-37° N	-1.2	-0.2	-2.0	0.2	-3.0	1.5
Australia	140°-150° E	20°-30° S	-1.3	-0.8	-1.3	-0.4	-1.4	0.9
California	114°-120° W	32°-40° N	-2.2	-0.9	-3.1	0.0	-4.3	1.6
North-West China	90°-100° E	30°-40° N	-1.5	-2.3	-2.6	-2.5	-4.1	-2.1
Germany	5°-15° E	47°-52° N	1.6	3.2	2.0	5.5	3.0	10.1
India (Gujarat)	70°-80° E	20°-30° N	-3.2	-1.8	-5.0	-2.4	-8.3	-2.7
Saudi Arabia	40°-50° E	20°-30° N	-1.9	-1.2	-3.2	-1.1	-4.7	-0.1

South Africa	15°-25° E	20°-35° S	-2.3	-0.7	-4.0	-0.4	-6.0	0.8
Spain	0-8°W	37°-42° N	-0.5	1.9	-1.2	2.8	-1.8	5.2

**Table 1.** Change in PV and CPV output over selected regions. The impact from geoengineering (combined with climate change) (SSI) is provided alongside the impact from climate change alone (RCP4.5).

## Results

Maps are presented in figure 1 showing the change in PV and CPV output attributable to the impact of geoengineering averaged over 2040 - 2059. Note that climate change from greenhouse gas emissions is included for the simulations both with and without geoengineering. It is apparent that stratospheric aerosol geoengineering has a negative impact on output for all technologies for most locations on land. The global average change in output over land is -1.0% for PV, -2.8% for tracking PV, and -5.9% for CPV. While the reductions in output are notable, the optimal locations for solar power do not change significantly. The different response from different technologies can be understood by recognising that tracking PV and CPV utilise increasing fractions of direct irradiance. The stratospheric aerosols transform direct irradiance into diffuse irradiance through increased scattering.

The data shown in table 1 presents changes in PV and CPV outputs over selected regions, where large solar farms are either installed or planned. The impact from geoengineering (combined with climate change), and climate change alone are provided in separate columns. Germany alone receives a positive impact from geoengineering, but this is entirely attributed to the locally positive impact of climate change. Unfortunately, CPV is a less viable technology in Germany because of intermittent direct irradiance. The impacts of climate change alone are consistent with previous studies making use of different climate models [2,8,9]. Through sensitivity analysis, changes in radiation, rather than changes in temperature, are largely responsible for impacts from both geoengineering and climate change. The incident solar spectrum will change under stratospheric aerosol geoengineering, and it

possible that the cell material could be selected for this modified spectrum in order to offset some of the negative impacts.

## Conclusions

Electricity output for fixed-angle PV reduces by 1% on average, and for tracking PV by 3%. A reduction in CPV output by more than 10% in some regions near the equator is seen, with a decrease of 6% on average. The different response from different technologies can be understood by recognising that tracking PV and CPV utilise increasing fractions of direct irradiance. The stratospheric aerosols transform direct irradiance into diffuse irradiance through increased scattering.

For an extensive presentation and interpretation of this work, we refer the reader to our recent article [5].

## Acknowledgements

The authors thank participants from the Integrated Assessment of Geoengineering Proposals (IAGP), participant modelling centres of the GeoMIP project (NorESM, MIROC, GISS), and ESGF, BADC, BNU, CCCMA. The authors also acknowledge financial support from EPSRC and NERC through a number of grants (EP/I014721/1, EP/I01473X/1, EP/G036608/1).

## References

- [1] Boucher, O., et al, 2013: Clouds and Aerosols. Climate Change 2013: The Physical Science Basis. Contribution of Working Group I to the Fifth Assessment Report of the Intergovernmental Panel on Climate Change, T. F. Stocker, et al, Eds., Cambridge University Press, 571-634.
- [2] Crook, J. A., L. A. Jones, P. M. Forster, and R. Crook, 2011: Climate change impacts on future photovoltaic and concentrated solar power energy output. Energy Environ. Sci., 4, 3101-3109.

- [3] Murphy, D., 2009: Effect of Stratospheric Aerosols on Direct Sunlight and Implications for Concentrating Solar Power. *Environ. Sci.. Technol.*, 43, 2784-2786.
- [4] SM Osprey et al., Stratospheric Variability in Twentieth-Century CMIP5 Simulations of the Met Office Climate Model: High Top versus Low Top. *J. Climate*, 26, 1595-1606.
- [5] CJ Smith, JA Crook, R Crook, LS Jackson, SM Osprey, PM Forster, 2017: Impacts of stratospheric sulfate geoengineering on global solar photovoltaic and concentrating solar power resource. Accepted for publication in *Journal of Applied Meteorology and Climatology*.
- [6] Smith, C. J., P. M. Forster, and R. Crook, 2016: An all-sky radiative transfer method to predict optimal tilt and azimuth angle of a solar collector. *Sol. Energy*, 123, 88-101.
- [7] Evans, D. L., 1981: Simplified method for predicting photovoltaic array output. *Sol. Energy*, 27, 555-560.
- [8] Wild, M., D. Folini, F. Henschel, N. Fischer, and B. Müller, 2015: Projections of long-term changes in solar radiation based on CMIP5 climate models and their influence on energy yields of photovoltaic systems. *Sol. Energy*, 116, 12-24
- [9] Jerez, S., and Coauthors, 2015: The impact of climate change on photovoltaic power generation in Europe. *Nat. Commun.*, 6.

# Uncertainty Contributions in Photocurrent Linearity Measurements of PV Devices using a Flash Solar Simulator

M. Bliss\*, B.V. Mihaylov, G. Koutsourakis, T.R. Betts, R. Gottschalg

Centre for Renewable Energy Systems Technology (CREST), Wolfson School Mechanical, Electronic and Manufacturing Engineering, Loughborough University, Loughborough, Leicestershire, LE11 3TU, UK

\*Corresponding Author [M.Bliss@lboro.ac.uk](mailto:M.Bliss@lboro.ac.uk)

## Abstract

Especially for reference devices, the linearity of photocurrent over irradiance is an important characteristic that requires a low measurement uncertainty. This work investigates the uncertainty contributions when using a typical flash solar simulator with attenuation masks to determine the linearity characteristics of a device. Due to the complexity in measurement correlations, a Monte-Carlo simulation model was developed to estimate the final uncertainty. Results show that attenuation masks are not necessarily spectrally neutral and, if left uncorrected, this can significantly impact the measurement results. Furthermore, uncertainty in linearity is also dependent on the linearity of the sample under test itself. A shunted, non-linear device can have double the linearity uncertainty in low light conditions than a similar, linear sample.

## 1 Introduction

The linearity of photocurrent output over irradiance incident on a solar cell is an important factor especially for reference devices. In solar simulator measurements, reference PV devices are used to set and monitor the irradiance incident on the device under test (DUT). Thus, a non-linear reference cell can cause direct undesirable errors on performance measurements. Similarly, a nonlinear monitoring device in the field affects irradiance measurements of the PV system and leads to wrong interpretation of total system performance. International standards require a reference device to be linear over the range of interest [1]. Furthermore, the energy rating standard [2, 3] requires linearity to be measured on tested modules. If found to be linear, spectral response measurements and measurements under varying irradiance and temperature can be significantly simplified. Hence, high levels of uncertainty can lead to higher testing costs or errors in the predicted energy output.

Multiple methods are detailed in the IEC60904-10 [4] standard for linearity measurements of a PV device. The first two methods acquire linearity with use of a reference device under either outdoor sunlight or indoor solar simulated light. The 3<sup>rd</sup> applies the two lamp method first reported in [5] and does not require a reference.

In this work, the solar simulator method was applied using a typical flash solar simulator with attenuation masks to measure linearity of small solar cells up to full sized modules. The specific requirements of light uniformity and spectral stability when changing the solar simulator intensity can introduce some issues when using this method. If these requirements are not met, a device under test (DUT) can quickly be falsely identified as non-linear or its non-linearity corrections will have large uncertainties attached to them. To gain an insight into the measurement uncertainty when using the outlined set-up, a full analysis of the measurement uncertainty has been carried out. Due to the extra complexity of linear fitting to calculate the non-linearity and because of significant correlations between measurements at different light intensity, this work utilises the Monte-Carlo method to estimate the final linearity measurement uncertainty.

The measurement configuration and the employed method with applied corrections are described in detail. The uncertainty contributing factors with the uncertainty model are explained. The impact of uncertainty is discussed on three measurement cases.

## 2 Measurement Equipment and Method

A Pasan 3B flash solar simulator was used for linearity measurements. The system was modified with an external 16bit data acquisition (DAQ) system. The irradiance is adjusted via four attenuation masks (10, 20, 40 and 70% transmittance) and via  $\pm 10\%$  lamp intensity adjustment. Reference cell (RC) and DUT are under the same illumination and are set at a room temperature of  $25 \pm 1^\circ\text{C}$ . The spectral output of the pulsed light is measured in situ using a CCD spectroradiometer. Each point in the linearity curve is an average of four measurements.

The measurement method employed is based on the procedure with solar simulator detailed in the IEC 60904-10 [4]. As detailed in the following, spectral mismatch factor (MMF) and uniformity corrections are applied, since specific requirements of light uniformity and spectral stability are not met when changing the solar simulator intensity.

## 3 Uncertainty contributing factors

Uncertainty is considered separately for short circuit current ( $I_{SC}$ ), irradiance ( $G$ ) and current Linearity ( $L_I$ ). The evaluation of uncertainty in  $I_{SC}$  and  $G$  is not explained in detail. Instead, this work focusses on the specific factors influencing  $L_I$  uncertainty ( $U_{L_I}$ ) because it does not directly translate from uncertainty in  $I_{SC}$  and  $G$  ( $U_{I_{SC}}$  and  $U_G$ ). It is mostly effected by relative changes in conditions, since absolute uncertainty factors such as RC calibration and current scale are fully correlated and have no impact on  $L_I$  itself.

### 3.1 Reference cell non-linearity

Since the RC is used as a linearity reference, it has a direct influence on  $U_{L_I}$ . In the presented case, the RC  $L_I$  was measured using the two-lamp method in a custom set-up with a maximum non-linearity of 0.1%. This method, as detailed in [4, 5], does not require a reference, but also does not measure a continuous curve but only the linearity between two points. The intermittent data points can be translated into a curve that can be used to correct for the non-linearity of the RC (see [6]). However, in this work, the RC  $L_I$  has not been corrected, due to its high linearity. Apart from verifying the RC linearity, the results of the two-lamp linearity measurement also provide an uncertainty value.

### 3.2 Spectral mismatch factor (MMF)

During this work it has been observed that the spectral output of the flash lamps changes significantly with lamp intensity, as well as when changing the attenuation masks. This has been corrected for using in-situ spectral measurements. The absolute value of MMF only affects  $G$  and  $I_{SC}$ . However, the relative variation of the MMF between measurements at different irradiances does contribute to  $U_{L_I}$ . This relative uncertainty depends strongly on how well the true value of the MMF is represented overall and on the repeatability of spectral measurements.

### 3.3 Temperature variations

As long as the linearity of the DUT itself is not affected by the temperature, static deviations to the 25°C given in standard test conditions do not contribute to  $U_{L_I}$ . However, the variation of the RC and DUT temperature between measurement points does affect linearity, depending on the temperature coefficient and degree of temperature change.

### 3.4 Light intensity uniformity

In theory, any static variations of light intensity uniformity affect only current and irradiance measurements of the DUT and RC. However,  $L_I$  is directly affected by changes in uniformity between RC and DUT. Those can be introduced when adjusting the intensity using attenuation masks. This effect has been measured on RC

sized samples with a 2x2cm active area by swapping the positions of the RC and DUT (see Table 1). For larger samples the uniformity variation can only be estimated using full uniformity field measurements and thus may not be as accurate.

Mask	$\Delta DUT I_{SC}$	Correction
No Mask	-0.27%	1.0013
70%	-0.40%	1.0020
40%	-0.06%	1.0003
20%	-0.43%	1.0022
10%	-0.83%	1.0042

Table 1: Spatial uniformity correction; measured deviation of irradiance corrected DUT  $I_{SC}$  between swapped RC and DUT positions and correction factor applied.

### 3.5 Spectral uniformity

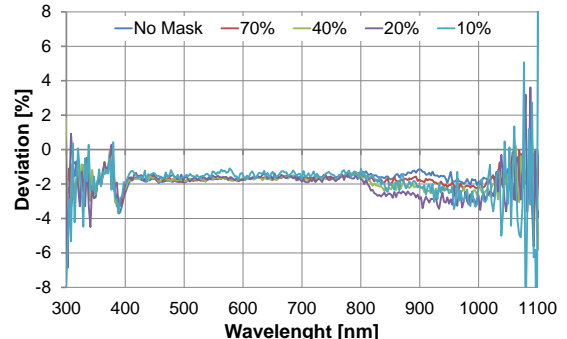


Figure 1: Deviation between spectrum at spectroradiometer and at sample position; a change in spectrum is observed in the 800-1050nm region.

Similar to light intensity uniformity, spectral uniformity affects  $L_I$  only if it varies during the linearity measurement. Measurements of the spectrum at various positions over the solar simulator target area demonstrate that spectral non-uniformity worsens significantly when higher density attenuation masks are used, as presented in Figure 2. The spectral variations have been corrected when measuring small devices, but such a correction becomes impractical with larger DUTs and modules due to the size difference in the spectroradiometer detector input and the sample.

### 3.6 Irradiance correction and $I_{SC}$ extraction

A point-by-point irradiance correction to the average measurement irradiance was applied to the current measurements of the DUT. The contribution to  $U_{L_I}$  lies mainly in the irradiance and current signal noise and digitalisation error.

The  $I_{SC}$  was extracted by linear regression. The final contribution to  $U_{L_I}$  is dependent on the irradiance corrected current signal noise and the number of fitting points used, assuming that the IV curve of the DUT is linear around the  $I_{SC}$  point.

### 3.7 Signal data acquisition

$U_{LI}$  is unaffected by static signal scale and offset calibration errors. Only if the measurement range is changed within a  $L_I$  measurement cycle the relative changes in scale and offset contribute to  $U_{LI}$ . Another factor to include is the signal drift due to external short term effects such as temperature variation.

The relative digitalisation error and signal noise increases with reduction in signal and adds to  $U_{LI}$  due to its random nature. The digitalization error is in many cases much smaller than noise, but can have a much larger impact on low resolution DAQ systems (i.e. 12 instead of 16bit). The Linearity of the measurement signal conversion itself does impact  $U_{LI}$ , but is normally negligible compared to other effects.

### 3.8 Linearity measurement repeatability:

Even though the repeatability of linearity measurements should be fully represented when an uncertainty calculation is complete, it is useful to add the measured repeatability into the calculation to make sure factors not considered are included. The repeatability uncertainty is the variation in the mean value over the measurements taken.

## 4 Determining final uncertainty

Because it is difficult to estimate the final uncertainty contributions on linearity by direct calculation and due to its dependence on the actual DUT linearity, the Monte-Carlo method was applied. The measurement process was modelled with the uncertainty sources introduced at the point at which they are generated. Figure 3 shows the complete model flow chart. Inputs of the model are the specifications, measured RC

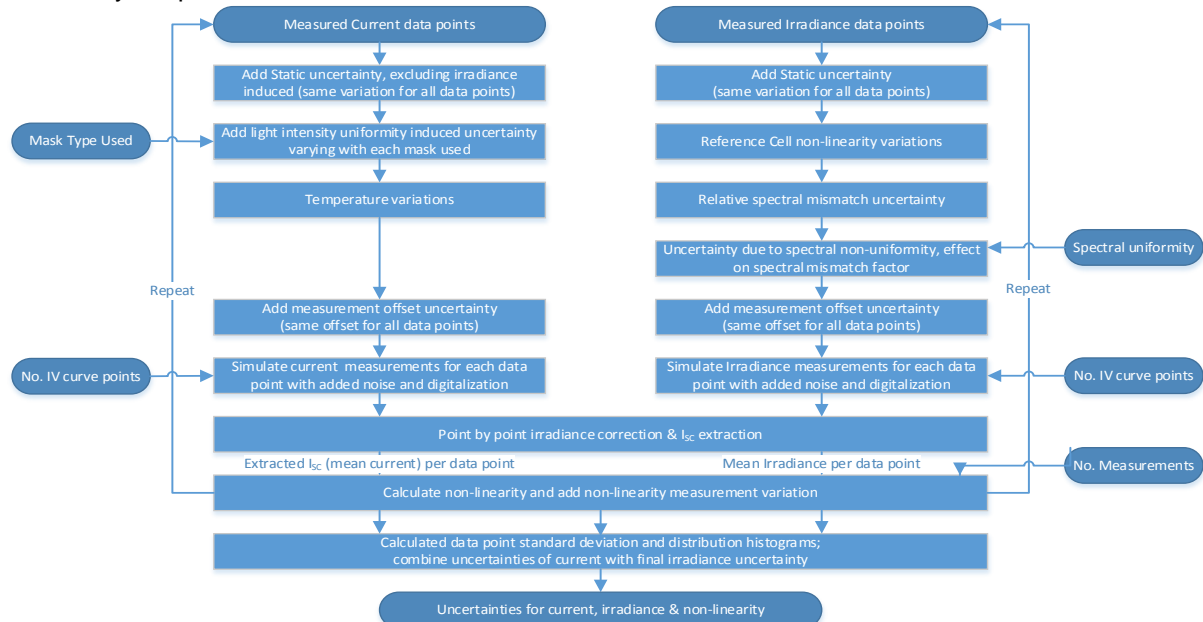


Figure 2: Monte-Carlo simulation flow chart for calculating final  $I_{sc}$ ,  $G$  and  $L_I$  uncertainty.

irradiance and DUT  $I_{sc}$  and other conditions such as mask type, spectral uniformity correction factor and measurement repeatability. The outputs are the final uncertainty for  $I_{sc}$ ,  $G$  and  $L_I$ .

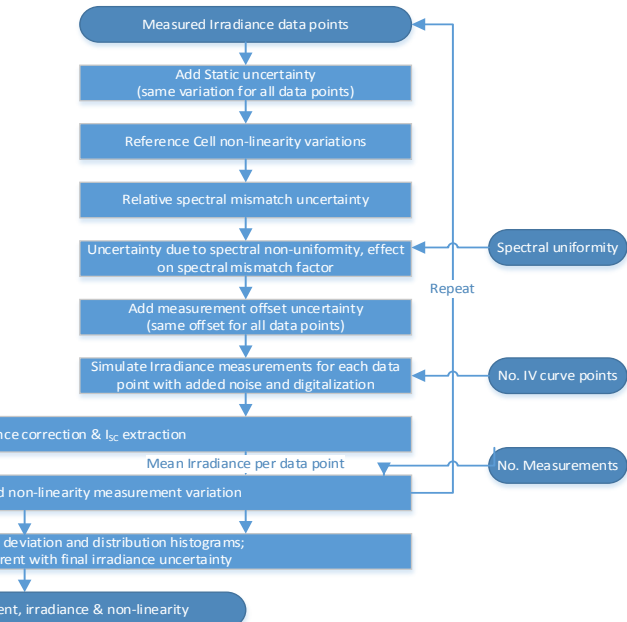
## 5 Case Study Results

To demonstrate the behaviour of  $U_{LI}$  in different cases, results of three samples are presented. The first DUT is a 600nm long pass filtered reference cell to highlight measurement deviations induced by spectral changes in the light. The second is a highly non-linear shunted cell of the same size than the first DUT to observe uncertainty in extreme cases. The third is a full size poly-crystalline PV module.

Factor ( $U k=1$ )	Small DUTs	Module	Distr.
$I_{sc}$ Static [%]	0.25	0.25	Gauss
$G$ Static [%]	1.3	1.3	Gauss
MMF [%]	0.1	0.2	Gauss
Temp. [°C]	1	1	Rec
RC $L_I$ [%]	0.1	0.1	Gauss
Uniformity [%]	0.2	0.4	Rec
$I_{sc}$ Noise [ $\mu A$ ]	42	600	Gauss
$I_{sc}$ Offset [ $\mu A$ ]	200	6600	Rec
$I_{sc}$ Digital [ $\mu A$ ]	10	330	
$G$ Noise [ $W/m^2$ ]	0.2	0.2	Gauss
$G$ Offset [ $W/m^2$ ]	1	0.1	Rec
$G$ Digital [ $W/m^2$ ]	0.05	0.05	
$I_{sc}$ Points	200	200	
Nu meas.	4	4	

Table 2: Uncertainty factors and distribution for RC size DUTs and full modules used in Monte-Carlo simulation model.

Table 2 details the uncertainty parameters used for  $U_{LI}$  simulations. The main difference between small DUTs and the module is that for



small samples, data was additionally corrected for light intensity and spectral non-uniformity. Due to the size of the DUT, those corrections are not possible for the case of the PV module. Furthermore, the spectral response (SR) of the small samples was measured in a dedicated system and the SR of the module was measured in the solar simulator using a spectral fitting method, described in [7]. This increases uncertainty in MMF calculations.

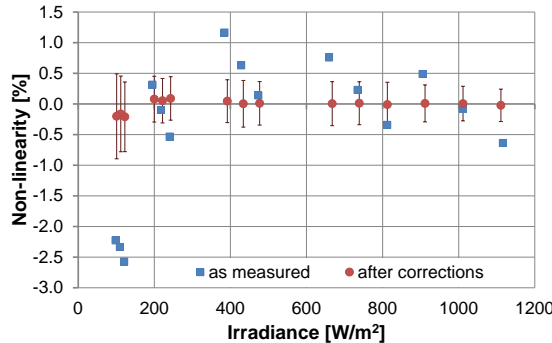


Figure 3: Comparison of non-linearity before and after applied corrections; error bars show the calculated  $L_1$  uncertainty ( $k=2$ )

The uncorrected results of the filtered RC sample shown in Figure 4, indicate that the sample is non-linear. However, after corrections, the non-linearity is significantly reduced. The main factor influencing the results is the change in spectral output caused by adjusting the lamp power and changing the attenuation masks. Both affect the red to infrared region of the output spectrum the most, thus the effect is amplified on this filtered sample. Results show that the MMF correction works efficiently and clearly highlight the importance of using a spectrally matched RC to monitor irradiance.

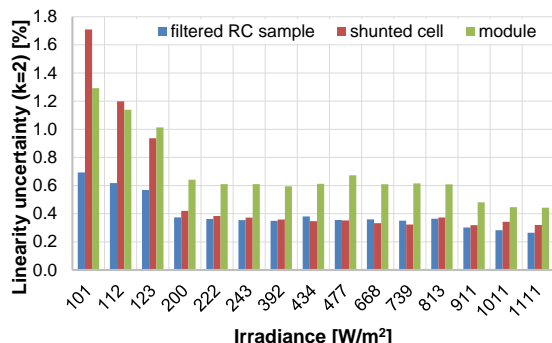


Figure 4: Expanded final linearity uncertainty estimated using Monte-Carlo simulations.

Figure 5 compares the calculated  $U_{LI}$  from the Monte-Carlo based simulation approach of all three cases. As one would expect  $U_{LI}$  increases with at low irradiance. This is partly due to the increase in uncertainty of the signal DAQ system but also due to how non-linearity is calculated. Data points at low irradiance are more affected

by fluctuations of the zero cross point (intercept) of the linear fit. Thus, the uncertainty increases to a larger degree than to what is just caused by the signal DAQ. This effect is more pronounced on highly nonlinear devices as shown in the shunted sample. Here the uncertainty is double than that of the linear filtered RC sample.  $U_{LI}$  of the module is higher throughout the measurement range due to higher uncertainty in MMF and uniformity.

## 6 Conclusions

This work details the uncertainty contributing factors when measuring photocurrent linearity using a solar simulator with attenuation masks. An uncertainty calculation model has been developed that uses the Monte-Carlo method to estimate the final linearity measurement uncertainty.

Linearity measurement results show that it is critical to correct for spectral variations that occur in a solar simulator when adjusting the intensity using attenuation mask or by changing the lamp power.

The uncertainty in current and irradiance does not directly translate to linearity uncertainty. Furthermore, uncertainty in linearity is dependent on the device linearity itself. Thus, it is recommended to assess uncertainty especially for highly non-linear devices separately. This increases trust in measurements and in linearity correction.

## Acknowledgements

The research work leading to this article was carried out within the EMRP ENG55 project Towards an Energy-based Parameter for Photovoltaic Classification. The EMRP is jointly funded by the EMRP participating countries within EURAMET and the European Union.

## References

- [1] IEC 60904-2:2015.
- [2] IEC 61853-1:2011.
- [3] IEC 61853-2:2016.
- [4] IEC 60904-10:2009.
- [5] K. Emery, et al, "Linearity Testing of Photovoltaic Cells," in 2006 IEEE 4th WCPEC 2006, vol. 2, pp. 2177–2180.
- [6] B. H. Hamadani, et al, "Non-linearity measurements of solar cells with an LED-based combinatorial flux addition method," *Metrologia*, vol. 53, no. 1, pp. 76–85, Feb. 2016.
- [7] H. Alhusna, et al, "Validation of Spectral Response Polychromatic Method Measurement of Full Size Photovoltaic Modules using Outdoor Measured Data," in PVSAT -12, 2016, pp. 157–160.

# Flexible Cu<sub>2</sub>ZnSn(S,Se)<sub>4</sub> solar cells made from nanoparticle inks

Xinya Xu\*, Guillaume Zoppi, Yongtao Qu, Vincent Barrioz and Neil S. Beattie

Department of Mathematics, Physics and Electrical Engineering, Ellison Building, Northumbria University,  
Newcastle upon Tyne NE1 8ST, UK

\*Corresponding Author [x.xu@northumbria.ac.uk](mailto:x.xu@northumbria.ac.uk)

## Abstract

Cu<sub>2</sub>ZnSn(S,Se)<sub>4</sub> (CZTSSe) photovoltaic absorbers are prepared from Cu<sub>2</sub>ZnSnS<sub>4</sub> (CZTS) nanoparticle inks fabricated by injection of metallic precursors into a hot surfactant. Both rigid (soda lime glass) and flexible (Mo foil) substrates are used to prepare identical CZTSSe solar cells. The device on soda lime glass (SLG) achieved an efficiency of 3.65 %, while the device on Mo foil exhibited a lower efficiency of 1.47 %. A thick layer of MoSe<sub>2</sub> is formed when the precursor is directly coated on the Mo foil, and this thick MoSe<sub>2</sub> layer can be reduced by pre-sputtering Mo film on Mo foil. Despite these losses, the device open circuit voltage is preserved at 270 mV on the flexible substrate.

## 1. Introduction

CZTSSe is considered as a promising photovoltaic absorber materials due to its high theoretical power conversion efficiency, ideal direct energy band-gap and large absorption coefficient in visible range [1]. Earth-abundance and low-cost properties make it suitable for large area manufacture. In addition, fabrication on flexible substrates has the potential to create lightweight solar cells that offer a wide range of application, such as roll-to-roll manufacturing and integration on curved surfaces. CZTSSe solar cells on rigid glass substrates have achieved efficiency as high as 12.6% [2], while CZTSSe solar cells based on nanoparticle ink processing have also reached 9.3% [3]. However, research on CZTS nanoparticle inks on flexible substrates is still comparatively limited. In this work, CZTSSe photovoltaic absorbers are prepared from CZTS nanoparticle inks [4,5]. Both rigid and flexible substrates are used to prepare identical solar cells and the behaviour of both CZTSSe photovoltaic absorbers and solar cells is studied.

## 2. Experimental details

CZTS nanoparticles were fabricated by injection of metallic precursors into a hot surfactant. In the synthesis, Cu(acac)<sub>2</sub>, Zn(acac)<sub>2</sub>, and Sn(acac)<sub>2</sub>Cl<sub>2</sub> were used as cation precursors, and elemental sulphur was used as an anion precursor. Oleylamine (OLA)

was used as surfactant and solvent to prevent aggregation and enable dispersion. Appropriate volumes of 0.75 mmol starting solutions were mixed to yield metal precursor molar ration of Cu/ (Zn+ Sn) = 0.79 and Zn/Sn= 1.27. The cation precursors were mixed with 10 mL OLA in a 100 mL three-neck flask. Both precursor solutions were initially heated to 65 °C to fully dissolve. In parallel, the two flasks were degassed by evacuating for 5 min and then purged with nitrogen. 3 mL of 1M S in OLA was then injected into the cation precursor after heating up to 225 °C and holding the temperature constant for 30 min under a nitrogen atmosphere. Following the reaction, the solution was washed in toluene and isopropanol (IPA) three times. The collected nanoparticles were then dispersed into 1-hexanthiol as the CZTS nanoparticle inks.

0.1 mm thick Mo foil (Sigma Aldrich) and a soda lime glass (SLG) microscope slides (dimensions: 25 mm x 25 mm x 1 mm) coated with 500 nm Mo film were used as substrates. Both were initially cleaned in deionized (DI) water and IPA for 15 min in ultrasonic bath. Additionally, the Mo foil substrate was plasma cleaned for 5 min. To fabricate the solar absorber, CZTS nanoparticle inks were spin-coated on the Mo coated glass and Mo foil substrates 10 times to obtain a precursor film thickness of ~1 μm.

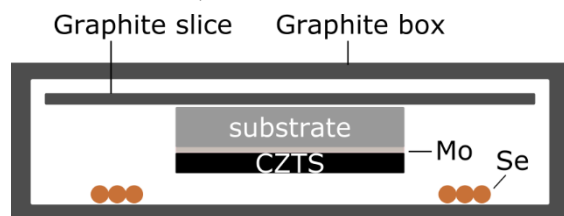


**Figure 1** Sample in graphite box during selenisation cross sectional sketch.

The precursor films were annealed in a tube furnace under selenium atmosphere for 20 min at 500 °C to form the CZTSSe absorber layers. During the selenisation process, the samples were placed in a graphite box with selenium pellets placed underneath as shown in Figure 1. The solar cell structures were completed by subsequently depositing a thin CdS layer by chemical bath deposition and a bilayer intrinsic

ZnO layer and indium doped tin oxide (ITO) by magnetron sputtering. Finally, a Ni/Al front contact grid was deposited by electron beam evaporation through a shadow mask. Each substrate was mechanically scribed to define nine  $0.16 \text{ cm}^2$  individual devices.

The morphology of CZTS precursor thin films was investigated using tapping mode atomic force microscopy (AFM, Veeco Dimension-3100), and scanning electron microscope (SEM, Tescan Mira 3). The structure of the CZTS nanocrystals was examined using X-ray diffraction (XRD, Siemens D-5000) using a Cu K $\alpha$  radiation source ( $\lambda = 0.154 \text{ nm}$  for K $\alpha 1$ ). Elemental depth profiling was performed by secondary ion mass spectroscopy (SIMS) using a Hiden Analytical gas ion gun and quadrupole detector. Photocurrent density-voltage characteristic of the CZTSSe solar cells on SLG and Mo foil substrates were measured under a standard air mass 1.5 solar illumination with an intensity of  $100 \text{ mW/cm}^2$ . The external quantum efficiency (EQE) measurements were operated using a double grating monochromator with illumination normalized against calibrated silicon and germanium detector.

### 3. Results and discussion

#### Material characterisation

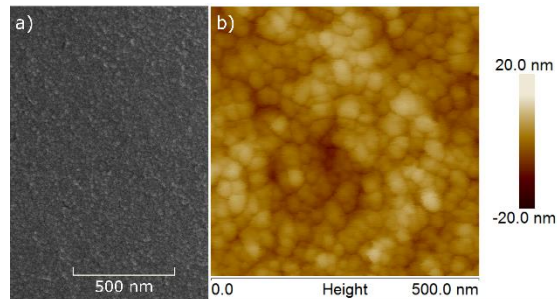


**Figure 2** CZTS film spin-coated from nanoparticle inks: a) SEM image and b) scanned with AFM.

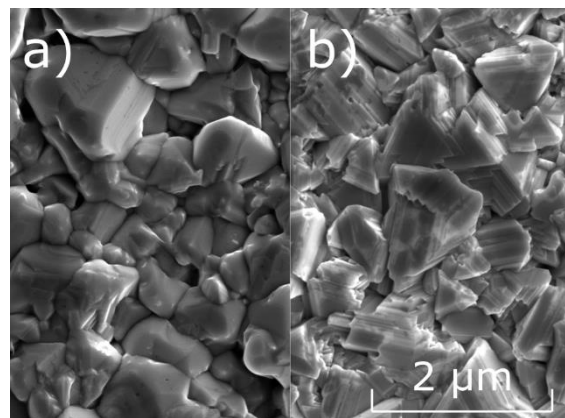


**Figure 3** SEM top view of CZTSSe sample on a) glass and b) molybdenum foil.

Figure 2 shows the SEM and AFM images of the CZTS precursor films created by depositing nanoparticles inks via spin coating. As observed from the SEM image, the CZTS film is reasonably uniform with an average particle size of  $21 \pm 6 \text{ nm}$ . No difference was observed between the samples prepared on SLG and Mo foil susbrates.

On the other hand, after selenisation, the different substrates exhibit distinguishable grain morphologies in the resulting CZTSSe films. As shown in Figure 3, CZTSSe films deposited on the SLG results in dense and rounded grain morphologies, while CZTSSe films on the Mo foil results in highly faceted grains. The apparent improved crystallinity may be a consequence of the better thermal coupling between the absorber and the substrate for the Mo foil but also of the different Mo crystallographic orientation.

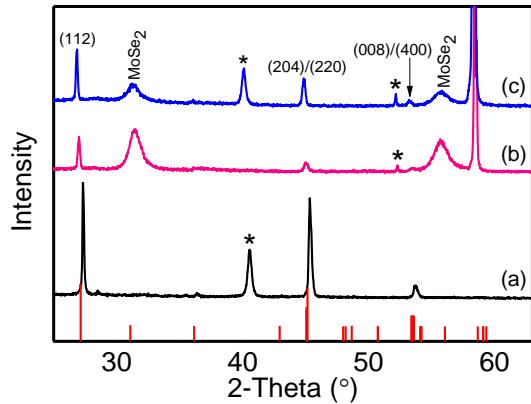


**Figure 4** XRD patterns of absorber samples on different substrates. (a) Absorber on Mo film coated SLG, (b) absorber on Mo foil, and (c) absorber on Mo foil with pre-sputtered Mo film. Peaks labelled \* marks: belong to the Mo substrates.

Figure 4 shows the XRD patterns for the prepared CZTSSe absorbers. The peak at  $40.69^\circ$  of Figure 4 (a) corresponds to the (110) plane of the Mo film. The peaks at  $52.2^\circ$  and  $58.45^\circ$  of Figure 4 (b) are unique to Mo foil indicating different crystal orientation between Mo film and foil. Additionally, the peaks at  $31.35^\circ$  and  $55.78^\circ$  shown on Figure 4 (b) correspond to MoSe<sub>2</sub>. CZTSSe deposited on SLG (Figure 4 (a)) exhibits peaks at  $37.36^\circ$ ,  $45.28^\circ$ , and  $53.68^\circ$ , which can be identified as corresponding to the (112), (204/220) and (008/400) planes respectively. Comparing with the CZTSe (PDF-026-0575) pattern, the peaks shift to larger angles due to residual sulphur in the absorber. The peaks for the absorber on Mo foil exhibited clear peaks at  $26.84^\circ$ ,  $44.91^\circ$  and  $53.42^\circ$ , corresponding to (112), (204/220) and (008/400) planes. These peaks are in good agreement with the CZTSe (PDF-026-0575) pattern. The film growth on foil

undergoes a change of crystal orientation from (112) to (204/220) as indicated by the change in peak ratio from 1.15 to 2.61 for the film grown on SLG and foil, respectively.

The SEM cross section image of a finished solar cell on SLG is shown in Figure 5. Both devices on SLG and Mo foil show the similar typical bi-layer structure of the CZTSSe absorber, composed of large grain layer on the top of a fine grain layer which has previously been found to be carbon rich [6] and therefore associated with residual precursor. In addition, for the flexible structure a thick (up to 7  $\mu\text{m}$ ) MoSe<sub>2</sub> layer was observed between the absorber layer and Mo foil, as shown in Figure 6. The presence of this layer is consistent with the XRD data on the flexible structure and confirmed by X-ray microanalysis.

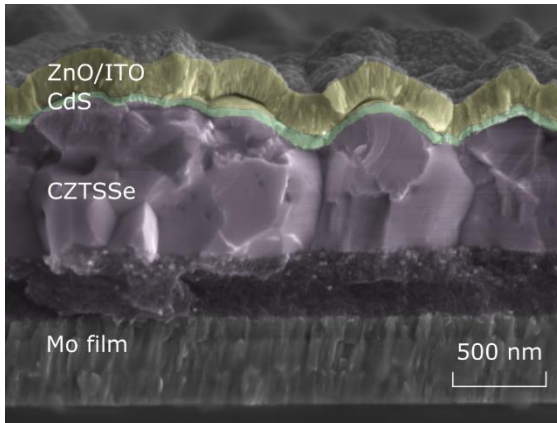


**Figure 5** SEM cross section image of CZTSSe solar cell on SLG

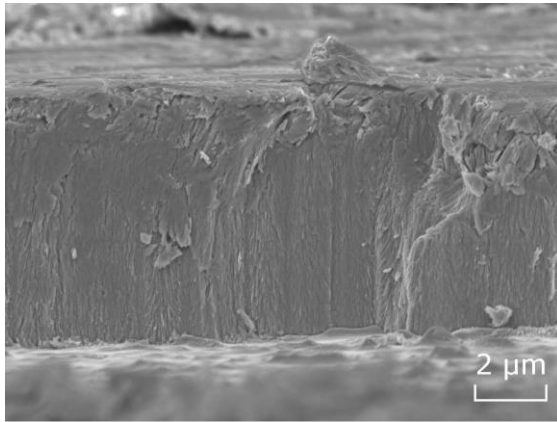


**Figure 6** Thick MoSe<sub>2</sub> layer around 7  $\mu\text{m}$ .

### Device performance

As shown in Figure 7, the device on SLG exhibited a power conversion efficiency (PCE) of 3.65 % with short circuit current density ( $J_{SC}$ ) of 31.2 mA cm<sup>-2</sup>, open-circuit voltage ( $V_{OC}$ ) of 270 mV, fill factor (FF) of 43.4%. While the device on flexible Mo foil substrate obtained the PCE of 1.47 % with  $J_{SC}$  of 19.9 mA cm<sup>-2</sup>,  $V_{OC}$  of 270 mV, FF of 27.3 %, respectively. Comparing the data from these two devices,

the flexible cell has a reduced  $J_{SC}$  and FF, which results in lower efficiency. The series resistance ( $R_s$ ) for the flexible cell is calculated to be 12.2  $\Omega$  cm<sup>2</sup>, whereas on SLG it is 3.2  $\Omega$  cm<sup>2</sup>. The formation of a thick MoSe<sub>2</sub> layer on the Mo foil is considered to be the main reason for the significant increase in  $R_s$  and corresponding poor FF. The shunt resistance ( $R_{sh}$ ) of the flexible cell is calculated to 17.2  $\Omega$  cm<sup>2</sup>, and the one of rigid cell is 86.3  $\Omega$  cm<sup>2</sup>. The drop of  $R_{sh}$  also strongly decreased  $J_{SC}$ .

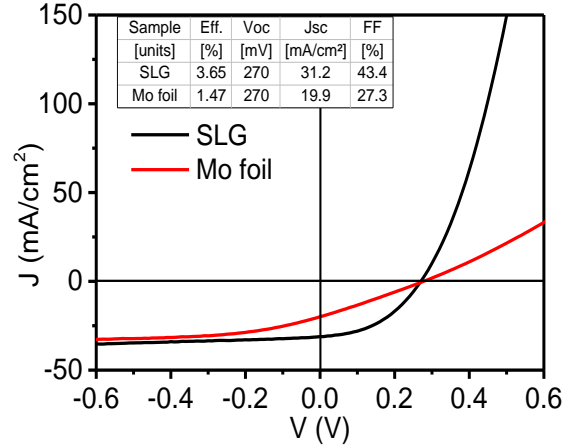


**Figure 7** JV curves of solar cells on rigid and flexible substrate.

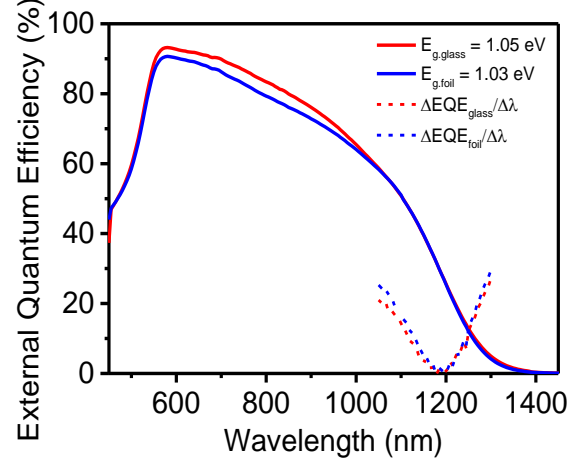


**Figure 8** EQE spectrums of the devices.

The results of external quantum efficiency (EQE) measurements are shown in Figure 8. These data show the spectral composition of  $J_{SC}$  together with bandgap values  $E_g$  extracted from the inflection point of the EQE spectrum in the long-wavelength range. The superior performance of the device on SLG may be a consequence of sodium diffusion from the substrate which has been previously observed to improve performance [7]. To investigate this possibility, SIMS was performed on the absorbers and the results were shown in Figure 9. This confirmed the Na content in sample on SLG is much higher especially at the back contact interface and large grain layer.

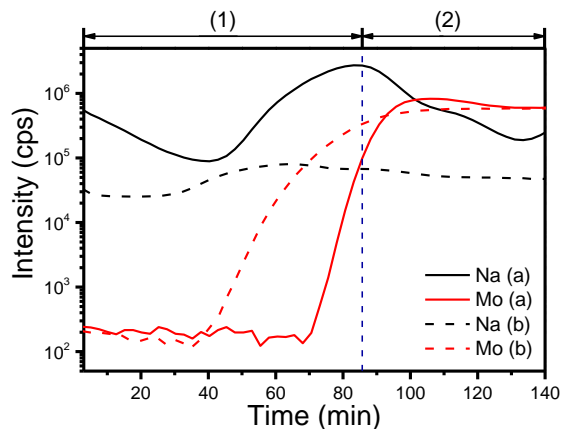


**Figure 9** SIMS depth profiles of (a) absorber on Mo coated SLG and (b) absorber on bare foil. (1) CZTSSe layer, (2) MoSe<sub>2</sub> layer.

Integration of EQE spectra yields photocurrent of 33.5 mA cm<sup>-2</sup> for the rigid cell and 32.6 mA cm<sup>-2</sup> for the flexible cell. The value for the rigid cell is in good agreement with  $J_{SC}$  obtained from  $J-V$  measurements. However, the  $J_{SC}$  of the flexible cell from  $J-V$  measurements is 19.9 mA cm<sup>-2</sup>, which is much lower than the value obtained from EQE. The reasons for this difference may be (i) local variations in the material quality which are not accounted for in the EQE measurement due to the limited beam size and (ii) large recombination rate in the space charge region. Despite the overall loss in  $J_{SC}$ , the EQE measurements indicate promising potential for both cells.

From the  $J-V$  curves, it can be seen that the  $V_{OC}$  values for the two solar cells were the same. This is consistent with the deduced energy band gaps for the two absorbers which were obtained from the  $EQE$  curves at the long-wavelength. These were found to be 1.03 eV and 1.05 eV for flexible and rigid cell, respectively.

In order to reduce the thickness of the MoSe<sub>2</sub> layer that was observed on the flexible devices, a 750 nm Mo film was pre-sputtered on the Mo foil before the spin coating process. That was followed by the same selenisation process. Importantly, the thick MoSe<sub>2</sub> was not observed in cross-sectional SEM analysis. This may be because the sputtered Mo film has a compact grain morphology which acts as a barrier and limits diffusion of Se into deep Mo foil. The nature of the CZTSSe absorber on SLG and flexible Mo foil with a sputtered Mo thin film barrier was qualitatively the same.

The XRD patterns for the CZTSSe absorber on Mo foil with pre-sputtered Mo film is as shown in Figure 4 (c). The peaks from CZTSSe on both Mo foil and Mo foil plus Mo film are indicated. The pattern of absorber on foil plus Mo film has similar reflexes with the absorber

on bare foil as well as the absorber on SLG. However, the peaks corresponding to CZTSSe are sharper and more obvious, for example, the ratio of the (204/220) peak intensity between spectrum (b) and (c) is 2.25 and similarly, 1.53 for the (112) plane. On the other hand, the peaks corresponding to MoSe<sub>2</sub> are weaker and broader with the ratio of the intensity of the peaks at 31.35° and 55.78° decreasing to 0.57 in (c). This is consistent with the apparent lack of MoSe<sub>2</sub> in the cross-sectional SEM.

#### 4. Conclusions

In this work, both rigid and flexible CZTSSe solar cells are successfully synthesized from the CZTS nanoparticle inks. A range of characterisation techniques are used to study the behaviour of both CZTSSe photovoltaic absorbers and solar cells. The rigid device achieved an efficiency of 3.65 %, while the flexible device exhibited a lower efficiency of 1.47 %. The decrease in efficiency for the flexible CZTSSe solar cell can be partly attributed to the formation of a relatively thick MoSe<sub>2</sub> layer on the Mo foil during the selenisation process. Sputtering a thin Mo film on the Mo foil before deposition of the CZTS nanoparticle ink was found to effectively limit the formation of this layer and should benefit the performance of flexible CZTSSe solar cells on Mo foil.

#### 5. Acknowledgements

The authors would like to thank Stefan Haass, from Swiss Federal Laboratories for Materials Science and Technology, Switzerland, for the supply of Mo coated SLG.

#### 6. Reference

- [1] X. Liu, Y. Feng, H. Cui, F. Liu, X. Hao, G. Conibeer, D.B. Mitzi, M. Green, *Progress in Photovoltaics: Research and Applications* 24 (2016) 879.
- [2] W. Wang, M.T. Winkler, O. Gunawan, T. Gokmen, T.K. Todorov, Y. Zhu, D.B. Mitzi, *Advanced Energy Materials* 4 (2014) 1301465.
- [3] C.J. Hages, M.J. Koeper, C.K. Miskin, K.W. Brew, R. Agrawal, *Chemistry of Materials* 28 (2016) 7703.
- [4] Y. Qu, G. Zoppi, R.W. Miles, N.S. Beattie, *Materials Research Express* 1 (2014) 045040.
- [5] Y. Qu, G. Zoppi, N.S. Beattie, *Progress in Photovoltaics: Research and Applications* 24 (2016) 836.
- [6] T.J. Huang, X. Yin, C. Tang, G. Qi, H. Gong, *ChemSusChem* 9 (2016) 1032.
- [7] H. Zhou, T.-B. Song, W.-C. Hsu, S. Luo, S. Ye, H.-S. Duan, C.-J. Hsu, W. Yang, Y. Yang, *Journal of the American Chemical Society* 135 (2013) 15998.

# Remote monitoring and failure detection for distributed small-scale PV systems

E. Koubli\*, D. Palmer, Paul Rowley and R. Gottschalg

Centre of Renewable Energy Systems and Technology, Loughborough University, LE11 3TU, UK

\* Corresponding Author [e.koumpli@lboro.ac.uk](mailto:e.koumpli@lboro.ac.uk)

## Abstract

An automatic failure detection procedure for distributed small scale photovoltaic (PV) systems is presented. The procedure is based on a few input parameters where only energy output is available and irradiance and temperature are derived from a network of ground based meteorological stations. The employed PV system model is described and the fault detection is demonstrated for three cases in Nottingham. The strengths and limitations of remote monitoring are also shown.

## 1. Introduction

Monitoring the performance of PV systems, of any size, is an important requirement in order to detect and identify system faults as early as possible. This allows a system owner to detect and repair faults thus minimising downtime and maximising return on investment. Typically, maintenance takes place on scheduled visits or not at all depending on the ownership arrangements. It is therefore likely that a fault would remain unresolved until the next planned visit, if it is not detected with automated monitoring. Moreover, in small scale systems (say up to 10 kWp) weather monitoring is usually not available for cost reasons. In such cases performance assessment and fault detection must be realised via remote monitoring procedures.

Typically, global horizontal irradiance (GHI) and ambient temperature are derived via satellite and/or ground based meteorological stations. These two variables are then translated onto system specific parameters, namely plane-of-array irradiance and module temperature, knowing the location, installation angles and technical characteristics (such as system size, PV panel and inverter model) of the PV system.

As a next step, actual to expected (modelled) electrical output is compared and their difference is evaluated according to the following formula:

$$|Q_{meas} - Q_{sim}| = \epsilon < \text{threshold} \quad (1)$$

Where  $Q_{meas}$  and  $Q_{sim}$  is the compared measured and simulated quantity respectively.

For normal operation, this difference must lie within margins specified by a threshold which will distinguish between actual faults and false alarms. A remote failure detection routine is introduced in [1] based on satellite derived irradiance and failure patterns according to which, fault diagnosis is realised. Failure patterns are particularly useful where only energy output is available, which is the most common case in domestic monitoring. However, the uncertainty deriving from the absence of on-site in-plane irradiance is quite high, compromising the accuracy of the detection procedure and causing the thresholds to increase. In this work, irradiance and temperature are derived from 88 ground based meteorological stations combined with Kriging interpolation to achieve higher accuracy in GHI estimation. The procedure is tested against various case studies taken from 1800 PV systems in Nottingham which are broken down into smaller neighbourhoods of 4 to 10 systems of similar characteristics namely, clusters. Various performance indices of neighbouring PV systems are compared with a theoretical value as well as each other at hourly time step and for longer time spans whereby the low-performing systems are recognised.

## 2. The PV simulation model

The applied model to determine the theoretical systems' output is the well-known one-diode model as presented in for a module [2]:

$$I = I_{PH} - I_0 \left[ e^{\frac{q(V+IR_S)}{nN_S kT}} - 1 \right] - \frac{V + IR_S}{R_{SH}} \quad (2)$$

Where the electron charge q, and Boltzmann's constant k are known, n is the usual ideality factor, N<sub>S</sub> is the number of cells in series and T is the module temperature. The five parameters to be determined for the model are the ideality factor n, series resistance R<sub>S</sub>, shunt resistance R<sub>SH</sub>, diode saturation current I<sub>0</sub> and photocurrent I<sub>PH</sub> (of the module). Using the Kirchhoff laws (for voltage and current) equation (3) can describe the whole array [3]. In order to determine the 5 parameters of the model the methodology suggested by [4] was applied by using manufacturer's data for each specific PV panel characteristics. In-plane

irradiance is calculated by separation into beam and diffuse components [5]) and translation to the inclined surface [6], [7]. Finally, module temperature is determined by the Ross thermal model [8]:

$$T_m = T_a + k \cdot G \quad (1)$$

Where  $T_a$  is ambient temperature,  $T_m$  is module temperature and  $G$  is in-plane irradiance and  $k$  is the coefficient which depends on the mounting configuration of the array. Here it is taken equal to  $0.03 \text{ Km}^2/\text{W}$  for building attached systems. The fitting results can be seen in Figure 1 for a specific module.

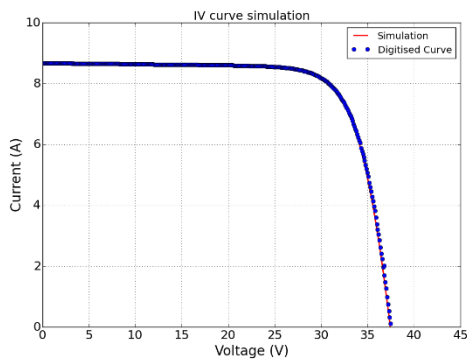


Figure 1. IV curve simulation by extracting the five parameters from manufacturer datasheets (Trina Solar 245).

To calculate system output an inverter model is incorporated based on inverter efficiency as a function of input voltage and power. The efficiency surface is shown in Figure 2 for a chosen inverter.

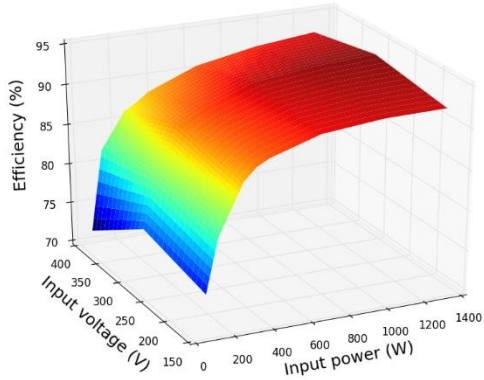


Figure 2. Interpolated surface for a Fronius IG15 inverter.

Additional system losses such as mismatch losses, spectral losses and soiling are added as a total 9% loss in the final output [1].

### 3. Definition of thresholds for irradiance

As shown in previous work [9] and in [1], there is random and bias errors which derive from the inference of global horizontal and in-plane irradiance, which depend on the irradiance intensity. Namely, for lower values this error tends to be higher whereas for higher values of irradiance this error decreases. Thus, the thresholds to the fault detection method (as described in equation (1)) are affected by the accuracy of the derived irradiance. To account for this uncertainty lower and upper limits of in-plane irradiance were added based on the error analysis carried out for Loughborough (where both measured and modelled data are available) in [9]. To avoid higher random error and false positive alarms, only irradiance data over  $50 \text{ W/m}^2$  are taken into account.

### 4. Fault detection domains

For the detection of faults several steps are carried out in the same order. Undersized and oversized inverters are initially spotted as this will determine systems' performance at higher and lower irradiance respectively. Then measured against simulated output is checked per a) hour, b) sun elevation c) neighbouring system and d) over time. Hourly performance is checked in order to define the ratio of hours where the system is found to under-perform, and sun elevation before and after noon in order to determine morning and/or afternoon shading respectively. The neighbouring systems are used as an additional criterion due to the irradiance uncertainty. The over-time performance is used in order to a) evaluate whether the potential faults are random occurrences and b) to determine if the observed fault has been causing loss over time possibly due to soiling, degradation, or module defects. Thus at every (daily) check a number of indicators are produced whereby the performance of the system is determined as normal, potentially faulty-needs further validation, and faulty. The overtime check and the system's performance pattern on a day with high clearness index is used to determine the final state of the system. The purpose is to apply this automated procedure on a frequent basis depending on the available data. The PV systems are categorised into neighbourhoods of a maximum radius of 150m where global horizontal irradiation is expected to be the same across this distance.

### 5. Case demonstration

Initial results are shown in Figure 3 for a normal and a “faulty” system, which presents morning shading (installation fault) and constant energy loss (disconnected/defect modules or wrong input information). Inverter sizing is within limits for the particular system. This system is a single string which comprises 8 modules. The deviation from the lower threshold is evaluated throughout the day. Even in non-clear sky conditions, this deviation is detected. It is more pronounced in the morning, although the system under-performs throughout the day. This is also determined by comparing to a neighbouring system of the same characteristics, for one day and over 10 days.

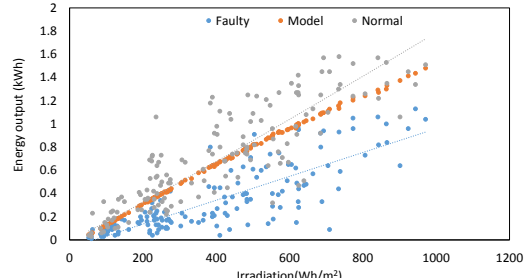
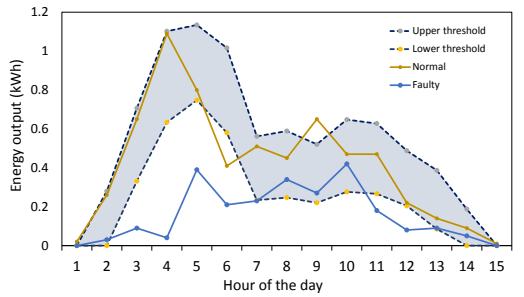


Figure 3. Detection outcome for two neighbouring PV systems of similar characteristics: hourly time step (top) on a random day and hourly output vs irradiation for 10 days (bottom).

The “faulty” system shows constant underperforming behaviour and morning hour shading with regards to its neighbouring system and the model.

The identification of the fault (other than shading) is not always straightforward since, in the case of domestic monitoring I, V data are usually not available. Comparing various output power patterns for a string with disconnected modules, showed that the particular system behaves as if two of its modules have been disconnected or this is simply due to wrong input information.

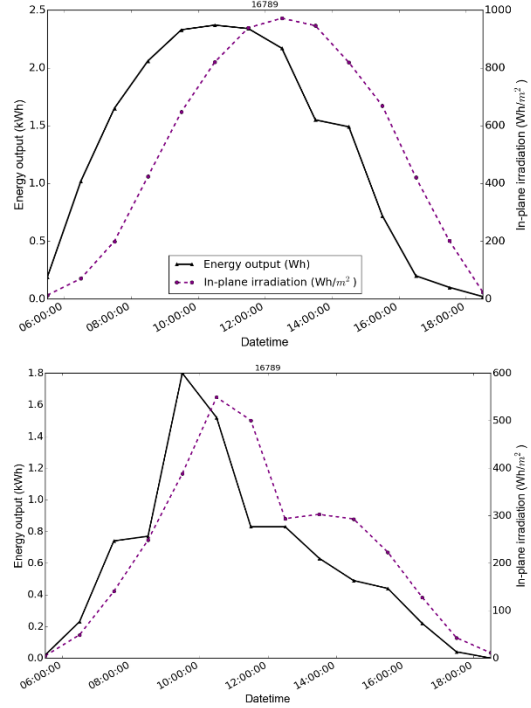


Figure 4. Power output of a PV system on a clear day (top) and on a partly cloudy day (bottom).

The second case demonstrates a PV system with wrongly declared orientation. This issue appears very often. By applying fault detection this case is picked up on a clear day. Graphical representation of energy output with in-plane irradiation shows this characteristic pattern where irradiation curve is shifted with regards to energy output curve (see Figure 4). For partly cloudy days small shifts such this, cannot be readily determined and further checks are required.

The third case demonstrates systems which were picked up by using simulated output but the comparison to a neighbouring system failed to yield a reliable result. The reason being that both systems were found to present early morning shading, a typical shading pattern in domestic monitoring from near objects such as chimneys (see Figure 5). This proves that by only comparing to neighbouring systems is not always a reliable method in failure detection, especially when neighbours are constrained to only a couple of systems.

## 6. Conclusions

A fault detection procedure is demonstrated for three random PV neighbourhoods in the area of Nottingham. These case studies have been found to produce lower output than expected based on comparison with a performance model and their neighbouring

systems. Automatic checks took place on a daily basis.

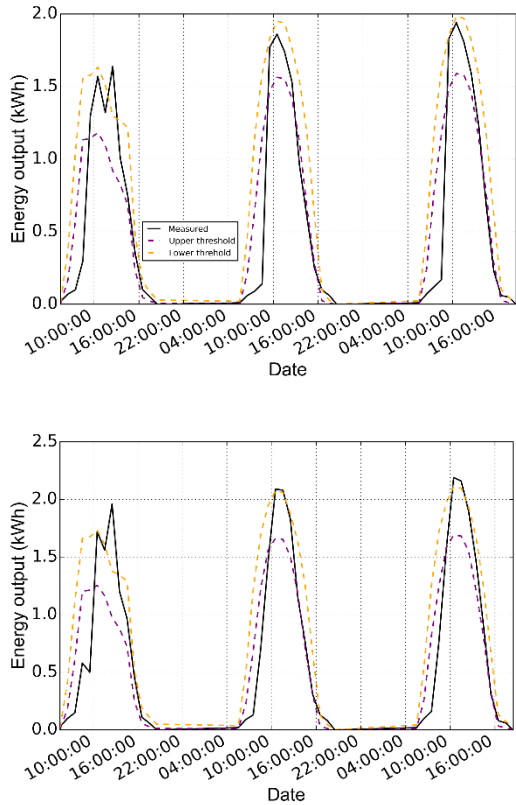


Figure 5. Energy output for three days for two neighbouring systems where both systems present morning shading.

The main obstacles in the detection and identification of faults is irradiance uncertainty and wrong or inadequate input information. Irradiance uncertainty is however smaller than similar studies using free versions satellite data allowing the detection of severe faults even at partly cloudy days. Irradiance uncertainty, is partly remedied by comparing system performance ratios with neighbouring systems. However, in the same neighbourhood, more than one systems can be found faulty or shaded which indicates that comparing to neighbouring systems (if any) is not a panacea. Moreover, the detection method's efficiency increases significantly for clear days and in such circumstances the results from simulated output are more reliable than comparing to other systems. Generally, effects that cause more than 10% reduction in hourly output are readily detected in clear days. Shading can be validated via mapping software and commonly via free satellite maps and wrong input orientation can be confirmed on a clear day. To assure the existence of more complicated faults requires further confirmation by the

administrators and owners of the systems. Simulating faults and re-producing failures may also give an indication of the type of fault, however this is yet to be automated and integrated in the overall procedure, as part of future improvement.

### Acknowledgements

The authors would like to acknowledge the support of Nottingham City Homes for supplying the data and especially Heather Dickens and John Carr for making this study possible.

### References

- [1] A. Drews, A. C. de Keizer, H. G. Beyer, E. Lorenz, J. Betcke, W. G. J. H. M. van Sark, W. Heydenreich, E. Wiemken, S. Stettler, P. Toggweiler, S. Bofinger, M. Schneider, G. Heilscher, and D. Heinemann, "Monitoring and remote failure detection of grid-connected PV systems based on satellite observations," *Sol. Energy*, vol. 81, no. 4, pp. 548–564, Apr. 2007.
- [2] W. De Soto, S. a. Klein, and W. a. Beckman, "Improvement and validation of a model for photovoltaic array performance," *Sol. Energy*, vol. 80, no. 1, pp. 78–88, Jan. 2006.
- [3] H. Tian, F. Mancilla-David, K. Ellis, E. Muljadi, and P. Jenkins, "A cell-to-module-to-array detailed model for photovoltaic panels," *Sol. Energy*, vol. 86, no. 9, pp. 2695–2706, Sep. 2012.
- [4] M. Villalva, J. Gazoli, and E. Filho, "Comprehensive Approach to Modeling and Simulation of Photovoltaic Arrays," *IEEE Trans. Power Electron.*, vol. 24, no. 5, pp. 1198–1208, 2009.
- [5] B. Ridley, J. Boland, and P. Lauret, "Modelling of diffuse solar fraction with multiple predictors," *Renew. Energy*, vol. 35, no. 2, pp. 478–483, Feb. 2010.
- [6] J. E. Hay, R. Perez, and D. C. McKay, "Estimating Solar Irradiance on Inclined Surfaces: A Review and Assessment of Methodologies," *Int. J. Sol. Energy*, vol. 4, no. 5, pp. 321–324, 1986.
- [7] D. Reindl, W. Beckman, and J. Duffie, "Evaluation of hourly tilted surface radiation models," *Sol. Energy*, vol. 45, no. 1, pp. 9–17, 1990.
- [8] J. Ross, R. G., "Interface design considerations for terrestrial solar cell modules," in *12th IEEE Photovoltaic Specialist Conference*, 1976, pp. 801–806.
- [9] E. Koubli, D. Palmer, P. Rowley, and R. Gottschalg, "Inference of missing data in photovoltaic monitoring datasets," *IET Renew. Power Gener.*, vol. 10, no. 4, pp. 434–439, Apr. 2016.

## Very high humidity fabrication of perovskite solar cells

Joel Troughton\*, Katherine Hooper\* and Trystan Watson\*

\* SPECIFIC – Swansea University, A224 Engineering East, Bay Campus, Swansea, SA1 8EN,

\* Corresponding Author: T.M.Watson@swansea.ac.uk

### Introduction

During the short time since their discovery, organic-inorganic halide perovskites have exploded in popularity as promising light harvesters for photovoltaic devices with published power-conversion efficiencies (PCEs) now exceeding 21%.<sup>[1–3]</sup>

Currently, the majority of research pertaining to perovskite photovoltaics involves the use of controlled atmospheric conditions, usually in the form of nitrogen-filled gloveboxes. This is necessitated by the moisture sensitivity of some perovskite precursor components including halogenated organic cation salts such as methylammonium iodide (MAI), methylammonium bromide (MABr) and formamidinium iodide (FAI).<sup>[4–7]</sup>

One popular perovskite deposition technique involves the spin-coating of a perovskite precursor containing the aforementioned materials, as well as a lead halide compound and a blend of polar solvents such as dimethylformamide (DMF) and dimethylsulfoxide (DMSO). Termed “solvent engineering”,<sup>[8]</sup> a high quality perovskite film is achieved by quenching the perovskite precursor during spin-coating with a so-called “anti-solvent” which causes a rapid formation of an intermediate phase between the solvent and perovskite precursor components. Upon heating, any residual solvent is removed and high quality perovskite film is achieved. Unfortunately, this intermediate phase is reportedly unstable in the presence of moisture, preventing the atmospheric processing of high quality films.<sup>[9]</sup>

In this work, we present a processing technique which allows for the spin-deposition of newly emerging mixed cation perovskite films in very humid environments.

### Experimental

The general solar cell device architecture used in this study is illustrated in Figure 1. FTO-coated glass was patterned by etching select regions with Zn powder, followed by HCl. Substrates were cleaned

in a solution of detergent, followed by sonication in deionised water, acetone and isopropanol before undergoing an oxygen plasma treatment to remove any residual organic species.

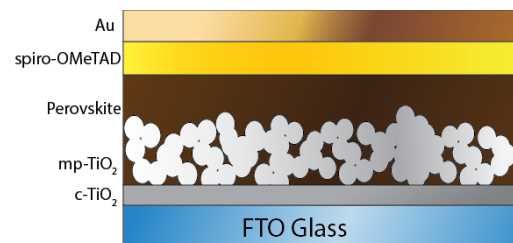


Figure 1. Schematic diagram of the perovskite solar cell architecture used in this study.

A 50nm thick TiO<sub>2</sub> hole blocking layer was deposited by spray coating a solution of titanium diisopropoxide bis(acetylacetone) in isopropanol onto heated substrates, before sintering at 550°C for 30 minutes. Upon cooling, a suspension of TiO<sub>2</sub> nanoparticles (Dyesol 30NR-D diluted in ethanol) was spin-coated onto films and sintered again at 550°C to produce a mesoporous TiO<sub>2</sub> electron accepting layer. Next, a perovskite precursor solution containing 1M FAI, 0.2M MABr, 1.1M PbI<sub>2</sub> and 0.2M PbBr<sub>2</sub> in a 4:1 blend of DMF:DMSO was spin-coated onto the substrates at 6,000rpm for 30 seconds. 20 seconds from the end of the spin-coating cycle, 200µl of anti-solvent was dripped onto the film. Films were annealed at 100°C for 10 minutes before a solution containing spiro-OMeTAD, lithium Bis(trifluoromethane)sulfonimide and 4-tert-butylpyridine in chlorobenzene was spin-coated to form a hole transporting layer. Finally, a gold metal electrode was evaporated onto the devices. For air-processed samples, relative humidity was maintained at 75%RH using a humidity controlled chamber.

## Results & Discussion

One common anti-solvent used to produce perovskite films using the anti-solvent method is chlorobenzene, which is miscible with the DMF and DMSO perovskite solvents, but not a solvent of the perovskite precursor salts themselves. Another potential anti-solvent to be explored is ethyl acetate,<sup>[10]</sup> which possesses similar properties to the conventional chlorobenzene regarding its reaction with the perovskite materials used in this study.

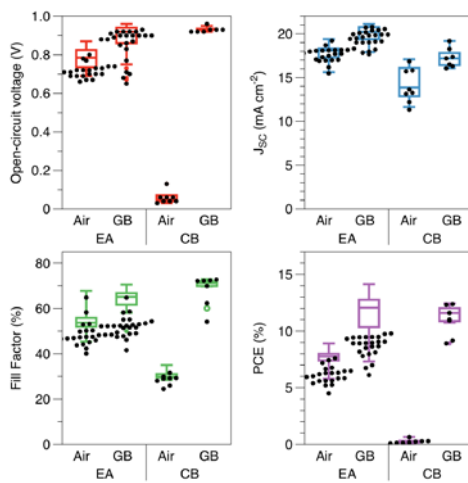


Figure 2. J-V statistics for solar cells produced in air (Air) and in a N<sub>2</sub>-filled glovebox (GB) using both chlorobenzene (CB) and ethyl acetate (EA) as anti-solvents. Boxes represent Voc-Jsc scans whereas black dots represent Jsc-Voc scans.

Figure 2. shows J-V statistics for solar cells produced in both air and a moisture-free glovebox using both chlorobenzene and more novel ethyl acetate anti-solvents. An insight into the degree of hysteresis within the devices is shown by comparing the boxes (the more favourable Voc-Jsc scan) with the dots (Jsc-Voc scan). As Figure 2. shows, there is a small variation between the two anti-solvents when processed under an inert atmosphere: Peak power conversion efficiency (PCE) in both cases exceeds 13%, with a maximum PCE of more than 14% for the ethyl acetate processed device. Interestingly, hysteresis appears more pronounced in the ethyl acetate devices which may be a result of a different in perovskite grain morphology and charge build-up at grain boundaries

which are not present in chlorobenzene-processed devices.

Perhaps most interestingly, there is a dramatic difference between devices processed in humid air with different anti-solvents. Where the ethyl-acetate processed devices show a modest decrease in Voc and Jsc compared to their glovebox produced counterparts, the chlorobenzene-utilising cells suffer a much larger drop in Voc, Jsc as well as fill factor. This is attributed to the presence of far larger pinholes and morphological disorder within chlorobenzene-processed perovskite films.

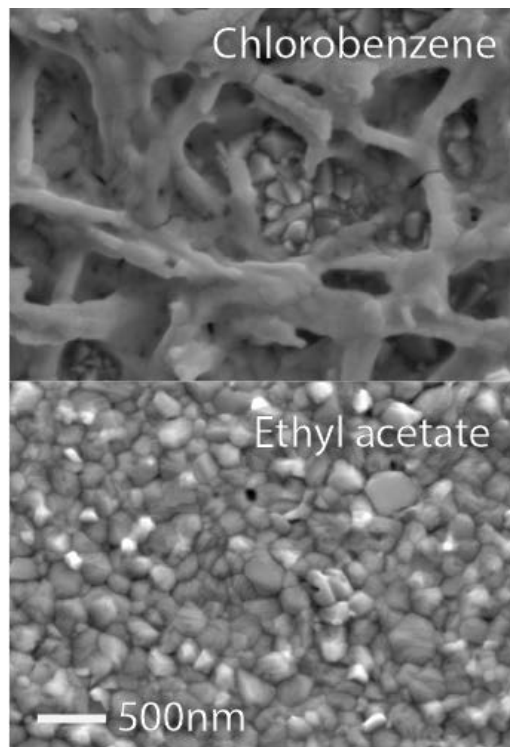


Figure 3. SEM micrograph of perovskite films processing in air using chlorobenzene or ethyl acetate as an anti-solvent.

Figure 3. shows micrographs of CH<sub>3</sub>NH<sub>3</sub>PbI<sub>3</sub> perovskite films produced in air using the two anti-solvents used in this study. The chlorobenzene-produced film exhibits large pinholes exposing the FTO crystals in the underlying substrate. By comparison, films produced using ethyl acetate exhibit no pinholes across the surface.

## Conclusions

We have demonstrated a method for producing high quality perovskite films under high humidity atmospheric conditions. Using ethyl acetate as an anti-solvent, we were able to fabricate triple cation-containing perovskite solar cells with PCEs around 9%, compared to 14% when fabricated within a nitrogen-filled glovebox. By comparison chlorobenzene, another popular anti-solvent, entirely fails to produce functional devices under the same processing conditions. The reason behind such a dramatic reduction in performance appears to be the breakdown in perovskite morphology and a substantial increase in pinhole density owing to moisture present within the atmosphere during processing. These findings allow the possibility of processing efficient perovskite solar cells in uncontrolled environments and laboratories where stringent atmospheric control is not available.

- [9] J. W. Jung, S. T. Williams, A. K.-Y. Jen, *RSC Adv.* **2014**, *4*, 62971.
  - [10] M. Yin, F. Xie, H. Chen, X. Yang, F. Ye, E. Bi, Y. Wu, M. Cai, L. Han, *J. Mater. Chem. A* **2016**, *4*, 8548.
- 
- [1] A. Kojima, K. Teshima, Y. Shirai, T. Miyasaka, *J. Am. Chem. Soc.* **2009**, *131*, 6050.
  - [2] M. M. Lee, J. Teuscher, T. Miyasaka, T. N. Murakami, H. J. Snaith, *Science (80- )* **2012**, *338*, 643.
  - [3] H.-S. Kim, C.-R. Lee, J.-H. Im, K.-B. Lee, T. Moehl, A. Marchioro, S.-J. Moon, R. Humphry-Baker, J.-H. Yum, J. E. Moser, M. Gratzel, N.-G. Park, *Sci. Rep.* **2012**, DOI 10.1038/srep00591.
  - [4] J. H. Noh, S. H. Im, J. H. Heo, T. N. Mandal, S. Il Seok, *Nano Lett.* **2013**, *13*, 1764.
  - [5] G. Niu, W. Li, F. Meng, L. Wang, H. Dong, Y. Qiu, *J. Mater. Chem. A* **2014**, *2*, 705.
  - [6] Z. Song, A. Abate, S. C. Wattage, G. K. Liyanage, A. B. Phillips, U. Steiner, M. Graetzel, M. J. Heben, *Adv. Energy Mater.* **2016**, *6*, 1600846.
  - [7] J. Yang, B. D. Siempelkamp, D. Liu, T. L. Kelly, *ACS Nano* **2015**, *9*, 1955.
  - [8] N. J. Jeon, J. H. Noh, Y. C. Kim, W. S. Yang, S. Ryu, S. Il Seok, *Nat. Mater.* **2014**, *13*, 1.



## Satellite or Ground-based Irradiation Data: which is closer to reality?

Diane Palmer \*, Elena.Koubli, Ian Cole, Tom Betts and Ralph Gottschalg

Centre of Renewable Energy Systems and Technology, Loughborough University, LE11 3TU, UK

\* Corresponding Author [d.palmer@lboro.ac.uk](mailto:d.palmer@lboro.ac.uk)

### Abstract

Satellite-derived hourly global horizontal irradiance is compared with that measured by ground-based weather stations. The satellite accuracy is compared to the error which arises as a function of distance when the ground data is extrapolated or interpolated. A number of factors are examined to allow identification of the optimal resource.

### Introduction

Insolation data is necessary to calculate the potential output of PV systems. The two main sources of global horizontal irradiance (GHI) data are ground-based measurements and satellite-derived data. It is generally accepted that well-prepared ground-based values are more accurate, at or close to, the point of measurement. They represent the irradiation actually received at ground level, where solar systems are located. Satellites do not record the solar flux itself, but rather capture cloud images. A series of models is applied to convert these images into GHI data.

Where no ground-based data is available for a given site, it is general practice to use the data from the next nearest point or points. However, as the distance between the point of measurement and site (where data is required) increases, the likelihood of variation of weather conditions at the two sites also increases. In general, a distance decay effect may be observed in the accuracy of this method, due to weather fronts and terrain. There reaches a theoretical distance where the decreasing accuracy of the ground-based data equals and then falls below the otherwise less accurate satellite-modelled data. This cross-over or break-even distance was determined as 34 km for hourly averaged GHI data by Perez et al in 1997 [1].

Perez' original work referred to *extrapolation* of ground data, whereas a number of well-known ground data sources (Meteonorm, original PVGIS) use *interpolation*. The last 20 years have seen considerable advances in satellite modelling. Interpolation techniques have

been in existence for some time, but more powerful computers have enabled their widespread use and enhanced understanding. Advances in networking and communication technology have led to increased availability of data. The focus of this paper is the re-examination of the break even distance in the current data climate. Recent work on daily GHI found the accuracy of the SARAH satellite model surpassed that of ordinary kriging interpolation when the distance to the closest measurement station exceeded 20 – 30 km [2]. This suggests that modern satellite models ought to deliver a much longer break-even distance for hourly GHI than Perez' 1997 figure of 34 km.

This paper quantifies the accuracy of both ground-based and satellite-modelled GHI in terms of root mean square error (RMSE) and mean bias error (MBE). The following comparisons will be made: (1) pair-wise comparison of weather station reading to nearest weather station value; (2) interpolated ground-measurement to nearest weather station record at various distances; and (3) satellite-derived value to nearest weather station reading at various distances.

### Data and Methods

All data used is hourly data for the complete year of 2014, unless otherwise stated. The case study area is Great Britain. 2014 produced the highest photovoltaic output in the UK of recent years.

### Ground Data

Ground-based solar irradiance measurements at hourly intervals are used from the UK Meteorological Office Integrated Data Archive System - MIDAS (Met Office, 2006) [3]. The UK Met Office currently has a network of over 80 automatic weather stations throughout the UK which observe irradiance as well as other meteorological conditions. The distribution is somewhat uneven. 30% of the stations are clustered in the South East and Midlands i.e. approximately one-third of the weather stations are positioned in one-fifth of the nation. In other words,

although stations are typically about 40 km apart, this can more than double, particularly in Wales and Scotland.

There are two ways of treating data as distance from the point of measurement increases. The simplest is nearest neighbour extrapolation which simply involves taking the value of the closest weather station to the point of interest. The distance decay error of this technique is calculated as follows. Take GHI values from two nearest neighbour weather stations (1 and 2). Imagine that the value of station 2 is unknown. Accordingly it becomes necessary to use the data from station 1. Validate the accuracy of station 1 data in these circumstances by comparing it to the real data from station 2. The distance decay is the distance between the two stations. This procedure is repeated for each closest weather station pair until all the data has been used. The nearest neighbour extrapolation method is included in this research because this is the only method available to many GHI data users.

The second way of extending ground-based measurements to cover greater distance is interpolation. This takes the values from several weather stations surrounding the point of interest. These are input into a mathematical algorithm and weighted according to distance to the desired location to calculate a GHI value for the unknown site. This paper employs the kriging interpolation technique. (See [4] for further explanation of selection of kriging and details of its application.)

The reduction in accuracy of interpolation due to distance decay is assessed by leave-one-out-cross-validation (LOOCV). This may be applied as follows. Interpolate with 79 weather stations and leave the 80<sup>th</sup> out. Compare the interpolated value obtained at the 80<sup>th</sup> station with the measured value from that site. (Calculate the RMSE). This is repeated for all stations (i.e. 80 times). Plot the RMSEs as a function of distance to nearest interpolating site. (That is, the distance between the location of the “missing” station and the closest of the other 79).

### Satellite Data

Models which generate irradiance from satellite observations may be classified as one of three types: physical, statistical and hybrid. Physical models utilize radiative transfer equations and require detailed information on the composition of the

earth's atmosphere (e.g. gridded aerosol properties and water vapour) as inputs. Statistical models are based on regression between satellite reflectance and corresponding ground measurements. Lastly, hybrid models simplify the physical processes but combine them with empirical observations.

Three models are investigated here. (1) SARAH-E [5] is a hybrid model. It has a spatial resolution of 0.05° (5.6 km) and requires the following atmospheric data as inputs: temperature, wind, humidity, ozone, surface pressure. SARAH-E data was available for 11 years (2005-2015). (2) CAMS [6] utilises the Heliosat-4 physical model for satellite image-to-ground irradiance conversion. It has a spatial resolution and atmospheric inputs similar to SARAH\_E but additionally requires aerosol optical depth as a parameter. (3) Solargis [7] uses a hybrid approach. In addition to the inputs taken by the two models above, it includes elevation and terrain shading in the model. Satellite elevation data is available at higher resolution, enabling Solargis to deliver a spatial resolution of 250 m.

## Results and Discussion

### Extrapolation versus interpolation

Initially, the relative accuracies of extrapolation and interpolation of ground-based data were assessed. The findings are presented in Fig. 1 which plots the nRMSE (normalised by mean of inputs) as a function of distance.

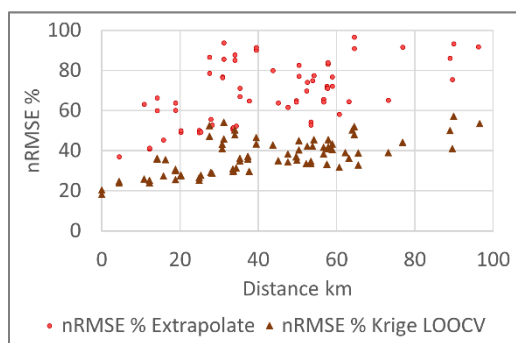


Figure 1: Extrapolation and kriging LOOCV nRMSEs as a function of the closest site distance.

It may be seen that, in contrast to Perez' original work, kriging delivers a large improvement over nearest neighbour extrapolation. This is because, in this instance, many more ground station readings are available (80 plus as

compared to 12 in [1]) and the sophisticated kriging interpolation technique is employed, rather than Perez' simpler IDW. (IDW is necessary when data is sparse.) Most analysis will now focus on the more accurate kriging method.

### Comparison of Accuracy of Satellite-derived and Kriging GHI

Discrepancies between ground-measured data and satellite-derived values arise because the weather station records at a specific location, whereas most UK satellite observations represent an area of about  $25 \text{ km}^2$  (the pixel size). Unfortunately, this is unavoidable.

The next step is to compare the average satellite prediction accuracy to extrapolation and interpolation trendlines of ground measurements (Fig. 2). This illustrates the significance of choice of satellite model. It also shows all satellite models performing better than extrapolation, with the exception of SARAH\_E. This model "breaks even" (equals and then becomes less accurate than) with extrapolation at a distance 10 km (Fig. 2. (1)). CAMS data breaks even with kriging at a distance of 35 km (Fig. 2. (2)) (similar to [1].) Solargis equals the nRMSE of kriged ground data at zero distance (Fig. 2. (3)).

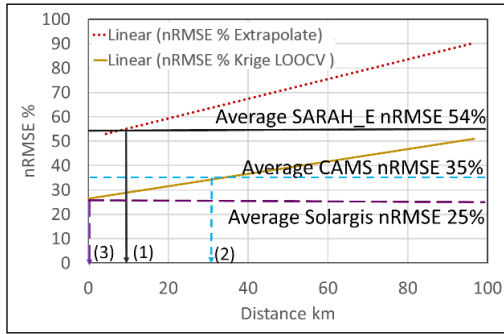


Figure 2: Average Satellite Prediction Accuracy relative to ground-based extrapolation & interpolation nRMSE trends.

When ranges of satellite accuracy are plotted against *actual* kriging LOOCV figures (rather than trendlines) (see Fig. 3), a different, less clear picture emerges. The break-even distances of satellite data compared to kriging values vary as follows: SARAH\_E 28 – 97 km, CAMS 18 – 65 km and Solargis 0 – 25 km. Evidently, another analytical approach is required.

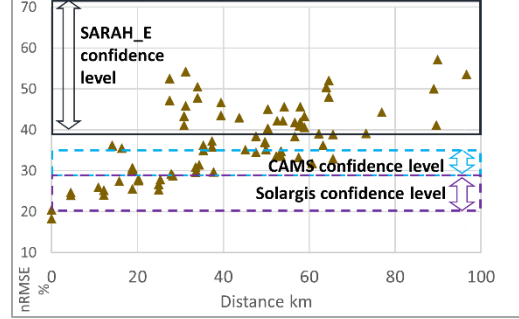


Figure 3: Kriging nRMSE as a function of closest site distance compared to satellite accuracy ranges.

So far, averages have been compared with trendlines, or ranges with values. In Fig. 4 the satellite error (nRMSE) at each weather station is subtracted from the kriging error. That is, like is set against like at each specific location. The difference in errors is plotted against inter-station distance. When the difference becomes negative, (i.e. satellite accuracy is greater than kriging accuracy) break-even has been attained.

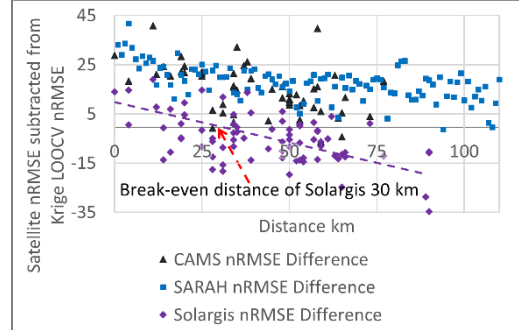


Figure 4: Difference between satellite and kriging nRMSEs at each weather station, plotted as a function of increasing inter-station distance

This more realistic technique indicates that although SARAH\_E and CAMS data displays a downward trend with distance to nearest neighbour, neither attains a negative value. If the trends are continued this would be achieved at hypothetical distances of well over 100 km. This is far greater than any UK inter-station distance. In contrast, Solargis / kriging nRMSE differences become negative at a distance of 30 km. Thus Solargis data is the only satellite model tested which possesses a break-even distance that is usable. Currently, it is the single accurate alternative to kriging of ground-based measurements.

### Relative Accuracy of Kriging of Ground Measurements and Solargis by Location

An investigation of exactly where either kriging or ground data or Solargis performed best was carried out (Fig. 5).

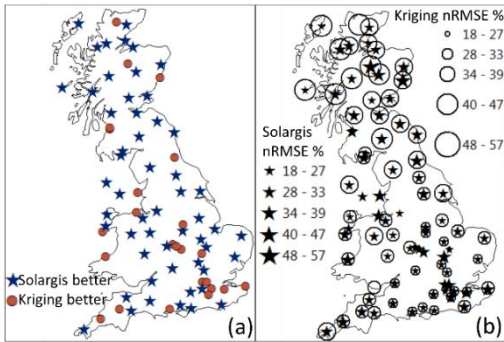


Figure 5: (a) Map of weather stations showing whether kriging of ground values or Solargis has greater accuracy. (b) Map of weather stations indicating nRMSE of kriging and Solargis at each location.

Fig. 5a reveals that kriging is most accurate where weather stations cluster in the centre and southeast. Fig. 5b illustrates the tendency of the satellite model to produce higher errors in coastal locations. However, kriging also has high nRMSEs close to the coast due to edge effects of the algorithm. Solargis is less accurate in the north (increasing latitude). This is a well-known difficulty with satellite models [7]. On the other hand, kriging also performs less well in the north. This is not linked to latitude, it is due to the greater dispersal of weather stations in northern areas. Thus both techniques are delivering similar values of accuracy at the same locations but for different reasons. But both satellite and kriged values are affected by elevation in upland areas where each furnishes higher errors. Once again this is a known problem for satellite models. The kriging algorithms only interpolates in the x and y planes and does not account for changes in the z plane.

Solargis outperforms kriging at two-thirds of weather stations. Yet the mean difference between the two approaches is low: 32 kWh/m<sup>2</sup> or 4%. In general, both satellite and interpolated data are affected by similar inter-related errors.

## Conclusion

The situation is not as straightforward as a simple distance based decision between satellite-modelled and ground-based GHI data. The relative accuracies of satellite-derived or ground-based values depend on: (1) whether the weather stations

measurements are extrapolated or interpolated; (2) the number of weather stations reporting values which, in turn, dictates the interpolation technique; (3) inter-station distance and clustering of weather stations; and (4) the satellite model employed. If the satellite model provides a usable break-even distance (currently Solargis only), the precise location of where interpolated measurements or satellite data is most accurate is hard to predict. Solargis outperforms kriging in the majority of the UK. However, kriging has higher accuracy in some (not all) coastal areas. This will form the basis of further investigation.

Break-even distance is not a helpful concept for identifying the optimal GHI resource. More useful guides are: (1) number of weather stations in the country/region. Interpolation can only deliver accurate results with more than 20. (2) Budget. This influences whether free public or more accurate commercial satellite data is used.

## References

- [1] R. Perez, R. Seals, and A. Zelenka, "Comparing satellite remote sensing and ground network measurements for the production of site/time specific irradiance data," *Sol. Energy*, vol. 60, no. 2, 89–96, 1997.
- [2] R. Urraca, E. Martinez-de-Pison, A. Sanz-Garcia, J. Antonanzas, and F. Antonanzas-Torres, "Estimation methods for global solar radiation: Case study evaluation of five different approaches in central Spain," *RenewSustainEnergyRev*'16
- [3] UK Met Office, "MIDAS: UK Hourly Weather Observation Data. NCAS British Atmospheric Data Centre," 2006. [Online]. <http://catalogue.ceda.ac.uk/uuid/916ac4bbc46f7685ae9a5e10451bae7c>.
- [4] D. Palmer, I. Cole, T. Betts, and R. Gottschalg, "Interpolating and Estimating Horizontal Diffuse Solar Irradiation to Provide UK-Wide Coverage: Selection of the Best Performing Models," *Energies*, vol. 10, no. 2. MDPI, p. 181, 05-Feb-2017.
- [5] A. Amillo, T. Huld, and R. Müller, "A New Database of Global and Direct Solar Radiation Using the Eastern Meteosat Satellite, Models and Validation," *Remote Sens.*, vol. 6, no. 9, pp. 8165–8189, Aug. 2014.
- [6] M. Schrödter-Homscheidt, "The Copernicus Atmosphere Monitoring Service (CAMS) Radiation Service in a nutshell," no. 2015, 2016.
- [7] R. Perez, T. Cebecauer, M. Suri, 2013 "Chapter 2 - Semi-Empirical Satellite Models". In: J. Kleissl (ed) *Solar Energy Forecasting and Resource Assessment*. <http://dx.doi.org/10.1016/B978-0-12-397177-7.00002-4>.

# Agent-based modelling of the effect of government policy on the adoption of domestic photovoltaic systems in Great Britain

Phoebe Pearce\* and Raphael Slade\*

\* The Blackett Laboratory, Department of Physics, Imperial College London, SW7 2AZ

• Centre for Environmental Policy, Imperial College London, SW7 2AZ

\* Corresponding Author: phoebe.pearce15@imperial.ac.uk

## Abstract

Feed-in tariffs for small-scale solar PV currently support over 2GW of installed capacity in Great Britain, at an estimated cost of around £600 million/year. An agent-based model is used to assess feed-in tariff policy by exploring alternative historical pathways under alternative subsidy strategies, showing that more installation could have likely been achieved at a lower subsidy cost. Projections are made assessing future installation under the feed-in tariff scheme up to 2022, showing that the current tariffs are so low that they do little to encourage adoption which would not have happened in the short term (within five years) otherwise if commercial PV costs continue to fall.

## Introduction

Since 2010, feed-in tariffs (FiTs) for small-scale renewable energy installations including solar photovoltaics (PV) have been available to individuals, communities, and industrial and commercial organisations in Great Britain, as part of the UK's climate change mitigation strategy. The majority of FiT installations (over 99%) are solar photovoltaics (PV) [1].

The cumulative peak capacity of small-scale (up to 10 kW) PV systems installed with support from the FiT scheme now exceeds 2 GW [1,2]. However, supporting this generation comes at significant cost to utilities and thus their customers, and costs continue to rise as the scheme remains open to registrations while payments to existing installations remain guaranteed for 20 to 25 years. Given the scheme's significant cost as well as the importance of increasing the share of renewable energy in electricity generation, a review of the implementation of the FiT scheme, both over the period 2010-2016 and policy announced up to 2019, is relevant. Specifically, investigating if FiT policy encouraged installation in an effective manner in the period 2010-2016, and predicting the outcome of future policy in the short term (up to 2022) can provide relevant insights for policy-makers. To assess policy success, this work uses a new agent-based model (ABM) constructed

specifically to investigate the adoption of small-scale PV by households in Great Britain (feed-in tariffs are not available in Northern Ireland and thus do not cover all of the UK). While this model focuses on the effect of FiTs, it also includes other economic factors and the effect of a social network on adoption decisions.

## Background

Great Britain's FiT scheme was set out in the 2008 Energy Act and took effect from April 2010, supporting electricity generation from renewable technologies including PV [3]. The FiT scheme is intended for installations under 5 MW.

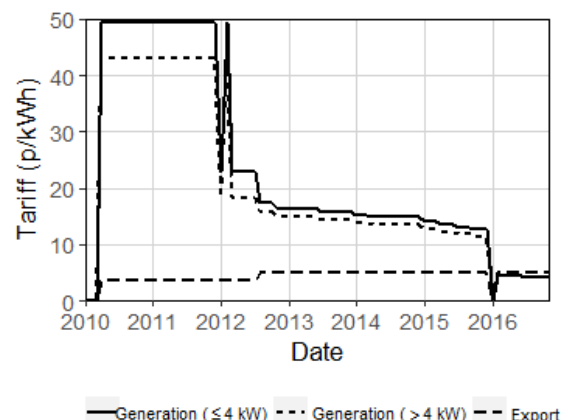


Figure 1. Generation and export tariff levels (on a monthly basis) for small scale PV installations ( $\leq 10$  kW). These are the 2016 levels of the FiT, adjusted for the April 2016 RPI. Data from [4].

The scheme operates by requiring electricity suppliers to pay owners of registered renewable energy installations for the total electricity produced (the generation tariff) and the electricity exported to the grid (the export tariff). Most generators under 30 kW capacity do not have an export meter installed so their electricity exports are deemed to be half of the total production [5,6]. The model assumes this "deemed export" for all installations, since it focuses exclusively on  $\leq 10$  kW systems. Feed-in tariffs (specifically the generation tariff) have varied significantly since the introduction of the scheme in 2010, as shown in Figure 1.

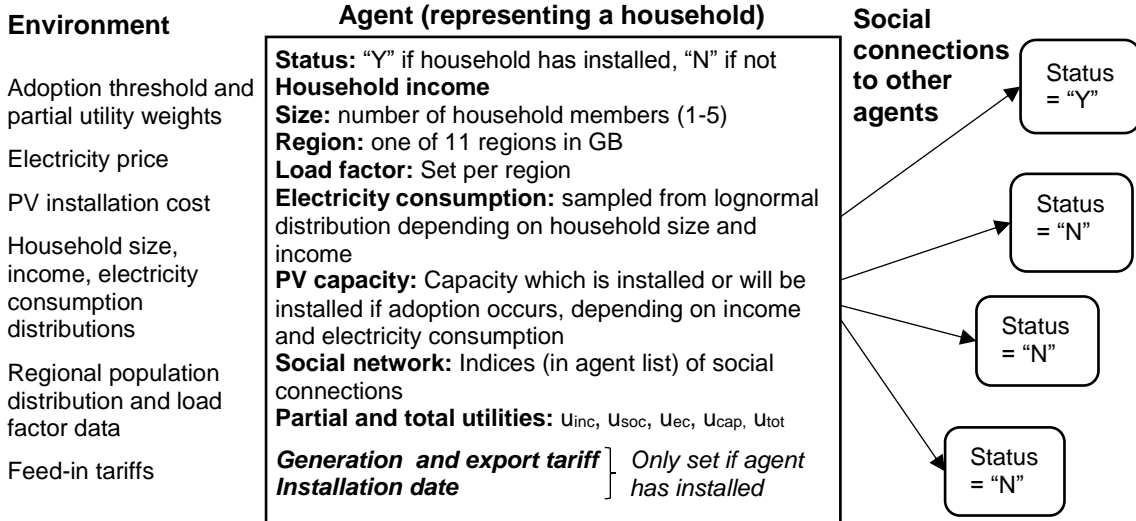


Figure 2. A schematic showing the key parts of the ABM: an individual agent representing a household, and its environment, which includes social links to other agents.

Following a consultation on the FiT scheme in 2015 [7], the scheme was paused from 15 January to 8 February 2016, after which FiTs for smaller-scale installations were reduced. The scheme now includes deployment caps which limit the amount installed under each tariff level and the total capacity which can receive FiT incentives [8,9]. The aim of the deployment caps is to keep the additional cost of supporting new systems installed between 2016 and 2019 below £100 million/year [10]. For every quarter, a feed-in tariff and deployment cap are set [8,9]. If the deployment cap is reached before the end of the quarter, this triggers degression, which is a reduction in the FiT to the next lowest tariff. Excess capacity is carried forward. Even if the cap is not reached, the FiT will reduce at the start of the next quarter. Deployment caps and FiTs are currently set until 31 March 2019, although the total available capacity (700 MW) may run out before this date.

The majority of small-scale ( $\leq 10$  kW) PV systems are supported by the FiT scheme, and most installations under 10 kW are domestically-owned, meaning household adoption of PV under the FiT scheme is the most relevant category to investigate for predicting small-scale PV installation in Great Britain.

The market for rooftop solar PV in the UK is currently dominated by mature technologies, predominantly crystalline silicon [11]. The model does not differentiate between different PV technologies, assuming one average installation cost per kW of peak power installed, and the same load factor for all installations in the same region. The total system cost of a

small-scale PV system has fallen from around £5000/kW to £1600/kW since 2010.

### Model specification

The model aims are to predict adoption decisions (if, when, and how much PV is installed) and translate the information on individual adoptions into cumulative installed capacity and production data, while tracking associated subsidy and capital costs. The model assigns realistic agent and environment characteristics relevant to decision-making, implements a decision-making strategy, and scales the results to the GB population. In order to provide useful projections and alternative historical outcomes, the model was calibrated to observed PV deployment in the period 2010–2016. The model was implemented in the R language using RStudio [12], an integrated development environment (IDE) for R. The basic modelling elements are the agents, which in this model represent individual households. The model generates a population of agents of the desired size (populations of 5000 agents were used to generate the results presented here), assigning each agent relevant and realistic characteristics as summarised in Figure 2. The overall dynamics of the system emerge from the decisions made by individual agents; the model population size is scaled to the number of households occupying properties they own ("owner-occupiers") in Great Britain (around 17 million).

The decision strategy used by agents is a "utility function" made up of four components which influence the adoption decision, similar to previous work in the field [13–15]. The four partial utilities, and the factors which determine them are:

1.  $u_{inc}$ : Household income
2.  $u_{ec}$ : Economic attractiveness of the investment, based on the simple payback period
3.  $u_{soc}$ : Social environment, based on how many adopters an agent is linked to
4.  $u_{cap}$ : Capital cost barrier, based on household income and the capital cost of installing a PV system.

Each of these partial utilities 1-4 is described by a linear or logistic function relating the characteristics relevant to the partial utility to a number in the range [0, 1]. The weighted sum of these partial utilities is compared to some threshold  $t$ ; an agent (household)  $k$  will adopt if

$$W_{inc}U_{inc,k} + W_{ec}U_{ec,k} + W_{soc}U_{soc,k} + W_{cap}U_{cap,k} \geq t$$

Where the  $w$  are partial utility weights. The partial utility weights and threshold are set globally and were calibrated so the model output matched observed installation when FiTs, electricity and PV costs, etc. in the model were set according to real values over the period 2010-2016. The results of this calibration are shown in Figure 3.

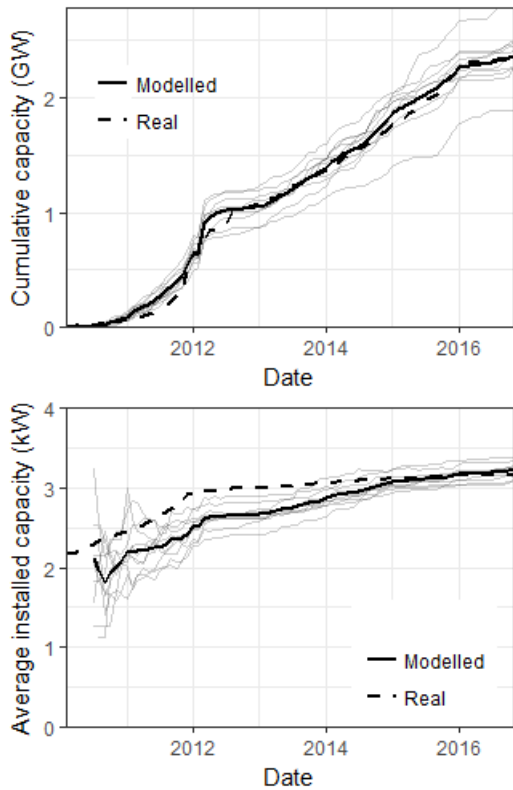


Figure 3. Real PV capacity data [1] and the output of the calibrated model run. The thin grey lines show the ten individual model runs, each using a unique population of 5000 agents; the model result is the average of these individual runs. Top: cumulative installed capacity. Bottom: average installation capacity (cumulative capacity divided by number of adopters).

Because agent characteristics are assigned according to probability distributions, the agent population and thus modelling outcome will vary with each run; to generate results, the model was run 10 times for each scenario investigated, using the mean outcomes as the final results.

## Results

### Historical simulations (2010-2016)

To compare real FiT policy in the period 2010-2016 to alternative scenarios utilising various degression strategies for reducing the generation tariff gradually, a large number of alternative scenarios were modelled. The modelled cumulative capacity by October 2016 varying with total expected subsidy cost based on expected electricity production for these alternative scenarios is shown in Figure 4. This shows that there are a number of scenarios using any of the alternative degression strategies which are predicted to have a better outcome than the realistic (calibration) scenario. The main issue with FiT policy was that initially, there was no mechanism in place for reducing tariffs, which led to rapid cost escalation in late 2011 and early 2012. Alternative scenarios with lower initial feed-in tariffs and/or pre-planned tariff reduction strategies avoid this cost escalation.

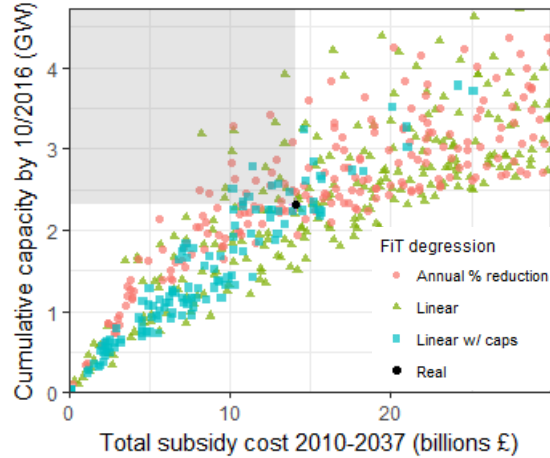


Figure 4. Total expected subsidy cost and cumulative installed capacity by the end of the simulation period (October 2016). The shaded area covers scenarios which achieve more installation at a lower cost.

### Projections (2016-2022)

The results for projections under four different viable policy scenarios are shown in Figure 5. These scenarios are a) no subsidy from October 2016 onwards; b) deployment cap policy as currently in place; c) an extension of the announced policy; or d) linear degression of the generation tariff without deployment caps.

Figure 5 compares total installed capacity and total expected subsidy cost under these policy scenarios as well their dependence on various trends for the price of electricity and PV installation. Clearly, the rate at which total PV system cost reduces is of critical importance to predicting the installation rate. Figure 5 also shows that with the exception of the significantly more expensive policy without deployment caps in place, the continued existence of the FiT scheme has little effect on how much capacity will be installed by January 2022.

## Conclusions

It is possible to construct an ABM which, using demographic data to generate agent populations and simulating agent decision-making based on four factors, can be calibrated to replicate the observed installation patterns of small PV systems well. Using this model to investigate both historical and future policy shows that using a reasonable degression strategy, it would have been possible to achieve a higher installed capacity by 2016 at a lower expected subsidy cost. Using the model to project future installed capacity shows the current FiTs are so low that they have little effect in encouraging adoption, with PV cost reduction being a far more important driver.

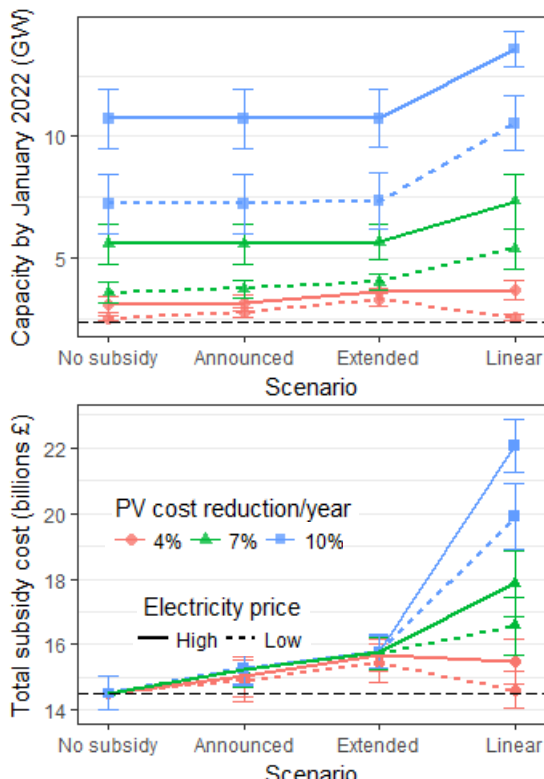


Figure 5. Top: modelled capacity installed by January 2022 under the four different future policy scenarios. Bottom: expected total subsidy (2010-2042) cost of these scenarios. The error bars show the standard deviation of the 10 individual model runs each using a unique agent population.

The full model code is available at [github.com/phoebe-p/FiTABM](https://github.com/phoebe-p/FiTABM).

## References

- [1] Ofgem. Feed-in Tariff Installation Report 30 September 2016 2016. <https://www.ofgem.gov.uk/publications-and-updates/feed-tariff-installation-report-30-september-2016> (accessed November 1, 2016).
- [2] Department for Business Energy & Industrial Strategy. Solar photovoltaics deployment. Feed Tarif Stat 2016. <https://www.gov.uk/government/statistics/solar-photovoltaics-deployment> (accessed January 4, 2016).
- [3] Parliament of the United Kingdom. Energy Act 2008. 2008.
- [4] Ofgem. Feed-in Tariff Generation & Export Payment Rate Table for Photovoltaic Installations - FIT Year 7 (2016/17) 2016. [https://www.ofgem.gov.uk/system/files/docs/2016/04/version\\_2\\_-feed-in\\_tariff\\_scheme\\_tariff\\_table\\_1\\_april\\_2016\\_-31\\_march\\_2017\\_pv\\_only.pdf](https://www.ofgem.gov.uk/system/files/docs/2016/04/version_2_-feed-in_tariff_scheme_tariff_table_1_april_2016_-31_march_2017_pv_only.pdf) (accessed July 8, 2016).
- [5] Energy Saving Trust. Measuring the electricity you export n.d. <http://www.energysavingtrust.org.uk/sites/default/files/reports/Measuring the electricity you export.pdf> (accessed July 19, 2016).
- [6] Department of Energy & Climate Change. Annex B : Electricity use in households with solar PV. 2015.
- [7] Department of Energy & Climate Change. Consultation on a review of the Feed-in Tariffs scheme 2015.
- [8] Ofgem. Feed-in Tariff Deployment Caps Quarterly report for Tariff Period 02 Deployment. 2016.
- [9] Ofgem. Feed-in Tariff Deployment Caps Monthly report for February 2016. 2016.
- [10] Department of Energy & Climate Change. Review of the Feed-in Tariffs Scheme: Government response. 2015.
- [11] Department of Energy & Climate Change. UK Solar PV Strategy Part 1: Roadmap to a Brighter Future. 2013.
- [12] RStudio Team. RStudio: Integrated Development for R 2015.
- [13] Iachini V, Borghesi A, Milano M. Agent Based Simulation of Incentive Mechanisms on Photovoltaic Adoption, 2015, p. 136–48. doi:10.1007/978-3-319-24309-2\_11.
- [14] Palmer J, Sorda G, Madlener R. Modeling the diffusion of residential photovoltaic systems in Italy: An agent-based simulation. Technol Forecast Soc Change 2015;99:106–31. doi:10.1016/j.techfore.2015.06.011.
- [15] Zhao J, Mazhari E, Celik N, Son Y-J. Hybrid agent-based simulation for policy evaluation of solar power generation systems. Simul Model Pract Theory 2011;19:2189–205. doi:10.1016/j.simpat.2011.07.005.

# Development of ZnO/CdS/CdTe core-shell nanorod-based solar cells with an extremely thin absorber

G. Kartopu<sup>1,\*</sup>, S. Yerci<sup>2</sup>, H.E. Ünalancı<sup>2</sup>, V. Barrioz<sup>3</sup>, P. Aurang<sup>2</sup>, W. Hadibrata<sup>2</sup>, Y. Qu<sup>3</sup>, C. Özcan<sup>2</sup>, L. Bowen<sup>4</sup>, A.K. Gürlek<sup>1</sup>, P. Maiello<sup>3</sup>, R. Turan<sup>2</sup>, and S.J.C. Irvine<sup>1</sup>

<sup>1</sup> Centre for Solar Energy Research, College of Engineering, Swansea University, OpTIC Centre, St. Asaph Business Park, LL17 0JD, UK

<sup>2</sup> Centre for Solar Energy Research and Applications (GÜNAM), Middle East Technical University, 06800 Ankara, Turkey

<sup>3</sup> Department of Physics and Electrical Engineering, Ellison Building, Northumbria University, Newcastle upon Tyne NE1 8ST, UK

<sup>4</sup> G.J. Russell Microscopy Facility, Durham University, South Road, Durham DH1 3LE, UK

\* Corresponding Author [giray.kartopu@swansea.ac.uk](mailto:giray.kartopu@swansea.ac.uk)

## I. Introduction

Electrically conducting ZnO nanorod (NR) arrays would form an interesting front contact for superstrate inorganic (e.g. CdTe) solar cells with an extremely-thin-absorber (eta). A combination of the improved areal density of the semiconductor junction (due to the large surface area of the NR array available for deposition) and also the light trapping effects observable in such nanostructures [1] are expected to improve the photocurrent and spectral response. However, a survey of the related literature on solar cells involving NR arrays suggests this is not straightforward to realise. In practice, there seems to be many technical issues related to material properties and deposition uniformity, resulting in poor and even non-functional one-dimensional PV structures. Major *et al.* recently reported on the deposition of a CdTe solar cell structure on ZnO NR array films [2]. The ZnO NR film served as a highly resistive buffer layer as it was found that core-shell structure was not achieved via the deposition method used.

We carried out a study into the effects of using a ZnO NR scaffold on the growth and performance of CdS/CdTe solar cells, deposited by MOCVD. A ZnO/CdS/CdTe core-shell NR based device structure, modelled using the finite-difference time-domain (FDTD) method for light-trapping prediction, was fabricated using hydrothermal and MOCVD methods for the deposition of ZnO and CdS/CdTe, respectively. Thin film properties and device performance are reported for nanorod based eta-CdTe cells.

## II. Experimental Details

ZnO NRs aligned perpendicularly to the substrate were synthesized via a hydrothermal method [3]. First, a 9-10 nm thick ZnO film serving as the self-catalytic seed layer for the ZnO NR growth was deposited by radio-frequency magnetron sputtering onto a commercial indium tin oxide (ITO)/boro-aluminosilicate glass. The seed layer coated substrate was then dipped into the hydrothermal solution for 45 - 180 min, giving ZnO NRs of 0.5 - 1.4  $\mu\text{m}$  length. A conventional (horizontal, atmospheric pressure) MOCVD reactor was used to deposit CdS/CdTe layers as well as to perform CdCl<sub>2</sub> activation treatment for the devices [4]. The cells were typically dot contact type with a diameter of 1 mm (0.8  $\text{mm}^2$  area), but larger ones with 5 mm  $\times$  5 mm (0.25  $\text{cm}^2$  area) dimensions were also used for spectral response measurements. The simulations of the structures were performed using a commercially available FDTD simulation tool, LUMERICAL™. The calculation of absorption for CdTe/CdS/ZnO rods was performed on 2D slices of a 3D structure with square mesh of 2 nm.

AM1.5 J-V curves were collected using an Abet Technologies Ltd. solar simulator with the light power density calibrated using a GaAs reference cell. The external quantum efficiency (*EQE*) measurements were carried out using a Bentham spectral response system under unbiased conditions. The system response was corrected by scanning the output of a c-Si reference detector.

### III. Results

From SEM images the near-perpendicular orientation of the NRs on the growth substrate was confirmed, as per Ref. 2. The mean rod diameter for a NR length of 0.75  $\mu\text{m}$  was determined to be ~50 nm. After the growth of ZnO NRs the sheet resistance of on the ITO/glass increased from ~8 to 20  $\Omega/\text{sq}$ . while the carrier density decreased from  $1.2 \times 10^{21}$  to  $1.3 \times 10^{20} \text{ cm}^{-3}$  and the electron mobility slightly increased from 41 to 44  $\text{cm}^2 \text{ V}^{-1} \text{ s}^{-1}$ .

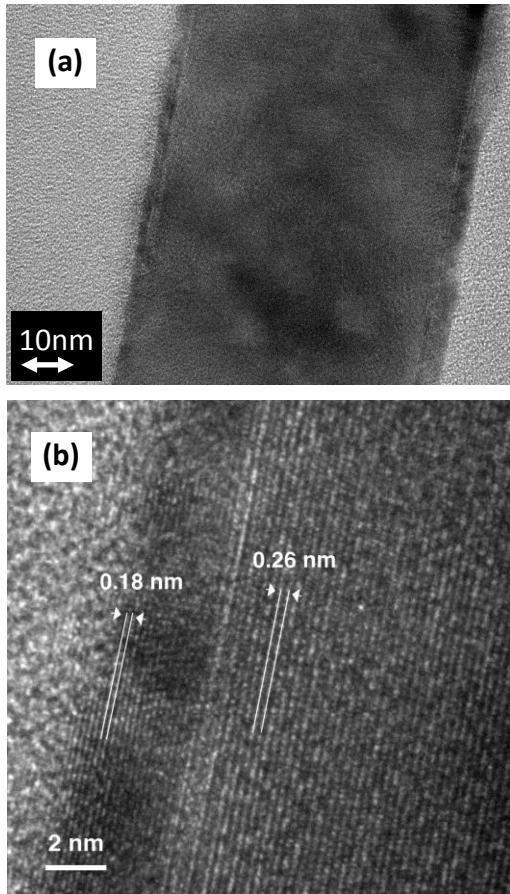


Fig 1 (a) TEM image of a single CdS/ZnO nanorod, (b) HRTEM view of the CdS/ZnO interface.

The transition in the total (direct and scattered) and scattered light transmittance of the ITO/glass substrate upon the sequential deposition ZnO NRs and ZnO/CdS core-shell NRs were measured and modelled. Fig. 2 shows the haze results, where a good agreement can be seen between experimental and simulated results. Compared to pristine ITO/glass substrate, the growth of ZnO

NRs shifted the high energy absorption edge towards the ZnO band edge (~370 nm) and induced significant haze in the visible range (Fig. 2a), giving the samples a milky appearance. For the 0.5  $\mu\text{m}$  ZnO NRs, the total transmittance remained as high as that of starting substrate (not shown). When the NR length is increased to 1.4  $\mu\text{m}$ , the intensity of the scattered light increased significantly. The absorption onset shifted to the CdS bandgap (~520 nm) and both the intensity and width of the scattering component increased on the growth of CdS shells on ZnO NRs (Fig. 2b). The strong scattering observed is a desirable effect for a thin solar absorber to be deposited onto the ZnO NR array in order to increase the absorber performance.

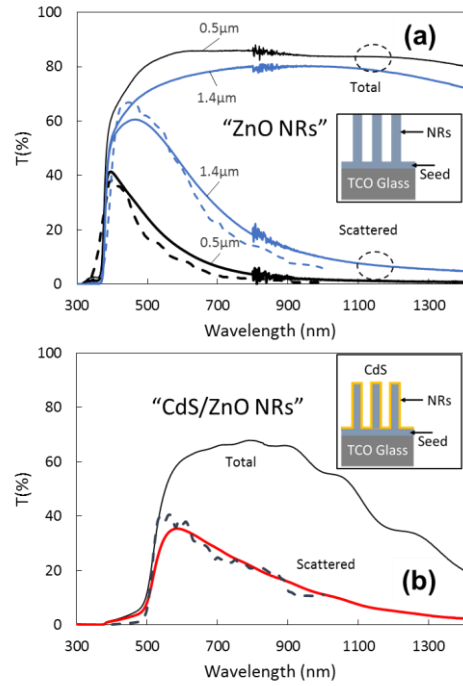


Fig 2 Total transmittance and scattered light due to ZnO NRs (a) and ZnO/CdS core-shell NRs (with ~20 nm CdS shell) (b). Dashed lines are the model results for the corresponding haze data.

The amount of light absorbed in each material was also calculated which indicate that 30 nm thick CdTe film deposited on ZnO NR array absorbs more light when compared to planar CdTe film with a thickness of 50 nm (not shown). Additionally, 50 nm thick CdTe deposited on NR array produces over twice more

photocurrent when compared to the one deposited on planar structure.

Cross-sectional EDS maps of the key elements in CdTe/CdS/ZnO and CdTe/ZnO solar cell structures are shown in Fig. 3a and 3b, respectively. The device structure with CdS window showed superior J-V response (Fig. 3c).

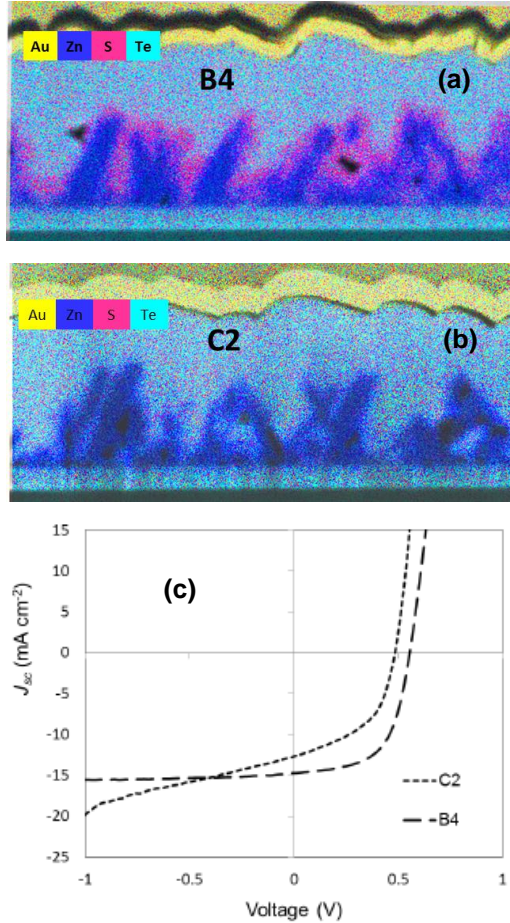


Fig 3 EDS maps of (a) CdTe/CdS/ZnO and (b) CdTe/ZnO nanorod devices, with corresponding light J-V curves (c). In both cases, ZnO nanorods are buried inside the CdTe absorber and the back contact layer is evaporated gold.

The device performance of the best nanostructured solar cell is given in Fig. 4. In agreement with the simulations the blue part of the spectrum is strongly absorbed by CdS layer and caused  $J_{sc}$  losses in case of ZnO NR array. Additionally, the planar device had a much thinner CdS layer, resulting in enhanced transmittance and improved spectral response. Volume thickness of the CdTe absorber deposited on the NRs and planar substrate was

determined to be about 400 and 550 nm, respectively. This corroborates to the poorer red response with the NR-device.

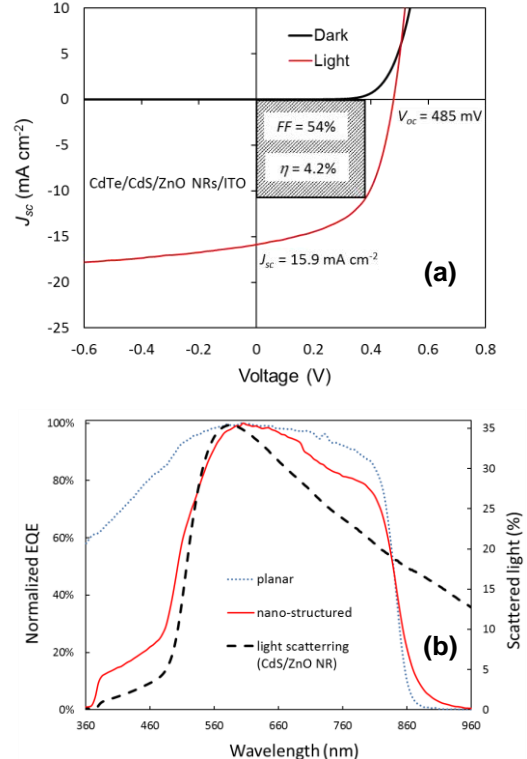


Fig 4 (a) J-V curves, (b) spectral response (EQE) of the best CdTe/CdS/ZnO nanorod based solar cell. In (b) EQE spectrum of the planar device, grown alongside the nanorod cell, as well as light scattering due to a CdS/ZnO nanorod array are also shown for comparison.

#### IV. Discussion

As can be seen from Fig. 3a and 3b, deposition uniformity of CdS on ZnO NRs was not very high. Therefore, to enable the development of larger area devices, the deposition uniformity needs to be improved. This may be achieved using a suitable surface preparation method, such as mild plasma treatment or atomic layer deposition of an ultrathin buffer oxide film.

The NR-based cells showed an improved collection in the near infrared, 830–930 nm (e.g. Fig. 4b). When compared to the light scattering from a ZnO/CdS NR array (dashed line, Fig. 4b) it can be understood that this gain is due to light trapping, a prominent feature of the one-dimensional nanostructures.

## V. Conclusions

The light trapping, emanating from the scattering due to underlying ZnO/CdS NR array structure, was observed to contribute to the better spectral response of the nanostructured solar cells in the near infrared range (830–930 nm). 4% best cell efficiency was obtained using CdTe/CdS/ZnO NRs.

Overall, these results show that the inorganic thin film coated ZnO NR solar cell structures with engineered optical properties has good prospects in the improvement of extremely thin absorber (eta) solar cells.

## Acknowledgements

Funding provided by TÜBITAK - British Council through the bilateral project DETACELL (Grant no. 115F518) is gratefully acknowledged.

## References

- [1] M.D. Kelzenberg, S.W. Boettcher, J.A. Petykiewicz, D.B. Turner-Evans, M.C. Putnam, E.L. Warren, J.M. Spurgeon, R.M. Briggs, N.S. Lewis, H.A. Atwater, "Enhanced absorption and carrier collection in Si wire arrays for photovoltaic applications", *Nat. Mater.* 9 (2010) 239-244.
- [2] J.D. Major, R. Tena-Zaera, E. Azaceta, L. Bowen, K. Durose, "Development of ZnO nanowire based CdTe thin film solar cells", *Sol. Ener. Mat. & Sol. Cells* 160 (2017) 107–115.
- [3] M.C. Akgun, Y.E. Kalay, H.E. Unalan, "Hydrothermal zinc oxide nanowire growth using zinc acetate dihydrate salt", *J. Mater. Res.* 27 (2012) 1445-1451.
- [4] G. Kartopu, A.J. Clayton, W.S.M. Brooks, S.D. Hodgson, V. Barrioz, A. Maertens, D.A. Lamb, S.J.C. Irvine, "Effect of window layer composition in  $Cd_{1-x}Zn_xS/CdTe$  solar cells", *Prog. Photovolt: Res. Appl.* 22 (2014) 18-23.

# Enhanced Stability in CsSnI<sub>3</sub> Perovskite Photovoltaics

K. P. Marshall<sup>1</sup>, M. Walker<sup>2</sup>, R. I. Walton<sup>1</sup>, and R. A. Hatton<sup>1\*</sup>

<sup>1</sup>Department of Chemistry, University of Warwick, CV4 7AL, UK.

<sup>2</sup>Department of Physics, University of Warwick, CV4 7AL UK.

\* Corresponding Author, email: Ross.Hatton@warwick.ac.uk

## Abstract

The 3-dimensional orthorhombic perovskite B- $\gamma$  CsSnI<sub>3</sub> offers near ideal optoelectronic properties for a single junction photovoltaic (PV) device, including a direct band gap of ~ 1.3 eV, high charge carrier mobilities and a very small exciton binding energy. However, Sn perovskite PVs, including those based on B- $\gamma$  CsSnI<sub>3</sub>, have not benefitted from the same intensity of development that has propelled lead perovskite PVs to a power conversion efficiency of >22%, due to the ease with which Sn vacancy defects form during synthesis (which limits device fill-factor) and the susceptibility of Sn perovskites to oxidation in air. Herein we provide comment on, and further analysis of, our recent work pertaining to the performance of CsSnI<sub>3</sub> based perovskite PV devices [*Nature Energy* 1, 16178 (2016)], with particular emphasis on the findings of the device stability tests, which provide compelling motivation for the advancement of this class of lead-free perovskite PV.

## Introduction

Sn halide perovskites are attractive as an alternative to their lead analogues for PV applications because they offer narrower band gaps, closer to the optimal for a single junction PV, and do not include the toxic element Pb.[1] The latter is a particular concern because some of the decomposition products of lead halide perovskites, that form upon exposure to ambient air and moisture, are water soluble lead compounds.[2,3] Consequently, failure of the PV module encapsulant or improper disposal at the end of life risks contamination of the environment with a heavy metal well known to have adverse effects on human health when present in water at low levels.[2] Whilst there is currently debate as to the true magnitude of this risk, it is clear that lead-free alternatives would be preferable particularly for a large

area, widely distributed application such as PVs.[1] The environmental risks associated with the degradation of Sn perovskites have not yet been comprehensively investigated [2,3], although the evidence to date indicates that the toxicity of Sn halide perovskites stems from the evolution of strong acid upon decomposition in air, rather than the toxicity of the Sn decomposition products themselves.[2]

Reports relating to the use of Sn halide perovskites as the light harvester in PVs are relatively sparse [1] and have focused on using CH<sub>3</sub>NH<sub>3</sub>SnI<sub>3-x</sub>Br<sub>x</sub> (where x = 0 to 3), CsSnI<sub>3-x</sub>Br<sub>x</sub> (where x = 0 to 3) and HC(NH<sub>2</sub>)<sub>2</sub>SnI<sub>3-x</sub>Br<sub>x</sub>. Encouragingly the potential to achieve high short circuit current density ( $J_{sc}$ ) - which follows from the narrow band gap - has been demonstrated [4]. Device fill-factor ( $FF$ ) has also been progressively improved by reducing the background carrier density, of which Sn vacancy defects are the primary source.[4,5] The Sn vacancy concentration is most easily minimised by synthesising the Sn perovskite under Sn-rich conditions using an additive such as SnI<sub>2</sub>,[5] SnF<sub>2</sub> [4,6] or SnCl<sub>2</sub> [7]. We have identified SnCl<sub>2</sub> as being particularly effective for improving the  $FF$  in CsSnI<sub>3</sub> based inverted architecture PVs.[7] What is special about SnCl<sub>2</sub>, as compared to the other Sn halide additives, is that Cl<sup>-</sup> is not incorporated into the perovskite lattice and so the surface of the CsSnI<sub>3</sub> crystallites is decorated with SnCl<sub>2</sub>. We have shown that, in the context of inverted PV devices using PC<sub>61</sub>BM as the electron transport layer, the SnCl<sub>2</sub> at the surface of the CsSnI<sub>3</sub> film diffuses into the adjacent PC<sub>61</sub>BM layer where it serves as an n-type dopant improving device  $FF$  and reducing the adverse effect of pin-holes in the CsSnI<sub>3</sub> film. Remarkably a  $FF$  of ~0.7 has been achieved in using a fullerene electron transport layer *without* the need for a hole-blocking layer or any special procedure to minimise pin-holes in the CsSnI<sub>3</sub> film.[7]

In practice the gradual ingress of oxygen and moisture into PV devices is inevitable, and so a central challenge is to develop strategies that can be used in conjunction with device encapsulation to reduce the rate of oxidation of Sn perovskite enough for applications. To date there have been remarkably few reports relating to the stability of Sn perovskites [1]: Kumar *et al.*[4] have reported that devices based on  $\text{CsSnI}_3$  between  $\text{TiO}_2$  and triphenylamine charge transport layers ( $FF \sim 0.3$ ) are stable when stored under nitrogen, although the stability in air and/or under continuous illumination was not reported. Hao *et al.*[8] have shown that after 24 hours storage in nitrogen the power conversion efficiency of devices based on  $\text{CH}_3\text{NH}_3\text{SnI}_3$  perovskite using  $\text{TiO}_2$  and spiro-OMeTAD charge extraction layers ( $FF \sim 0.48$ ) was reduced by 64%, even with encapsulation. Similarly, Noel *et al.*[9] reported that PPVs devices based on  $\text{CH}_3\text{NH}_3\text{SnI}_3$  with the same architecture ( $FF \sim 0.5$ ) degraded within minutes when tested under ambient conditions. Zhang *et al.*[10] have also reported that unencapsulated PV devices based on  $\text{HC}(\text{NH}_2)_2\text{SnI}_2\text{Br}$  perovskite using PEDOT:PSS and  $\text{PC}_{61}\text{BM}$  charge extraction layers failed within minutes of exposure to air.

Herein we highlight, and provide further analysis and comment on, the results of our recent stability tests on PV devices based on a simple  $\text{CsSnI}_3$  perovskite / fullerene bilayer architecture [*Nature Energy* 1, 16178 (2016)] which show that Sn perovskites may yet prove sufficiently stable for applications.

## Results and Discussion

The device architecture used for the stability studies was: ITO glass /  $\text{CsSnI}_3$  (50 nm) /  $\text{PC}_{61}\text{BM}$  (60 nm) : bathocuproine (6 nm) : Al. Notably, this structure does not include a hole-extracting / electron blocking layer at the interface between the ITO electrode and  $\text{CsSnI}_3$  layer. This simplified architecture does not compromise device power conversion efficiency because the fullerene electron transport layer is *n*-doped by the  $\text{SnCl}_2$  additive at the surface of the  $\text{CsSnI}_3$  film, forming a Schottky barrier to (unwanted) electron extraction by the ITO electrode at the site of pinholes in the perovskite film.[7] Importantly, in addition to simplifying the fabrication process, this architecture simplifies the interpretation of device stability tests data by reducing the

number of possible device degradation pathways.

The stability data shown in Figure 1 is for 6 mm<sup>2</sup> devices without encapsulation tested under continuous one sun simulated solar illumination in ambient air (humidity 25-30%).

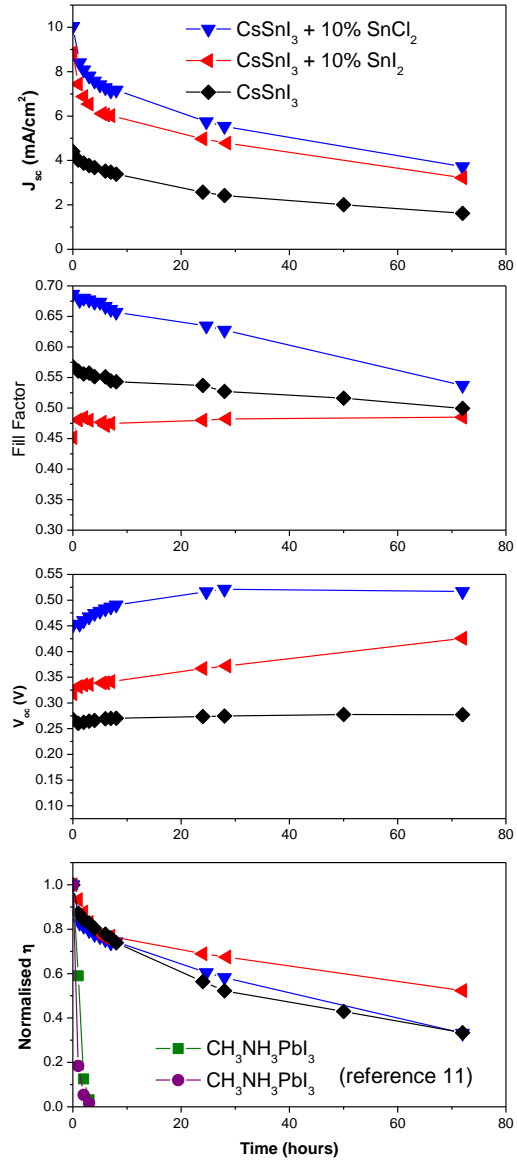


**Figure 1:** Evolution of current-voltage characteristics for representative unencapsulated devices tested in air under continuous 1 sun simulated illumination. The devices have the structure: ITO glass /  $\text{CsSnI}_3 + X$  /  $\text{PC}_{61}\text{BM}$  / BCP / Al, where  $X = 10 \text{ mol\% SnCl}_2$  (blue),  $10 \text{ mol\% SnI}_2$  (red) or no additive (black). The humidity was 25-30% and the temperature under the lamp stabilised at  $\sim 50^\circ\text{C}$  after 45 minutes.

The stability of these devices is exceptional for unencapsulated Sn perovskite PVs tested in ambient air [1], and is an order of magnitude better than that achieved using the archetypal lead halide perovskite;  $\text{CH}_3\text{NH}_3\text{PbI}_3$ , in place of  $\text{CsSnI}_3$  for devices with identical structure tested under identical conditions.[7,11] When using  $\text{SnCl}_2$  as the additive the power conversion efficiency of the average device reduced to 70% of its starting value only after  $\sim 7$  hours, with the best performing devices taking 11 hours with no additive, 16 hours with 10 mol%  $\text{SnCl}_2$ , and 22 hours using  $\text{SnI}_2$  as the additive.

It is evident from Figure 1 that, in all cases, the primary reason for device degradation is a continuous decline in  $J_{sc}$ , similar to that previously exhibited by  $\text{CsSnI}_3$  PV devices using copper iodide as the hole extraction layer and  $\text{SnI}_2$  as the halide additive.[5] Whilst the origin of the continuous degradation in  $J_{sc}$  is almost certainly multi-faceted, it is interesting to note that it does not correlate with a large deterioration in device  $FF$ . (Notably the more rapid decline in  $FF$  for the device using  $\text{SnCl}_2$  after 30 hours is only observed in  $\sim 50\%$  of devices, with the remaining exhibiting an evolution of  $FF$  comparable to that shown for the case of  $\text{SnI}_2$  additive [7].) This observation is consistent with the fact that  $\text{B}-\gamma\text{-CsSnI}_3$  degrades into the one-dimensional yellow form;  $\text{Y}-\text{CsSnI}_3$ , upon exposure to moisture, and then into the zero-dimensional  $\text{Sn(IV)}$  salt  $\text{Cs}_2\text{SnI}_6$  with exposure to oxygen.[7,12,13] Like  $\text{CsSnI}_3$ ,  $\text{Cs}_2\text{SnI}_6$  is a narrow band gap semiconductor with a high electron and hole mobility.[13,14] However, the conduction band edge of  $\text{Cs}_2\text{SnI}_6$  is  $\sim 0.2$  eV below that of  $\text{CsSnI}_3$  [14] and  $\text{Cs}_2\text{SnI}_6$  is a much weaker absorber of visible light. [7,14] Consequently, the inevitable ingress of air and moisture into the device results in the formation of  $\text{Cs}_2\text{SnI}_6$  at the interface between the  $\text{PC}_{61}\text{BM}$  layer and the remaining  $\text{CsSnI}_3$  that does not dramatically impede electron extraction, although does erode light absorption due to its lower absorption coefficient. Evidence to support this hypothesis is provided by our earlier report on the performance of  $\text{CsSnI}_3$  based PVs [5] in which we show that exposure of the  $\text{CsSnI}_3$  layer to ambient air for 1 minute immediately prior to the deposition of the  $\text{PC}_{61}\text{BM}$  layer results in the formation of a  $\text{Cs}_2\text{SnI}_6$  at the  $\text{CsSnI}_3$  surface, the primary effect of which is to

degrade  $J_{sc}$ , with relatively small degradation of device  $FF$ .

It is also evident from Figure 1 that the stability of devices with and without Sn halide additive is comparable. Since one of the roles of the Sn halide additive is to suppress the formation of Sn vacancy defects[4-7], the comparable device stability is evidence that the decline in  $J_{sc}$  observed over 70 hour continuous illumination in air is not strongly related to the Sn vacancy density in the  $\text{CsSnI}_3$  film. Using a Sn halide additive does however offer the advantage of improved power conversion efficiency and reduced sensitivity of device parameters to pin-holes.[7]

## Conclusion

In summary we have recently shown that PV devices with a simplified inverted architecture offer remarkable stability under continuous illumination that far exceeds that previously reported for Sn perovskite PVs, and devices with the same architecture using widely used methylammonium lead iodide perovskite – the work horse of perovskite PV research to date. The discussion and further analysis of the lifetime data provided herein, highlights the significance of these findings and provides further insight into the extent to which Sn vacancy defects in the  $\text{CsSnI}_3$  film determine device degradation over the first 70 hours under continuous illumination in air, insights that it is hoped will help to stimulate interest in advancing this promising class of lead-free perovskite PV.

## References

1. Yang, S., Fu, W., Zhang, Z., et al. (2017) Recent Advances in Perovskite Solar Cells: Efficiency, Stability and Lead-free Perovskite. *J. Mater. Chem. A*, DOI: 10.1039/C7TA00366H.
2. Babayigit, A., Ethirajan, A., Muller, M., and Conings, B. (2016) Toxicity of organometal halide perovskite solar cells. *Nat. Mater.*, **15** (3), 247–251.
3. Babayigit, A., Duy Thanh, D., Ethirajan, A., et al. (2016) Assessing the toxicity of Pb- and

- Sn-based perovskite solar cells in model organism *Danio rerio*. *Sci. Rep.*, **6**, 18721.
4. Kumar, M.H., Dharani, S., Leong, W.L., et al. (2014) Lead-Free Halide Perovskite Solar Cells with High Photocurrents Realized Through Vacancy Modulation. *Adv. Mater.*, **26**, 7122–7127.
  5. Marshall, K.P., Walton, R.I., and Hatton, R.A. (2015) Tin Perovskite / Fullerene Planar Layer Photovoltaics: Improving the Efficiency and Stability of Lead-Free Devices. *J. Mater. Chem. A*, **3**, 11631–11640.
  6. Chung, I., Lee, B., He, J., et al. (2012) All-solid-state dye-sensitized solar cells with high efficiency. *Nature*, **485** (7399), 486–489.
  7. Marshall, K.P., Walker, M., Walton, R.I., and Hatton, R.A. (2016) Enhanced stability and efficiency in hole-transport-layer-free CsSnI<sub>3</sub> perovskite photovoltaics. *Nat. Energy*, **1** (November), 16178.
  8. Hao, F., Stoumpos, C.C., Cao, D.H., et al. (2014) Lead-free solid-state organic–inorganic halide perovskite solar cells. *Nat. Photonics*, **8** (6), 489–494.
  9. Noel, N.K., Stranks, S.D., Abate, A., et al. (2014) Lead-Free Organic-Inorganic Tin Halide Perovskites for Photovoltaic Applications. *Energy Environ. Sci.*, **7**, 3061–3068.
  10. Zhang, M., Lyu, M., Yun, J.-H., et al. (2016) Low-temperature processed solar cells with formamidinium tin halide perovskite/fullerene heterojunctions. *Nano Res.*, **9**, 1570–1577.
  11. Zhang, Y. et al. (2016) Flexible, hole transporting layer-free and stable CH<sub>3</sub>NH<sub>3</sub>PbI<sub>3</sub>/ PC61BM planar heterojunction perovskite solar cells. *Org. Electron.* **30**, 281–288.
  12. Stoumpos, C.C., Malliakas, C.D., and Kanatzidis, M.G. (2013) Semiconducting tin and lead iodide perovskites with organic cations: phase transitions, high mobilities, and near-infrared photoluminescent properties. *Inorg. Chem.*, **52** (15), 9019–9038.
  13. Lee, B., Stoumpos, C.C., Zhou, N., et al. (2014) Air-Stable Molecular Semiconducting Iodosalts for Solar Cell Applications: Cs<sub>2</sub>SnI<sub>6</sub> as a Hole Conductor. *J. Am. Chem. Soc.*, **136**, 15379–15385.
  14. Zhang, J., Yu, C., Wang, L., et al. (2014) Energy barrier at the N719-dye/CsSnI<sub>3</sub> interface for photogenerated holes in dye-sensitized solar cells. *Sci. Rep.*, **4**, 6954.

# MOCVD of SnS with large grains and stoichiometry control for thin film photovoltaics

Andrew J. Clayton<sup>\*1</sup>, Stuart J. C. Irvine<sup>1</sup>, Peter Siderfin<sup>1</sup> and Cecile M. E. Charbonneau<sup>2</sup>

<sup>1</sup>Centre for Solar Energy Research, College of Engineering, Swansea University, St. Asaph, UK

<sup>2</sup>SPECIFIC / Sêr Cymru, College of Engineering, Swansea University Bay Campus, Swansea, UK

Email: Andrew.J.Clayton@Swansea.ac.uk

## Introduction

Tin Sulphide (SnS) has received attention in recent years for solar cell applications, but to date the highest certified conversion efficiency has only reached 4.4% [1]. Small grain sizes have been determined [1, 2] to be a contributing factor for low cell efficiencies, with high density of grain boundaries where defects acting as recombination centres typically reside. Post-growth annealing of SnS thin films results in grain growth [1-3] and improves photovoltaic (PV) cell efficiencies. SnS thin films are typically deposited by thermal evaporation [4], spray pyrolysis [5] atomic layer deposition (ALD) [6] and plasma enhanced chemical vapour deposition (PE-CVD) [7].

Metal organic chemical vapour deposition (MOCVD) offers an alternative deposition process [8], employing higher growth temperatures than other processes necessary for achieving large SnS film grain sizes. In the study presented in this paper, MOCVD of SnS thin films was carried out using the chemical precursors tetraethyltin (TET) and ditertiarybutylsulphide (DtBS) with process temperatures > 400°C.

## Experimental

Tetraethyltin (TET) and ditertiarybutylsulphide (DtBS) were used as chemical precursors using a MOCVD process for production of SnS thin films. The carrier gas was hydrogen (H<sub>2</sub>) or nitrogen (N<sub>2</sub>), or a mix of the two using a H<sub>2</sub>/N<sub>2</sub> 56:44 ratio. Precursor delivery was directly over the substrate with deposition on to indium tin oxide (ITO) coated boroaluminosilicate glass, with area of 75 x 50 mm<sup>2</sup> and thickness of 1.1 mm.

Growth temperatures 400 - 480 °C were used to deposit SnS films. The temperature was controlled using a k-type thermocouple inserted into the graphite susceptor. The graphite block could be moved back and forth under the injector, but was kept static during

these deposition runs. A N<sub>2</sub> cooling gas was employed at all times at the upstream and downstream (exhaust) sections of the MOCVD chamber.

The TET and DtBS partial pressures ranged from 2.2 - 8.6 × 10<sup>-4</sup> and 2.2 - 4.4 × 10<sup>-3</sup> atm. respectively, which gave S/Sn input ratios of 2.5 – 20.0. Different S/Sn ratios were employed for different temperature regimes focusing on 432°C and 470°C set points. The growth chamber pressure was at atmospheric pressure with total flow (F<sub>total</sub>) of 500 standard cubic centimetres per minute (scm). Depositions were carried out between 30 and 60 minutes.

*In situ* mass spectroscopy using a Cirrus portable instrument was employed to monitor by-product formation sampling from the exhaust gas to determine the reaction species involved in depositing thin film SnS.

Scanning electron microscopy (SEM) and energy dispersive X-ray spectroscopy (EDX) were carried out with a Hitachi TM3000 bench top instrument and used to assess grain size/shape and approximate stoichiometry of the SnS<sub>x</sub> deposits. High resolution (HR)-SEM was carried out with an Hitachi S-4800 instrument equipped with field emission gun (FEG) using beam settings at 10 keV and 10 µA. UV/Visible spectroscopy was used with a Varian Cary 5000 to measure the optical properties and X-ray diffraction (XRD) was used with a Phillips X'PERT MPD instrument to determine the thin film crystal structure.

## Results and discussion

Film deposition was achieved more efficiently when only using H<sub>2</sub> as carrier for the precursors. Experiments were carried out using N<sub>2</sub> as carrier gas without the presence of H<sub>2</sub>, but no film deposition was observed on the substrate. A 56/44 H<sub>2</sub>/N<sub>2</sub> carrier mix resulted in scarce film coverage on the substrate.

(i) *In situ* mass spectroscopy

In order to deposit SnS on to the substrate the chemical precursors need to dissociate efficiently to release the organic groups from the molecules. *In situ* mass spectroscopy (MS) was used to monitor exhaust gas species and to obtain insight into the role of the H<sub>2</sub> carrier. Figure 1 below shows a real time MS recording of exhaust gas species over an approximate 2 hour timeframe. Figure 1 (a) shows the TET by-products and 1 (b) shows the DtBS by-products. During this time, the carrier was changed from N<sub>2</sub> to H<sub>2</sub> at growth temperature set point with reacting species injected into the chamber. It was evident from MS that some level of precursor dissociation occurs in an inert N<sub>2</sub> atmosphere. However, when the carrier gas was switched to H<sub>2</sub> there was a significant change in concentration of dissociated chemical species in the exhaust gas. The addition of H<sub>2</sub> brought about the detection of H\* radicals, which are considered by the authors to be essential for chemical dissociation and for reducing the oxidation state of the Sn from +4 to +2 in order for single phase SnS to be achieved.

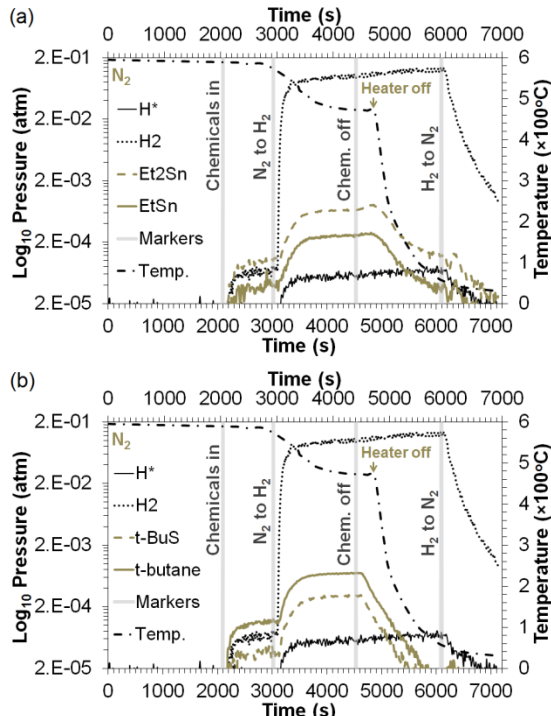


Figure 1: *In situ* mass spectroscopy of (a) TET and (b) DtBS exhaust gas species during MOCVD using typical growth conditions.

The increased break down of the TET and DtBS molecules coincide directly with the

addition of H<sub>2</sub> in Figures 1 (a) and (b), respectively.

Figure 1 (a) shows the TET by-product species with dissociation of the first 2 ethyl groups (Et<sub>2</sub>Sn) was greater in concentration than a further dissociated TET species (EtSn) with one remaining ethyl group. Further dissociation to release a remaining organic group from an organometallic compound typically requires more energy to free the metal, with larger activation energies to break the final metal-organic bond [9].

The DtBS dissociated species shown in Figure 1 (b) are observed to have similar concentrations to the dissociated species of TET. The higher vapour pressure of DtBS relative to TET caused a more rapid drop in exhaust gas S-based species when the chemical precursor injection was stopped.

(ii) Film optical properties

The absorbance of 3 film samples deposited at 470°C and different S/Sn ratios is shown in Figure 2. Absorbance was greatest over the visible region of the solar spectrum for the sample TS124 which was deposited at S/Sn = 6.2.

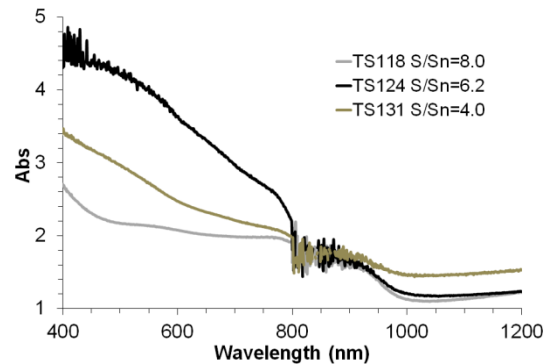


Figure 2: Absorbance spectroscopy of 3 SnS<sub>x</sub> film samples deposited on to ITO using S/Sn ratios from 4.0 to 8.0.

All films show an absorption edge around 950 nm which is equivalent to a band gap ( $E_g$ ) of 1.3 eV using the relationship:

$$\frac{E}{1.6 \times 10^{-19}} \text{ (eV)} = \frac{hc}{\lambda} \quad (1)$$

A plot of absorption coefficient multiplied by energy squared versus energy ( $\alpha E^2$ ) vs.  $E$  was used to approximate the  $E_g$  for each film from the absorbance spectra. Samples TS118 and TS131 have  $E_g \sim 1.25$  eV whereas sample TS124 has  $E_g \sim 1.4$  eV. The derived

$E_g$  suggest there may be some undesired phase(s) present in each film, but that the appropriate S/Sn ratio for single phase SnS is within this range.

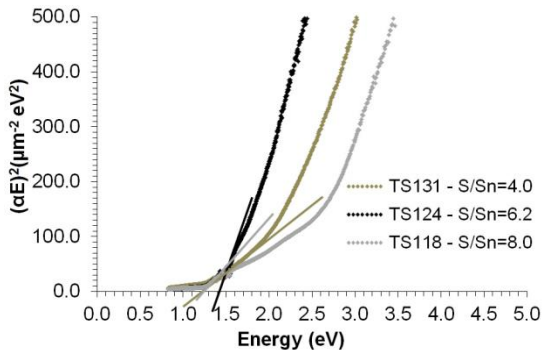


Figure 3:  $E_g$  approximation using  $(\alpha E)^2$  vs.  $E$  for  $\text{SnS}_x$  films deposited on to ITO with S/Sn ratio from 4.0 to 8.0.

#### (iii) Film composition and phase

The composition of the films were characterised using EDX with beam energies of 5 kV and 15 kV. Films with thickness  $\geq 1 \mu\text{m}$  were generally characterised at 5 kV in order to prevent detection of the Sn in the underlying ITO. In some cases, as in Figure 4, 15 kV was used with no In detection, indicating that the ITO was not contributing to the Sn at.%. Sample TS124 gave the closest 1:1 ratio of S:Sn.

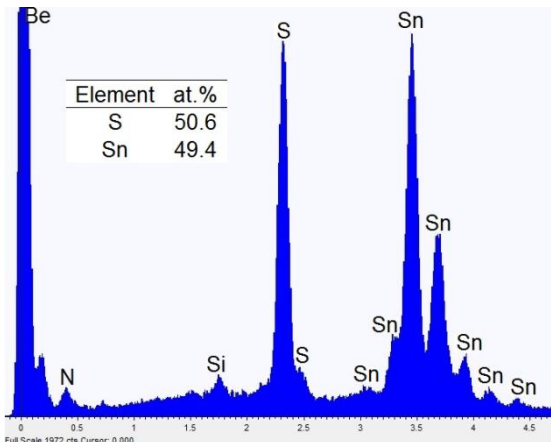


Figure 4: EDX of sample TS124 using incident energy of 15 kV.

XRD was used to determine what phases were present in the polycrystalline films. Sample TS124 with S/Sn = 6.2 was observed to have a composition closest to single phase SnS out of all the films, with a small presence of the S-rich  $\text{Sn}_2\text{S}_3$  phase evident at a  $2\theta$  diffraction angle of  $21.4^\circ$ . A direct comparison

was made to commercially available SnS powder with stated purity of 99.99%. Both the TS124 film sample and the 99.99% SnS powder had preferred orientation in the 0, -4, 0 plane at  $32.0^\circ$ .  $\text{Sn}_2\text{S}_3$  was detected at diffraction angle  $48.5^\circ$  in the commercially supplied SnS powder with 99.99% purity. Figure 5 shows that a S/Sn ratio just below 6.2 should remove all presence of  $\text{Sn}_2\text{S}_3$  to achieve single phase SnS.

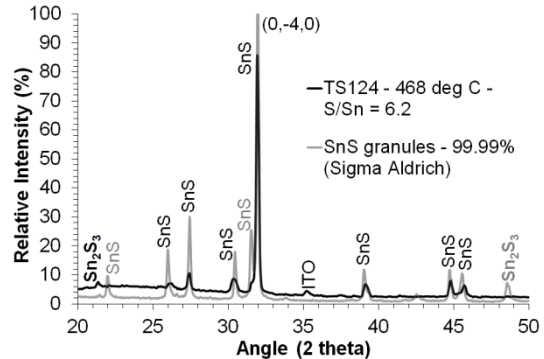


Figure 5: XRD of sample TS124 with S/Sn = 6.2 and commercially available 99.99% SnS powder.

For the different temperature regimes at  $432^\circ\text{C}$  and  $470^\circ\text{C}$  the S/Sn ratio had to be controlled differently using the S and Sn chemical precursor partial pressures. This was due to the difference in vapour pressure between Sn and S, with the higher vapour pressure of S resulting in film desorption at the higher temperatures. Therefore, larger S/Sn ratios were necessary at the higher growth temperatures.

#### (iv) Grain size

Grain size was compared using SEM, shown in Figure 6 (a) and (b), of film samples deposited at different temperature. It was found that higher process temperatures led to larger grain size as has been reported [10] for other thin film materials such as CdTe.

Sample TS123 grains were varied in shape (Figure 6 (b)) with some nanowire structures observed at the surface. Some of the grains were more elongated than others, which was a trait when S-rich conditions were used in the deposition process.

The grain enlargement at the higher process temperature, shown in Figure 6 (b) for sample TS124, was significant with growth of average grain size from  $\sim 0.5 \mu\text{m}$  at  $432^\circ\text{C}$  to  $> 1 \mu\text{m}$  at  $470^\circ\text{C}$ . The grain boundary

density was therefore much lower for sample TS124 than for TS123 due to the higher temperature conditions during growth. The higher growth temperature will be necessary for producing SnS films with reduced recombination centres which typically reside at grain boundaries.

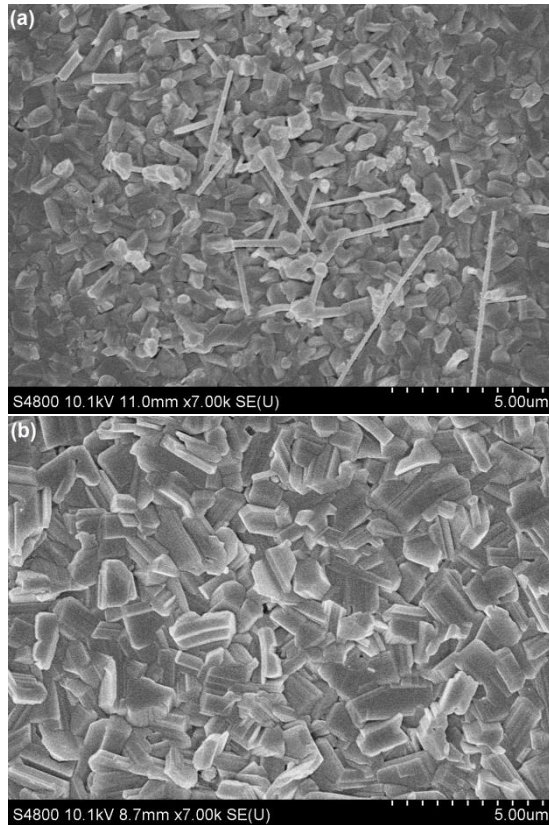


Figure 6: SEM of (a) TS123 deposited at 432°C using S/Sn=4.5 and (b) TS124 deposited at 470°C using S/Sn = 6.2.

One of the advantages that MOCVD has as a process for SnS is the capability to inject the necessary concentration levels of S into the films at the higher process temperatures in order to limit desulfurisation. This is considered a limitation for SnS photovoltaics [11]. Large grains and SnS phase control will be essential when the SnS films are incorporated into thin film solar cell devices.

## Conclusions

MOCVD has been shown to have capability of producing thin film SnS at high process temperatures without loss of S. This was achieved by adjusting the S/Sn ratio according to the process temperature used. Large grains were achieved for the higher

process temperatures to produce near single phase SnS films. Further optimisation of the S/Sn ratio will realise single phase SnS.

Mass spectroscopy revealed the importance of the H<sub>2</sub> carrier for generating H<sup>\*</sup> radicals necessary to enhance chemical precursor dissociation and SnS film growth on the substrate.

## Acknowledgements

The authors would like to acknowledge the European Regional Development Fund (ERDF) and the Welsh European Funding Office (WEFO) for funding the 2<sup>nd</sup> Solar Photovoltaic Academic Research Consortium (SPARC II) which supported this research.

## References

1. P. Sinsermsuksakul, L. Sun, S.W. Lee, H.H. Park, S.B. Kim, C. Yang and T.G. Gordon, *Adv. Energy Mater.* (2014) 1400496.
2. B. Ghosh, M. Das, P. Banerjee and S. Das, *Sol. Energy Mater. Sol. Cells* **92** (2008), 1009.
3. O.E. Ogah, K.R. Reddy, G. Zoppi, I. Forbes and R.W. Miles, *Thin Solid Films*, **519** (2011) , 7425.
4. V. Steinmann, R. Jaramillo, K. Hartman, R. Chakraborty, R.E. Brandt, J.R. Poindexter, Y.S. Lee, L. Sun, A. Polizzotti, H.H. Park, R.G. Gordon and T. Buonassi, *Adv. Mater.* (2014) 02219.
5. K.T. Ramakrishna Reddy, N. Koteswara Reddy and R.W. Miles, *Sol. Energy Mater. Sol. Cells* **90** (2006) 3041.
6. P. Sinsermsuksakul, J. Heo, W. Noh, A.S. Hock and R.G. Gordon, *Adv. Energy Mater.* **1** (2011) 1116.
7. P. Sinsermsuksakul, K. Hartman, S.B. Kim, J. Heo, L. Sun, H.H. Park, R. Chakraborty, T. Buonassisi and R.G. Gordon, *Appl. Phys. Lett.* **102** (2013) 053901.
8. A.J. Clayton, S.J.C. Irvine, C.M.E. Charbonneau, P. Siderfin and V. Barrioz, *Mater. Res. Innov.* **19** (2015) 477.
9. A.J. Clayton and S.J.C. Irvine, *J. Cryst. Growth* **300** (2007) 277.
10. K. Durose, M.A. Cousins, D.S. Boyle, J. Beier and D. Bonnet, *Thin Solid Films* **403-404** (2002) 396.
11. S. Di mare, D. Menossi, A. Salavei, E. Artegiani, F. Piccinelli, A. Kumar, G. Mariotto and A. Romeo, *Coatings* **7** (2017) 34.

# A Simple Optical Setup for Current Mapping of Small Area PV Devices Using Different Sampling Strategies

G. Koutsourakis\*, S. R. G. Hall•, M. Bliss\*, T.R. Betts\* and R. Gottschalg\*

\*Centre for Renewable Energy Systems Technology (CREST), School of Electronic, Electrical and Systems Engineering, Loughborough University, Loughborough, Leicestershire, LE11 3TU, UK,

• National Physical Laboratory (NPL), Hampton Road, Teddington, Middlesex, TW11 0LW, United Kingdom, UK

\* Corresponding Author: [G.Koutsourakis@lboro.ac.uk](mailto:G.Koutsourakis@lboro.ac.uk)

## Abstract

An optical setup for current mapping of photovoltaic devices is presented. It is based on a digital micro-mirror device (DMD) and a small number of additional optical elements making the implementation simple and cost effective. The specific properties of the DMD chip enable the application of two different sampling methods; point by point sampling and compressive sampling. Both sampling strategies are compared and cases when each one of them performs better are investigated. It is shown that compressive sampling can significantly enhance weak current signals and provide current maps in the cases when the point by point current signal is below the noise threshold.

## Introduction

Spatial non-uniformities can have a severe impact on the overall performance of a photovoltaic (PV) device. For this reason, the development of spatial characterisation methods is significant for the acquisition of local information on defects and inhomogeneities of solar cells. Light/Laser Beam Induced Current (LBIC) methods have been developed as a non-destructive characterisation technique which can be used for mapping the local current response of PV cells [1]. For its implementation, a light beam scans the PV sample and the induced current response is measured at each point. However, complicated experimental layouts are required for the realisation of such techniques. In addition, the method lacks speed, as the small size spot has to scan the entire area under measurement for a complete current map. On the other hand, the resolution that can be achieved with LBIC can reach sub-micrometre levels, which is difficult to be accomplished with other imaging methods of PV devices.

In this work a simple approach for realising an alternative type of current mapping system is demonstrated. The experimental

layout is based on a Digital Micromirror Device (DMD) [2]. Two different approaches are adopted for sampling; the standard point by point scan and compressive sampling (CS). Using a DMD to apply compressive sampling for current mapping of PV samples has been demonstrated in previous work [3]. By applying compressive sampling, one can measure a  $N$  element signal by only acquiring  $M \ll N$  linear measurements [4]. For solar cell current mapping applications, this is achieved by projecting a series of binary patterns on the sample and measuring the current response for each pattern. The current map is then reconstructed using an optimisation algorithm.

The aim of this work is twofold: the first is to introduce a simple and innovative current mapping setup for PV devices, based on a DMD chip. The setup is able to apply both point by point and compressive sampling. The second is to provide a pixel by pixel comparison between the two sampling strategies. Experimental results acquired with different samples show that each of these sampling methods has both advantages and drawbacks. Compressive sampling is preferable when high levels of noise are present, while raster scans can provide slightly better accuracy when noise levels are low, although measurements take more time.

## Experimental Setup

The experimental setup is presented in figure 1. The available laser sources are a 40mW laser at 658nm wavelength and a 100mW laser at 785nm. Both sources are single mode fibre coupled. The light output of the fibre is collimated at a size so that the beam overfills the micro-mirror array area of the DMD. The DMD is a V-7000 module, consisting of a 1024x768 pixel micromirror array, each micromirror having a pixel size of  $13.7 \times 13.7 \mu\text{m}$ . The collimated beam is incident on the DMD at an angle and only the central region of the beam is used. The

plane of the micromirror area is perpendicular to the spatial filter system. A mirror is finally used for guiding the beam onto the sample, which is placed horizontally on a z-stage platform. The measurement area is 1cm by 1cm,

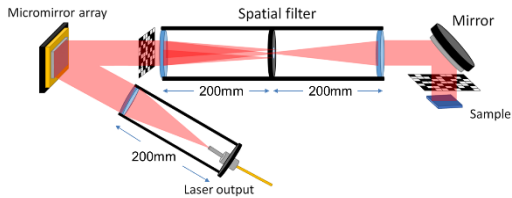


Figure 1: The optical setup of the current mapping system based on a DMD chip.

A National Instruments PXIe-4139 system source measure unit (SMU) is used for measuring the current response of the sample. As shown in figure 2, the experimental layout is kept as compact as possible, in order to demonstrate that the realisation of such a system is simple and a small amount of space and optical elements are required. A sampling rate of 10 measurements per second is achieved. The sample is placed at the focal plane of the last lens, so that the scanning spot or the patterns are actually projected on the sample. Nevertheless, a small misplacement from this plane has almost no effect on measurements due to spatial filtering. The optical setup is suitably enclosed for minimising external light contamination as well as for laser safety reasons.

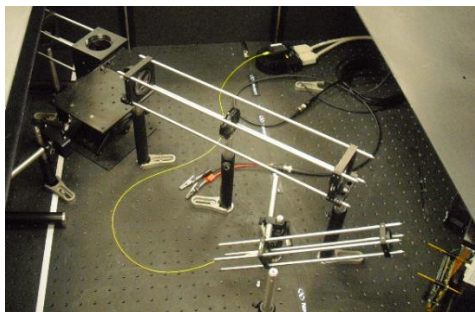


Figure 2. Picture of the current mapping setup at NPL based on the DMD device.

A Copper indium gallium selenide (CIGS) and a mc-Si PV samples (see Figure 3) are used for measurements. The patterns projected on the PV cells are also visible in the picture. The CIGS cell used for measurements had a size of 1cm by 1cm and is contacted with probes. The mc-Si sample has a size of 8cm by 8cm and only a small 1cm by 1cm area is measured.

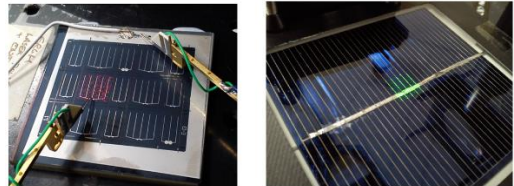


Figure 3. The CIGS sample on the left and the mc-Si sample on the right, which are used for measurements in this work.

## Sampling Methods

In order to apply a point by point scan, a number of micro-mirrors are grouped together depending on the desired optical resolution. When only one pixel of the micromirror array is used for the scan, the signal is rather low, which results in very noisy measurements. For this reason, the minimum group of pixels used in this series of measurements is 9 pixels (3x3), which results in an optical resolution of 41.1 $\mu\text{m}$  and the maximum is 49 (7x7), which gives a resolution of 96 $\mu\text{m}$ . 100x100 pixel current maps were acquired in the case of CS current mapping, in order to achieve a straightforward performance analysis of the measurement system.

During compressive sampling, a series of test functions  $\Phi=\{\varphi_m\}_{m=1}^M$  are projected onto the PV device. Random binary matrices of ones and zeroes can be used as patterns, as they are easy to implement and satisfy the requirements for compressive sampling [5]. For every projected pattern the current response of the PV device is measured, populating the measurement vector  $\mathbf{y}$ . Since the projected patterns are known, constructing sensing matrix  $\Phi$ , the solution to the underdetermined problem is the  $\mathbf{x}$  vector with the minimum  $\ell_1$  norm [6].

$$\hat{\mathbf{x}} = \underset{\mathbf{x}}{\operatorname{argmin}} \|\mathbf{x}\|_1 \text{ subject to } \Phi \mathbf{x} = \mathbf{y} \quad (1)$$

With this method, current maps can be acquired with much fewer measurements than what a raster scan would require.

## Results

In Figure 4, two current maps of the CIGS PV cell are presented, using a different optical resolution each time, acquired with a point by point scan. It is clear that by grouping different number of micromirrors together one can focus on different areas of a sample with different levels of resolution. This is a very convenient feature of a DMD based system, as it allows much more freedom of settings, such as changing the

size of the spot that realizes the scan or selecting specific areas of interest. In Figure 4, the PV cell's current response appears to be rather uniform, apart from local tiny spots. The probe used for contacting the cell is also visible. A slight general non-uniformity of approximately 10% is due to the initial non-uniformity of the Gaussian collimated beam that overfills the DMD.

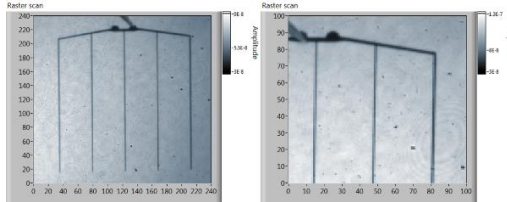


**Figure 4:** On the left 3x3 groups of micro-mirrors are used for the point by point scan, measuring the whole cell. On the right 4x4 groups are used for measuring a smaller area of the sample.

For the compressive sampling case 7x7 groups of micro-mirrors were used and 100x100 pixel current maps were produced, imaging the whole PV cell. As the aim of compressive sampling is to apply fewer measurements in order to reconstruct the final current map, different levels of undersampling were investigated. The unique property of this experimental layout is that it can apply both point by point and CS current mapping. This means that a pixel by pixel comparison can be realised, for a more accurate experimental optimisation and evaluation of CS current mapping.

In Figure 5, the reconstructed current maps are expressed as percentages, expressing the ratio of samples (projected patterns) acquired for reconstruction by the total number of pixels or equivalently, the ratio of CS measurements taken by the number of measurements a point by point would need. The total number of pixels of the current maps is 10000. The contacting grid pattern of the PV cell start becoming visible from 3000 measurements (30%) while current maps including all the features are acquired above 50%. By adding more measurements the reconstructed map converges to the actual current map.

The curve of the correlation coefficient for is presented in Figure 6, as a function of number of measurements acquired. The small local decrease observed at 50% of measurements is thought to be due to the interaction of the DCT transform with the symmetry of the cell. Apart from the small

local spots and imperfections, the PV cell is rather symmetric, which has an influence when Fourier based transforms are used. The results confirm that compressive sampling is a reliable current mapping method that requires fewer measurements than a point by point scan.

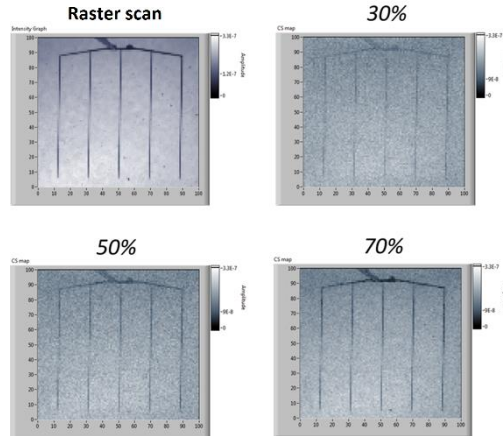


**Figure 5.** Reconstructed current maps of the PV cell using different number of measurements compared to the point by point scan.

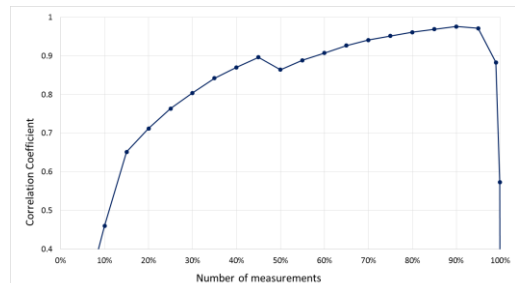


**Figure 6.** The correlation coefficient between the CS current maps and the LBIC map, as a function of number of measurements acquired.

In some cases compressive sampling is necessary because a point by point scan does not provide reliable results due to signal to noise issues. This is clear when the large 8cm by 8cm mc-Si PV cell is used and a small 1cm by 1cm area of the cell is measured, known to contain cracks and spots. A raster scan results in an extremely noisy current map, where even the sharpest features of the cell area are barely distinguishable. Since this is a large area sample, the noise levels are very high compared to the current signal of the point by point scan. Thus the very weak signal is lost within the background noise. A lock-in technique has not been applied during measurements, which could help reduce measurement noise. However, when using compressive sampling, the current signal is

greatly enhanced, since half the measured area is illuminated and not just a single spot. The reconstructed current maps are presented in figure 7. Both laser sources were used for measurements. Using the IR laser the crack starts becoming visible, although the light still doesn't penetrate deep enough into the cell to make this feature sharper. Current maps with the LBIC system in CREST [7] are presented in the same figure for confirming the validity of measurements.

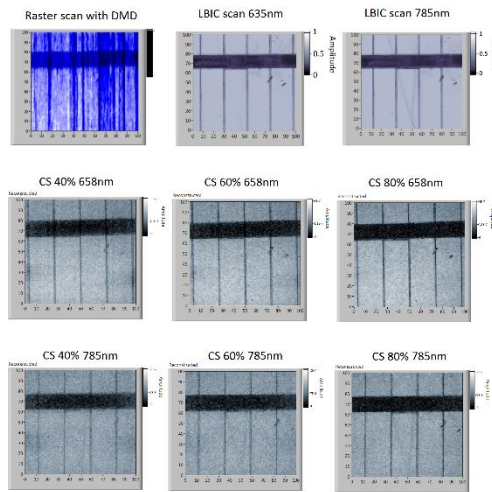


**Figure 7.** CS current mapping results using two different laser sources, for different levels of undersampling compared to the point by point scans using a DMD and from the CREST LBIC system.

## Conclusions

A current mapping optical system is realised in this work in a very simple and straightforward way without moving parts, complicated optical elements or lock-in methods to achieve high optical resolution and sampling rate. It also offers the unique opportunity for an experimental pixel by pixel comparison of LBIC and CS current mapping. It is shown that compressive sampling yields reliable results always with fewer acquired measurements than point by point sampling, although the difference sometimes can be small. On the other hand, the application of compressive sampling is necessary in cases with very high noise levels, where the signal levels must be enhanced for meaningful sampling above the noise threshold.

This simple DMD system can be utilized for reliable current mapping not only for PV devices, but also for photodiodes and other semiconductor devices. Such a setup can easily be realised at any PV research

laboratory to provide a useful tool for spatial characterisation of small area PV devices. Moreover, it offers the opportunity to investigate the performance of different algorithms and sensing matrices for compressive sampling, as a direct comparison with a raster scan is possible.

## Acknowledgements

This work was funded by the CASE awards of EPSRC and through the European Metrology Research Programme (EMRP) Project ENG55 PhotoClass, which is jointly funded by the EMRP participating countries within EURAMET and the European Union.

## References

- [1] M. Padilla, B. Michl, B. Thaidigsmann, W. Warta, and M. C. Schubert, "Short-circuit current density mapping for solar cells," *Sol. Energy Mater. Sol. Cells*, vol. 120, pp. 282–288, Jan. 2014.
- [2] L. J. Hornbeck, "The DMDTM Projection Display Chip: A MEMS-Based Technology," *MRS Bull.*, vol. 26, no. 4, pp. 325–327, 2001.
- [3] G. Koutsourakis, M. Cashmore, S. R. G. Hall, M. Bliss, T. R. Betts, and R. Gottschalg, "Compressed Sensing Current Mapping Spatial Characterization of Photovoltaic Devices," *IEEE J. Photovoltaics*, pp. 1–7, 2017.
- [4] E. J. Candes, J. Romberg, and T. Tao, "Robust uncertainty principles: exact signal reconstruction from highly incomplete frequency information," *IEEE Trans. Inf. Theory*, vol. 52, no. 2, pp. 489–509, Feb. 2006.
- [5] R. Baraniuk, M. Davenport, R. DeVore, and M. Wakin, "A Simple Proof of the Restricted Isometry Property for Random Matrices," *Constr. Approx.*, vol. 28, no. 3, pp. 253–263, Jan. 2008.
- [6] R. G. Baraniuk, "Compressive sensing," *IEEE Signal Process. Mag.*, vol. 24, no. 4, pp. 1–9, 2007.
- [7] M. Bliss, G. Koutsourakis, T. R. Betts, and R. Gottschalg, "Development of a Solar Cell Spectral Response Mapping System using Multi-LBIC Excitation Multi-LBIC local SR system First Measurements," in *PVSAT-12 Proceedings*, 2016, pp. 55–58.

# A comparison of different selenisation approaches for solution-processed Cu(In,Ga)(S,Se)<sub>2</sub> solar cells

S. Uličná<sup>1\*</sup>, P. Arnou<sup>1</sup>, C.S. Cooper<sup>1,2</sup>, L.D.Wright<sup>1</sup>, A.V. Malkov<sup>2</sup>, J.M. Walls<sup>1</sup> and J.W. Bowers<sup>1</sup>

<sup>1</sup>Centre for Renewable Energy Systems Technology (CREST), Wolfson School of Mechanical, Electrical and Manufacturing Engineering, Loughborough University, Loughborough, Leicestershire, LE11 3TU, UK

<sup>2</sup>Department of Chemistry, Loughborough University, Loughborough, Leicestershire, LE11 3TU, UK

\* Corresponding Author [S.Ulicna@lboro.ac.uk](mailto:S.Ulicna@lboro.ac.uk)

## Abstract

Hydrazine-free Cu(In,Ga)Se<sub>2</sub> (CIGS) absorbers were fabricated using a low-cost atmospheric deposition method. The structural and electrical properties of thin film absorbers and the resulting solar cells processed using two different selenisation approaches were compared. A double selenisation process showed improved crystal structure compared to a single selenisation step, resulting in improved absorption throughout the spectrum and conversion efficiencies reaching 9.3%.

## Introduction

The chalcopyrite semiconductor Cu(In,Ga)Se<sub>2</sub> (CIGS) is currently the best performing polycrystalline thin film solar cell technology reporting a record power conversion efficiency (PCE) of 22.6% (ZSW) [1]. The most efficient devices so far are typically fabricated by expensive vacuum-based techniques such as co-evaporation and sputtering. Atmospheric processing of CIGS solar cells becomes an attractive alternative to the vacuum-based techniques due to its lower production costs and the compatibility with roll-to-roll processing [2]. The best true solution-based device reached PCE of 17.3% using the extremely hazardous and toxic solvent hydrazine [3]. Recently, a much safer solvent mixture of 1,2-ethylenediamine and 1,2-ethanedithiol was found to successfully dissolve nine bulk V<sub>2</sub>VI<sub>3</sub> chalcogenide semiconductors [4]. In our previous work, the same solvent mixture was used to effectively dissolve copper sulphide, indium sulphide and gallium in the presence of excess selenium for thin film chalcopyrite solar cell applications. Solar cells deposited by spray-coating of these precursors followed by selenisation exhibited PCEs of 8% for CIS and 9.8% for CIGS [5]. The performance of the final photovoltaic device is closely related to the grain size and the film quality (cracks, voids and adhesion), therefore selenisation is a

critical step in the absorber formation. The resulting film quality is dependent on the selenisation reactor configuration and the parameters used, such as the temperature, pressure and heating duration [6].

The purpose of this work is to study the effect of selenisation approaches on the morphological and electrical properties of the sprayed CIGS absorber films. Typically, the solution processed absorbers suffer from incomplete recrystallization upon selenisation [7]. With the aim to fully recrystallize the absorber, an alternative double selenisation method was applied and compared to the baseline process, which is a single selenisation step.

## Experimental

The CIGS absorber films were prepared by a two-step process, consisting of spraying the precursor solutions onto a Mo-coated substrate and post-deposition selenisation. The solution preparation and deposition procedure were identical as in our previous work [5]. The Cu<sub>0.9</sub>In<sub>0.7</sub>Ga<sub>0.3</sub>Se<sub>2</sub> precursor solution was deposited in atmospheric conditions using a chromatography atomizer. The final film consisted of 6 sprayed layers in total. In between each spraying a drying step was performed to evaporate excess solvents. The as-deposited films were then thermally annealed in Se atmosphere to recrystallise the absorber. Two different selenisation approaches were performed using a tube furnace with two separately heated zones. The sample was positioned inside a partially closed graphite box containing Se pellets. The graphite box was then placed in the one zone of the furnace heated at 540°C for 50 min, including the ramping (~40°C/min). The working tube was purged with nitrogen three times prior to the annealing and the starting pressure was set to 400 Torr. "Single selenisation" is the case where the

film is selenised after depositing 6 separate layers. For the “double selenisation”, a thinner absorber layer (3 sprayed layers) was selenised using the same starting conditions, then the spraying and selenisation was repeated [8]. The first and the second selenisation lasted for 30 and 40 min respectively. The devices were completed with the chemical bath deposition of CdS followed by intrinsic ZnO and Al doped ZnO (AZO) deposited by RF magnetron sputtering.

The grain structure of the absorber films was characterised using a JEOL JSM-7800F Field Emission Scanning Electron Microscope (FE-SEM). The electrical characterisation includes JV measurements under  $1000 \text{ W/m}^2$  illumination. A Multi-laser LBIC (Laser-Beam Induced Current) measurement system using 11 diode lasers covering wavelengths ranging from violet (405nm) to the near infrared region (1060nm) was used to investigate the local spectral response and external quantum efficiency (EQE) of the device [9].

## Results and Discussion

The SEM cross-sections of the two devices processed by single and double selenisation are shown in Fig. 1.

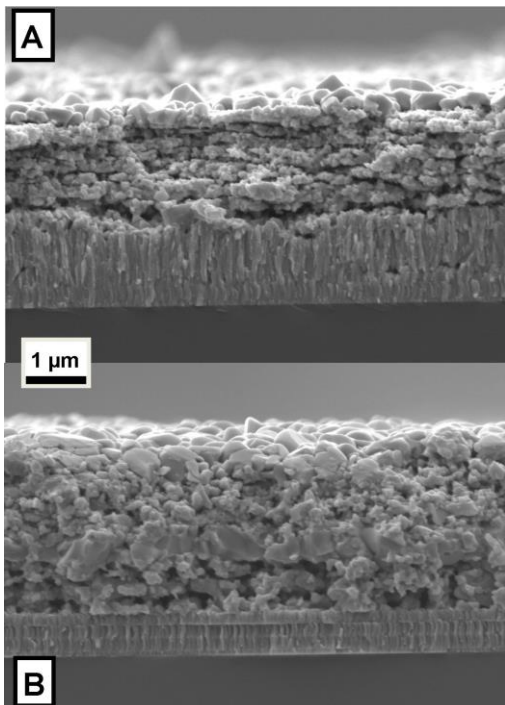


**Figure 1** SEM cross-sections of a) single b) double selenised CIGS absorber

The single-time selenised absorber is incompletely-crystallised with slightly

bigger grains on the top and a relatively porous bulk, where the individual sprayed layers can clearly be seen. Variation of selenisation conditions in terms of temperature, pressure and duration conditions for this selenisation configuration did not significantly improve crystallisation. Instead, the fine-grained layer persisted with the same thickness underneath the crystallised top layer. Moreover, the higher starting pressures result in excessively thick  $\text{MoSe}_2$  layer contributing to the high series resistance ( $R_S$ ) of the device and occasionally causing delamination. In the cross-section of the double selenised absorber, the first deposited stack of layers is clearly distinguished from the second. The large grains, normally visible on the top of a selenised stack, are now present in the middle of the absorber (top of the first selenised stack of layers), as well as on the top surface. The presence of large grains in the bulk and not only on the surface is expected to improve carrier collection. Therefore this selenisation approach seems to improve the absorber grain structure and it is expected that it will have an effect on the device electrical properties. However, the absorber is still incompletely crystallised. In addition, the back contact in this device shows only a thin  $\text{MoSe}_2$  layer. This is due to a  $\text{Mo/MoN}_x/\text{Mo}$  multilayer that was used instead of a bare Mo, in order to prevent delamination due to a very thick  $\text{MoSe}_2$  layer, which would form for selenisation times longer than 70 min.  $\text{MoN}_x$  is acting as a barrier layer to the Se diffusion and hence limiting the  $\text{MoSe}_2$  formation [10].

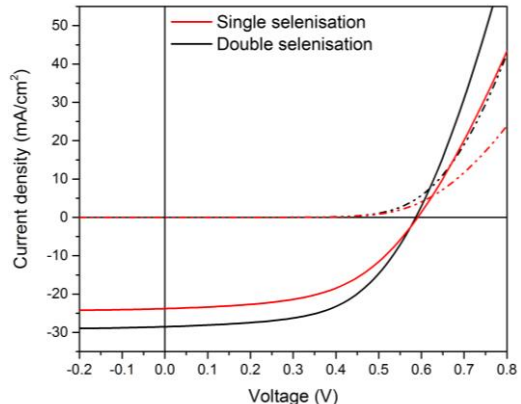


**Figure 2** JV curves for different selenisation configurations

The light and dark JV characteristics for the samples processed with each selenisation approach are displayed in Fig. 2. The fundamental PV parameters e.g.

open circuit voltage ( $V_{OC}$ ), short circuit current density ( $J_{SC}$ ), fill factor (FF) and efficiency are shown (Table 1).

**Table 1** Electrical performance of the three types of selenisation

	$V_{OC}$ (V)	FF (%)	$J_{SC}$ (mA/cm <sup>2</sup> )	Eff (%)
Single	0.591	52.5	23.8	7.38
Double	0.586	55.7	28.5	9.30

The box plots of the key performance indicators measured on six adjacent cells of each device are shown in Fig. 3.

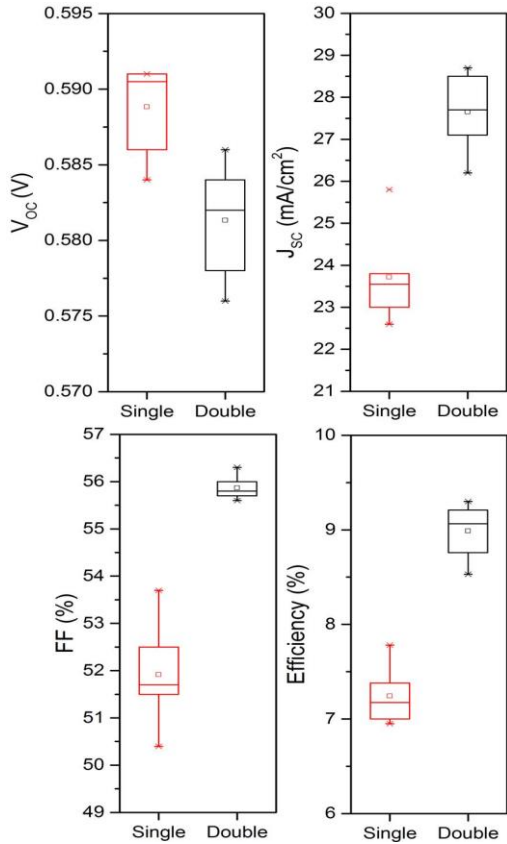


**Figure 3** Box plots showing the key performance indicators of the solar cells obtained using the two selenisation approaches

The cells processed with the single selenisation step show a slightly better  $V_{OC}$ . However the  $J_{SC}$  and FF are significantly increased for the double selenisation step, leading to efficiencies up to 2% higher than the single selenised absorber. The  $\text{MoN}_x$  barrier layer at the back contact can play a part in the improvement of the  $R_S$  seen on the JV curves; however it could also be responsible for the lower voltage. In fact, when the barrier layer was combined with a single selenised absorber, it resulted in

low  $V_{OC}$  of 460 mV. The overall improved electrical performance of the device with double selenised absorber is in agreement with the SEM cross-section showing improved crystallisation in the bulk. To test the absorption properties of both devices, a multi-laser LBIC measurement was performed on the same cell. The EQE spectra measured on each point of the cell was mapped and is displayed at four different wavelengths for both solar cells in Fig. 4.

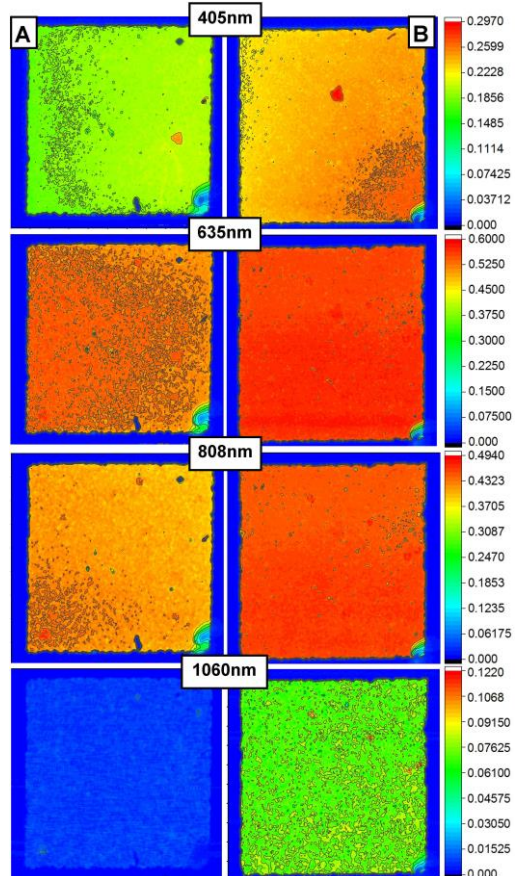


**Figure 4** Spectral response of a) single selenised, b) double selenised sample at four wavelength using multi-laser LBIC system

The 405nm laser shows the absorption near the surface and the 1060nm laser the absorption near the back contact region. The double selenised device generates more current than the single selenised device throughout the whole thickness of the device. This improved absorption can be related to improved quality of the absorber, owing to bigger grains, as seen in the cross-section in Fig. 1. Moreover, both cells look relatively homogeneous over the whole cell area with only few dark spots or pinholes that might have been caused by accidental scratching or manipulation during the measurements.

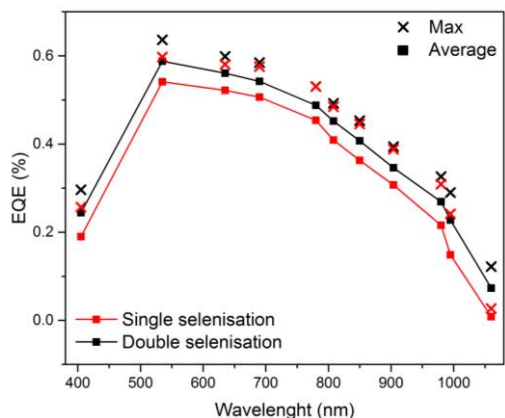


**Figure 5** Average EQE from all the points of the cell area and maximum values

Fig. 5 shows the EQE values extracted from the LBIC data from 11 lasers. An average curve for all the points at the surface ( $>2,200 \text{ pt/mm}^2$ ) of the cell are plotted for both selenisation approaches as well as the maximum value reached at each wavelength. The average and maximum points of the EQE are higher for the double selenised cell. The absorption seems to be improved similarly in the front and in the back of the device. However, the maximum value is only slightly higher than 60%, which is still relatively low. The EQE drops gradually at long wavelengths ( $>700\text{nm}$ ). This can be attributed to the recombination at the back, where the absorber is still poorly crystallised.

## Conclusion

In this work, two selenisation approaches were investigated for hydrazine-free, solution-processed CIGS absorber layers. The first, “single selenisation” consisted of selenisation of the entire absorber at the end of the deposition. In the second approach, “double selenisation”, half of the absorber thickness was selenised prior to the deposition and selenisation of the second half. It was shown that the double selenisation improves the grain structure of the absorber resulting in higher generated current and better absorption in the entire spectrum. Consequently, the double selenised cells reached PCEs up to 2% higher than the single selenised absorber. However, the progressive decay of the EQE curve at long wavelengths suggests that the selenisation step could be further improved to reduce the recombination in the bulk. In order to do so, repeating the spraying-selenisation steps multiple times on even thinner sprayed precursor layers may aid in the

complete recrystallisation of the whole film thickness.

## References

- [1] P. Jackson, R. Wuerz, D. Hariskos, E. Lotter, W. Witte, and M. Powalla, “Effects of heavy alkali elements in Cu(In,Ga)Se<sub>2</sub> solar cells with efficiencies up to 22.6%,” *Phys. status solidi - Rapid Res. Lett.*, 2016.
- [2] D. Lee and K. Yong, “Non-vacuum deposition of CIGS absorber films for low-cost thin film solar cells,” *Korean J. Chem. Eng.*, 2013.
- [3] T. Zhang, Y. Yang, D. Liu, S. Tse, W. Cao, Z. Feng, S. Chen, and L. Qian, “High efficiency solution-processed thin-film Cu(In,Ga)(Se,S)<sub>2</sub> solar cells,” *Energy Environ. Sci.*, 2016.
- [4] D.H. Webber and R.L. Brutchey, “Alkahest for V<sub>2</sub>Vl<sub>3</sub> chalcogenides: dissolution of nine bulk semiconductors in a diamine-dithiol solvent mixture”, *Journal of the American Chemical Society*, 2013.
- [5] P. Arnou, C. S. Cooper, S. Uličná, A. Abbas, A. Eeles, L. D. Wright, A. V. Malkov, J. M. Walls, and J. W. Bowers, “Solution processing of CuIn(S,Se)<sub>2</sub> and Cu(In,Ga)(S,Se)<sub>2</sub> thin film solar cells using metal chalcogenide precursors,” *Thin Solid Films*, 2016.
- [6] S. Ahn, K. H. Kim, J. H. Yun, and K. H. Yoon, “Effects of selenization conditions on densification of Cu(In,Ga)Se<sub>2</sub> (CIGS) thin films prepared by spray deposition of CIGS nanoparticles,” *J. Appl. Phys.*, 2009.
- [7] D. Zhao, Q. Fan, Q. Tian, Z. Zhou, Y. Meng, D. Kou, W. Zhou, S. Wu, J. Mater, D. Zhao, A. Qingmiao Fan, A. Qingwen Tian, A. Zhengji Zhou, A. Yuena Meng, A. Dongxing Kou, A. Wenhui Zhou, and S. Wu, “Eliminating fine-grained layer in Cu(In,Ga)(S,Se)<sub>2</sub> thin films for solution-processed high efficient solar cells,” *Journal of Materials Chemistry A*, 2013.
- [8] M. Neuwirth, H. Zhou, T. Schnabel, E. Ahlsweide, H. Kalt, and M. Hetterich, “A multiple-selenization process for enhanced reproducibility of Cu<sub>2</sub>ZnSn(S,Se)<sub>4</sub> solar cells,” *Appl. Phys. Lett.*, 2016.
- [9] M. Bliss, G. Koutsourakis, T. R. Betts, and R. Gottschalg, “Development of a solar cell spectral response mapping system using multi-LBIC excitation,” *PVSAT-12 Proc.*, 2016.
- [10] C. W. Jeon, T. Cheon, H. Kim, M. S. Kwon, and S. H. Kim, “Controlled formation of MoSe<sub>2</sub> by MoN<sub>x</sub> thin film as a diffusion barrier against Se during selenization annealing for CIGS solar cell,” *J. Alloys Compd.*, 2015.

# **Accelerated weathering test for evaluating “transparent encapsulants on steel substrate” and prediction of lifetime improvement of solar cell**

Sanjay Ghosh<sup>a</sup>, Vasil Stoickov<sup>a</sup>, Luke Haponow<sup>a</sup>, Jeff Kettle<sup>\*a</sup>, Ana L. Martínez<sup>b</sup>, David Gómez<sup>b</sup>, Pascal Sánchez<sup>b</sup>

<sup>a</sup>School of Electronic Engineering, Bangor University, Bangor, Gwynedd LL57 2UT, UK<sup>\*</sup>

<sup>b</sup>ITMA Materials Technology, Photonic Area, C/ Calafates, 33417 Avilés, Spain

\* Corresponding Author [j.kettle@bangor.ac.uk](mailto:j.kettle@bangor.ac.uk)

## **Abstract**

In this work, a brief review of transparent flexible encapsulant for PV modules based on steel substrates is presented followed by our recent work on developing a new easily implementable, cost effect and robust method for selecting best encapsulant for steel as the substrate is discussed. The developed method is laboratory based accelerated weathering test conducted following IEC guidelines.

## **Introduction**

In order to maintain high efficiency of the solar cell during their life time, encapsulation plays the most important part of protecting the solar cell from degradation from the external environment, particularly by blocking ingress of gas and water molecules. Traditionally, glass has been used as encapsulant for solar cell, however with the advance of flexible solar cells, for instance, solar cells fabricated onto flexible plastic and thin steel substrate, the need for efficient flexible transparent encapsulant has been growing. The desired properties of encapsulant required for PV module protection include resistance to UV-visible radiation driven discoloration reaction, embrittlement, and delamination. In addition, release of by-product from the encapsulant into the integral part of solar cell should be stopped or minimised, for example, commonly use encapsulant ethylene vinyl acetate (EVA), releases acetic acid as decomposition by-product which increases the corrosion rate of metallic contacts and lower the performance of solar cells.<sup>1,2</sup> Therefore, new material or combination of different existing material is needed to overcome this issues to make a better encapsulates. In this work, we highlight the use of different low temperature polymer films combination as encapsulant for protecting steel as substrate. The data will enable assessing best encapsulate for protecting and

increasing lifetime of PV modules in the real outdoor environment.

In the following, a brief literature review on flexible transparent enacapsulant in the context of using to protect PV module is presented.

### *Ethylene tetrafluoroethylene: Front and back sheet*

Ethylene tetrafluoroethylene (ETFE) was used in sheet form for encapsulation as it is highly transparent to light, retains its transparency and strength for over 30 years, has a high level of heat retention and has been widely used as building material in recent years.<sup>3,4</sup> ETFE usually employed as a front sheet for solar cells. ETFE coated with a hydrophobic silicon oxide (ETFE-SiO<sub>x</sub>) nanomaterial has been also been reported to significantly improve the barrier properties of the substrate towards water and oxygen.<sup>5,6</sup>

### *Ethylene-vinyl acetate: adhesion and bonding*

Ethylene-vinyl acetate is inherently flexible, tough, clear, has hot-melt adhesive water proofing properties and UV radiation resistance.<sup>7</sup> Some of the other application of EVA includes sealants in meat and dairy packaging, insulation of cables and wires, foot wares as a shock absorber, and various outdoor applications.<sup>8</sup> EVA has also been used as an encapsulating material for crystalline silicone in the industrial production of PV modules.<sup>9,10</sup> It has been recently reported that the effect of temperature and relative humidity on the adhesion and debonding properties of EVA as an encapsulating layer on PV module could be used as a measure to predict their long-term reliability or to develop accelerated aging test model.<sup>11</sup> It has been reported that using fluorescent organic dyes dissolved in the pre-existing EVA encapsulation layer results in 0.18% absolute higher efficiency of commercial screen-printed multi-crystalline silicon

photovoltaic modules and improved stability to UV degradation.<sup>12</sup>

#### *Polyvinyl butyral: adhesion and bonding*

Polyvinyl butyral (PVB) has strong binding, adhesion to many surfaces and film-forming properties, excellent optical transparency, high compatibility with other polymer and flexible properties. PVB major applications include laminated safety glass for automobile windshields, binders for ceramics and metal powders, adhesive, and printing ink for packaging.<sup>13</sup> PVB as encapsulant material for PV module has been investigated, relatively recently, for their high stability against UV radiation and the high adhesive force to glass and other PV substrates.<sup>14,15</sup> An advantage of PVB ( $T_g = 35^\circ\text{C}$ ) over EVA ( $T_g = -16^\circ\text{C}$ ) is its higher glass transition temperature which makes it suitable for PV module operating in a cold region.<sup>15</sup>

#### *Polyethylene terephthalate: barrier layer*

Polyethylene terephthalate (PET) is a transparent, very lightweight, a semi-crystalline resin in its natural state and can be semi-rigid to rigid depending on its processing. It is normally processed by sheets as expensive extruding equipment is otherwise necessary. PET is excellent water and moisture barrier material, widely used as plastic bottles for soft drinks and food packaging, and are 100% recyclable.<sup>16</sup> It has been investigated as back sheet material for PV module protection with improvement in barrier properties when coated with silicon oxide (PET-SiO<sub>x</sub>).<sup>5,17,18</sup> PET has been reported to effectively protect the polymeric multilayer from UV degradation and damage due to moisture when used as back sheet for PV modules.<sup>19,20</sup> Planarised PET is widely used as substrate for manufacturing flexible transparent electrodes for optoelectronic applications.

#### *Polyethylene napthalate: barrier layer*

Polyethylene napthalate (PEN) is a polyester-based barrier layer and provides very good oxygen barrier properties and consider as emerging material for electronic industry.<sup>21,22</sup> Other important properties of PEN include good thermo-oxidative resistance, high strength and modulus, chemical and hydrolytic resistance and ultraviolet light barrier resistance.

Some of the important properties of the polymer films of EVA, PVB, ETFE, PET and

PET are summarised in table 1. All the polymers possessed good transparency (T) for considering as transparent encapsulate. The UV durability (X) is highest for ETFE and most commonly use as front sheet material, which provides the necessary shield against the harmful UV-radiation.

**Table 1** Properties of transparent polymers

	$T_g$	T	X
EVA	-16 °C	93.9%	++
PVB	35 °C	93.9%	++
ETFE	-	90%	+++
PET	67-81 °C	95%	++
PEN	122 °C	95%	+

$T_g$  = Glass transition temperature, T = Light transmittance, X =UV durability (under 42 suns at 6000h of exposure)<sup>23,15</sup>

## Results and discussion

The transparent polymer films considered for the encapsulation of steel samples in this work comprising a combination of ETFE, EVA, PVB, PET and PEN having films thickness above 100 microns. Different combination of polymer films were trialled as encapsulation materials, by considering their physical properties known in the literature as protective front sheet, back sheet, sealant, and encapsulate for PV modules.

ETFE has been primarily used as outer protecting layer front sheet for the encapsulation of steel samples because it is available in sheet form and can be applied to substrates of steel using an adhesive. EVA and PVB were used as encapsulating layers, as these provide adhesive binding between the films as well as strong adhesion with the underlying steel substrates. PET and PEN were considered as barrier layer owing to their excellent gas and moisture barrier properties. As both of these materials are applied in sheet form, an adhesive (such as EVA or PVB) is needed to be used in combination with the PET/PEN.

The testing protocol for evaluating the encapsulant for steel substrate is shown in figure 1. The polymer films and their different combinations were subjected to QUV accelerated weathering test to simulate the outdoor weathering condition. The test conducted according to ISO guideline (4982-3:2006). The performance was evaluated on the basis of change in percentage transmission (%T) and yellow index (YI). After QUV test, the selected films combination were used to

encapsulate two types of steel for further evaluation by thermal cycling (TC) and thermal humidity cycling test (THC) following IEC guideline (61646). Based on the extent of decomposition assessed by combination of visual inspection, microscopy, Raman spectroscopy, XRD and adhesion measurement best encapsulant type is predicted.

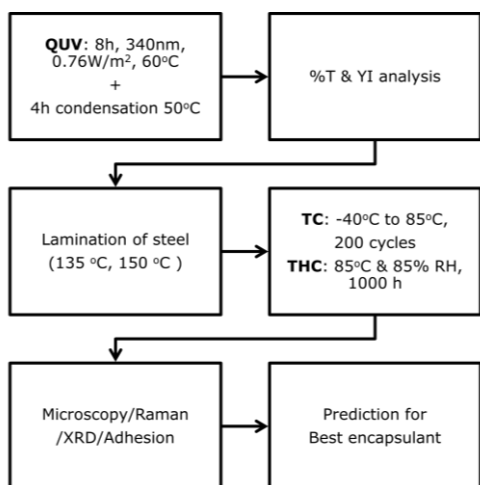


**Figure 1** Test protocol for selecting encapsulant.

Figure 2 depicts the QUV test carried out for the combination of polymers films. The films selected for next level of study must have the transparency greater than 85% and yellow index less than 5%. Several polymer combination e. g. ETFE/PVB/PET/PVB, ETFE/EVA and ETFE/PVB was found to be passed the QUV test and were consider for lamination of steel sample. For illustration, an example of lamentoed steel sample (4 cm x 4cm area) is shown in figure 3.

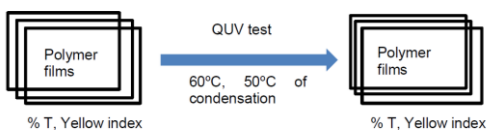


**Figure 2** Combination of polymer films exposed to QUV test.

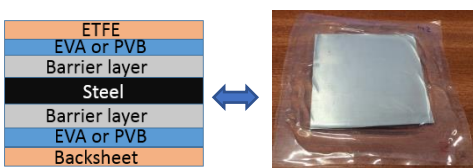


**Figure 3** Laminated steel sample.

The laminated steel samples were subjected to thermal cycling test. No visual

decomposition was observed after thermal cycling test indicating the potential of the the encapsulate to survive outdoor weathering condition for about 10 years. A more stringent test was performed by thermal-humidity test using climate chamber. Noticeable difference were observed even by visual inspection. For illustration, an encapsulated steel sample after THC of 1000 hour is shown in figure 4. The extent of corrosing and decompostion of encapsulant was analysed by combination of micrscopy, Raman spectrsocopy, XRD, and adehesion measurement. The combined results were used to predict the best encapsulant that can be used to protect the PV module in outdoor environment for more than 15 years. The combination ETFE/PVB/PET/PVB was found to best among the different combinations investigated in this study. The best combination encapsulate has been under investigation for protecting OPV modules for outdoor weathering test. The results will be presented elsewhere.

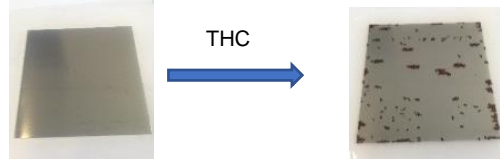


**Figure 4** An encapsulated steel sample exposed to thermal humidity cycling (THC).

## Conclusion

We have presented a low cost, easily implementable and robust test method to evaluate performance of low temperature, transparent flexible encapsulate for protecting steel substrate. The data generated through the method can be used for selecting best encapsulant to protect and maintain high efficiency in their lifetime of PV module exposed to outdoor environment.

## Acknowledgement

We are grateful to European Union's Research Fund for Coal and Steel (RFCS) for funding STEELPV project under grant agreement no. [RFSR-CT-2014-00014](#).

## References

- 1 M.D. Kemp, "Ultraviolet light test and evaluation methods for encapsulants of photovoltaic modules," *Sol. Energy Mater. Sol. Cells*, 94, 246-253, **2010**.
- 2 M. Jørgensen, K. Norman, F. C. Kerbs, Stability/degradation of polymer solar cells, *Sol. Energy Mater. Sol. Cells*, 92, 686-714, **2008**
- 3 Designing Building Wiki, The construction industry knowledge base, **2016** [online] <https://www.designingbuildings.co.uk/wiki/ETFE>
- 4 S. Robinson-gayle, M. Kolokotroni, A. Cripps, and S. Tanno, "ETFE foil cushions in roofs and atria," *Construction and Building Materials*, 15, 323-327, **2001**.
- 5 Rossi G, Altavilla C, Scarfato P, Ciambelli P, "Incarnato L. Deposition of transparent and flexible nanolayer barrier on standard coating materials for photovoltaic devices" *Surf Coat Tech.*, 239, 200-5, **2014**
- 6 G. Rossi, C. Altavilla, P. Scarfato, P. Ciambelli, and L. Incarnato, "Durability study of transparent and flexible nanolayer barrier for photovoltaic devices," *Polym. Degrad. Stab.*, 112, 160-166, **2015** [<http://dx.doi.org/10.1016/j.polymdegradstab.2014.12.022>].
- 7 Nikwax Water proofing, 2016 [Online] [http://www.nikwax.com/en-us/how\\_nikwax\\_works/introduction.php](http://www.nikwax.com/en-us/how_nikwax_works/introduction.php)
- 8 EVAX® EVA copolymer resin, 2016 [online] <http://www.dupont.co.uk/products-and-services/plastics-polymers-resins/ethylene-copolymers/brands/elvax-ethylene-vinyl-acetate.html>
- 9 A. W. Czanderna and F. J. Pern, "Encapsulation of PV modules using ethylene vinyl acetate copolymer as a pottant : A critical review," *Solar Energy Materials and Solar Cells*, 43, 101-181, **1996**.
- 10 F. J. Pern and S. H. Glick, "Photothermal stability of encapsulated Si solar cells and encapsulation materials upon accelerated exposures," *Sol. Energy Mater. Sol. Cells*, 61, 153-188, **2000**.
- 11 F. D. Novoa, D. C. Miller, and R. H. Dauskardt, "Adhesion and debonding kinetics of photovoltaic encapsulation in moist environments," *Prog. Photovolt: Res. Appl.*, 24, 183-194, **2016**.
- 12 E. Klampaftis and B. S. Richards, "Improvement in multi-crystalline silicon solar cell efficiency via addition of luminescent material to EVA encapsulation layer," *Prog. Photovolt: Res. Appl.*, 19, 345-351, **2011**.
- 13 Kuraray, Polyvinyl butyral (PVB) resins for secure bonding. 2016 [online], <http://www.kuraray.eu/en/produkte/product-groups/polyvinyl-butyral/>
- 14 K. Agroui, B. Koll, G. Collins, M. Salama, A. H. Arab, and A. Belghachi, "Characterization of encapsulant materials for photovoltaic solar energy conversion," Proc. SPIE7048, Reliability of Photovoltaic Cells, Modules, Components, and Systems, 70480G (September 10, **2008**). [<doi:10.1117/12.794012>].
- 15 O. Hasan and A. F. M. Arif, "Performance and life prediction model for photovoltaic modules: Effect of encapsulant constitutive behavior," *Sol. Energy Mater. Sol. Cells*, 122, 75-87, **2014** [<http://dx.doi.org/10.1016/j.solmat.2013.11.016>]
- 16 Plasticsinfo.org, Better living with plastics, The safety of Polyethylene Terephthalate (PET), **2016** [online], <https://plasticsinfo.org/Main-Menu/MicrowaveFood/Need-to-Know/Plastic-Bev-Bottles/The-Safety-of-Polyethylene-Terephthalate-PET.html>
- 17 G. Oreski and G. M. Wallner, "Aging mechanisms of polymeric films for PV encapsulation," *Solar Energy*, 79, 612-617, **2005**.
18. M. P. Nikiforov, J. Strzalka, and S. B. Darling, "Solar Energy Materials & Solar Cells Delineation of the effects of water and oxygen on the degradation of organic photovoltaic devices," *Sol. Energy Mater. Sol. Cells*, 110, 36-42, **2013**.
19. C. Lin, P. J. Krommenhoek, S. S. Watson, and X. Gu, "Chemical depth profiling of photovoltaic backsheets after accelerated laboratory weathering," *Proc. SPIE* 9179, Reliability of Photovoltaic Cells, Modules, Components, and Systems VII, 91790R (October 8, **2014**); [<doi:10.1117/12.2066400>].
20. X. Gu, P. J. Krommenhoek, C. Lin, L. Yu, and S. S. Watson, "Depth profiling of mechanical degradation of PV backsheets after UV exposure," *Proc. SPIE* 9563, Reliability of Photovoltaic Cells, Modules, Components, and Systems VIII, 956305 (September 23, **2015**); [<doi:10.1117/12.2187171>]
21. H. Han, D. Adams, J. W. Mayer, T. L. Alford, and H. Han, "Characterization of the physical and electrical properties of Indium tin oxide on polyethylene naphthalate Characterization of the physical and electrical properties of Indium tin oxide on polyethylene naphthalate," *J. App. Phys.*, 98, 083705, **2005**
22. M. B. O. Regan, M. Hildner, S. Prakash, and M. Sellars, "Plastic displays: recent developments at DuPont Displays," *Proc. SPIE* 5214, Organic Light-Emitting Materials and Devices VII, 11 (February 16, **2004**); [<doi:10.1117/12.515249>].
23. M. Kempe, Overview of scientific issues involved in selection of polymers for PV applications, in: Proceedings of 37<sup>th</sup> IEEE Photovoltaic Specialists Conference, Seattle, **2011**, pp.85-90.

# **Sr<sub>4</sub>Al<sub>14</sub>O<sub>25</sub>: Eu, Dy as a potential downconverter for crystalline-silicon solar cells.**

**Joseph Day\*, S. Senthilarasu, Tapas K. Mallick**

Environmental and Sustainability Institute, University of Exeter, Penryn Campus, Cornwall TR109FE,  
UK

\*Corresponding Author [jd553@exeter.ac.uk](mailto:jd553@exeter.ac.uk)

**Abstract:** Sr<sub>4</sub>Al<sub>14</sub>O<sub>25</sub>: Eu, Dy is a luminescent material which exhibits photon downconversion. This phenomenon could be utilised to enhance the efficiency of solar cells. Thin-films containing this compound were prepared and applied via spin-coating on top of silicon photovoltaic devices. A quantitative comparison of their performance, before and after the modification is presented.

## **1. Introduction**

A major factor in limiting the efficiencies of today's solar cells is their poor response to short wavelength light. This fundamental problem arises because when photons with energies in excess of the cell's band gap are absorbed, electrons promoted to the conduction band possess additional kinetic energy which is dissipated as heat. These are known as thermalization losses and account for 33% of the incident solar energy being wasted [1]. The Shockley-Queisser limit accounted for these unavoidable processes and set the maximum efficiency of a 1.1 eV single junction cell to be approximately 30% [2]. However, if the incident spectrum could be modified to match the band gap of the cell before being absorbed, then these thermalization losses would be reduced and device efficiency increased. There is a physical process called downconversion which can realise this by effectively splitting a high energy photon into two photons of lower energy. Trupke et al [3] predicted a 38.6% theoretical efficiency limit for a 1.1 eV silicon cell if an optimal downconversion layer could be placed on top of a cell.

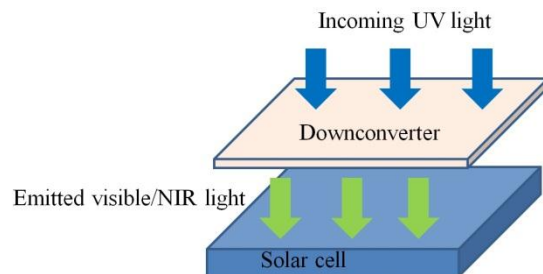


**Fig. 1- A downconversion layer atop a solar cell. The layer absorbs short wavelength radiation and emits at photon energies better suited to the cell, increasing overall efficiency.**

In practice, the materials used for downconverters consist of rare earth ion containing compounds since their ladder like [4] energy level structure makes them ideal for absorbing and re-emitting photons at desirable wavelengths. Crucially in order to realistically improve device performance, a downconversion layer must have a high transmittance in areas of the spectrum where the cell has a decent spectral response. In terms of the rare earth ions used in downconversion-solar cell experiments, europium has stood out as an excellent candidate reported as being used to enhance efficiency and UV response of crystalline silicon, dye sensitized and perovskite cells [5-7]. In this investigation Sr<sub>4</sub>Al<sub>14</sub>O<sub>25</sub>: Eu, Dy was studied as a potential downconverter for crystalline silicon solar cells due to its excitation peak of 365nm and emission peak of 495 nm [8]; where the spectral response is an order of magnitude greater. Hence if a layer containing this compound demonstrated effective downconversion and high transmittance above 400nm, one could expect

a modest improvement in solar cell performance.

## 2. $\text{Sr}_4\text{Al}_{14}\text{O}_{25}$ : Eu, Dy in Sylgard184 results

$\text{Sr}_4\text{Al}_{14}\text{O}_{25}$ : Eu, Dy powder of mean particle size 62 $\mu\text{m}$  and Eu, Dy doping concentrations of 2% and 3% respectively was sourced from Sigma. Due to being in powder form, a method of fixing this material atop the solar cell was required, so Sylgard184 (Dow Corning) was chosen as an embedding medium. Sylgard184 was selected for its optical transparency, stability and ease of application. Four 1.1g samples of Sylgard184 were prepared (by mixing vigorously 1g of base with 0.1g of curing agent and degassing in a vacuum oven) of which two were subsequently combined with 0.1g of  $\text{Sr}_4\text{Al}_{14}\text{O}_{25}$ : Eu, Dy via rapid stirring and further degassing. These solutions were then spin-coated on four silicon solar cells of 1 $\text{cm}^2$  (NAREC, front and rear contacts soldered in-house) at 8000 rpm for 5 minutes followed by heating at 75°C for 5 minutes. The devices were then tested under illumination by a 1000 W/ $\text{m}^2$  solar simulator (Wacom Co. Ltd, WX5-2105-20, AM 1.5G) to record their power conversion efficiencies and compared with the previously measured bare cells. Similarly, a Bentham PVE300 system was used to determine the external quantum efficiency (EQE) and reflectance of the cells, before and after coating.

	Bare efficiency (%)	Coated efficiency (%)	Change (%)
Sylgard cell a	15.10	14.75	-0.35
Sylgard cell b	15.01	15.27	+0.26
Sylgard + powder cell a	14.09	14.20	+0.11
Sylgard + powder cell b	14.14	13.74	-0.40

Table 1- A comparison of the efficiencies of the four cells before and after the coatings were added.

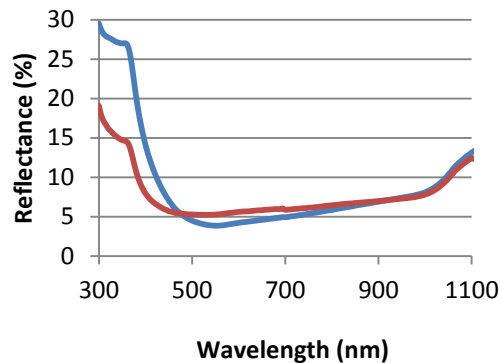


Fig 2- Obtained reflectance spectra of the silicon solar cell before (blue) and after (red) coating with a layer of Sylgard 184 + powder.

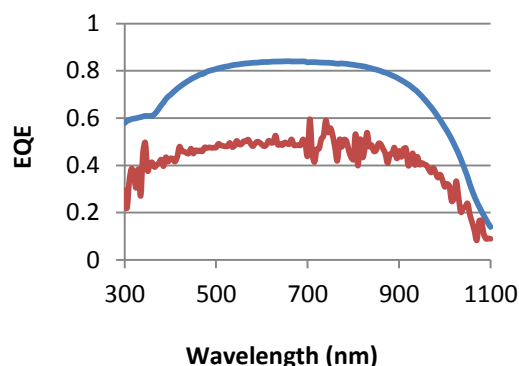


Fig 3- Obtained EQE spectra of the silicon solar cell before (blue) and after (red) coating with a layer of Sylgard 184. The

Unfortunately these results do not yield conclusive improvements in performance. This can, in part, be attributed to the thickness of the Sylgard184 coating leading to unwanted absorption and hence efficiency losses.

## 3. $\text{Sr}_4\text{Al}_{14}\text{O}_{25}$ : Eu, Dy in $\text{TiO}_2$ results

$\text{TiO}_2$  thin-films had been previously investigated by our group for application in emerging photovoltaic devices and showed a high optical transparency in the visible range. It was therefore deemed, they could potentially replace Sylgard184 as the embedding medium to give better results.  $\text{TiO}_2$  paste of 20nm particle size (Dyesol 18NR-T) was mixed with ethanol at ratio of 1:5 and then divided into two vials; in one vial, 10% of the solution's weight of  $\text{Sr}_4\text{Al}_{14}\text{O}_{25}$ : Eu, Dy powder was added. However, the standard  $\text{TiO}_2$  annealing

temperature of 450°C would have been too high for the silicon cells, so instead a temperature of 100°C was used and the heating time increased from 3 hours to 24 hours to compensate. Initially, these were spin-coated on 4cm<sup>2</sup> plain glass substrates at 3000 and 6000 rpm and optical properties analysed by a Perkin Elmer UV/VIS/NIR Spectrometer. The samples showed a high transmittance in the visible range and absorption in the 300-400 nm range, perhaps indicating the excitation profile of the downconversion material.

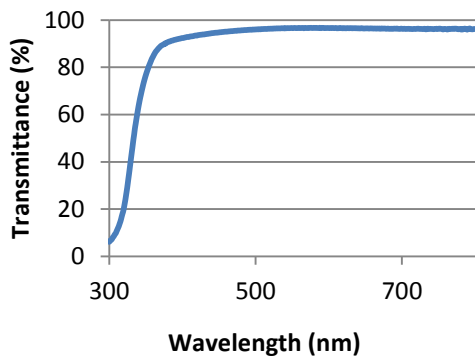


**Fig 4-** Obtained transmittance spectra of the TiO<sub>2</sub> + powder thin-film after spin-coating at 6000 rpm.

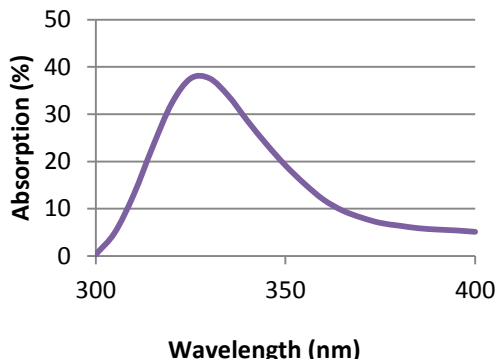


**Fig 5-** Calculated absorption spectra of the TiO<sub>2</sub> + powder thin-film after spin-coating at 6000 rpm.

Then, in a similar procedure to the previous experiment, the power conversion efficiency, EQE and reflectance were measured for four devices before and after coating; two being coated with pure TiO<sub>2</sub>-ethanol solution and two

with the Sr<sub>4</sub>Al<sub>14</sub>O<sub>25</sub>: Eu, Dy containing mixture, all at 6000 rpm and placed on hotplate at 100 °C for 24 hours. A further two silicon cells were left uncoated but underwent the same heating process in order to verify no detriment to their performance.

	Bare efficiency (%)	Coated efficiency (%)	Change (%)
TiO <sub>2</sub> cell a	10.96	13.42	+2.46
TiO <sub>2</sub> cell b	13.48	13.26	-0.22
TiO <sub>2</sub> + powder cell a	15.02	13.28	-1.84
TiO <sub>2</sub> + powder cell b	13.84	N/A	N/A

**Table 2-** A comparison of the efficiencies of the four cells before and after the coatings were added. Contacts had broken for one of the cells, so no result is presented.

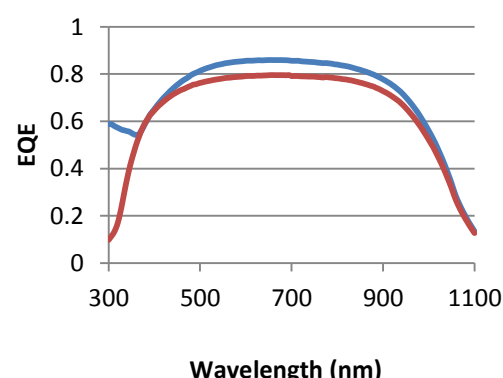


**Fig 6-** Obtained EQE spectra of the silicon solar cell before (blue) and after (red) coating with TiO<sub>2</sub> + powder.

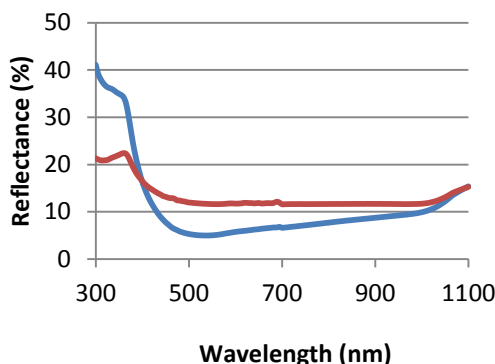


**Fig 7- Obtained reflectance spectra of the silicon solar cell before (blue) and after (red) coating with  $\text{TiO}_2$  + powder.**

Again these results have their shortcomings in that no-discernible enhancements are observed (with the exception of  $\text{TiO}_2$  cell a - which could arise from anti-reflective properties of the applied film). The non-uniformity of the coating and scattering from the relatively large downconversion particles may account for this. Although a fairly high EQE in the UV range could indicate some radiation is experiencing downconversion and reaching the cell and a better performance in the visible range means less parasitic absorption is occurring than with Sylgard184.

#### 4. Future outlook and conclusion

In going forward, it is vital to reduce the transmittance of the coatings in the visible range and optimize the layer for downconversion processes, if we are to attain consistent increases in the cell efficiency. These could be achieved by: (i) an improved experimental methodology (i.e. greater number of cells and better coating techniques), (ii) obtaining a photoluminescent excitation and emission spectra of the downconversion films before coating to cells, (iii) smaller  $\text{Sr}_4\text{Al}_{14}\text{O}_{25}$ : Eu, Dy particle size to reduce scattering losses (e.g. via ball milling) and (iv) a better choice of optically transparent embedding media (for example polymethylmethacrylate or ethylene vinyl acetate). The latter point will affect the cost per  $\text{cm}^2$  of the coating which would be a factor in any cost analysis (aimed to be a later part of this research, once technical enhancements are reported).

To summarise,  $\text{Sr}_4\text{Al}_{14}\text{O}_{25}$ : Eu, Dy powder was embedded in both a Sylgard184 and  $\text{TiO}_2$  thin-film and spin-coated atop silicon solar cells in an attempt to increase efficiency and short wavelength response. Unfortunately, these aims have not yet been met, but the reasons why are discussed and suggestions for improvements in future investigations made.

#### References

- [1] O. Semonin, J. M. Luther, M.C. Beard, Multiple exciton generation in a quantum dot solar cell, 26 March 2012, SPIE Newsroom. DOI: 10.1117/2.1201203.004146
- [2] W. Shockley, H. J. Queisser, Journal of Applied Physics, 1960, 32, 3, 510-519
- [3] T. Trupke, M. Green, P. Würfel, Journal of Applied Physics, 2002, 92, 3, 1668-1674
- [4] G. Chen, H. Ågren, T. Y. Ohulchanskyy, P.N. Prasad, Chem. Soc. Rev., 2015, 44, 6, 1680-1713
- [5] S. González-Pérez, J. Sanchiz, B. González-Díaz, S. Holinski, D. Borchert, C. Hernández-Rodríguez, R. Guerrero-Lemus, Surface & Coatings Technology, 2015, 271, 106-111
- [6] N. Yao, J. Huang, K. Fu, S. Liu, D. E, Y. Wang, X. Xu, M. Zhu, B. Cao, Journal of Power Sources, 2014, 267, 405-410
- [7] X. Hou, T. Xuan, H. Sun, X. Chen, H. Li, L. Pan, Solar Energy Materials & Solar Cells, 2016, 149, 121-127
- [8] H. Sun, L. Pan, G. Zhu, X. Piao, L. Zhang, Z. Sun, Dalton Transactions, 2014, 43, 14936

# Water Vapour Transmission Rate of Ethylene Vinyl Acetate (EVA) Encapsulant with different Curing Levels

Jiang Zhu\*, Christina Ng, Daniel Montiel-Chicharro, Thomas R. Betts, Ralph Gottschalg

Centre for Renewable Energy Systems Technology (CREST), Wolfson School of Mechanical, Electrical and Manufacturing Engineering, Loughborough University, United Kingdom,

\* Corresponding Author [J.Zhu@lboro.ac.uk](mailto:J.Zhu@lboro.ac.uk), +44 (0)1509 635313

## Abstract

Water vapour transmission rate of EVA sheets with different curing levels is investigated under a various temperature and relative humidity levels. The gravimetric cup method is used to measure the transmission rate. EVA samples' thermal and structural properties are measured and results confirm that the curing level does not affect material VAc contents or crystallinity, though their degrees of crosslinking are significantly different. For the EVA studied in this work, lower degrees of crosslinking (gel content <60%) show water transmission rate at about 35 g/m<sup>2</sup>/day under 23°C and 1 bar. The transmission rate reduces with the increasing crosslinking degree and reaches about 10 g/m<sup>2</sup>/day for samples of gel content >80%. Results also show the water transmission is able to be accelerated by temperature with an activation energy of about 7.5kJ/mol.

## Introduction

Photovoltaic (PV) modules consist of a series of interconnected solar cells sandwiched between two layers of encapsulants, a layer of front glass, and a back sheet. The lifetime of PV modules is expected to be 25 years or more, which is also the duration most manufacturers guarantee. The prediction of lifetime in dependence of operating environments, however, has not been established as correlations of failure modes, degradation mechanisms and environmental stresses are not yet fully understood.

Moisture ingress related degradation leads to corrosion, delamination, yellowing etc. In order to investigate the effect of moisture ingress into PV module in a realistic period of time, normally modules are subjected to accelerated testing at elevated humidity and temperature levels, which assume the rate of moisture transmitted through the encapsulant is accelerated and significantly higher. However, questions have been raised regarding the relevance and equivalence of accelerated tests to real outdoor conditions [1]. The overall process of degradation mechanism can be regarded as a chain of sub-processes. Each sub-process may lead to a different failure mode under a particular condition. The aim of this work is to bring insight for understanding the sub-processes, which can then be demonstrated to serve as a foundation in

translating accelerated testing conditions to realistic outdoor conditions.

PV modules rely on encapsulation materials to minimise the effect of moisture ingress. Typical wafer based PV modules use ethylene vinyl acetate (EVA) as encapsulant. EVA is a copolymer of ethylene and vinyl acetate (VA) with VA groups randomly distributed along the backbone. Important properties influencing the EVA's resistance to water ingress are material crystallinity, percentage of VAc contents and degree of crosslinking.

This work investigates the water vapour transmission rate (WVTR) of EVA with different curing levels. During PV module operation, water vapour permeates into module and slowly accumulates. It also reacts with EVA and generates acetate acid. The latter may chemically interact with the active element that causes degradation. The speed of this process is, based on past work, expected to depend on the degree of EVA crosslinking [2]. In order to understand the potential mechanisms and model the sub-process of moisture ingress into module, the first step is to measure the rate of water vapour transmitted through EVA, which is carried out in the paper under a various temperature and humidity levels for EVA samples of different curing levels.

## Methodology and Mathematical Model

The water vapour transmission rate is measured according to the standard ASTM E96 [3], which uses a gravimetric cup filled with either 25g of desiccant or 30g water, as shown in Fig 1. This is then sealed with the test sample, i.e. cured EVA sheets, and placed in an environmental chamber. The weight change of the gravimetric cup is monitored during the course of water vapour transmitting through the EVA sheet. It can be expressed as a function of time. The WVTR is calculated from the steady-state region.

Mathematically, the primary mechanism of water vapour permeated through EVA, can be expressed as an activated diffusion. This means that the permeant of water vapour dissolves in the film matrix at the higher concentration side and diffuses through the film and evaporates from the other surface. This is driven by concentration gradients. The diffusion is the key step and the rate depends on size, shape of the penetrating molecule of the permeant, which in this work is the water vapour. It

also depends on the thermal and structural properties of the EVA film, which will be investigated in this paper.

The water vapour diffusion through EVA can be described by the Henry and Fick's law, which relates the permeation rate with the area and thickness of the film as given below:

$$J = -P \left( \frac{p_1 - p_2}{l} \right) \quad (1)$$

where  $J$  is the diffusion flux,  $P$  is the permeation coefficient reflecting the speed at which the permeant diffuses through the EVA,  $p_1$  and  $p_2$  are the water vapour partial pressures at both surfaces of the EVA film and  $l$  is the EVA film thickness.

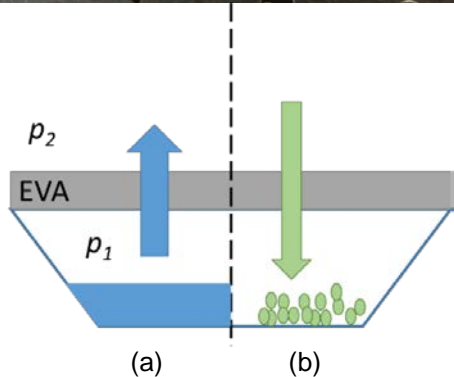


Fig 1: Illustration of the gravimetric cup method a) with water, and b) with desiccant.

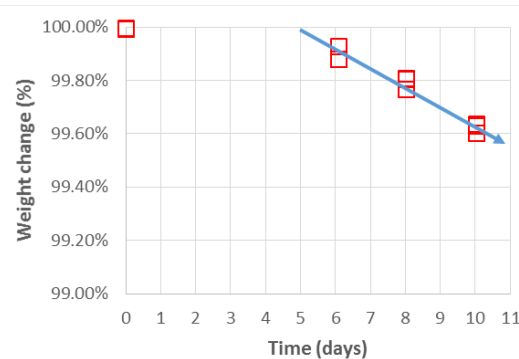


Fig 2: A typical WVTR measurement showing a transient phase at beginning.

In the experiment, the pressure difference  $\Delta p = p_1 - p_2$  ( $p_1 > p_2$ ) is constant as the water vapour partial pressures on both sides of the EVA film are assumed to be constant within the testing period. The diffusion flux  $J$  representing the total mass of

transmitted water per unit area per day ( $\text{g m}^{-2} \text{ day}^{-1}$ ) can be measured by the weight change of the gravimetric cup:

$$J = \frac{\Delta G}{tA} \quad (2)$$

where  $\Delta G$  is the weight change during the time  $t$ , and  $A$  is the testing area of EVA film. As the thickness of film varies, the water vapour transmission rate (WVTR) is normalised to film thickness  $l$  to obtain the specific rate:

$$\text{WVTR} = J \cdot l = \frac{\Delta G}{tA} l = -P \cdot \Delta p \quad (3)$$

where in this work all EVA sheets tested are corrected to the thickness of 0.42mm. Therefore, the WVTR is a function of permeation coefficient and the water vapour pressure difference between the two surfaces of EVA.

A typical measurement of WVTR is demonstrated in Fig 2. It shows that the transmission of water vapour was slower in the first five days and accelerated afterwards. Therefore the WVTR should be determined from the data points without the first data during the transient phase.

## Experimental

### 1 EVA samples of different curing levels

Samples of single layer EVA sheets laminated under a fixed time of 10 minutes, but different temperatures between 125°C and 150°C (L125 – L150) were produced in order to investigate the effect of curing level on WVTR.

The degree of EVA crosslinking was measured for samples of L125, L135, L145 and L150 by the standard method of Soxhlet-type extraction process [4]. Up to five samples were measured for each lamination condition.

### 2 Thermal gravimetric analysis (TGA)

Small EVA samples extracted from EVA sheets L125, L135, L145 and L150 were subject to TGA measurement to calculate the VAc contents. Samples were heated up from 30°C to 600°C at the rate of 10°C per minute. Three samples of about 5mg were measured for each laminating condition.

The VAc contents of EVA is related to the first weight loss between 280–380°C and calculated as below [5]:

$$VAc\% = \text{weight loss} \times \frac{M_{VAc}}{M_{HAc}} \quad (4)$$

where  $M_{VAc}$  is the atomic mass of VAc and  $M_{HAc}$  is the atomic mass of HAc.

### 3 Differential Scanning Calorimetry (DSC)

Small EVA samples extracted from EVA sheets L125, L135, L145 and L150 were also tested with DSC for two heating and cooling cycles between -25°C and 225°C at the rate of 10°C per minute to evaluate the EVA crystallinity. The first cycle is to remove the volatile impurities and erase the former thermal history [6]. The crystallinity,  $X_c$ , can be calculated from the second cooling cycle according to the equation below:

Table I: WVTR testing condition (W: water, D: desiccant, 30% - 85%: testing relative humidity).

Testing temperature		Sample lamination temperature					
		L125	L128	L135	L140	L145	L150
23°C	W, 30%	W, 30%	W, 30%	W, 30%	W, 30%	W, 30%	W, 30%
33°C	W, 30%	W, 30%	W, 30%	W, 30%	W, 30%	W, 30%	W, 30%
60°C					D, 60%	D, 85%	
70°C					D, 60%	D, 85%	
80°C					D, 60%	D, 85%	
85°C					D, 60%	D, 85%	

$$X_c = \frac{\Delta H_f}{\Delta H_f^*} \times 100\% \quad (5)$$

where  $\Delta H_f^*$  is the enthalpy of fusion of a perfect polyethylene crystal (which is 277.1J/g [7]), and  $\Delta H_f$  is the enthalpy of fusion of the EVA sample. Three samples of about 6mg were measured for each lamination condition.

#### 4 WVTR at different temperature and humidity levels

The test units of WVTR, as shown in Fig 1, were placed in environmental chambers. The chambers were set to a number of combinations of temperature and relative humidity levels as shown in Table I. For low temperatures, water was put in gravimetric cups, while desiccant was used when testing at high temperature levels. Each condition has tested two to four samples to ensure good repeatability. Tests at 23°C and 33°C were used to investigate the correlation of curing level and transmission rate. Tests at higher temperatures were used to evaluate the thermal activation effect.

## Results and Discussions

### 1 Gel content

Fig 3 plots the averaged values of gel contents for EVA samples L125, L135, L145 and L150. The L125 shows gel content less than 60%. Samples of L135, L145 and L150 show a linear increase in gel contents from 73% to 86%. EVA samples with a variety of crosslinking degrees, achieved by different lamination temperature, were used in the work.

### 2 VAc contents

The TGA measurements of EVA samples L125, L135, L145 and L150 are plotted in Fig 4. It clearly shows all the measured curves are the same, which means the VAc contents are the same for the samples though their degrees of crosslinking are significantly different. The calculated VAc contents are around 32% for these EVA samples.

### 3 Crystallinity

Crystallinity of EVA can be calculated according to Eq (5) from the peaks of DSC curves shown in Fig 5. The calculated crystallinity values are around 6% for all the samples, though there are minor shifts in the heat flow curves. This means the degree of crystallinity of EVA after different levels of crosslinking remains unchanged. VAc contents of EVA correlate with the crystallinity is reported in [8] as well.

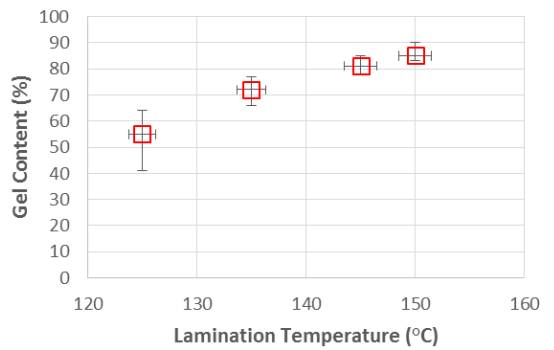


Fig 3: Averaged gel content of EVA versus lamination temperature.

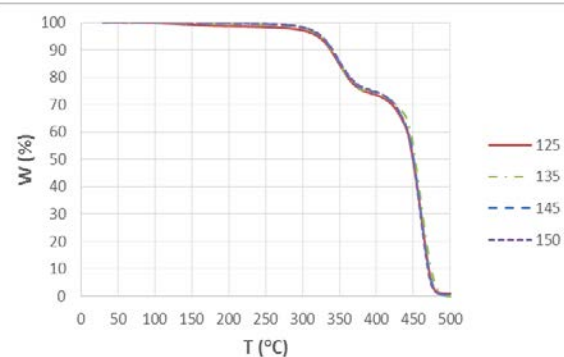


Fig 4: TGA curves of cross linked EVA cured at different temperature.

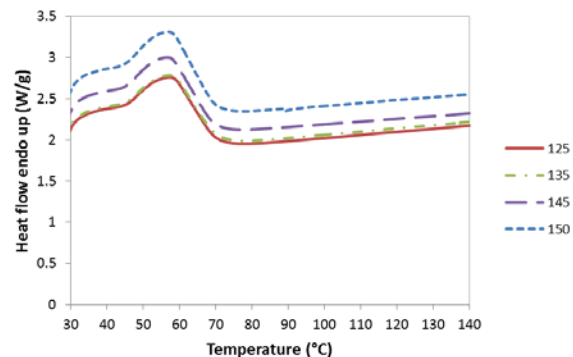


Fig 5: DSC curves of cross linked EVA cured at different temperature.

#### 4 WVTR and crosslinking degree of EVA

Thermal and structural properties of EVA material have been examined for all samples, which show no changes in VAc contents and crystallinity. Thus, influences from these two factors can be excluded.

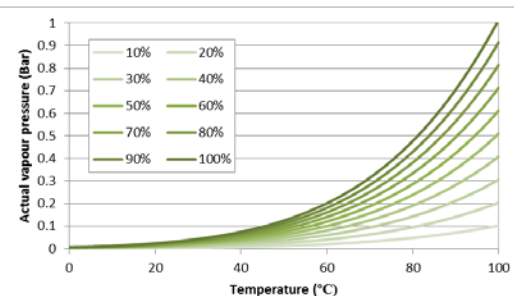


Fig 6: Actual water vapour pressure at different temperature and relative humidity.

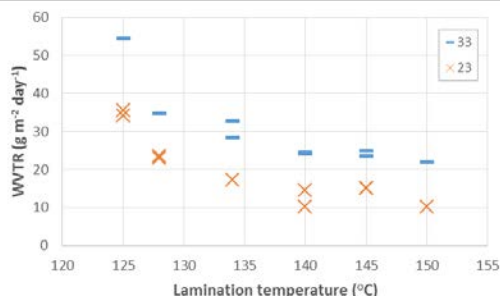


Fig 7: Normalised WVTR at 23°C and 33°C.

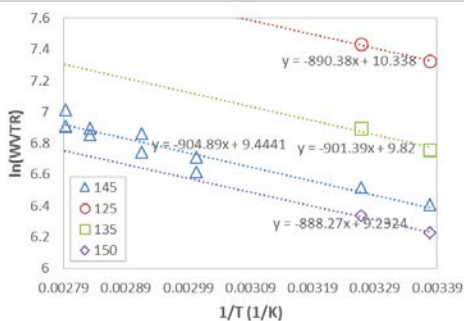


Fig 8: Arrhenius plot of normalised WVTR.

According to Eq (3), the WVTR is related to the pressure difference,  $\Delta p$ , between the two surfaces of EVA. The actual water vapour partial pressure varies at different temperature and relative humidity levels, which is estimated in [9] and plotted in Fig 6. The measured WVTR at different conditions for different samples needs to be corrected for the pressure difference. In this work, all results are normalised to pressure difference of 1 bar and reported as gram per square meter per day ( $\text{g}/\text{m}^2/\text{day}$ ) as shown in Fig 7. L125 samples, which are the low cross linked ones, have the largest transmission rate of about 35  $\text{g}/\text{m}^2/\text{day}$  at 23°C. As the degree of crosslinking increases, the WVTR decreases from 35 to 10-15  $\text{g}/\text{m}^2/\text{day}$ . At 33°C, the WVTR is generally higher due to thermal acceleration. Its dependency on crosslinking degree follows the similar trend as that at 23°C.

The transmission rate at different temperatures is found to be well described by the Arrhenius relation [10]. Fig 8 plots the measured WVTR at different conditions normalised to 1 bar against testing temperature. With result of L145 samples, the

activation energy can be estimated, which is 7.5kJ/mol. The results of L125, L135 and L150 samples so far exhibit similar activation energies.

## Conclusions

DSC and TGA measurements show no changes in VAc contents and crystallinity for EVA after curing to different degrees, which excludes the influences from these two factors. A clear correlation between EVA crosslinking degree and WVTR is observed. Less cross linked EVA samples exhibit significant higher transmission rate. This can be explained by the relative high existing free volume within the polymer and thus the mobility of water vapour is relatively easier. The WVTR is thermal activated and the rate is accelerated with an activation energy of 7.5kJ/mol for the EVA material investigated.

## References

- [1] S. Kurtz, et al, A framework for a comparative accelerated testing standard for PV modules, IEEE 39<sup>th</sup> Photovoltaic Specialists Conference, 2013.
- [2] J. Zhu, et al, The role of EVA encapsulation in the degradation of wafer based PV modules, in 12<sup>th</sup> Photovoltaic Science, Application and Technology Conference, 2016, Liverpool.
- [3] ASTM E96/E96M-16 Standard Test Methods for Water Vapor Transmission of Materials, ASTM International, West Conshohocken, 2016.
- [4] American Society for Testing and Materials, Standard Test Methods for Determination of Gel Content and Swell Ratio of Crosslinked Ethylene Plastics, ASTM D2765-11, 2006.
- [5] X.E. Cai, H. Shen, Apparent activation energies of the non-isothermal degradation of EVA copolymer, *Therm. Anal. Calorim.*, vol. 55, no. 1, pp. 67–76, 1999.
- [6] L.M. Huang, et al, The Evaluations of Physical Properties and Lamination Process Parameters of EVA Encapsulant by Thermal Analysis, in 24<sup>th</sup> European Photovoltaic Solar Energy Conference, Hamburg, Germany, 2009.
- [7] J. Brandrup, et al, Polymer handbook. Wiley-Interscience, New York, 1999.
- [8] X.M. Shi, et al, Non-isothermal crystallization and melting of ethylene-vinyl acetate copolymers with different vinyl acetate contents, eXPRESS Polymer Letters Vol.2, No.9, 2008, pp. 623–629.
- [9] A. Wexler, Vapor pressure formulation for water in range 0 to 100°C. A revision. *J. Res. Natl. Bur. Stand.* 80A, 1976, pp. 775-285.
- [10] J.R. Welty, et al, *Fundamentals of Momentum, Heat, and Mass Transfer*. Wiley, 2001.

# **Outdoor degradation, performance analysis and software modelling of Organic Photovoltaics (OPVs) fixed to a building prototype**

Vasil Stoichkov<sup>a</sup>, Noel Bristow<sup>a</sup>, Dr Tracy Sweet<sup>b</sup>, Dr Jeff Kettle<sup>a\*</sup>,

<sup>a</sup> School of Electronic Engineering, Bangor University, Bangor, Gwynedd, LL57 1UT, UK \* contact author; j.kettle@bangor.ac.uk

<sup>b</sup> Cardiff University School of Engineering, Centre for Integrated Renewable Energy Generation and Supply, Cardiff, CF24 3AA, United Kingdom

## **Abstract**

Here we present the analysis of eight consecutive months investigating the performance, power generation and degradation of OPV modules located in different positions at Bangor University. In order to facilitate our research a scaled-down building prototype was employed which accommodated a set of OPV modules installed on each available side (east, west, north, south and horizontal flat). All modules were encapsulated prior deployment using a technique developed at Bangor University. The output of each module was recorded and analysed over the course of two distinct seasons (summer and winter). The stability of the modules with respect to the variation in temperature and irradiance levels was investigated.

## **Introduction**

Building integrated photovoltaics (BIPVs)[1] are a composition of photovoltaic (PV) modules used as replacement for building components such as windows and facades. Contrary to building adopted photovoltaic (BAPV)[2] BIPVs do not require a completed structured prior to installation. Nevertheless, whilst the number of PV installations has been growing rapidly in Europe over the past 10 years, there is a low uptake on commercial buildings such as warehouses and factories. This is despite the consideration that 40% of the energy demand globally comes from buildings[3].

The warehouses and factories are well suited to large area BIPVs made from perovskite solar cells (PSCs) or OPVs. The latter can be directly installed using a coating line with the possibility of supplying the demands of large area building structures.

OPVs could present a good opportunity for such BIPV installations due to the relatively low anticipated cost per square metre of modules. At the same time warehouses are typically cuboid in nature, with vertical side walls and a flat roofs which currently presents an obstacle in terms of PV performance as each side of the building will experience different irradiation levels and undergo different temperature changes during the course of the day. This will affect the level of degradation which each module experiences.



*Figure 1 – A) The new Aldi distribution centre at Goldthorpe being one of the largest solar PV installations on a cold store facility in the UK[4]. B) Lyreco & Guinness Asset Management in Telford, West Midlands, the fourth largest rooftop solar array in the UK[5].*

## **Experimental**

### **Outdoor setup**

The outdoor experiments were performed for a period of 8 months, Dec 2015 – July 2016 at the School of Electronics, Bangor, Gwynedd, North Wales (53.23°N 4.13°W) with an altitude of

approximately 40m above sea level. Long term climatic average temperatures for the winter are 4.7 °C and for the summer are 14 °C, obtained from Meteorological Office for RAF Valley on Anglesey. The humidity levels for both summer and winter were very similar: with an average mean of 79%, an average maximum of 90%, and the average minimum being 61% in summer and 65% in winter. UV indices were very different with an average of 1.07 in the summer (average maximum 5.45) and 0.43 in the winter (average maximum 2.38).

The outdoor monitoring system at Bangor University is based on the roof of the School of Electronic Engineering. The system consists of two silicon reference modules which are monitored using an Egnitec PV measurement system. The modules are kept at maximum power point (MPP) in between periodic current-voltage (IV) sweeps (once every minute). Each module has a PT100 temperature sensor fixed to its backplane.

The organic building integrated photovoltaic (OBIPV) measurement system comprises a cuboid prototype aligned east-west/north-south, with two modules on each face (sides and top). The ten modules are monitored by two 8-channel Botest measurement systems, taking IV curves every 5 minutes.

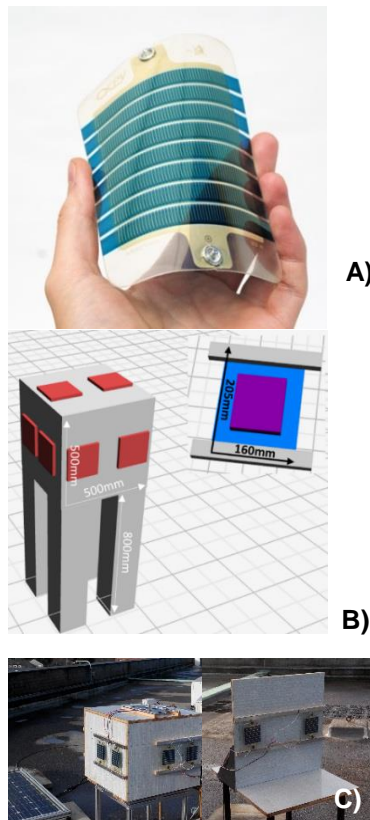


*Figure 2 – A) OPV modules supplied from InfinityPV, Denmark, at 3% efficiency[6]. B) Down-scaled illustration of building prototype constructed and deployed on roof of the Electronic Engineering Department of Bangor University, C) Cube during deployment*

### Module encapsulation

All modules were bonded to a rigid backplane. The encapsulation process followed by soldering of leads to the contact terminals, after which the entire was covered with a layer of PolyDiMethylSiloxane[7] (PDMS). A pre-cut DuPont Teijin PolyEthylene Naphthalate[8] (PEN) film was then fixed over the layer of PDMS isolating the top surface of the module from the extreme outdoor conditions. The PDMS is then allowed to cure at room temperature for 48 hours. The final stage of the encapsulation is sealing the edges of the modules with low temperature sealing epoxy supplied by Dyesol UK. The final product is then taken and re-measured under standard 1 sun AM1.5G solar simulator at STC temperature of 25 °C prior to outdoor installation.

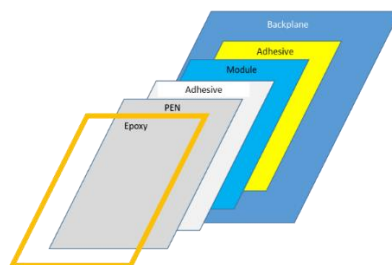


*Figure 3 –Cross-section view of the finalised encapsulated OPV purchased from InfinityPV.*

The ten modules were then laminated outdoors onto the cube structure (two per face).

### Results

#### Diurnal performance

In order to evaluate the diurnal performance, four contrasting days were selected; a sunny and cloudy day in both winter and summer. A sunny and cloudy day in the summer were defined as a day with 600-1000W/m<sup>2</sup> and 200-700W/m<sup>2</sup> respectively. A sunny and cloudy day in the winter were defined as a day with 100-400W/m<sup>2</sup> and 25-150W/m<sup>2</sup> correspondingly.

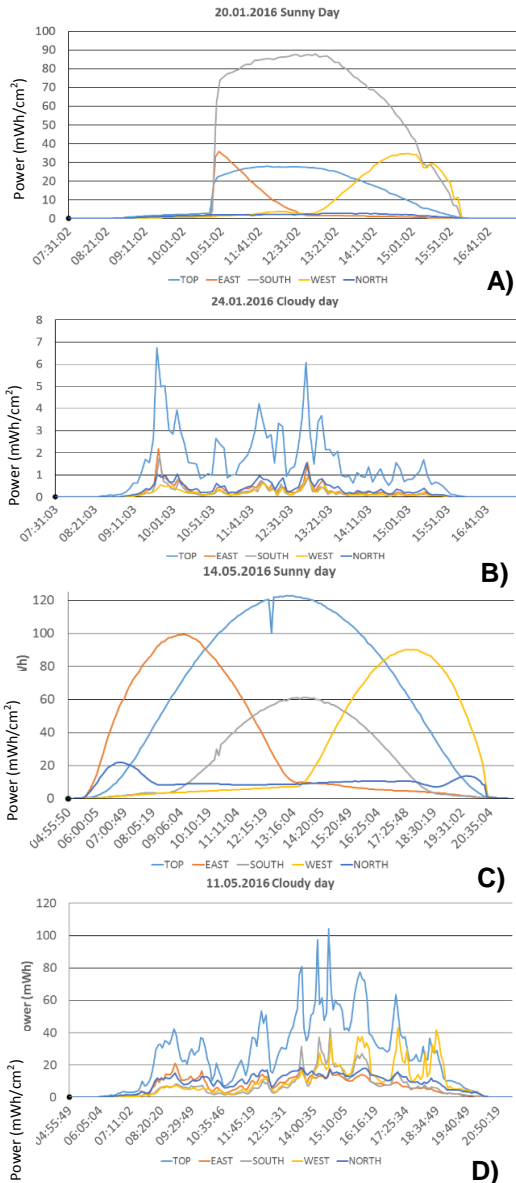


Figure 4 – A), B), C), D) illustrate the diurnal OPV performance recorded over four contrasting days, two in the summer and two in the winter.

### Monthly yield

During the winter period (December – February, UK) the south facing modules contribute the most to the electricity grid, accumulating the highest power for the period, due to the elevation of only 16.35° and natural diurnal sun path. In December, the horizontal modules generate 50% less power than the south facing ones, followed by west which generated 75% less than the south facing modules. East generated the same power as north during mid-winter and then from mid-January this gradually increased in east's favour. All modules followed a linear power generation increase over the course of this experiment, where in the spring

south rapidly reaches a threshold of power conversion, allowing east and west to advance. In April, as a result of the earlier sunrise, East increases its generated power during which period south still generates slightly more than west. Approaching May, nonetheless, east and west are evidently dominating over south which is attributed to the high sun elevation of 60.01° at noon, south facing modules peak time, which is only 24.73° and 36.13° at 08:00am and 05:20pm which are the east and west peak times respectively.

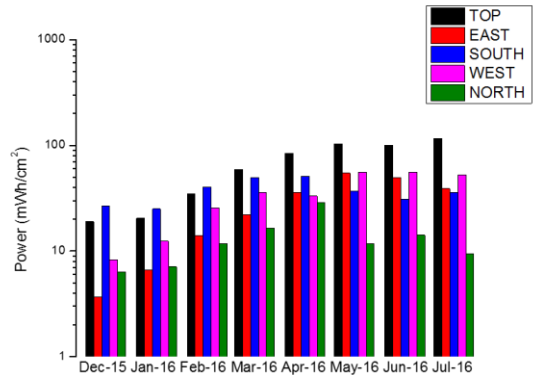
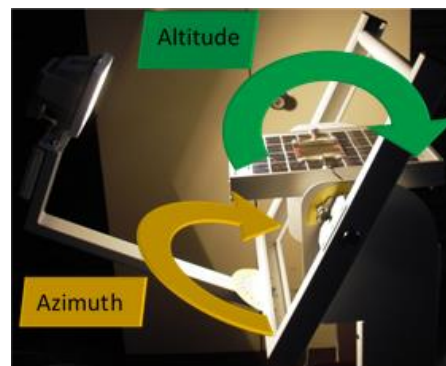


Figure 5 - Graph of the monthly power generation by all examined modules December 2015 through to July 2016.

### Software modelling

For the purpose of predicting outdoor performance of OPV modules, depending on their degree of incidence against the sun and geographical position, an indoor angular test was performed[9].

Each module positioned east, west, north, south and horizontal flat was measured across a range of azimuth and altitude angles and the collected data was then processed and compared against real life module performance (see figure 6).



*Figure 6 – Experimental setup for measuring diurnal performance of OPV modules Lucas Nuelle.*

The diurnal solar simulator allows for simulation of the sun course with  $15^\circ$  increments of azimuth, total of  $360^\circ$  and altitude with  $10^\circ$  increments with a complete sweep of  $180^\circ$ . The equipment allows for taking lifelike diurnal measurements of PV devices by changing the position of the light source in respect to the course of the sun during a full day. The recorded measurements experienced a lowered performance in comparison to illumination under standard AM1.5G simulator due to the spectral mismatch between the light sources.

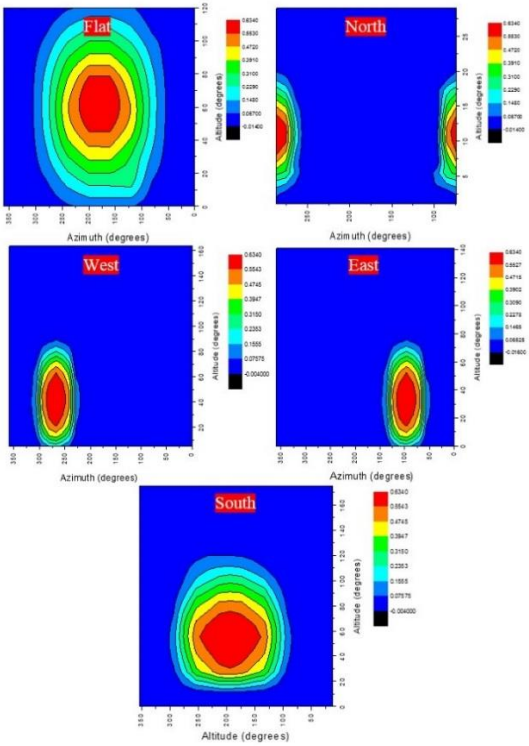


*Figure 7 – position dependent outdoor performance simulation constructed with data collected from indoor experiment (Lucas Nuelle solar simulator, Cardiff University).*

The simulation illustrated defines the summer solstice in the UK which was recorded on June 20<sup>th</sup> 2016. The simulation clearly shows the importance of careful module positioning, which will also depend on the geographical location of the installation (see fig 7).

As it can be seen the vertically positioned OPV modules, except the south facing due to this direction being situated directly towards the sun for a great portion during the summer days, have a very narrow window of normal incidence. The flat modules experience a very uniform illumination where south, in the summer, will

never reach its maximum of performance due to the high sun position by the time it reaches the most optimum illumination incidence. Similarly north harvests very low amount of light due to the natural position of the sun at sunrise and sunset.

## Conclusion

The outdoor performance of a set of OPV modules arranged in an OBIPV fashion has been examined over the course of 8 consecutive months where the energy yield, encapsulation state and module degradation has been constantly monitored. We showed how vital module orientation is to energy yield across diurnal and seasonal change. Finally, we showed how an indoor simulation can be used to predict performance of OPV modules outdoors.

## Acknowledgements

Vasil Stoichkov would like to thank the Sêr Cymru National Research Network for funding of his PhD studies.

## References

- [1] Heinstein, Patrick Ballif, Christophe Perret-Aebi, Laure Emmanuelle ‘Building Integrated Photovoltaics: An emerging market’.
- [2] T. James, A. Goodrich, M. Woodhouse, R. Margolis, and S. Ong, ‘Building Integrated Photovoltaics (BIPV) in the Residential Sector: An Analysis of Installed Rooftop System Prices’, *US Dep Energy*, no. November, p. 50, 2011.
- [3] P. Heinstein, C. Ballif, and L. E. Perret-Aebi, ‘Building integrated photovoltaics (BIPV): Review, potentials, barriers and myths’, *Green*, vol. 3, no. 2, pp. 125–156, 2013.
- [4] ‘The 1.5 MWp solar PV array Aldi Goldthorpe’.
- [5] ‘3.8 MW rooftop PV system completed in UK’.
- [6] ‘InfinityPV OPV modules’.
- [7] ‘Sylgard 184’.
- [8] ‘Teijin DuPont PEN’.
- [9] J. Kettle, N. Bristow, T. K. N. Sweet, N. Jenkins, G. A. dos Reis Benatto, M. Jørgensen, and F. C. Krebs, ‘Three dimensional corrugated organic photovoltaics for building integration; improving the efficiency, oblique angle and diffuse performance of solar cells’, *Energy Environ Sci*, vol. 8, no. 11, pp. 3266–3273, 2015.

# Functionalised Schottky Barriers on Steel

N E Ryall<sup>a</sup>, R. Crook<sup>a</sup> and J A Weinstein<sup>b</sup>

<sup>a</sup> School of Chemical and Process Engineering, University of Leeds, LS2 9JT

<sup>b</sup> Department of Chemistry, University of Sheffield, S10 2TN

\* Corresponding Author elner@leeds.ac.uk

## Abstract

Schottky barrier devices have been produced using silver nanowires and titania films on stainless steel for use as sensitized photovoltaic devices. A solvothermal method was used to produce titania sols and a dip coating method was used to coat steel substrates to form a thin film of TiO<sub>2</sub>. The sols were characterised by XRD and UV-vis spectroscopy and the devices by current-voltage, photocurrent and capacitance measurements. It was found the UV efficiency could be increased to a peak of above 1% by improvements in fabrication method, including the use of TiN substrates. Though the efficiency of these devices remains low, the active areas as estimated from the temperature profiles and capacitance suggests a very small active area and therefore, the area available for the separation of charge may be small. Functionalisation with a ruthenium dye yields a photocurrent response in the visible region.

## Introduction

Schottky barriers are formed at an interface between some metals and semiconductors when more energetic electrons are lost from a semiconductor into a metal. This loss continues until the Fermi level across the two materials is continuous across the interface resulting in a depletion region in the semiconductor. This can be used to separate charges by exciting electrons over the barrier and into the semiconductor (Figure 1). [1] This can include excited electrons travelling through a thin metal film by ballistic transport in Figure 1. [1]

Schottky barriers have been used to form solar cells, using dyes and quantum dots to excite electrons over the barrier. The efficiencies and stability of these devices tends to be low. [2] [3]

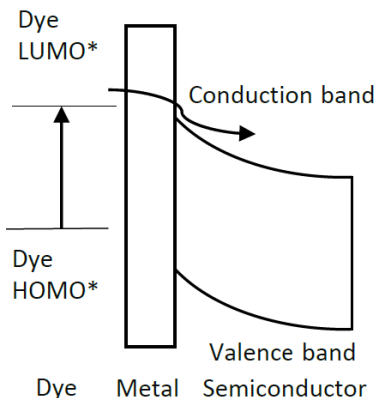


Figure 1: The working principle of a Schottky barrier photovoltaic device.

In this paper, a Schottky barrier is formed between silver nanowires and TiO<sub>2</sub>. The unfunctionalised device shows a UV response and after functionalisation with dyes can give a small photocurrent in the visible region. However, the photocurrent and UV studies suggest more than simply a light driven excitation of charge over the barrier. These devices show a significant response to the presence of water, showing a significantly improved photoresponse and changes in the IV characteristics and capacitance.

## Results

### Photocurrents

A typical device photocurrent is shown in Figure 2. It was found that functionalising with organic acids such as tartaric acid dramatically improved the photoresponse, as did the deposition of deionised water. Given the potential for photo-oxidation of organics on TiO<sub>2</sub> it is not yet clear whether the improvement in photocurrent with organic acids is due to breakdown of the acid or a passivation mechanism.

In order to demonstrate a visible response, the devices were soaked in a solution of Ru(dcbpy)<sub>2</sub>(NCS)<sub>2</sub> in EtOH, before being rinsed and dried. Again, larger photoresponses were seen where water

was deposited on the devices. Some example responses are shown in Figure 3.

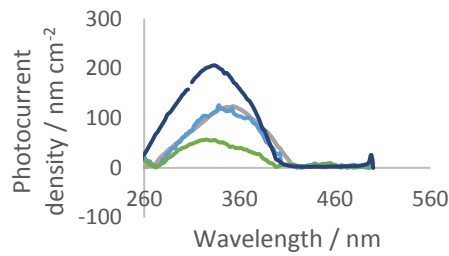


*Figure 2: Photocurrent measured showing a peak in the UV region for a range of devices.*

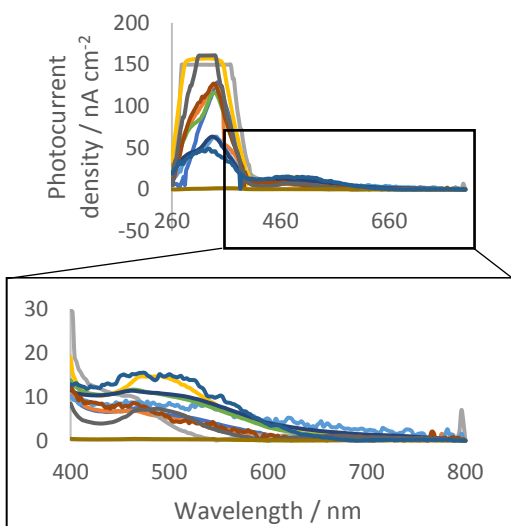


*Figure 3: Above; spectra of devices functionalised with  $\text{Ru}(\text{dcbppy})_2(\text{NCS})_2$  for a range of devices and detail of the above spectra in the visible region.*

Taking a high response of one of these devices, 15.4 nA at 506 nm, this corresponds to an efficiency of 0.0032%. This is not only extremely low, it compares unfavourably with the UV response, 0.04 % in this case.

However, estimates from thermionic emission theory give Schottky barrier areas of some tens to hundreds of square microns, a fraction of the geometric area, or even the area covered by silver nanowires. Whilst the capacitance measurements suggest the depletion region may extend by several hundred nanometres, which would be expected to increase the active area available for functionalisation, the areas are still expected to be small. These estimates are not yet accurate enough for the functionalised devices though given they are so low, an increase in efficiency through

improved architecture would be expected to increase efficiency.

A high efficiency device is shown in Figure 4, showing a peak centred on ~300 nm and an efficiency of 1.4% when deposited with water.

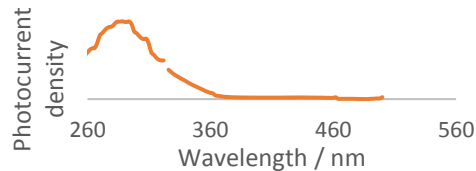


*Figure 4: A photocurrent response for a relatively high efficiency device.*

#### UV-vis studies

The description of a UV excited electron travelling over a Schottky barrier is likely incomplete as there is unexpected behaviour in the photocurrents measured. In an unfunctionalised device, there is very little response before a peak around ~320 nm (Figure 4). The lack of photoresponse below this wavelength is perhaps surprising, as the band-gap of 3.2 eV for anatase phase  $\text{TiO}_2$ , corresponding to ~387 nm.

Further, in experiments changing the solvothermal processing of the sols and processing conditions, the devices can show two opposing peaks (Figure 5).

This may be due to a plasmonic absorption by the silver nanowires and an interaction with the  $\text{TiO}_2$ . There is a weak correlation between the length of time of the hydrothermal treatment of a sol and the relative size of the peaks.

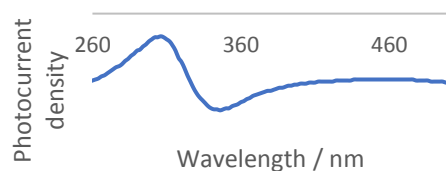


*Figure 5: Photocurrents for a device, showing opposing directions.*

It can also be seen in functionalised devices, with some devices showing evidence of this effect in the visible region (Figure 6).

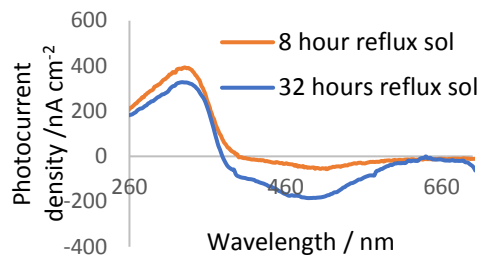


*Figure 6: Photocurrent showing peaks in both directions, including in the visible region for dye functionalised devices.*

UV-vis studies of the components of this device show non-linear dependencies on concentration for silver nanowires and an enhanced absorption for Ru(dcbpy)<sub>2</sub>(NCS)<sub>2</sub> in their presence. Figure 7 shows the spectra of silver nanowires and TiO<sub>2</sub> after removing the relevant background by subtracting the sum of the individual parts.

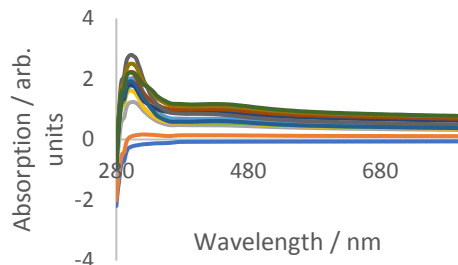


*Figure 7: UV-vis absorption for silver nanowires and TiO<sub>2</sub> for a range of TiO<sub>2</sub> and AgNW relative volumes, showing a peak at low wavelengths around 304 nm, despite the subtraction of the absorption of the individual components.*

The enhancement of absorption by silver or gold nanoparticles in Dye-sensitized solar cells (DSSCs) has been reported widely previously [4][5] and has even been shown with aluminium nanoparticles [6]. Plasmonic effects are also often used to explain the increased photocatalysis seen in TiO<sub>2</sub>/Ag composites. Whilst the UV-vis spectra and photocurrents of these devices is non-linear, the ability of measuring the directionality of photocurrent may provide an insight, relevant to photocatalysis, into the interaction of nanowires, TiO<sub>2</sub> and dye. These results are suggestive of more than one mechanism for the generation of photocurrent in these devices.

#### *Impact of water*

The photocurrents for these devices show a large improvement with soaking in water. The photocurrent of both the UV and visible region of the spectra improves (Figure 8).

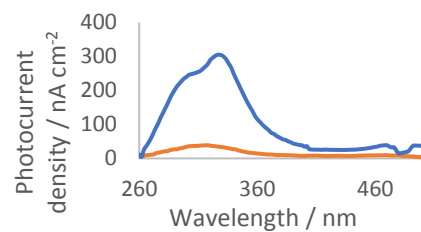


*Figure 8: Photocurrent of a functionalised device, showing a higher photocurrent for the device deposited with water.*

Water also has a significant impact on the IV characteristics of these devices, tending to show an increased forward current and changed diode characteristics.

Figure 9 shows the IV curves of a device in series with a 100 Ω resistor at the beginning of, and after purging a device with nitrogen whilst running IV curves. Under the nitrogen atmosphere, the water may be desorbed from the surface, resulting in a changed transport mechanism for charge through the device.

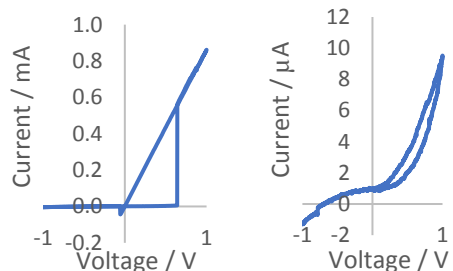


*Figure 9: IV curves under nitrogen. Left; at the beginning of the purge. Right; after 21 minutes under nitrogen flow. Note the change in magnitude of the forward current.*

To investigate the mechanism behind the change in characteristics with water, a study of an AC current through the device with increasing frequency was measured. Over ~180 kHz, there is a sudden drop in the current measured. This is considerably lower than frequency of dielectric breakdown for TiO<sub>2</sub>. Further, using the estimate of barrier width from capacitance studies, this would suggest the mechanism for transport that result in the high currents observed cannot 'respond' faster than some tens of μs for these devices under ambient conditions. Comparing this time, relative to the thickness of the TiO<sub>2</sub> layer used, to that reported for the speeds of oxygen vacancy drift under similar applied potential. [7][8] Oxygen vacancy drift as a mechanism has been reported on extensively in "memristor" applications of

$\text{TiO}_2$  metal sandwiches. [7][8] Hysteresis effects are often seen in the IV curves and studying the IV curves with increasing scan speed shows an increased reverse current at low scan speeds and an increased hysteresis at high scan speeds.

Given these results, it appears that drift of vacancies or other defects through the film has a significant role in the travel of electrons through the device and that this role is altered by the presence of water at the interface. The description of current through these devices may be better described, therefore, by defect assisted tunnelling or hopping conduction. For some devices, the IV curves showed unusual temperature dependencies that did not fit with modelling according to thermionic emission theory.

#### Device synthesis

The sol used for these devices needed to fulfil many requirements. It has been found in previous studies that the typical temperatures used in the production of  $\text{TiO}_2$  films used for photocatalysis and DSSC production were too high to prevent the diffusion of metal ions from the substrate, which are catastrophic for these devices. Given the low temperatures used here for annealing the  $\text{TiO}_2$  sols on the substrate, organic binders would not be burned off and crystallinity could not be achieved. For this reason, a solvothermal process to produce  $\text{TiO}_2$  sols was used and with extended reflux times large crystallite sizes could be achieved with size estimated from the FWHM of the XRD peaks. The UV-vis results showed a red shift of the absorption with longer reflux time, possibly due to the loss of confinement effects as the crystallite size increases.

#### Conclusions

Schottky barrier devices have been fabricated on stainless steel using oxidised TiN coatings or by dip coating in titania sol. The photocurrent of these devices is high despite the capacitance and thermionic emission studies suggesting low active areas. The response of these devices to water and the frequency and speed dependencies of their electrical characteristics suggest defect states play a role in electron transport through the device. Photocurrent studies suggest the participation of two mechanisms in the sensitization of these devices.

#### Experimental

There are two types of devices described in this paper, those produced by dip coating steel with sol produced by the hydrolysis of  $\text{Ti}(\text{OPr})_4$  in water with nitric acid followed by reflux times up to 32 hours. The substrates used were 304 or 316 stainless steel, for some devices, this was heated to high temperature prior to the dip coating process. The other method used was the oxidation of TiN coated 316 stainless steel, whereby the substrate was heated typically 500 °C for 6 hours in air. The IV curves were measured with a Gamry potentiostat with a 100 Ω resistor in series to limit current. To measure at different temperatures, a furnace was heated to ~120 °C and allowed to cool slowly, whilst a type K thermocouple and Picolog recorder was used to measure temperature. Photocurrent was measured using an Bentham arclamp, an amplifier and ammeter, the former produced in-house. A commercial Si diodes were used for calibration (Centronic OSD5.8-7Q) Capacitance was measured by use of a signal generator and lock in amplifier as described in [9]. To sensitize devices with  $\text{Ru}(\text{dcpbpy})_2(\text{NCS})_2$ , the devices were soaked in an ethanolic solution of the dye and rinsed with EtOH and air dried. All chemicals were procured from Sigma Aldrich and used without purification and substrates were from RS components (stainless steel) and Goodfellow (TiN coated stainless steel).

#### References

- [1] R.T. Tung, App. Phys. Rev., 2014, **1**, 1-53
- [2] E.W. McFarland and J. Tang, Nature, 2003, **421**, 616-618
- [3] 4) J. Luther et al., Nano letters, 2008, **8** 3488-3492
- [4] C. Wen et al., Sol. Energ. Mat. Sol. Cells, 2000, **61**, 339-351
- [5] J. Qi et al., ACS Nano, 2011, **5**, 7108-7116
- [6] Q. Xu et al., Opt. Express, 2014, **22**, 301-310
- [7] Y. J. Ou et al, Sci. Technol. Adv. Mater., 2015, **16**, 034902
- [8] N. R. McDonald and R. E. Pino, IEEE World Congress of Computational Intelligence, 2010
- [9] N.D. Reynolds et al., Am. J. Phys., 2014, **82**, 196-205

# Evaluation of Effective Carrier Lifetime of CdTe Solar Cells Using Transient Photovoltage Decay Measurements

Vincent Tsai\*, George Koutsourakis, Martin Bliss, Thomas R. Betts, Ralph Gottschalg

Centre for Renewable Energy Systems Technology (CREST), Wolfson School of Mechanical, Electrical and Manufacturing Engineering, Loughborough University, Loughborough, Leicestershire, LE11 3TU, UK

\* Corresponding Author [v.tsai@lboro.ac.uk](mailto:v.tsai@lboro.ac.uk)

## Abstract

A transient photovoltage decay (TPVD) measurement system is currently being developed at CREST and measurements were conducted on several CdTe solar cells. The extracted effective carrier lifetimes were around 100ns. The effect of external illumination biasing was investigated and was found to reduce the effect of junction capacitance and saturate trap states in the devices. This resulted in shorter extracted effective carrier lifetimes. Increasing the illumination of the pulsed-laser intensity also increased the effective carrier lifetime.

## Introduction

The carrier lifetime of solar cells is an important parameter as it is influenced by material quality and subsequently affects overall efficiency of photovoltaic (PV) devices. Therefore, measurement methods to extract its value are necessary for developing high efficiency PV devices. Usually time resolved photoluminescence systems are used for such measurements [1]. One alternative and not so well established characterisation technique for this purpose is transient photovoltage decay (TPVD).

During TPVD measurements, the PV device is contacted and connected directly to an oscilloscope. Excess minority carriers are created in the junction of the PV device using pulsed optical excitation, usually using a laser source. Each pulse creates excess carriers and thus generates a photovoltage. The subsequent voltage decay is measured as a function of time and the effective minority carrier lifetime can be extracted [2].

TPVD carrier lifetime values are affected by different physical processes in solar cells. They are mainly influenced by the recombination processes (radiative, non-radiative Shockley-Read-Hall (SRH) and Auger) but they are also affected by other factors, such as device junction capacitance, recombination current in the space-charge region, series and shunt resistances, or capacitance of the measurement system [3][4]. Furthermore, TPVD is strongly affected by the injection levels set by the measurement conditions [5].

In this work, TPVD measurements are conducted on several CdTe solar cell samples.

The effect on the variability in measurements by averaging will be examined. Furthermore, the effect on the carrier lifetime by applying external biasing and different laser intensities are investigated. It is demonstrated that TPVD measurements are straightforward to implement and have the potential to provide a cost effective way to measure the effective carrier lifetime of solar cells.

## System Setup and Methodology

A TPVD measurement system is being developed at CREST and is currently being tested. Figure 1 shows the experimental setup schematic. The transient photovoltage is stimulated by a 640nm picosecond pulsed laser head. The laser intensity and pulse frequency are controlled by a laser driver. For frequencies <2.5MHz, the laser driver is triggered by a function generator. The size of the collimated output beam was  $1.5 \times 3.5\text{mm}^2$  and was linearly polarised by collimation optics in the laser head. The sample is contacted by Kelvin probes which are connected to the sampling channel of an 11GHz digital sampling oscilloscope with a  $50\Omega$  input impedance via a matching SMA coaxial cable. The output synchronisation signal of the laser driver is connected to the trigger channel of the oscilloscope and is used as the external trigger for TPVD measurements. A tungsten halogen lamp was used to provide external biasing to the sample when required.

The oscilloscope was controlled by LabVIEW to automatically conduct multiple measurements and extract the decay time of the photovoltage decay. The resulting decay curves were fitted by the following single exponential decay function from which the effective carrier lifetime can be obtained [6]:

$$V(t) = A \times \exp(-t/\tau) + V$$

Where  $A$  is the initial peak value,  $\tau$  is the extracted effective carrier lifetime and  $V$  is the voltage offset.

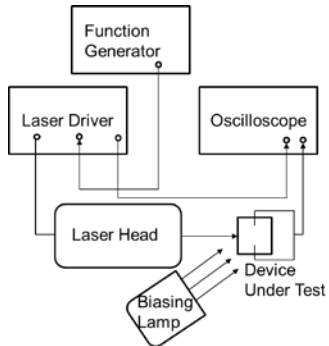


Figure 1 Experimental setup schematic

## Measurement Variability

Initial TPVD measurements were conducted on a Cadmium Telluride (CdTe) sample. The laser repetition rate was set to 1MHz and the maximum laser power was ~0.3mW.

Figure 2 shows the resulting TPVD curves of the CdTe cell from a single measurement and for an average of 100 measurements at both maximum intensity (denoted as I10) and half intensity (denoted as I5). The decay curves follow a similar trend; there is an initial rapid charging-up of voltage followed by a slower exponentially decay process. The exponential decay indicates the low-injection condition where the excess minority concentration is less than the equilibrium value [5]. From Figure 2, it can be observed that increasing the number of readings for each point increases the signal-to-noise ratio (SNR) of the measured decay curves, which is particularly useful at lower laser intensities (I5) where the measured decay curves are noisier.

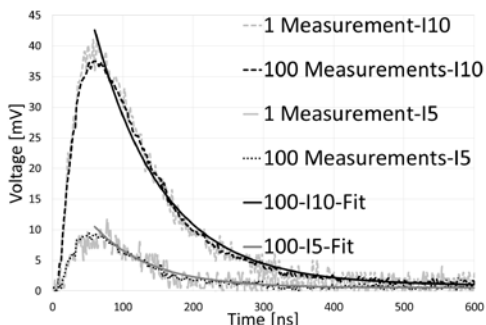


Figure 2 TPVD curves of the CdTe cell measured under 640nm wavelength, 1MHz frequency, laser at maximum (I10) and half intensity (I5), unbiased and at room temperature.

For this particular cell, the fitted values for  $\tau$  were found to be in the range of 96-110ns which is within the expected ns regime for CdTe carrier lifetime [1][7]. The values of  $\tau$  from a single reading can fluctuate by ~15% due to the low SNR of the decay curve. Averaging multiple measurements increased the SNR significantly and reduced the fluctuation of the results as shown in Figure 3.

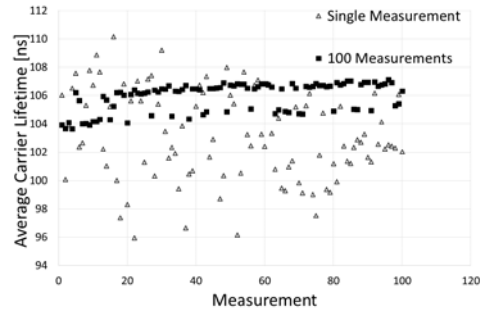


Figure 3 Fluctuation of carrier lifetime for single measurements versus an average of 100 measurements

## Further Measurements

Further TPVD measurements were conducted on two CdTe cells (denoted as C2 and D2) fabricated at CREST. CdS was deposited on 50x50mm<sup>2</sup> substrates using a sono-chemical bath resulting in ~200nm thick films. CdTe was deposited by a close-space sublimation resulting in 4-6μm thick films. Devices were finished by depositing ~80nm of gold to act as the back contact.

The laser setting was the same as the previous test. The aim of the measurements was to connect different device parameters with effective carrier lifetime values. Furthermore, the effects of applying external DC biasing as well as altering the laser intensity were studied. The cells' parameters, extracted carrier lifetimes at maximum laser intensity and IV curves are shown in Table 1 and Figure 4, respectively.

The effect of using external DC biasing was investigated by illuminating the entire device with a tungsten halogen lamp. For both cells, biased and unbiased measurements were conducted at the same laser excitation spot. It was found that under bias lighting, a shorter effective carrier lifetime is extracted than when no bias is applied. This is because without the bias illumination, the decay curves are dominated by junction capacitance effects and trap energy level capture effects [6]. This will result in longer measured photovoltage decay times and thus overestimate the extracted effective carrier lifetime [8]. The bias light saturates trap states and minimises the effects of junction capacitance, resulting in shorter measured lifetimes.

CELL	C2	D2
V <sub>oc</sub> (V)	0.58	0.54
I <sub>sc</sub> (mA)	3.37	5.56
R <sub>s</sub> (Ω)	0.025	0.041
R <sub>sh</sub> (kΩ)	12.94	4.87
FF	0.566	0.546
η (%)	4.42	6.5
T <sub>bias</sub> (ns)	73.1	88.19
T <sub>nobias</sub> (ns)	110.59	136.92

Table 1 Device parameters and extracted carrier lifetime of CdTe C2 and D2 cells

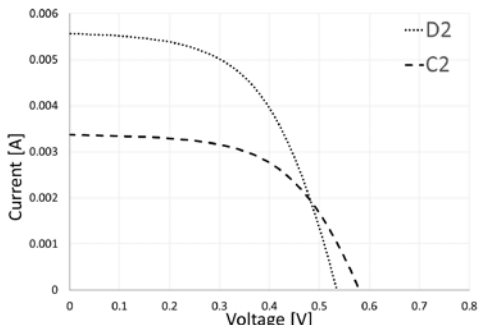


Figure 4 IV curves of CdTe C2 and D2 cells

It was observed for both biased and unbiased measurements that the higher efficiency cell D2 had a longer effective carrier lifetime than the less efficient cell C2 in both cases, with and without bias light application. Although C2 has a higher open circuit voltage ( $V_{oc}$ ) than D2, it has a lower short circuit current ( $I_{sc}$ ) as shown in the IV curves in Figure 4. This effect is also observed in the TPVD curves in Figure 5 where C2 is excited to a higher peak voltage than D2, but it decays faster. This is because the  $I_{sc}$  is affected by the charge collection efficiency of the device which also depends on the minority carrier lifetime. The lifetime determines if electrons which travel across the CdTe device are able to reach the p-n junction [9].

It should also be noted that due to the  $50\Omega$  input impedance of the oscilloscope, the cell is operating nearer to short circuit conditions. This can be seen from the peak voltages from the TPVD curves in Figure 5 and the corresponding current in the IV curves in Figure 4. The extracted carrier lifetime nearer short circuit conditions tend to occur at a faster timescale than nearer to open circuit conditions. This is because charge collection effects are more dominant in the decay curves which is a faster process than recombination [10].

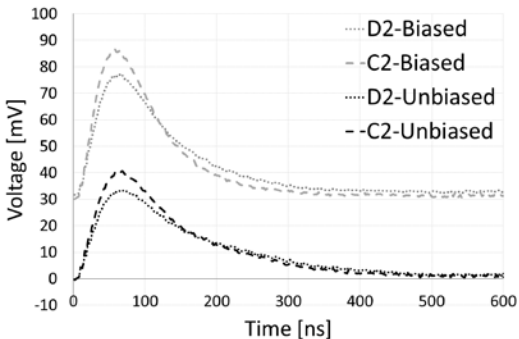


Figure 5 TPVD curves of CdTe samples under bias and no bias at maximum laser intensity

For both cells, different laser intensities were used to examine the relationship between extracted carrier lifetime and excitation laser intensity. The results are presented in Figure 6. The relative intensity of the figure is represented

as 10 being the highest and 4 being the lowest. For each intensity level, an average of 1000 measurements were acquired.

Figure 6 shows that the measured effective carrier lifetime increases with the laser intensity. At the lowest laser intensity (4) the extracted carrier lifetime value is similar for both cells when biased or unbiased. The curves are noisier and junction capacitance effects are more dominant than recombination and charge collection. However as the intensity increases, the extracted value begins to reflect the underlying recombination and collection effect in the cells.

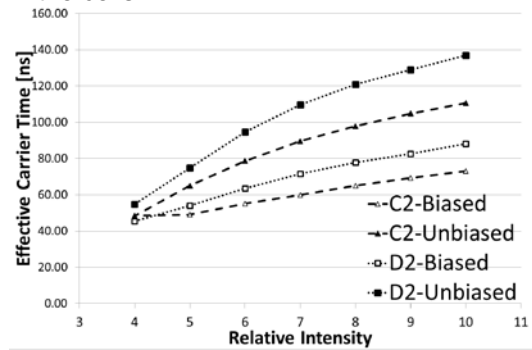


Figure 6 Comparison between cells C2 and D2 changing laser intensity and effect of external biasing

## Design Considerations

As TPVD measurements are conducted under very fast time scales (pico to nanoseconds), it is important to ensure that the acquired signal is as accurate as possible. Factors such as cable lengths and low frequency response of components can introduce delays and distort the acquired measurement signal.

As the pulse width of the laser is  $\sim 92\text{ps}$ , one would expect an almost instantaneous charge up in the voltage of the cell after a single laser excitation pulse. However, Figures 2 and 5 show that the peak voltage was reached after  $\sim 50\text{ns}$ . It was identified that the Kelvin probes introduced delays into the signal. As a result, TPVD measurements were conducted on another CdTe cell (denoted as D1) by altering the probes for each measurement.

The original coupling consisted of a component which connected the probes to a BNC to free end Pomona test lead. The two probes had two pins each and one was lifted up so only two pins contacted the sample rather than four (denoted Is and Vs Probes Single and 2 Single Probes no coupling). BNC to free end only used the test lead to contact the sample directly with no Kelvin probes. The results are presented in Figure 7. The measurement conditions were the same as the previous measurements.

It was observed that there was a delay in reaching the peak voltage of around 10-20ns

between the original coupling and BNC to free end only. The extracted carrier lifetimes for Original Coupling and BNC to Free End only were 101ns and 128ns, respectively. The extracted carrier lifetimes for the other probe settings were all ~117ns. Therefore, the probes only had a minor influence on the extracted charge carrier lifetimes. Further investigation is required to identify major sources of delay such as cable length, and improve the response time of the sample signal pick-up.

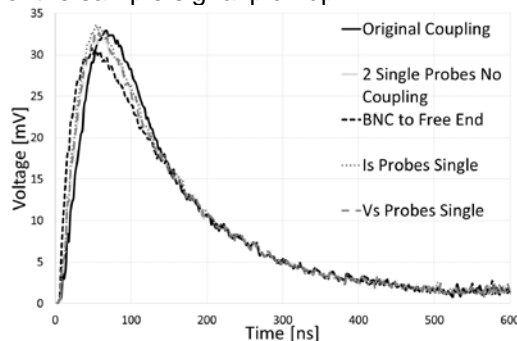


Figure 7 TPVD measurements on CdTe cell D1 using different probe setups

## Summary and Future Work

This TPVD measurement system has demonstrated the relatively straightforward and cost-effective setup to measure the effective carrier lifetime of CdTe solar cells. It was found that the extracted carrier lifetimes were in the expected timescales of nanoseconds which demonstrated the feasibility of this method. The use of external biasing reduced the effect of junction capacitance and saturated trap states resulting in shorter carrier lifetimes. Furthermore, certain components in the measurement system limited the response time of the measurements. Future work will involve finalising the measurement setup and improving the response time of the sample signal pick-up.

## References

- [1] W. Metzger, R. Ahrenkiel, and P. Dippo, "Time-resolved photoluminescence and photovoltaics," in *Department of Energy Solar Energy Technologies Program Review Meeting*, 2004, vol. 1, no. January, pp. 1–2.
- [2] U. Stutenbaumer and E. Lewetegn, "Comparison of minority carrier diffusion length measurements in silicon solar cells by the photo-induced open-circuit voltage decay (OCVD) with different excitation sources," *Renew. Energy*, vol. 20, no. 1, pp. 65–74, 2000.
- [3] M. A. Green, "Solar Cell Minority Carrier Lifetime Using OCVD," *Sol. Cells*, vol. 11, pp. 147–161, 1984.
- [4] K. Price, C. Lacy, and D. P. Hunley, "Photovoltage Decay in Cdte / Cds Solar Cells," in *Photovoltaic Energy Conversion, Conference Record of the 2006 IEEE 4th World Conference*, 2006, pp. 436–437.
- [5] J. E. Mahan, T. W. Ekstedt, R. I. Frank, and R. Kaplow, "Measurement of minority carrier lifetime in solar cells from photo-induced open-circuit voltage decay," *IEEE Trans. Electron Devices*, vol. 26, no. 5, 1979.
- [6] H. Cui, J. Wang, C. Wang, C. Liu, K. Pi, X. Li, Y. Xu, and Z. Tang, "Experimental Determination of Effective Minority Carrier Lifetime in HgCdTe Photovoltaic Detectors Using Optical and Electrical Methods," *Adv. Condens. Matter Phys.*, vol. 2015, pp. 1–6, 2015.
- [7] V. Buschmann, H. Hempel, A. Knigge, C. Kraft, M. Roczen, M. Weyers, T. Siebert, and F. Koberling, "Characterization of semiconductor devices and wafer materials via sub-nanosecond time-correlated single-photon counting," *J. Appl. Spectrosc.*, vol. 80, no. 3, pp. 449–457, 2013.
- [8] T. Pisarkiewicz, T. Stapiński, and P. Wójcik, "Influence of junction parameters on the open circuit voltage decay in solar cells," *Sci. Technol.*, vol. 12, no. 1, pp. 79–83, 2004.
- [9] A. Cuevas and D. Macdonald, "Measuring and interpreting the lifetime of silicon wafers," *Sol. Energy*, vol. 76, no. 1–3, pp. 255–262, 2004.
- [10] S. Wood, D. O. Connor, C. W. Jones, J. D. Claverley, J. C. Blakesley, C. Giusca, and F. A. Castro, "Solar Energy Materials & Solar Cells Transient photocurrent and photovoltage mapping for characterisation of defects in organic photovoltaics," *Sol. Energy Mater. Sol. Cells*, vol. 161, no. November 2016, pp. 89–95, 2017.

# **Analysis of Luminescent Solar Concentrator Performance Using a Ray Tracing Algorithm: Modelling, Optimization and Validation**

M. Rafiee<sup>\*</sup>•, S. Chandra<sup>•</sup>, H. Ahmed<sup>•</sup> and S. J. McCormack<sup>•</sup>

<sup>•</sup>Dept. of Civil, Structural and Environmental Engineering, Trinity College Dublin, Dublin2, Ireland,

<sup>\*</sup> Corresponding Author [rafeem@tcd.ie](mailto:rafeem@tcd.ie)

## **Abstract:**

In this paper, the behaviour of a LSC doped with Near-Infrared Quantum Dots (NIR-QD) in an epoxy host material is modelled by a ray tracing algorithm under different iteration numbers. It is shown that by increasing the number of input rays in the system improving the accuracy of simulation and the QDs emission spectra. However, increasing the number of the rays has linearly increased simulation iterations, hence the simulation time. This challenge is overcome by optimizing the program by avoiding recalculations of parameters in the program which significantly reduces the volume of calculations; thus, simulation time. As a case in point, in a simulation run for 126000 rays, the simulation time was decreased from around 107 hours in the primary program to around only 3 hours in the optimized version. Furthermore, in the simulation for around 718000 rays, the optimized program achieved the simulation time of roughly 18 hours with higher accuracy. The ray-trace model predicted optical efficiency compared with references results to validate the model and found to be in an excellent agreement.

**Keywords:** Luminescent Solar Concentrator, Ray Tracing, Modelling, Quantum Dot, Emission, Absorption

## **1- Introduction:**

Luminescent Solar Concentrators (LSCs) are known as efficient light collectors for solar energy and PV systems. PVs cells are not efficient in all ranges of wavelengths and different methods can be used to enhance the efficiency of the solar cells. Of these, the first method can be done by improving the electrical characteristics of photovoltaic (PV) cells and their structure; for instance, designing PV device with very narrow structure [1]. Although, this method is difficult and expensive, it has been resulted in fabricating new PV devices such as third generation PV cells including multi-junction, heterojunction and intermediate band gap solar cells. [2-4]

An alternative method to enhance the output efficiency of PV systems and

improve the spectral response is use of luminescent materials which can be done by two techniques. The first one is doping luminescent material in the encapsulation layer such as dye-doped plastic Luminescent Down-Shifting (LDS) layer in order to red-shift the illuminated spectrum. The second is using luminescent material in a transparent host material and fabricate a light-guiding concentrator such as a planner LSC whose structure can be seen in Figure 1. [5] LSC has been proposed as an interesting strategy in order to concentrate and convert sunlight to a single wavelength, where PV cells have higher efficiency. The idea of using luminescent materials in order to enhance the spectral response of solar cells was first introduced in 1970s and first generations were based on dyes. [6-8]

The use of LSC in PV systems has some advantages. LSCs are spectrum converters to manage photons in which molecules of fluorescent absorb photons with small wavelengths and emit them in longer wavelengths where PV cell has relatively high efficiency. Then, the photons are concentrated to the PV cells by Total Internal Reflection (TIR). This not only increases the efficiency of the system, but also reduces the required PV area; accordingly, decreases the cost of the solar panel. Furthermore, both diffuse and direct light can be concentrated and converted by LSC; hence, they are a very suitable technology where diffuse solar radiation is dominant, such as in northern European countries where over 50% of light is diffuse. [9]. They are low-cost and can be designed and constructed in transparent small and large scale windows with different colours. It has been proven that using LSC in building can enhance visual comfort, day lighting and correlated colour temperature. [10] Moreover, the combination of different LSC sheets can be used in order to generate a near-white light source [11]. These features make them a preferred choice for use in Building Integration Photovoltaic (BIPV) systems and façades of buildings which brings us closer to the goal of constructing buildings with zero

carbon energy consumption and buildings which are able to cover their required energy by renewable energies [12-14]. This can help to achieve the goal of the European Parliament and the Council of the European Union enacted in 2009 on using renewable energy to reduce pollution and fossil energy consumption. [15], [16].

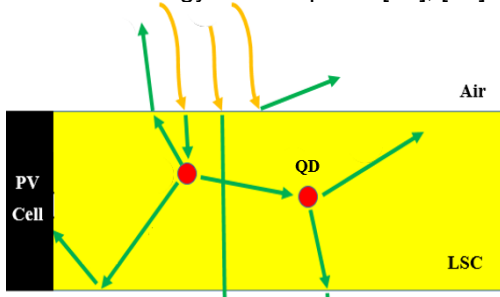


Figure 1: LSC device doped with QD in host material and PV cell installed on the edge

In this paper, the behaviour of a LSC including NIR-QD doped in an epoxy host material is modelled by a ray tracing algorithm. The program was optimized by reducing the amount of calculations in it so that the execution time of the program is decreased significantly. In the following; the basis of the ray tracing algorithm is explained and the model details are presented. Results were obtained and validated by comparing the results with the reference reported results.

## 2- Ray Tracing Basis and Modelling:

Monte Carlo ray tracing algorithm has a statistical nature and achieves the results by random sampling and solves the problems in an iteration loop. Generally, Monte Carlo method has been used in many applications in the fields of fluids, solids, optics and physics where the behaviour of the input parameters in problems are non-linear and have dramatic uncertainty. In other words, the inputs in these types of problems can be interpreted by probabilities and they cannot be solved by traditional methods [17-20].

Monte Carlo ray tracing algorithm can obtain the results by tracing a large number of photons which are generated based on the energy distribution of the input radiation light. The photons are irradiated to the modelled systems. Afterwards, in an iteration loop, the fate of each photon is calculated based on the probability of each event which may occur for that including reflection and refraction. If the ray is refracted to the LSC, it may be absorbed by

host material (lost as heat) or absorbed and then emitted by QDs. Since the host material are transparent in the visible range of solar radiation, it is believed that the irradiated light is absorbed by the luminescent species. The absorption is calculated by the Beer Lambert law as shown in equation 1 [19, 21, 22]:

$$A = -\log_{10} T \quad (1)$$

Where A is the Absorbance and T is the value of Transmittance of the material.

Monte Carlo ray tracing algorithm is based on the calculations in a “For” loop which is a time-consuming process. The number of the iterations in the loop is determined by the number of the photons irradiated to the LSC. Thus, increasing the number of the photons (in order to have more accurate results) leads to increase in the number of iterations and calculations; therefore, the simulation time.

In order to reduce the simulation time, the program's process and algorithm is optimized by eliminating unnecessary re-duplications and re-calculations of the same parameters in different places or functions of the program. In the optimized version, the constants and the similar parameters are only calculated once in the pre-processing stage of the program before the main iteration “For” loop. By using this idea, the number of the calculations in each iteration of the “For” loop is decreased which reduces the execution time of each iteration and the overall simulation time.

## 3- Results and Discussions:

The result of ray tracer program with and without the optimized steps were compared with the reported results in [23]. The modelled LSC had the dimensions of  $60 \times 60 \times 3$  mm and the host material was epoxy with refraction index of 1.5. The quantum yield of the used NIR QD was 85%. The input solar spectrum used was a Direct Sun Light (AM 1.5) radiation and the detector was placed at one of the edges of the LSC. The emission and absorption spectra of the NIR QD LSC is shown in Figure 2. Table 1 shows the optical efficiency of the NIR QD LSC calculated by the ray tracer program and compared with the reference value. The program was first run for a total number of 126000 rays (iterations). The simulation time was around 107 hours. The value obtained for the optical efficiency by the model was 7.33%. The optical efficiency of reference LSC was 7.59%. Figure 3 shows the emission spectrum detected at the

edge of the LSC by the model in comparison with the measured emission spectrum. As it can be seen from Figure 3, the emission spectrum obtained by the model is noisy due to the low number of input photons (iterations). Increasing the number of iterations is important in order to get more accurate results and smoother spectrum; however, it increases the simulation time.

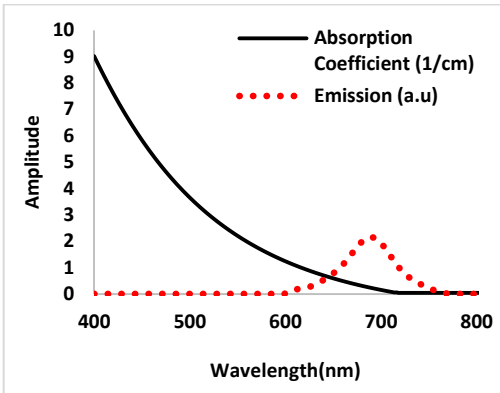


Figure 2: Absorption coefficient and emission spectra for NIR QD LSC [23]

The optimization steps to the ray tracer program was then important in order to reduce the time taken to run the model. The optimized program was run for the same number of iterations. It has been found that, the simulation time is reduced to around 3 hours and maintained the same optical efficiency. The program was run for higher number of iterations, 718000. The value of the optical efficiency was recorded 7.5% which was in a close match with the reference value, 7.59%. Figure 4 shows the emission spectrum obtained with iterations number of 718000 compared to reference emission spectrum. It appears that, the achieved and the reference results are in an excellent match.

Table 1: Comparison of the results obtained by ray tracer program (with and without the optimized steps) and reference [23]

	Ray tracer program	Ray tracer program (optimised)	Ray tracer program (optimised)
Iterations	126000	126000	718000
Optical Efficiency (In [23]: 7.59%)	7.33%	7.33%	7.50%
Simulation Time(s)	385462.5 (107 hours)	10821 (3 hours)	63772.1 (18 hours)

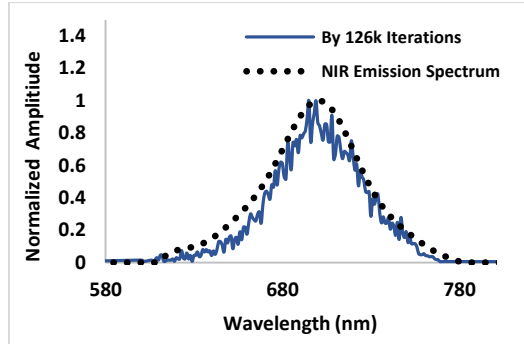


Figure 3: Comparison of the output spectra of the LSC under 126k rays and the emission spectrum of NIR QD

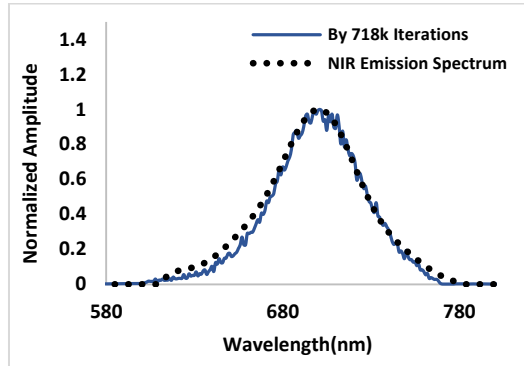


Figure 4: Comparison of the output spectra of the LSC under 718k rays and the emission spectrum of NIR QD

#### 4- Conclusion:

In this paper, a Monte Carlo ray tracer program was used in order to model a NIR QD doped LSC. In the program, the output results were obtained by detecting the fate of each input ray in an iteration loop. It has been observed that, by increasing the number of the input rays, more accurate results could be achieved. This however increased the simulation time. In order to overcome this limitation, an optimization steps were taken in the ray tracer program. As a result, the speed of the program was increased significantly. For example, the simulation time for 126k rays was reduced from 107 to 3 hours. Moreover, by increasing the number of the rays, the output modelled results were more precise and in an excellent match with the reference results.

#### Acknowledgment:

The authors would like to acknowledge the funding from the European Research Council grant entitled PEDAL: Plasmonic enhancement of advanced luminescent

solar devices (13379: 203889) and also to thank Dr. Manus Kennedy whose results were used for validation in this paper.

## References:

1. Hovel, H., R. Hodgson, and J. Woodall, *The effect of fluorescent wavelength shifting on solar cell spectral response*. Solar Energy Materials, 1979. **2**(1): p. 19-29.
2. Bedair, S., M. Lamorte, and J. Hauser, *A two-junction cascade solar-cell structure*. Applied Physics Letters, 1979. **34**(1): p. 38-39.
3. Taguchi, M., et al., *HITTM cells—high-efficiency crystalline Si cells with novel structure*. Progress in Photovoltaics, 2000. **8**(5): p. 503-514.
4. Luque, A. and A. Martí, *Increasing the efficiency of ideal solar cells by photon induced transitions at intermediate levels*. Physical Review Letters, 1997. **78**(26): p. 5014.
5. Yamada, N., L. Nguyen Anh, and T. Kambayashi, *Escaping losses of diffuse light emitted by luminescent dyes doped in micro/nanostructured solar cell systems*. Solar Energy Materials and Solar Cells, 2010. **94**(3): p. 413-419.
6. Weber, W. and J. Lambe, *Luminescent greenhouse collector for solar radiation*. Applied Optics, 1976. **15**: p. 2299.
7. Goetzberger, A. and W. Greube, *Solar energy conversion with fluorescent collectors*. Applied Physics, 1977. **14**(2): p. 123-139.
8. Goetzberger, A., *Fluorescent solar energy collectors: operating conditions with diffuse light*. Applied physics, 1978. **16**(4): p. 399-404.
9. van Sark, W.G., et al., *Luminescent Solar Concentrators-A review of recent results*. Optics Express, 2008. **16**(26): p. 21773-21792.
10. Aste, N., et al., *Integration of a luminescent solar concentrator: Effects on daylight, correlated color temperature, illuminance level and color rendering index*. Solar Energy, 2015. **114**: p. 174-182.
11. Earp, A.A., et al., *Optimisation of a three-colour luminescent solar concentrator daylighting system*. Solar Energy Materials and Solar Cells, 2004. **84**(1-4): p. 411-426.
12. Aste, N., R. Adhikari, and C. Del Pero, *Photovoltaic technology for renewable electricity production: Towards net zero energy buildings*. in *Clean Electrical Power (ICCEP)*, 2011 International Conference on. 2011. IEEE.
13. Pagliaro, M., R. Ciriminna, and G. Palmisano, *BIPV: merging the photovoltaic with the construction industry*. Progress in Photovoltaics: Research and Applications, 2010. **18**(1): p. 61-72.
14. Debije, M.G. and P.P. Verbunt, *Thirty years of luminescent solar concentrator research: solar energy for the built environment*. Advanced Energy Materials, 2012. **2**(1): p. 12-35.
15. UNION, P., *DIRECTIVE 2009/28/EC OF THE EUROPEAN PARLIAMENT AND OF THE COUNCIL of 23rd April 2009 on the promotion of the use of energy from renewable sources and amending and subsequently repealing Directives 2001/77/EC and 2003/30/EC*. 2009, EC.
16. Union, O.J.E., *Directive 2010/31/EU of the European Parliament and of the Council of 19 May 2010 on the energy performance of buildings (recast)*. 2010.
17. Jacques, S.L. and L. Wang, *Monte Carlo modeling of light transport in tissues*, in *Optical-thermal response of laser-irradiated tissue*. 1995, Springer. p. 73-100.
18. Joy, D.C., *Monte Carlo modeling for electron microscopy and microanalysis*. 1995: Oxford University Press.
19. Sahin, D. and B. Ilan, *Radiative transport theory for light propagation in luminescent media*. JOSA A, 2013. **30**(5): p. 813-820.
20. Sahin, D., B. Ilan, and D.F. Kelley, *Monte-Carlo simulations of light propagation in luminescent solar concentrators based on semiconductor nanoparticles*. Journal of Applied Physics, 2011. **110**(3): p. 033108.
21. Klampaftis, E., et al., *Enhancing the performance of solar cells via luminescent down-shifting of the incident spectrum: A review*. Solar Energy Materials and Solar Cells, 2009. **93**(8): p. 1182-1194.
22. Abderrezek, M., et al., *Numerical Simulation of Luminescent Downshifting in Top Cell of Monolithic Tandem Solar Cells*. International Journal of Photoenergy, 2013. **2013**.
23. Kennedy, M., et al., *Ray-trace Modelling of Quantum Dot Solar Concentrators*. 2008.

# Triple-Junction Concentrator Photovoltaic-Thermoelectric Hybrid Receivers: Robustness, Validation and Preliminary Reliability Studies

Matthew Rolley<sup>[1,a]</sup>, Tracy Sweet<sup>[1,b]</sup>, Vasil Stoichkov<sup>[2]</sup>, Noel Bristow<sup>[2]</sup>, Jeff Kettle<sup>[2]</sup>, Gao Min<sup>[1,c]</sup>

1. Cardiff School of Engineering, Cardiff University, Queens Buildings, The Parade, Cardiff, CF24 3AA

2. Bangor University School of Electronic Engineering, Bangor University, Dean street, Bangor, LL57 1UT

Corresponding Authors: a. [RolleyMH@Cardiff.ac.uk](mailto:RolleyMH@Cardiff.ac.uk), b. [SweetT@Cardiff.ac.uk](mailto:SweetT@Cardiff.ac.uk), c. [Min@Cardiff.ac.uk](mailto:Min@Cardiff.ac.uk)

## 1. Introduction

Multi-junction photovoltaic cells utilise the incident solar spectrum effectively with photon to cell efficiencies of up to 46% recently achieved for a wafer-bonded four-junction cell [1]. However even industry standard designs, such as monolithic lattice matched triple junction architectures, have high manufacturing costs. Optical concentration is an effective way of combining this technology with comparatively low-cost lenses to increase the incident light flux on the cell, achieving competitive parity cost per Watt with cell efficiencies over 50% [2], or in conditions with greater than  $1500\text{Wm}^{-2}$  irradiance [3]. Thermoelectrics (TE) are solid state semiconductor devices that can either exploit a temperature differential to generate power ( $\text{Bi}_2\text{Te}_3$  thermal to electrical conversion efficiency  $\approx 1\%$  at  $25^\circ\text{C } \Delta T$ ) [4], or inversely use electrical power to act as a heat pump (typical Coefficient Of Performance of  $\text{Bi}_2\text{Te}_3 \approx 1$  at  $25^\circ\text{C } \Delta T$ ) [4]. One of the barriers for large-scale deployment of Concentrator Photovoltaic (CPV) technology for energy generation is its technology legacy. Silicon based panels have had many years of performance and lifetime data and investment risk is low. Recent publications show an evolving trend of hybrid solar devices being evaluated, including that of CPV-TE monolithic devices. Optimisation and simulation studies are prevalent [5-10], but experimental data is sparse especially for triple junction solar cells [11, 12]. Experimental characterisation and reliability testing of CPV-TE hybrids are investigated in this paper.

## 2. The Hybrid Receiver

A III:V CPV-TE monolithic CPV-TE hybrid receiver “proof-of-concept” design was manufactured at Cardiff University. The receiver consists of a bi-layer PCB structure, built on a 3mm copper substrate and incorporates an (8 x 6 x 1.6) mm encapsulated  $\text{Bi}_2\text{Te}_3$  thermoelectric module. Bonded to this is

a triple junction solar cell, wire bonded to the PCB for electrical connection. The cell and thermoelectrics are then further encapsulated by a silicone elastomer for dust and humidity protection. A photo is given in Figure 1.

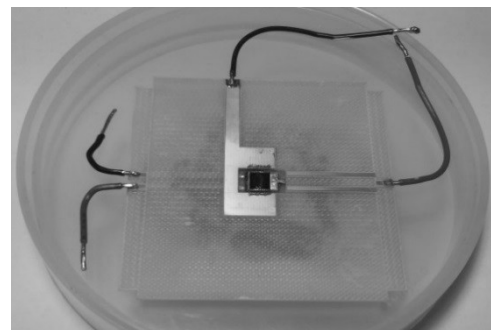


Figure 1. A Picture of “ALPHA”

To accurately evaluate device performance at  $25^\circ\text{C}$ , current-voltage (I-V) characterisation scans under Standard Test Conditions (STC) were measured at Cardiff University. The receiver was then measured at Loughborough University’s Centre for Renewable Energy Systems Technology (CREST) for cross-correlation analysis.

## 3. Experimental Methods

Three solar simulators were used for testing. Cardiff University’s system, a LOT Oriel solar simulator, ABB rated according to ASTM E927-10. Bangor University has a plasma lamp simulator which achieves high incident flux for accelerated ageing and a Xenon lamp, ABB rated, for electrical I-V evaluation. A calibrated Kipp and Zonen Pyranometer, Silicon reference cell, and Spectroradiometer were used to characterise the solar simulator and confirm experimental performance comparable to the standard. A series of thermal images were taken during initial receiver I-V tests at Cardiff University to investigate thermal characteristics in the “ALPHA” receiver design (Figure 2).

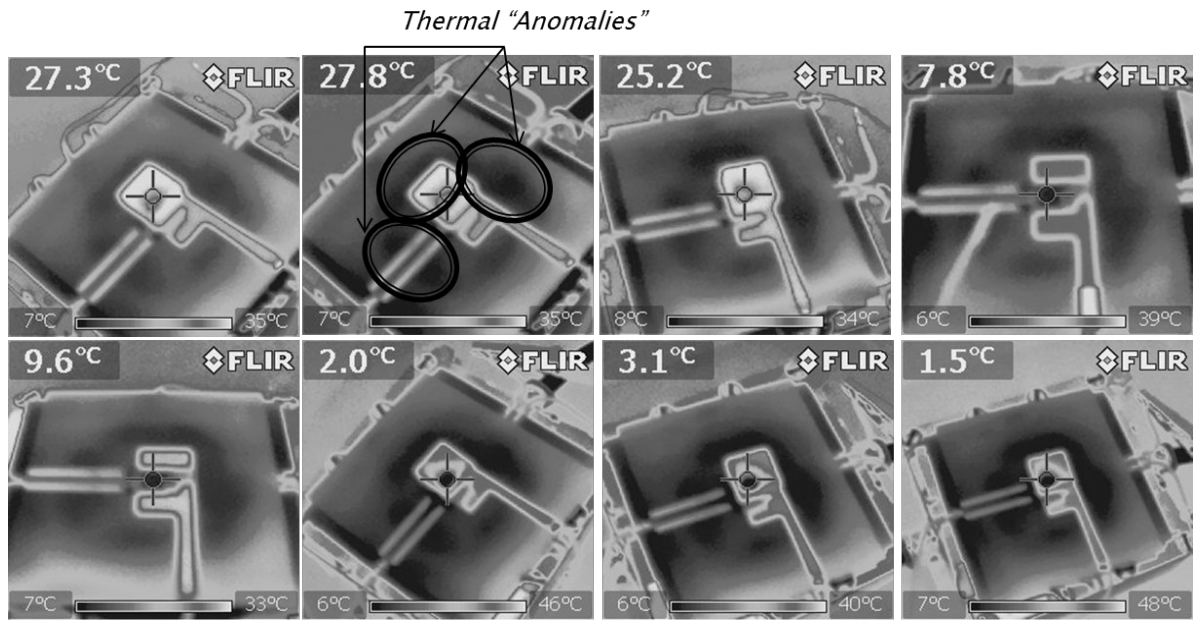


Figure 2. Thermal Images of ALPHA during Experimental Testing

#### 4. Results

The data obtained from the STC receiver evaluation experiments at Cardiff and Loughborough CREST are shown in figure 3. The short circuit current and open circuit voltages obtained at Cardiff agreed to CREST data within 2% for  $I_{sc}$ , and the  $V_{oc}$  was identical to six decimal places, thereby substantiating the experimental methodology used at Cardiff. Experimental repeatability was also tested at Cardiff, and the  $I_{sc}$  was found to be within 1.1% for a complete takedown and setup (data shown in Figure 4).

Preliminary thermal simulations were undertaken using COMSOL to investigate and predict the thermal distributions of the PCB

design under fixed incident light flux and bottom cold-side temperature as constraints. 10°C was chosen as experimentally representative to data obtained throughout water cooled receiver testing at Cardiff. Water-cooling and cell temperature control were crucial to the experimental setup when obtaining electrical characterisation STC data. Figure 5 shows the thermal distributions obtained from the preliminary COMSOL study, alongside a photograph of the ALPHA receiver post-accelerated ageing. Preliminary receiver accelerated ageing testing was undertaken on the ALPHA CPV-TE hybrid at Bangor University CLARET for 1200 hours. This data was used to evaluate current performance, and for estimation of future device long-term

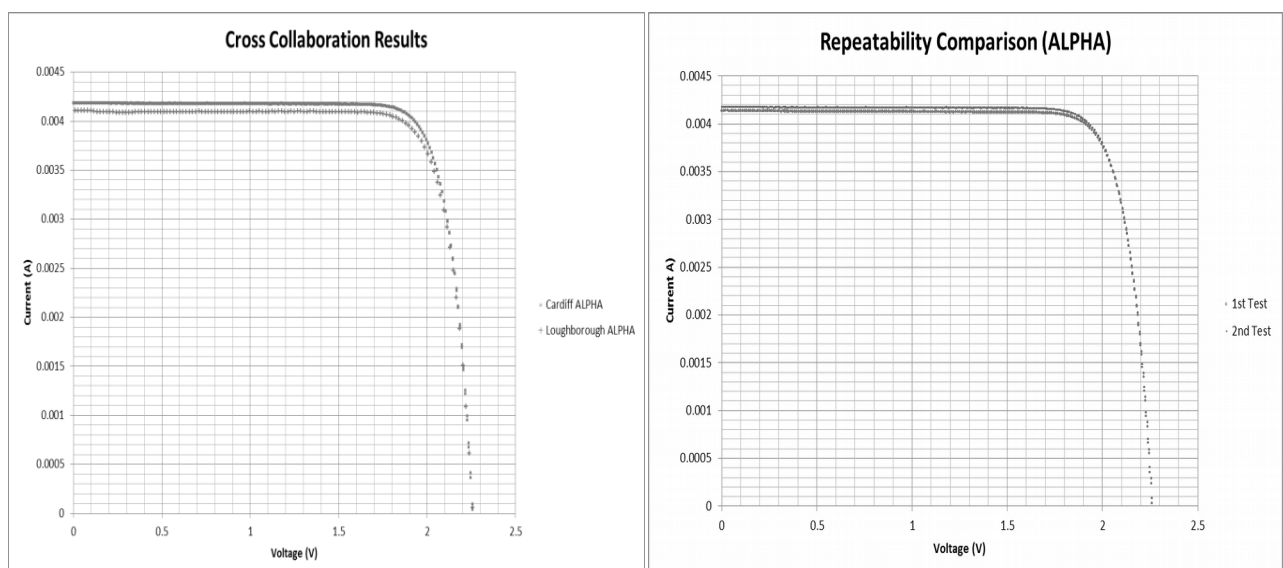


Figure 3. Cross correlation results Loughborough – Cardiff.

Figure 4. Repeatability Comparison (ALPHA) Cardiff.

performance and hence highlight possible premature failure areas to solve before progressing to large number / module testing. The testing involved a 600 hour study at 1 sun and 2 sun light soaking, achieving elevated cell temperature measurements (thermal camera) of approximately 80°C and 120°C respectively.

### 5. Discussion

General heat degradation of the PCB fibreboard can be clearly seen by the discolouration in the comparison of the COMSOL model and the images of ALPHA post-reliability testing, shown in Figure 5. Included above (Figure 2) is a series of thermal images taken throughout the pre-ageing experimental testing of the ALPHA receiver at Cardiff. The areas of specific damage caused by the accelerated ageing process are also visible in the thermal images as a temperature

PCB structure to ensure mechanical integrity. These thermal distributions occur if the epoxy layer is a non-uniformly applied – an effect previously thought negligible. This preliminary testing shows that a homogeneous adhesive application throughout the manufacture process would eliminate epoxy based hotspots from occurring, and hence eliminate a premature failure mode. Likewise, the PCB overhangs gave a secondary area of premature ageing for the PCB through an inadequate thermal contact to the copper substrate and hence heat flow path, as shown by the COMSOL simulation. With the exception of the aforementioned points, no other obvious degradation method was visible and the receiver exhibited good mechanical stability throughout testing.

From the long term performance data, the first 600 hour period of testing showed an overall

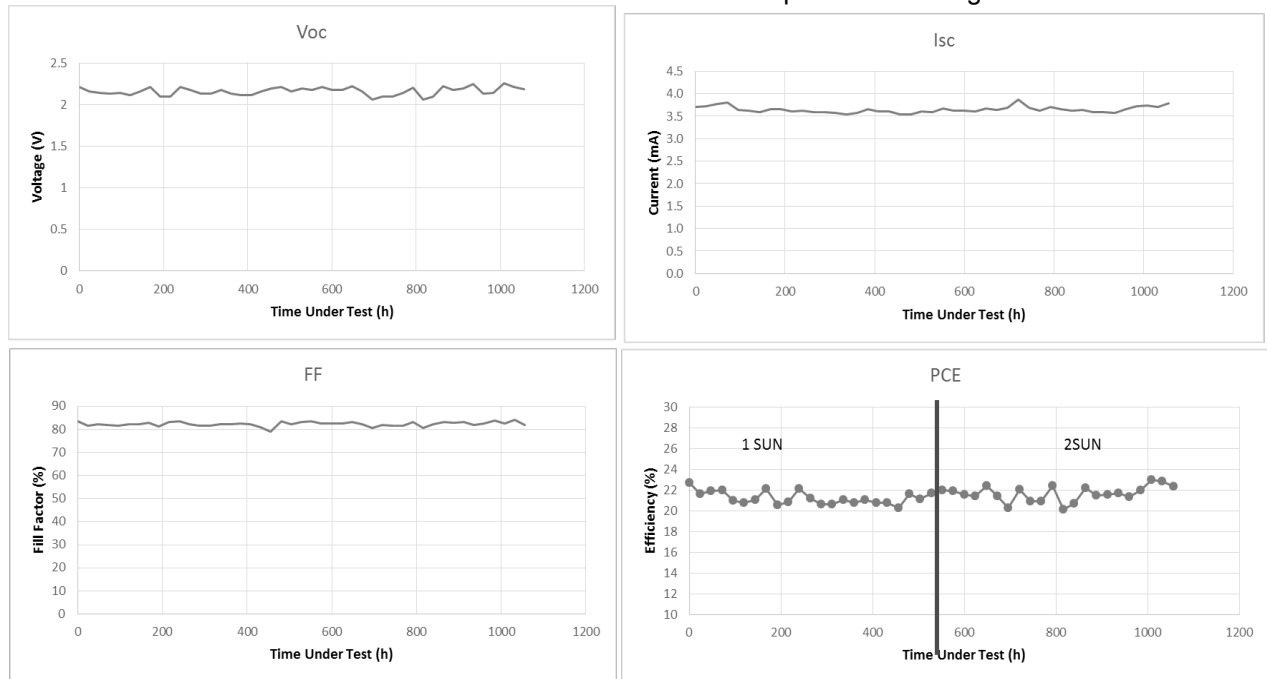


Figure 6. Reliability Testing Data of ALPHA from Bangor's CLARET

inhomogeneity as compared to the rest of the board – a “thermal anomaly”.

Multiple temperatures were tested throughout this series of experiments, compensating for any temperature accuracy drifts of the camera exhibiting these distributions as spurious. Multiple orientations were photographed, thereby plausibly eliminating spectral or reflection errors that would also give anomalous dark spots on the images of Figure 2. Investigating this further, during manufacture, epoxy is used within the bi-layer

degradation of approximately 2% power conversion efficiency, with the fill factor remaining comparable within experimental error. The 2 sun light soaking testing produced an elevated temperature of 120°C to further increase the thermal stress on the solar cell operating conditions. This temperature was obtained due to receiver surface-convection being exhibited as the predominant cooling mechanism in the ageing setup, as the receiver was placed on an insulated platform. During the successive 600hours testing the solar cell exhibited a power conversion efficiency degradation of a further 1%, once

more showing promising long-term performance for these preliminary CPV-TE hybrids, regardless of the additional thermal resistance added by the thermoelectric being within the cooling heat flow path. Temperatures of 120°C are in excess of the rated operating temperature for all components involved in the hybrid's construction. However, the receivers gave good electrical characteristics after ageing tests. Future testing will focus greater on updated receiver design change evaluation, further device testing and thermal management with passive and active cooling methods for the hybrid CPV-TE receiver. It is clear that ALPHA remains stable under 1-2 sun testing conditions. Therefore to increase the degradation rate, higher irradiance levels, thermal cycling and humidity stressing is needed.

## 6. Conclusion

Pre-ageing, an experimentally observed repeatability within 1.1% and accuracy of measurement within 2% of an independent test centre was exhibited by the CPV-TE receiver. Preliminary accelerated lifetime and performance degradation testing was undertaken on a CPV-TE hybrid receiver for the first time. One sun showed 2% conversion efficiency degradation over 600 hours. Visible analysis highlights areas of PCB thermal degradation improvement and premature failure prevention. Two sun testing presented elevated temperatures up to 120°C, and an additional 1% degradation over a further 600 hours. This work shows great promise for the longevity possible with further developed CPV-TE hybrid solar receivers. Future work will investigate testing under higher concentration ratio and irradiance conditions. The thermal management of the receiver will be investigated further and optimised receiver configurations of the hybrid design will be manufactured and tested.

## Acknowledgements

The authors would like to thank the Sêr Cymru National Research Network (<http://www.ernw.ac.uk/en/>) for financial support, IQE plc for supply of III:V triple-junction cells, Cardiff School of Physics for cleanroom facilities, Loughborough CREST for cross-correlation data and EPSRC SUNTRAP consortium (EP/K022156/1) for collaboration.

## References:

1. Dimroth, F., et al., *Four-Junction Wafer-Bonded Concentrator Solar Cells*. IEEE Journal of Photovoltaics, 2016. **6**(1): p. 343-349.

2. Ekins-Daukes, N.J., et al., *What does CPV need to achieve in order to succeed?* AIP Conference Proceedings, 2016. **1766**(1): p. 020004.
3. Fairley, P., *New Scientist Gamechangers: Energy*. 2015.
4. Goldsmid, H.J., A.R. Sheard, and D.A. Wright, *The performance of bismuth telluride thermojunctions*. British Journal of Applied Physics, 1958. **9**(9): p. 365.
5. Kugele, R., et al. *Thermoelectric generators in photovoltaic hybrid systems*. in *Thermoelectrics, 1996., Fifteenth International Conference on*. 1996. IEEE.
6. Vorobiev, Y., et al., *Thermal-photovoltaic solar hybrid system for efficient solar energy conversion*. Solar energy, 2006. **80**(2): p. 170-176.
7. Kraemer, D., et al., *Photovoltaic-thermoelectric hybrid systems: A general optimization methodology*. Applied Physics Letters, 2008. **92**(24): p. 243503.
8. Van Sark, W., *Feasibility of photovoltaic-thermoelectric hybrid modules*. Applied Energy, 2011. **88**(8): p. 2785-2790.
9. Chávez-Urbiola, E., Y.V. Vorobiev, and L. Bulat, *Solar hybrid systems with thermoelectric generators*. Solar energy, 2012. **86**(1): p. 369-378.
10. Zhu, W., et al., *High-performance photovoltaic-thermoelectric hybrid power generation system with optimized thermal management*. Energy, 2016. **100**: p. 91-101.
11. Beeri, O., et al., *Hybrid photovoltaic-thermoelectric system for concentrated solar energy conversion: Experimental realization and modeling*. Journal of Applied Physics, 2015. **118**(11): p. 115104.
12. Sweet, T.K., et al. *Scalable solar thermoelectrics and photovoltaics (SUNTRAP)*. in *AIP Conference Proceedings*. 2016. AIP Publishing.

# Influence of sulfur loading during sulfurization of Cu<sub>2</sub>ZnSnS<sub>4</sub> absorber layers for thin film solar cells.

S. Mazzamuto<sup>1\*</sup>, S. Dale<sup>2</sup>, L.M. Peter<sup>2</sup>, N.M. Pearsall<sup>1</sup>, I. Forbes<sup>1</sup>

<sup>1</sup> NPAG, Department of Physics and Electrical Engineering, Northumbria University, Newcastle NE1 8ST, UK,

<sup>2</sup> Department of Chemistry, University of Bath, Bath, BA2 7AY, UK

\* Corresponding Author [samantha.mazzamuto@northumbria.ac.uk](mailto:samantha.mazzamuto@northumbria.ac.uk)

## Abstract

This paper presents a study on the synthesis and the characterization of CZTS layers prepared by varying the sulfur content during the conversion of sputtered metal precursors. Absorber layers are produced using a two-stage process. The first involves deposition of metallic Cu-Zn-Sn precursors by sputtering onto Mo-coated soda-lime glass substrates. The second involves conversion of the precursor films into the kesterite by heating the samples, together with sulfur and tin sulfide, in a graphite box to 550°C in a tube furnace under argon.

Scanning electron microscopy coupled with energy dispersive spectroscopy (SEM/EDS) were used to determine morphology and composition, whilst the structural and phase characterization was carried out using X-ray diffraction. External quantum efficiency (EQE) measurements were used to characterize the optoelectronic response of the samples.

## Introduction

Cu<sub>2</sub>ZnSn(S,Se)<sub>4</sub>-based kesterite materials are promising for photovoltaic applications due to their being primarily based on earth-abundant and non-toxic elements. The current record 12.6% efficiency for kesterite (CZTSSe) solar cells was reached by IBM [1]. To compete with other technologies, the performance will need to be improved. This will require control over the formation of secondary phases such as ZnS(e), Cu<sub>2</sub>S(e), SnS(e) and Cu<sub>2</sub>SnS(e)<sub>3</sub> that can reduce device performance [2]. The narrow phase window for pure kesterite results in one of the main challenges for achieving high efficiency Cu<sub>2</sub>ZnSnS<sub>4</sub> solar cells, which is the need to form this phase over large areas. Moreover, several authors have reported a blistering effect [3] and the formation of voids during the conversion both at the interface with the molybdenum [4] and on the surface [5-7] of CZTS films. Another challenge concerns the spatial uniformity in composition of the material and, as a consequence, the optoelectronic properties. It has been shown that the use

of H<sub>2</sub>S for the conversion leads to greater uniformity of the material across the whole area of the sample because the gas promotes formation of large-grained CZTS films with a uniform diffusion of the elements [8]. However, H<sub>2</sub>S is highly toxic, which effectively excludes its use for future industrial scale-up.

In this work, co-sputtered Cu-Zn-Sn precursors were converted into CZTS by placing the samples in a graphite box together with sulfur and SnS and heating in a tube furnace. The investigation compared CZTS films converted in the presence of different amounts of sulfur with all other conversion parameters (i.e. temperature profile and magnitude, conversion time and ambient pressure) unchanged

## Experimental

Processing: Cu, Zn and Sn metallic precursors were deposited by magnetron sputtering onto 500 nm thick Mo-coated 25 mm x 50 mm x 1mm soda lime glass. The Cu, Zn and Sn targets have respectively 6N, 4.5N and 5N purity, and the deposition powers used were 130 W, 55 W and 90 W, respectively. A working argon pressure of 1.3x10<sup>-3</sup> torr and deposition times of 30 min were used for all samples. The precursor thickness was 500 nm, and the composition was Cu-poor and slightly Zn-rich with Cu/(Zn+Sn) ≈ 0.8 and Zn/Sn ≈ 1.2.

The precursors were placed in a graphite box together with S (from Aldrich, 99.998% purity) and SnS (Alfa Aesar, 99.5% purity). The well-sealed graphite box was placed in a tube furnace, heated to 550 °C and kept at this temperature for 30 min at 5 mbar argon pressure. Finally, the samples were allowed to cool naturally over several hours to room temperature.

This study shows a series of four samples converted by keeping the SnS loading (20 mg) constant during the conversion and varying the S loading, which was 100 mg for sample A, 150 mg for sample B, 200 mg for sample C and 300 mg for sample D.

Characterisation: All the absorbers were characterised by scanning electron microscopy (SEM) on TESCAN instrument

combined with an Oxford Instruments energy dispersive X-ray (EDS) spectroscopy system in order to measure the elemental compositions of the samples. EDS was carried out using an accelerating voltage of 15 kV.

The structural and phase characterisation was carried out using X-ray diffraction (XRD) with a Siemens D-5000 diffractometer in the Bragg–Brentano geometry using a Cu-K $\alpha$  radiation source ( $\lambda = 1.5418 \text{ \AA}$ ) with insufficient Ni-filtered Cu-K $\alpha$  radiation.

Finally, in order to characterise the optoelectronic response of the samples, electrochemical, external quantum efficiency measurements were performed at the University of Bath using a transparent electrolyte contact. Before the EQE measurements, samples were etched for 30 s in 10 % aqueous KCN solution and then coated with a ca. 50 nm thick CdS layer deposited by CBD. Measurements were performed in a standard three electrode cell using a Pt gauze counter electrode and a Ag/AgCl (3 M KCl) reference electrode, with an applied potential of -0.3 V versus an Ag/AgCl reference electrode. Acetate buffer (pH 4.7) was used as the electrolyte. The illuminated area has an approximate area of 2 mm<sup>2</sup>.

## Results and discussion

Sputter deposition of the Cu-Zn-Sn precursors resulted in a set of layers with values of Cu/(Zn + Sn) = 0.8 and Zn/Sn = 1.2, measured using EDS. The precursors were sulfurized using four different quantities of sulfur, as described in the experimental section. The composition of the absorber layers produced, together with the name of the sample and the S quantity used during the conversion, is shown in Table 1.

Sample → S quantity	Cu/(Zn + Sn)	Zn/Sn	S/M
Precursor	0.8	1.2	-
A → 100mg	1.0	1.3	0.9
B → 150mg	1.0	1.3	0.9
C → 200mg	1.0	1.1	1.0
D → 300mg	0.9	1.1	1.2

**Table 1.** List of absorbers, S quantity used and Atomic ratios (determined using EDS) of the starting precursors and all the four absorbers of this study.

Table 1 shows that all the absorber layers are Zn-rich, with a Zn/Sn ratio that decreases when the S quantity is increased, and they show an almost

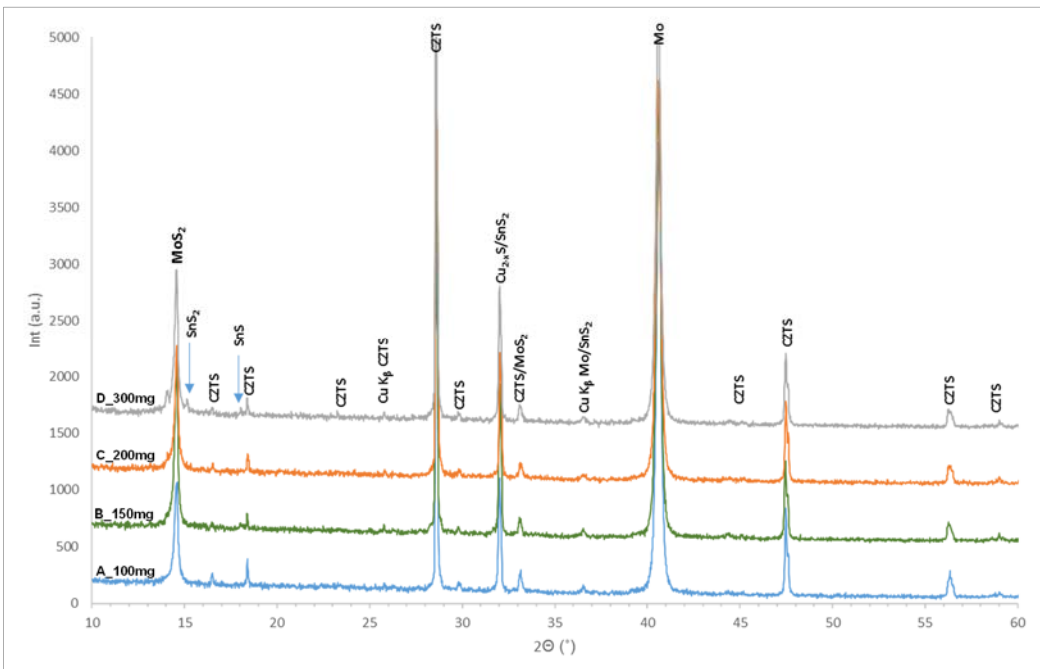
stoichiometric ratio Cu/(Zn+Sn) that decreases below 1 when the S quantity increases. Moreover, the sulfur/metals (S/M) ratio was increased by increasing the sulfur loading.

Figure 1 shows the XRD patterns for the sulfurized samples. The diffractograms were compared with the CZTS powder pattern (JCPDS data file no. 26-0575). The most intense peaks at 2-theta values of 28.45°, 32.98°, 47.34° and 56.16° were clearly observed in all the patterns and correspond to the Miller indices 112, 004/200, 220 and 312, respectively. Furthermore, the low intensity peaks 002, 101 were observed at 2-theta values of 16.29°, 18.26° respectively. These peaks are consistent with the formation of tetragonal CZTS phase over the whole set of samples used for this study. Moreover, signals coming from the Mo substrate (40.51°) and from the MoS<sub>2</sub> (14.55°) phase were observed. Finally, a Sn-S phase was observed in all diffractograms. This SnS phase is converted into SnS<sub>2</sub> by increasing the S loading during the conversion. In fact, starting with the sample converted using 100mg of S, the diffractograms show the formation of SnS and SnS<sub>2</sub> phases. By increasing the sulfur quantity, the SnS phase is reduced and converted into the SnS<sub>2</sub> phase. The higher S/metals ratio of sample D (Table 1) could be related to an increase in the formation of the SnS<sub>2</sub> phase.

Figure 2 shows the EQE spectra obtained for the series of samples. The maximum EQE increases from about 20% for sample A to 60% for the sample B (150 mg of S) but then reduces to 35-40% when the sulfur quantity in the box is increased further to 200 mg and 300 mg, respectively. The energy gap values, which are calculated by extrapolating Tauc plots of [hv × ln(1-EQE)]<sup>2</sup> vs. hv [9] (inset plot in Fig 2), were 1.49 eV for sample A and 1.58 eV for sample B, 1.56 eV for sample C and 1.58 eV for sample D.

For sample B, the sample showing the highest EQE value in the series, a fit (not shown here) was made by assuming that the diffusion length L<sub>n</sub> is sufficiently small that the EQE can be approximated by

$$\text{EQE} = 1 - \exp(-\alpha W) \quad (1)$$



**Figure 1.** XRD patterns of the CZTS samples converted using a sulfur quantity of A) 100 mg, B) 150 mg, C) 200 mg and D) 300 mg. XRD patterns show a formation of Sn-S phase by increasing the S quantity as indicated by the two blue arrows

where  $\alpha$  is the absorption coefficient and  $W$  is the width of the space charge region. By the fitting, a  $W=0.3\mu\text{m}$  was found, which would correspond to a doping density of around  $6 \times 10^{15} \text{ cm}^{-3}$ . SEM top view images of the samples prepared with different S loadings are shown in Figure 3. Sample A (Fig 1A) does

not exhibit voids, while an increase in void density at the surface of the samples is produced by increasing the S quantity. The morphology also changes: the grains gradually become larger with increasing S loading. Sample A shows grains of about  $1\mu\text{m}$ , sample B shows grains of

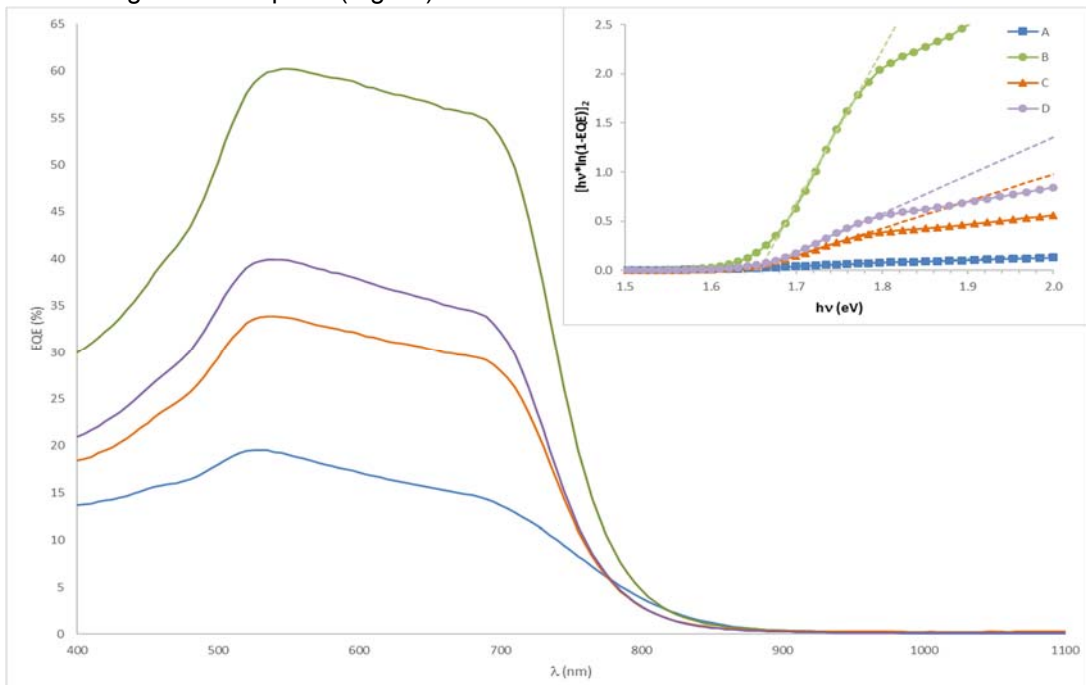


**Figure 2.** EQE measurements of the CZTS samples converted with a S supply of A) 100 mg, B) 150 mg, C) 200 mg, D) 300 mg; inset: the band gaps of the CZTS absorber layers calculated by extrapolating the plots of  $[\text{hv} \times \ln(1-\text{EQE})]^2$  vs.  $\text{hv}$ .

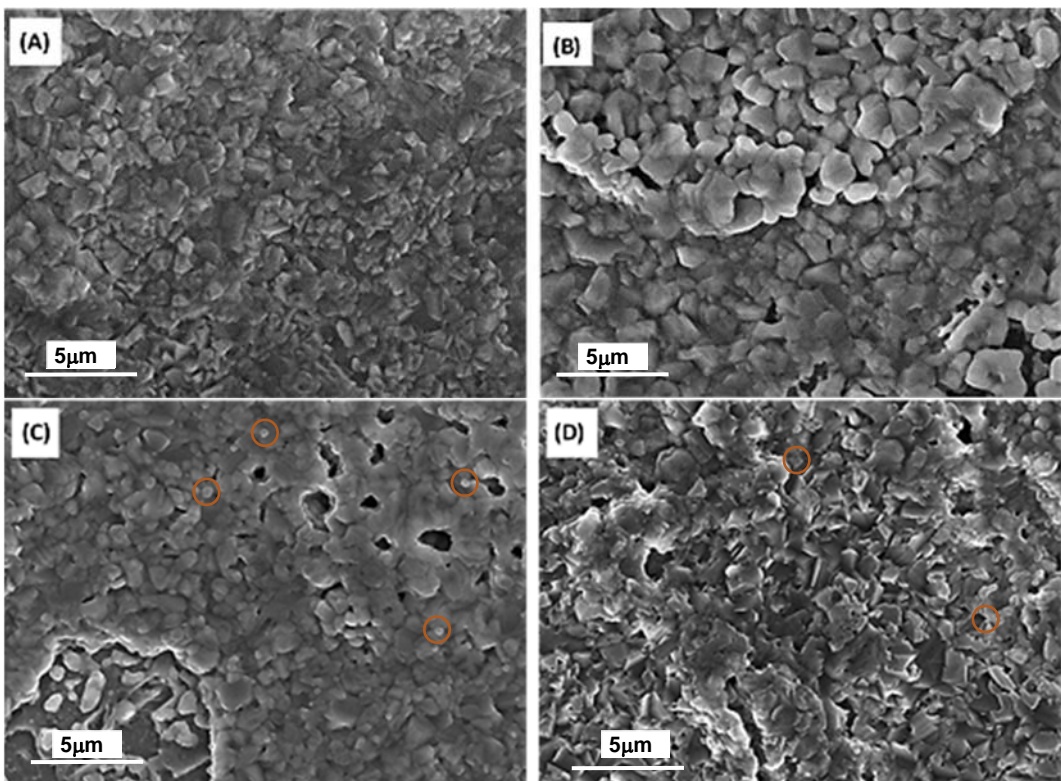


**Figure 3** Plan-view SEM images of absorbers converted varying the S quantity (A) 100 mg, (B) 150 mg, (C) 200 mg, (D) 300 mg. The images were taken using a 15kV acceleration voltage and a view field of 25 $\mu$ m. The orange circles in (C) and (D) highlight the ZnS presence on the surface of the samples.

approximately 1.5 - 2 $\mu$ m. The grain size then reduces with further increases of S loading. Samples C and D show smaller grains than the first two samples, with sample (D) converted with 300 mg of S, exhibiting triangular grains. From the SEM images, it can also be seen that increasing the S loading increases the formation of bright crystals on the surface (indicated with orange circles in Fig.3-C and Fig.3-D). Based on our experience and on EDS mappings, these crystals are identified as ZnS. Finally, the shape of the grains is better defined for samples A and B, with grain boundaries clearly visible.

### Conclusions

This study of the kesterite formation has revealed the important influence of sulfur loading during conversion of sputtered metallic precursors.

The best performing CZTS absorber, as judged by the peak EQE of 60%, was synthesised using 150 mg of S and 20 mg of SnS in the graphite box during the conversion. The samples produced with these conditions exhibited well-defined crystals with a low concentration of secondary phases and a reduced the density of voids.

The results presented here provide insights into the formation of CZTS films and will

assist the design of a CZTS formation processes that minimise the formation of secondary phases and voids.

### Acknowledgements

This work has been undertaken as part of the EPSRC-funded PVTeam project (EPSRC Ref.: EP/L017792/1).

### References

- [1] Wang, W.; et al. Advanced Materials, 2013. **4** (7): 1301465.
- [2] Vanalakar, S.A., et al. Solar Energy Materials and Solar Cells, 2015. **138**: p. 1-8.
- [3] Bras, P., et al. Journal of Vacuum Science & Technology A, 2015. **33**(6): p. 061201.
- [4] Liu, F., et al. ACS Applied Materials & Interfaces, 2015. **7**(26): p. 14376-14383.
- [5] Jung, H.R., et al. Ceramics International, 2015. **41**(10, Part A): p. 13006-13011.
- [6] Johnson, M.C., et al. Chemistry of Materials, 2015. **27**(7): p. 2507-2514.
- [7] Fernandes, P.A., P.M.P. Salomé, and A.F. da Cunha. Thin Solid Films, 2009. **517**(7): p. 2519-2523.
- [8] Khalkar, A., et al. International Journal of Photoenergy, 2015. **2015**: p. 7.
- [9] Zoppi, G., et al. Progress in Photovoltaics: Research and Applications, 2009. **17**(5): p. 315-319.

## Metrology of Dye-sensitized Solar Cells

Leo Furnell<sup>a</sup>, Peter J. Holliman<sup>a\*</sup>, Rosie Anthony<sup>a</sup>, Arthur Connell<sup>a</sup>, Eurig W. Jones<sup>a</sup>,

Christopher P. Kershaw<sup>a</sup>

<sup>a</sup> College of Engineering, Swansea University, Swansea,

\* p.j.holliman@swansea.ac.uk

### Introduction

Due to growing interest in the increased levels of atmospheric CO<sub>2</sub> from the burning of fossil fuels, which contribute to climate change; there is a drive towards mitigating these negative effects. One mitigation method to be considered is the use of renewable energy, such as solar energy [1]. Harvesting energy from the sun *via* the development of photovoltaic (PV) technology has the potential to produce more energy for the planet than is required if harvested efficiently [2]. PV devices use the energy from the sun and convert it into electricity using photochemical reactions [2]. In 1991, O'Regan and Grätzel reported a new type of dye-sensitized solar cell (DSCs), which was a breakthrough in technology using mesoporous TiO<sub>2</sub> sensitized with Ru-bipyridyl dye to enhance photo-current [3]. Since this, there has been significant progress and interest in DSC devices, due to their potential to be low cost, their ease of preparation, good performance and potential to have a positive environmental impact. DSCs are an attractive source of renewable energy due to being made from earth abundant materials, low toxicity, low light operation and potential to be recycled at the end of their lifetime. However, in order to be able to compete with fossil fuels and be commercially viable, DSCs must have a scalable process and it is essential to have lifetimes of at least 20 years [4,5].

For industrial application, continuous processing is preferable, rather than batch processing and this means there needs to be a mechanism of understanding and improving the process. It is important to develop a method of obtaining feedback information in order to achieve in-line processing control, thus enabling flexibility of processing. Metrology is the scientific study of measurement and can be used to gain quantifiable information of a process *in situ* in order to enable and support production by improving quality and productivity [6]. In this paper, we propose that in-line metrology using digital imaging methods can be used as a mechanism to

provide this feedback data continuously, leading to process control in an upscaling context of a production system. This feedback loop can allow the production line to work at an optimum by providing quality control and leading to the optimum yield being produced. We will use fast dyeing as an example of upscaling a process. Fast dyeing DSCs is favoured over the traditional and expensive passive dyeing process. Previous work has been carried out to optimise the fast dyeing process, providing a rapid and efficient method of sensitising DSCs [7].

It is believed that by providing a feedback loop in real time, in-line metrology will improve yield, productivity, speed of process, whilst reducing the costs [8]. An example of this, is the setting of lower and upper limits of dye loading. This monitoring of the dye uptake using process control software would allow the process to stop when a certain level is met, thus allowing homogeneous dyeing at a fraction of the cost. Dye loading is an important aspect of DSC technology as it is important to utilise as many of the dye sites as possible on the surface of the titania for maximum efficiency of the cell [9]. As such, co-sensitisation of dyes is a technique that may improve cell efficiencies by absorbing light at different wavelengths [10].

We would also like to propose the interrogation of different wavelengths of available light as a method to investigate device processing and monitoring. Imaging processes under different  $\lambda$  of light means that our current view of the process could be expanded and inevitably new things may be seen, allowing further control.

### Experimental

#### Metrology of Dye Solutions

Dye solutions of N719, D131, D35, SQ1, SQ2 and methylene blue were prepared in ethanol at a concentration of 0.5mM (Figure1a). Each dye solution was split into two and added to separate sample bottles. The first bottle of each dye was left as stock solution and the second bottle had an

additive of (10mM) 2,2,6,6-tetramethyl-4-piperidinol. Solutions were then sonicated and placed on a south-westerly facing window to allow for natural light exposure. Images were taken after using a Canon EOS 1100D camera with an 18-55 VR lens at 0, 21 and 64 days.

#### Device Fabrication

Electrodes were constructed from TEC7 conductive glass (Pilkington) and cleaned by sonication in acetone for 15 min. Photo electrodes were constructed by doctor blading (Dyesol) Active Opaque paste onto the glass and sintered at 550°C in a Carbolite ashing furnace. Counter electrodes were constructed using (Dyesol) PT-01 platinum paste which was deposited on the surface of the glass with a pipette. The electrodes were then sintered at 450°C in a Carbolite tube furnace. The two electrodes were joined together with a 20µm Surlyn™ (DuPont) thermoplastic gasket at 150°C using a heat press. The electrolyte was then injected into the cell cavity and the cell was sealed with additional Surlyn™ and a glass microscope slide using a soldering iron.

#### Metrology of DSC Devices

For light soaking samples, devices were exposed simultaneously in a Photosimile 200 lightbox with a consistent light intensity of 5Wm<sup>-2</sup> (6000lux). Images were taken using time-lapse photography every 5 seconds using a Canon EOS 1100D camera and an 18-55 VR lens. Contrast controls were also added to give 100% baselines for black and white. A clock was added to ensure images were taken on the correct timescale. A grid was used to organise samples and ensure the correct position was used for image analysis. This was essential, as a macro was used with the program (Sigma Scan Pro 5) to select the active area of each device and measure the values of red, green and blue on the RGB colour model (0-255). The macro also allowed the control area to be analysed to monitor for changes in light levels.

#### UV Imaging

Images were taken using a Nikon D70 with a Nikkor 50mm lens. These were selected due to the lack of UV filters in older camera equipment, as anti-reflective coatings were applied to camera lenses for general use in 1941 [11]. Images were illuminated under a Spectrolite e-series UV lamp with an output wavelength of 365 nm.

## Results and Discussion

### Natural Light Exposure

We have investigated the colour of dye solutions during light soaking and quantified changes with RGB analysis. This established a strong correlation between dye degradation and a change in RGB values.

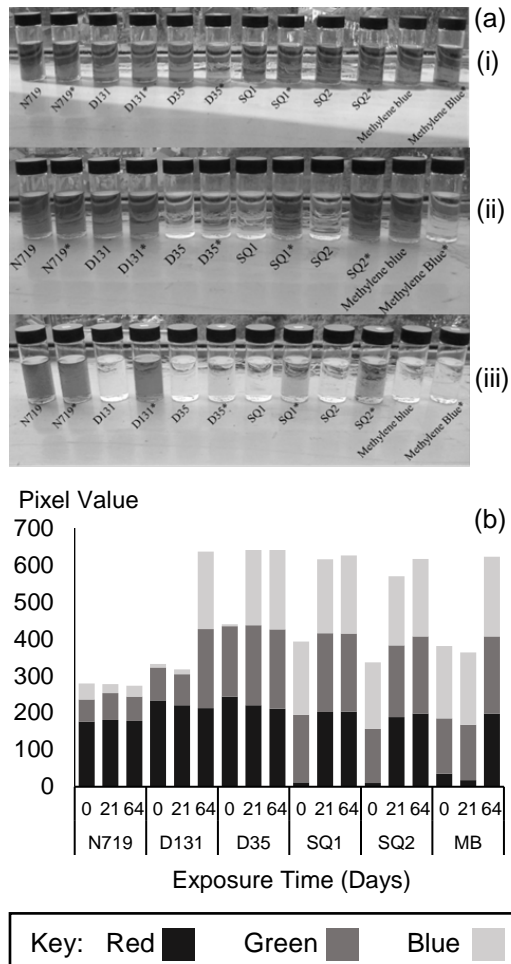


**Figure 1a.** Dye solutions (0.5mM) (i) before light exposure, (ii) after 20d light exposure and (iii) after 2 months exposure. Dyes marked \* had an additive of 10 mmol 2,2,6,6-tetramethyl-4-piperidinol added to the solution. Images were recorded with a 28mm lens, ISO 100 and white balance of 0. Note: the samples that appear white in the image have degraded significantly and the darker solutions have not degraded.

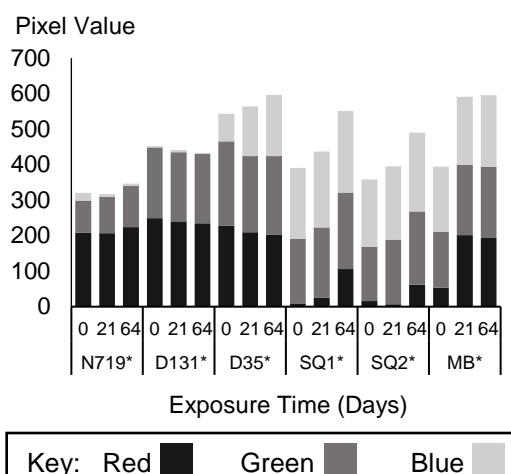
**Figure 1b.** Red, green and blue (RGB) analysis of dye solutions at 0, 21 and 64 days of natural light exposure.

Figure 1a shows dye colour changes when exposed to natural light. These colour changes suggest degradation of the dye has occurred resulting in a decreased colour intensity. The images also show

differences between the rates that dyes degrade as D35 shows a significant difference between 0 and 64 days whereas N719 shows very little change.

Figure 1b shows a significant range in stabilities between dye solutions. N719 shows very little change in RGB values, indicating a high stability. D131 shows a small change initially but after 64 days all three colours are roughly equal. This indicates that the solution has turned transparent showing that the dye has significantly degraded. D35 shows equal RGB values after just 21 days indicating a high rate of degradation. SQ1 also shows a high rate of degradation with almost equal RGB values after 21 days and equal values after 64 days. SQ2 shows a slightly slower rate of degradation than SQ1. The RGB values for SQ2 are similar after 21 days indicating degradation has started to occur. After 48 days the values are roughly equal indicating significant degradation. Methylene blue dye shows some initial degradation after 21 days and a more substantial degradation after 48 days.

To investigate stability, an additive of 2,2,6,6-tetramethyl-4-piperidinol (TMP) was added each of the dye solutions. This was intended to slow degradation caused by oxygen radicals [12], since TMP is a free radical scavenger [13]. The solutions with the additive were exposed at the same time as the solutions without additive. This ensured that light exposure levels would be consistent between the two. The data from the RGB analysis is shown in Figure 2.

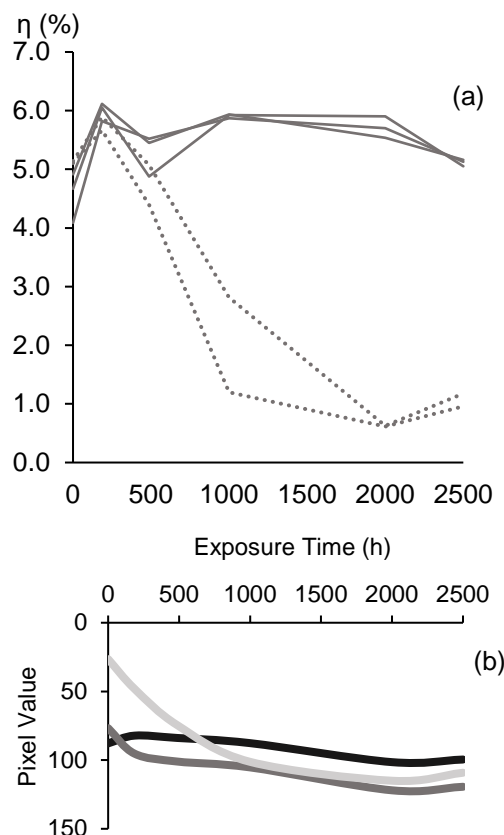


**Figure 2.** Red, green and blue (RGB) analysis of dye solutions with 2,2,6,6-tetramethyl-4-piperidinol at 0, 21 and 64 days of natural light exposure.

Figure 2 shows that the rate of degradation has been slowed in D131, D35, SQ1 and SQ2 dye solutions with D131 stabilised to 64 days. This is indicated by an increase in the time taken for all three values to become roughly equal. TMP had the opposite effect in N719 and methylene blue solutions and increased the rate of degradation. These data suggest that the use of TMP with these two dyes would be inadvisable in full operation. Overall, however, the majority of the dyes were stabilised by the TMP, making it a useful additive for extending dye lifetime.

#### Metrology of DSC Devices

Previous work by this group focused on comparing RGB analysis to IV data obtained from solar simulation. The solar simulator data is shown in Figure 3.



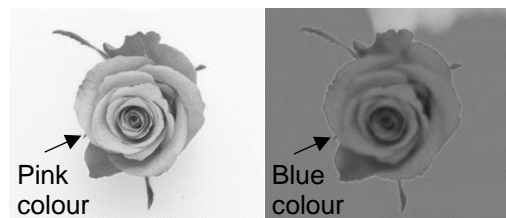
**Figure 3a.** Efficiency against time for selected N719 DSC devices, measured over 2500h of light soaking. **Figure 3b.** RGB analysis of the electrolyte colour in devices without a UV filter. Redrawn from work published previously by this group<sup>4</sup>.

Figure 3a is concordant with the literature that devices made with N719 remain highly stable, with little change in efficiency over 2500 h [14]. Conversely, the devices without UV filters degrade significantly in

the first 1000 h. Figure 3b shows RGB analysis of an unfiltered cell with a gradual increase in the blue value. An increase in the blue value corresponds to a decrease in yellow colour as they opposing colours. Further analysis of device area (dyed TiO<sub>2</sub> vs only electrolyte) indicates bleaching of the electrolyte which is the cause of the degradation in the devices<sup>15</sup>. This shows a clear link between the device efficiency and colour of the electrolyte.

#### Wavelength Imaging

In addition to looking at the visible range of light we are also studying the UV and NIR ranges. As an example, images taken of a rose under UV light show a very different picture compared to what we see under visible light, as shown in Figure 4.



**Figure 4.** Image of a rose (left) under normal light and (right) under UV light.

The possibility of imaging devices in the same way has great potential. UV light may indicate features which would otherwise be invisible to the naked eye.

#### Conclusions

Using in-line digital imaging metrology to provide continuous data in a real-time feedback loop, is an innovative and highly useful mechanism to provide process control within a production system. We have shown that the method works well with the study of device lifetime and it is likely that this approach will prove to be a useful tool with processing. Allowing a greater level of control, during continuous processing when upscaling a process, will not only be useful but time and cost effective in an industrial context.

#### Acknowledgements

We gratefully acknowledge funding provided by the European Union and Welsh Government for Sparc II (LF, RA), from the Welsh Government for Sêr Cymru (PJH) and NRN (CPK) and from EPSRC EP/M015254/1 (AC, EWJ), the EPSRC UK National Mass Spectrometry Facility at Swansea University and Pilkington-NSG for TEC™ glass.

#### References

1. J. G. Canadell, C. Le Quéré, M. R. Raupach, C. B. Field, E. T. Buitenhuis, P. Ciais, T. J. Conway, N. P. Gillett, R. A. Houghton, G. Marland, *Proceedings of the National Academy of Sciences of the United States of America*, 2007, **104**, 18866–18870.
2. J. Wu, Z. Lan, J. Lin, M. Huang, Y. Huang, L. Fan, G. Luo, *Chemical Reviews*, 2015, **115**, 2136–2173.
3. B. O'Regan, M. Grätzel, *Nature*, 1991, **353**, 737–740.
4. L. Furnell, P. J. Holliman, A. Connell, E. W. Jones, R. J. Hobbs, C. P. Kershaw, R. Anthony, J. R. Searle, T. M. Watson, J. McGettrick, *Sustainable Energy Fuels*, 2017, DOI: 10.1039/C7SE00015D.
5. R. Harikisun, H. Desilvestro, *Solar Energy*, 2011, **85**, 1179–1188.
6. H. Kunzmann, T. Pfeifer, R. Schmitt, *CIRP Annals- Manufacturing Technology*, 2005, **54**, 155–168.
7. P. J. Holliman, M. L. Davies, A. Connell, B. Vaca Velasco, T. M. Watson, *Chemical Communications*, 2010, **46**, 7256–7258.
8. R. M. Swanson, *Prog. Photovolt: Res. Appl.*, 2006, **14**, 443–453.
9. M. Grätzel, *Inorganic Chemistry*, 2005, **44**, 6841–6851.
10. S. L. Bayliss, J. M. Cole, P. G. Waddell, S. McKechnie, X. Liu, *Journal of Physical Chemistry C*, 2014, **118**, 14082–14090.
11. B. Salt, *Film Quarterly*, 1976, **30**, 19–32.
12. I. K. Konstantinou, T. a. Albanis, *Applied Catalysis B: Environmental*, 2004, **49**, 1–14.
13. P. Pospíšil, *Biochimica et Biophysica Acta - Bioenergetics*, 2012, **1817**, 218–231.
14. N. Kato, Y. Takeda, K. Higuchi, A. Takeichi, E. Sudo, H. Tanaka, T. Motohiro, T. Sano, T. Toyoda, *Solar Energy Materials and Solar Cells*, 2009, **93**, 893–897.
15. M. Carnie, D. Bryant, T. Watson, D. Worsley, *International Journal of Photoenergy*, 2012, 524590.

## **U-value calculation of CdTe thin film PV glazing using indoor characterization**

HAMEED ALRASHIDI, ARITRA GHOSH, WALID ISSA, NAZMI SELLAMI, SUNDARAM

SENTHILARASU, TOWNLEY STUART, MALLICK TAPAS

Environment and Sustainability Institute-University of Exeter Penryn Campus-Penryn

Cornwall TR10 9FE UK

\* Corresponding Author [Ha314@exeter.ac.uk](mailto:Ha314@exeter.ac.uk)

### **Abstract**

Adaptive PV glazing has potential to reduce the cooling system demand. The aim of this research is to investigate about the Overall heat transfer coefficient U-value and thermal performance of a 40% transparency – Cadmium Telluride (CdTe) thin film PV cell. Two test cells were made using insulation board, thin film PV was fitted to one of them while single glazing was fitted to the other. An indoor experiment using solar simulator (AAA standard) was carried out and 1D steady heat transfer equations were used for U-value calculation. In order to have better assessment of the thin film PV, its performance was compared to that of single glazing. Results showed that the U-value of the thin film PV (3.3 W/m<sup>2</sup>K) is less than that of the single glazing (5.8 W/m<sup>2</sup>K). Also, using the 40% transparency - thin film PV cell causes the temperature difference between inside and outside the test box to be higher than the temperature difference in case of using single glazing. These results show that there is a promising energy saving potential for thin film PV cells.

### **Keywords**

BIPV – Thin film PV cells – Overall Heat Transfer coefficient

### **Nomenclature**

**A** Area of glazing or PV (m<sup>2</sup>)

**hi** Convexion heat transfer coefficient inside the test cell (w/m<sup>2</sup>K)

**ho** Overall heat transfer coefficient outside the test cell (w/m<sup>2</sup>K)

**I** Solar irradiance (W/m<sup>2</sup>)

**K** Thermal conductivity (W/mK)

**L** Thickness of glazing or PV (m)

**R** Thermal resistance

**U** Overall heat transfer coefficient (W/m<sup>2</sup>K)

**α** Absorbance

**ΔT** Temperature difference between inside and outside the test cell (°C or K)

**τ** Transmittance

### **Introduction**

Building Integrated Photovoltaic (BIPV) is a breakthrough technology that if deployed in the glass windows, will allow the light to pass through into the building while it absorbs the heat from the sun. This technology will enable architectures in hot environment to use the advantages of large windows or even full glass facades in their design to have shiny and light interiors, while not allowing the heat from the sun to go inside the building. The amount of heat that passes through the glazing depends on the overall heat transfer coefficient (U-value) which is the parameter calculated in this research.

Thin film solar panels are favourable to be used in BIPV due to their low material usage and rising efficiencies. Cadmium Telluride (CdTe) is one of the main types of thin film PV and it is the studied type.

### **1. Literature Review**

N. Skandalos and D. Karamanis [1] stated that PV glazing is an innovative technology that doesn't only produce green energy, but also reduce the energy associated to cooling, heating and lighting. They also pointed that these benefits depend on the PV coverage ratio [2]. F.J. Moralejo-Vázquez et al. [3] concluded in their research that PV glazing is feasible and efficient when integrated in building facades and windows, because of their daylight and solar control. L. Lu and K. Law [4] agreed with the previously mentioned results when their analysis showed that the annual electricity benefits when using PV glazing are 900 KW-h for water-cooled air conditioning systems and 1300 KW-h for

air-cooled air conditioning systems. J. Han [5] went farther in their conclusion when they found that their new model of see-through PV glazing system provides visual comfort in addition to energy saving in air conditioning and lighting. W. Liao and S. Xu [6] have made a comparison between see-through PV glazing and single and double glazing. They found that PV glazing has better energy performance and cooling energy is the dominant factor. They also stated that PV glazing is more beneficial than traditional glazing when applied in shallow rooms with large windows or high ceilings. Previous researches showed a promising potential for semi-transparent PV glazing. In this research, Calculation of the U-value of 40% transparency CdTe thin film PV will be presented using indoor characterization and the result is compared to a single glazing.

## 2. Methodology

### 2.1 Experiment Set-up

In order to calculate the U-value of the 40% transparency CdTe - thin film PV, two test cells ( $0.22 \text{ m} \times 0.2 \text{ m} \times 0.18 \text{ m}$  each) were designed and implemented for an indoor experiment. The test cells were made of insulation board (U-value =  $0.02 \text{ W/m}^2\text{K}$ ). A PV cell whose dimensions are ( $0.15 \text{ m} \times 0.15 \text{ m} \times 0.06 \text{ m}$ ) was fitted to one of the cells, while an ordinary 100% transparency single glazing, of the same dimensions, was fitted to the other cell. An AAA standard – solar simulator was used to emit an irradiance of  $1000 \text{ W/m}^2$  so that a variation of temperatures could occur. In order to study the thermal performance of the PV and compare it to the ordinary single glazing, thermocouples were used to measure temperatures inside and outside the test cells and on the inner and outer surfaces of the PV and glazing. A spectrometer was used to measure the transmittance through the PV and a data acquisition system was used to monitor and save the required data.

The experiment set-up is shown in figure 1.

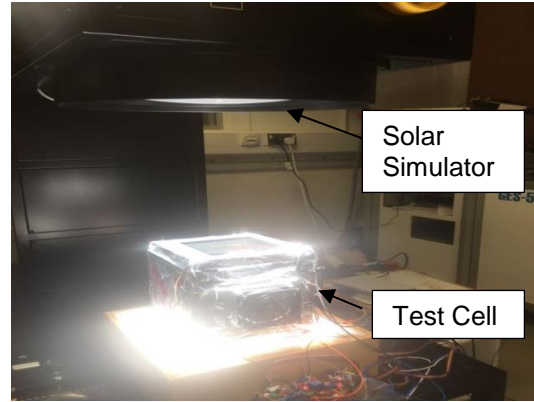


Figure1. Experiment Set-up

### 2.2 Equations

1D steady heat transfer equations as shown below were used in order to calculate the U-value.

$$IA\tau\alpha = \Delta T/R \quad (1)$$

$$R = 1/h_oA + 1/h_iA + L/K_A \quad (2)$$

$$\alpha = 2 - \log_{10} \% \tau \quad (3)$$

$$\text{U-value} = K/L \quad (4)$$

Table 1 shows the way how each parameter was measured or calculated.

I	Using AAA simulator
A	Area of glazing in $\text{m}^2$
$\tau$	Using spectrometer
$\alpha$	Using beer's Law
$\Delta T$	Using thermocouples
$h_o$	Assumed $9 \text{ W/m}^2\text{K}$
$h_i$	Assumed $8 \text{ W/m}^2\text{K}$

L	Thickness of glazing in m
K	Calculated through combining equations (1), (2) and (3) in W/m.K
U-value	Calculated through equation (4) in W/m <sup>2</sup> .K

Table1. Parameters' Measurement and Calculation

Thermal resistance method was used to calculate U-value of the 40% transparency thin film PV. Equations (1) and (2) show that the total heat supplied to the PV is the heat coming from solar simulator, and it faces three resistances, two of them are convection thermal resistances from air inside and outside the test cell, and the third is the conduction thermal resistance while the heat passes through the glazing. Equation (4) gives a direct formula between the conductivity of the PV and U-value. While equation (2) (Beer's Law) shows a relation between absorbance and transmittance.

Combining the previous equations and a proper use of equipment make it possible to study the thermal performance of the thin film PV and calculating the U-value.

## Results

The experiment was carried out for 4 hours to make sure that heat transfer is steady and equations can be applied. The temperature inside the test cell was recorded and plotted in Figure 2.

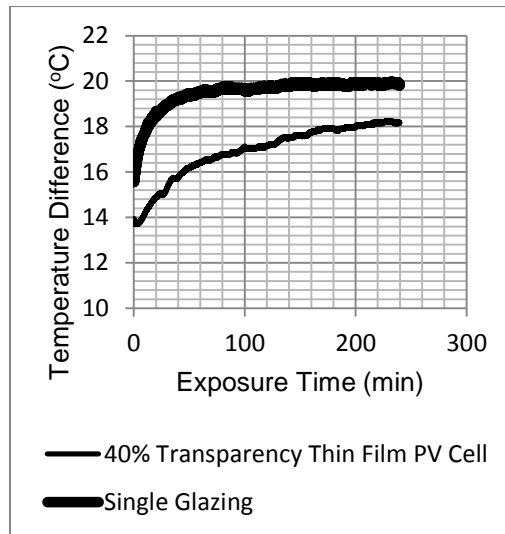


Figure2. Variation of Temperature inside the Test Cell with respect to time

Figure 2 shows that the temperature inside the box increases with time because of the 1000 W/m<sup>2</sup> irradiation emitted by the solar simulator, and then it becomes steady. For single glazing, steady state at the maximum temperature was reached after about 80 minutes. While for the 40% transparency thin film PV, steady state at maximum temperature was reached at 200 °C. This shows that heat transfer through the single glazing was faster than that in thin film PV cell.

Figure 3 shows the temperature difference between inside and outside the test cell. Plotted curves show that  $\Delta T$  for the single glazing is about 11.5 °C at steady state, less than that in case of PV single glazing that reached 14.5 °C at steady state. This result also confirms that the heat transfer through single glazing is higher than heat transfer through PV cell.

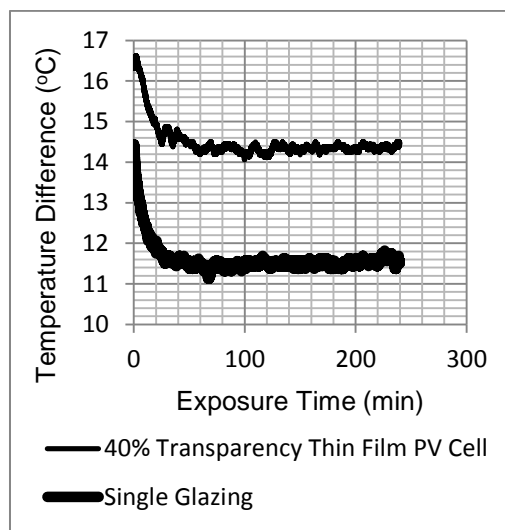


Figure3. Variation of temperature difference between inside and outside the test cells with respect to time

## Conclusion

Through figures 2 and 3 it is expected that the U-value of thin film PV cell is lower than that of single glazing. This result was approved by calculating the U-value throughout the previously presented equations.

Calculations showed that the U-value of single glazing is 5.8 W/m<sup>2</sup>K higher than that of the 40% transparency CdTe thin film PV that was found to be 3.3 W/m<sup>2</sup>k. These values show that the energy saving potential of PV thin film is promising.

Switchable Glazing”, Applied Energy, 362-369, 2015.

[8] Y.A. Cengel, “Heat Transfer a Practical Approach”, Second Edition, McGraw-Hill, New York, 2004.

## References

- [1] N. Skandalos, D. Karamanis. “PV Glazing Technologies” Renewable and Sustainable Energy Reviews, Vol. 49, 306–322, September 2015.
- [2] N. Skandalos, D. Karamanis. “Investigation of thermal performance of semi-transparent PV technologies” Energy and Buildings, Vol. 124, 19–34, 15 July 2016
- [3] F.J. Moralejo-Vázquez, N. Martín-Chiveleta, L. Olivieri, E. Caamaño-Martín. “Luminous and solar characterization of PV modules for building integration” Energy and Buildings, Vol. 103, 326–337, 15 September 2015.
- [4] L. Lu, K. Law, “Overall Energy Performance of Semi-Transparent Single Glazed Photovoltaic (PV) window for a Typical Office in Hong Kong” Renewable Energy, Vol. 49, 250-254, 2013.
- [5] J. Han, L. LU, H. Yang “Thermal Behavior of a Novel Type See-Through Glazing System with Integrated PV Cells” Building and Environment, Vol. 44, 2129-2136, 2009.
- [6] W. Liao, S. Xu, “Energy Performance Comparison Among See-Through Amorphous Silicon PV (PhotoVoltaic) Glazing and Traditional Glazings Under Different Architectural Conditions in China” Energy, Vol. 83, 267-275, 2015
- [7] A. Ghosh, B. Norton, A. Duffy  
“Measured Overall Heat Transfer Coefficient of a Suspended Particle Device

# Large Area Deposition of $\text{CH}_3\text{NH}_3\text{PbI}_3$ Films Using Aerosol-Assisted Chemical Vapour Deposition

Heather M. Yates\* and Mohammad Afzaal

Materials and Physics Research Centre, University of Salford, Salford, M5 4WT. UK,

\* Corresponding Author H.M.Yates@salford.ac.uk

## Abstract

World-wide interest in hybrid perovskite solar cells has yielded power conversion efficiencies in excess of 22%. Attempts to deposit high-quality perovskite layers,  $\text{CH}_3\text{NH}_3\text{PbI}_3$  by one or two-step solution processes such as spin coating are wide spread and are challenging to scale up. For large scale and cost-effective deposition of absorber layers with large grain sizes, chemical vapour deposition (CVD) processes are highly desired. Among CVD processes, ability to deposit uniform thin films at atmospheric pressure is appealing from a practicality point of view. Herein, we develop a process for the deposition of dense  $\text{CH}_3\text{NH}_3\text{PbI}_3$  thin films by aerosol-assisted CVD by both single and three step methods. By identifying and optimising deposition parameters, a range of films with various characteristics could be effectively produced at atmospheric pressure.

**Introduction** In the search for low cost, efficient solar cells perovskites have emerged as a possible candidate. They are direct band gaps semiconductors with excellent absorption coefficients and long diffusion lengths ( $> 1 \mu\text{m}$ ) for electrons and holes [1]. There has been a dramatic rise in efficiency from 3.8% [2] to presently over 22% [3]. However, there are two main drawbacks relating to stability and ease of industrial manufacture. The former is being improved by a variety of ways including use of alternative cations [4] or encapsulation [5]. A wide range of deposition techniques have been used, such as spin coating [6], doctor blading [7], spray coating [8] and Chemical Vapour Deposition (CVD) [9]. Not all of these are suitable for large area deposition due to sample size limitations, waste of large amounts of precursors or general complexity of manufacture.

Large scale deposition is critical to the production of commercial cell modules.

However, it is often found that cell efficiency can decrease by as much as 15% in relative terms on increasing cell size [10]. Hence the need to develop techniques capable of producing uniform, dense thin films over a wide area. The ideal film needs a large crystallite size to reduce transport problems due to grain boundaries, dense to remove pin-holes and relatively smooth to reduce detrimental deposition of the hole transport layer and final electrical contacts. These characteristics are highly dependent on the technique and deposition parameters applied.

Atmospheric pressure CVD is a technique with a proven ability to integrate into manufacturing processes such as the float-glass industry. It has been shown to achieve high volume, fast growth rates for continuous in-line growth processes. To use this process to meet the challenge of industrial scale, cost-effective deposition of dense perovskite coatings use of the CVD processes would be highly desirable.

In this paper we discuss the optimisation of CVD perovskite films and steps towards large area deposition.

**Experimental** All the chemicals were purchased from Sigma Aldrich Ltd and used as received. Films were deposited on 1.1 mm borosilicate glass substrates (Corning Eagle 2000). Both  $\text{CH}_3\text{NH}_3\text{I}_3$  and  $\text{CH}_3\text{NH}_3\text{PbI}_3$  were synthesized according to the reported method [11].

**Deposition of Thin films:** The system was purged under constant  $\text{N}_2$  at the required deposition temperature, before carrying out any experiments. After diluting  $\text{CH}_3\text{NH}_3\text{PbI}_3$  (MAI) (1.2 ml) with DMF (12 ml), experiments were conducted between 200–275 °C with a constant flow rate of 0.5 l/min at atmospheric pressure. For three step deposition,  $\text{PbI}_2$  (0.5g) in DMF (4ml) was deposited at 30 °C followed by heating at 70 °C to remove the solvent. After 5 mins, temperature was increased

to 220 °C where methylammonium iodide (0.346g) in DMF (4ml) was allowed to intercalate into the  $\text{PbI}_2$  structure. Experiments were conducted for 40 min. A standard CVD gas delivery system was used with the addition of a Vicks paediatric mini ultrasonic humidifier to deliver the nebulised precursors.

**Results and Discussion** Initially small area trials (2 cm x 10 cm) were carried out by the single step process to determine critical parameters. These were found to be the substrate temperature and its position relative to the precursor inlet.

Figure 1 shows the change in film colour from black to yellow as it is deposited further from the precursor inlet. This corresponds to a change in composition from the black perovskite to yellow lead iodide. This suggests that the mass transport of the MAI is the rate limiting step, resulting in a concentration gradient with most of the reaction taking place near the gas inlet and hence depleted further along with little to no MAI available for intercalation.



Figure 1, Image of film deposited via a single stage process.

The other major parameter was the substrate temperature. Too low a temperature (150 °C) led to only formation of  $\text{PbI}_2$ , needing  $\geq 200$  °C for perovskite formation. Figure 2 shows the XRD of films produced at these temperatures. Fig.2c shows only polycrystalline  $\text{PbI}_2$ , while fig.2a confirms the tetragonal perovskite structure.

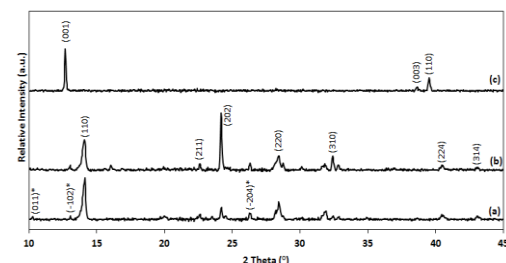


Figure 2, XRD, with deposition at (a) 225 °C (b) 250 °C and (c)  $\text{PbI}_2$

Further increases in substrate temperature showed a change in preferred orientation from (110) to (202) at  $\geq 250$  °C (fig.2b). This change is also mirrored in the SEM (fig.3) showing a change from a

continuous random network structures to a denser micron sized granular structure with large grain boundaries at the higher temperatures.

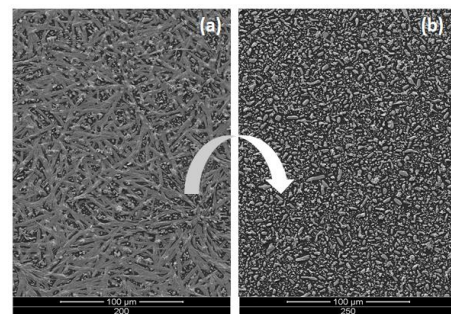


Figure 3, SEM images of films deposited at (a) 200 °C, (b) 250 °C

As is often the case, use of higher temperatures also led to an increased deposition rate illustrated by two films both deposited for the same time, but at 200 °C and 250 °C giving thicknesses of ~ 65 nm and 150 nm respectively. The increased deposition rate also led to the reduction in crystallite size as determined from the (110) reflection from 70 nm to 30 nm at the higher temperature.

Scaling up the process (22 cm x 10 cm) was not straight forward. Initially it was found that samples cooled under  $\text{N}_2$ , rapidly changed from black to white and then in air to brown. As seen in figure 4, the crystallographic structure is very different.

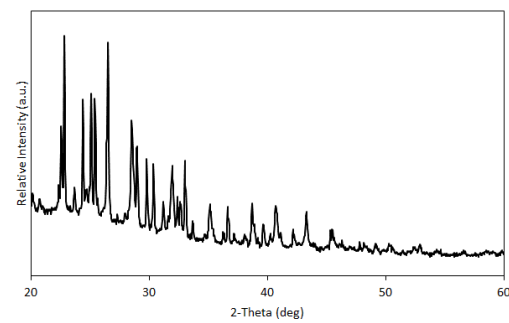


Figure 4, XRD of the brown film.

Similar effects have been seen previously on perovskite exposed to excess MAI due to the intercalation of MAI molecules into  $\text{PbI}_2/\text{MAPbI}_3$  lattices [12]. Reducing the film exposure to MAI and removing while still warm retained the black perovskite, as shown in figure 5.

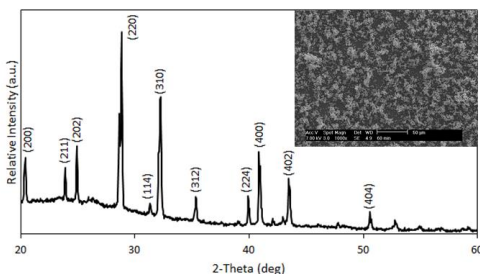


Figure 5, XRD of large scale deposition, with an inset SEM image.

The other more serious issue was the increase in homogeneous reactions, leading to the formation of very soft, powdery films. The change to a powder is clearly seen in the SEM image (fig.5, inset). Use of lower deposition temperatures still produced mainly powder. The production of a heterogeneous rather than homogeneous deposition also depends on the wettability of the reactants on the substrate. With this in mind deposition was attempted on alternative surfaces including  $\text{SnO}_2:\text{F}$  as used by Chen et al [13] and  $\text{TiO}_2$ . The latter is often used as the electron transfer layer in perovskite cells. This led to no improvement in the film quality.

To better control the film development, a three step process was tested with each precursor being added sequentially under different deposition conditions [13]. This was much more successful with the production of black films, which were relatively robust, and could not be brushed off. The formation of a film, rather than powder, was confirmed from SEM images, which showed deposition of highly dense and uniform  $\text{CH}_3\text{NH}_3\text{PbI}_3$  layers on glass (fig.6).

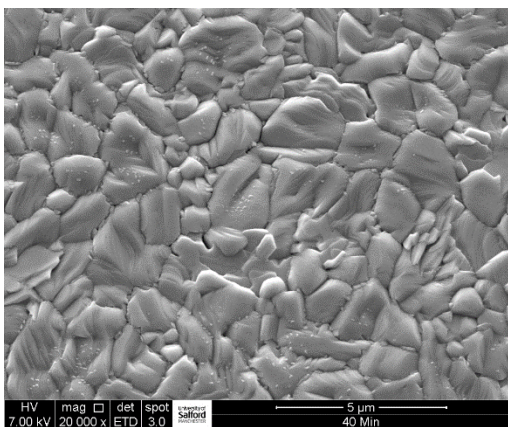


Figure 6, SEM image of the film deposited at 220 °C for 40 mins.

These films have a much larger feature size than those previously obtained using the single step process. In addition the grains are more tightly packed and show no pin-holes, which are often the result of too fast evaporation of the solvent. From the cross-sectional images the film thickness was estimated at 520 nm for a 40 min deposition time.

The onset of absorbance at 1.60 eV was determined from the transmittance and reflectance measurements (Fig.7) using

$$A = -\left[ \frac{T}{1-R} \right]$$

where  $A$  is absorbance,  $T$  is transmittance, and  $R$  is reflectance.

This is in line with values published elsewhere [9].

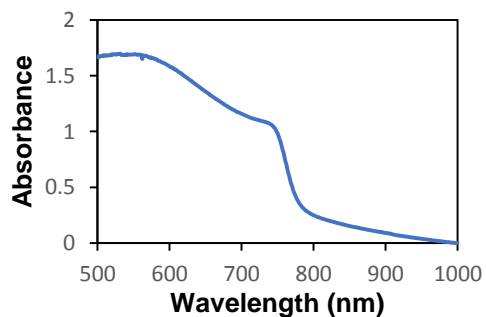


Figure 7, Absorbance spectrum for a perovskite film deposited under the three step process.

The optical bandgap of the films was determined from a Tauc plot using the  $(ahv)^2$  relationship, as shown in fig.8. The estimated direct bandgap (via linear extrapolation of the plot to the energy axis) was 1.54 eV and is again in agreement with previously published data [9, 13].

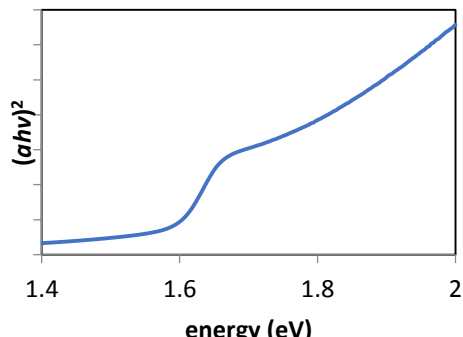


Figure 8, Tauc plot of a perovskite film deposited under the three step process.

**Conclusion** Atmospheric pressure CVD has been used to deposit thin films of polycrystalline perovskite on glass. A single step process worked successfully for small area deposition, but it was necessary to move to a three step process for large scale deposition of dense, pin-hole free perovskite films.

**Acknowledgements** This work was financed by EU Horizon 2020 grant H2020-LCE-2015-16-53296 CHEOPS “Highly Efficient photovoltaic Perovskite Solar cells”.

## References

- [1] C. Zuo, H.J. Bolink, H. Han, J. Huang, D. Cahen, L. Ding, *Adv.Sci.* 3 (2016) 1500324.
- [2] A. Kojima, K. Teshima, Y. Shirai, T. Miyasaka, *J.Am.Chem.Soc.* 131 (2009) 6050.
- [3] [www.nrel.gov/ncpv/images/efficiency\\_chart.jpg](http://www.nrel.gov/ncpv/images/efficiency_chart.jpg)
- [4] M. Saliba, T. Matsui, J.-Y. Seo, K. Domanski, J.-P. Correa-Baena, M.K. Nazeeruddin, S.M. Zakeeruddin, W. Tress, A. Abate, A. Hagfeldt, M. Gratzel, *Energy Environ.Sci.* 9 (2016) 1989.
- [5] C. Law, L. Miseikis, S. Dimitrov, P. Shakya-Tiladhar, X. Li, P.R.F. Barnes, J. Durrant, B.C. O'Regan, *Adv.Mater.* 26 (2014) 6268.
- [6] M.M. Lee, J. Teuscher, T. Miyasaka, T.N. Murakami, H.J. Snaith, *Science*, 338 (2012) 643.
- [7] A.T. Mallajosyula, K. Fernando, S. Bhatt, A. Singh, B.W. Alphenaar, J-C. Blancon, W. Nie, G. Gupta, A.D. Mohite, *Appl.Mater.Today*, 3 (2016) 96-102.
- [8] A. Barrows, A. Pearson, C. Kwak, A. Dunbar, A. Buckley, D. Lidzey, *Energy Environ.Sci.* 7 (2014) 1.
- [9] D.S. Bhachu, D.O. Scanlon, E.J. Saban, H. Bronstein, I.P. Parkin, C.J. Carmalt, R.G. Palgrave, *J.Mater.Chem.A* 3 (2015) 9071.
- [10] S.Razza, S. Castro-Hermosa, A. Di Carlo, T.M. Brown, *Apl.Maters.* 4 (2016) 091508.
- [11] S. Aharon, B.E. Cohen, L. Etgar, *J.Phys.Chem C* 118 (2014) 17160.
- [12] X. Chen, H. Cao, H. Yu, H. Zhu, H. Zhou, L. Yang, S. Yin, *J.Mater.Chem.* 4 (2016) 9124.
- [13] S.Chen, J.Briscoe, Y. Shi, K.Chen, R.M. Wilson, S. Dunn, R. Binions, *Cryst.Eng.Comm.*, 17 (2015) 7486.

## Process Development of Sublimated Cu-free CdTe Solar Cells

C. Potamialis, F. Lisco, B. Maniscalco, M. Togay, J. W. Bowers and J. M. Walls

Centre for Renewable Energy Systems Technology (CREST), The Wolfson School of Mechanical, Electrical and Manufacturing Engineering, Loughborough University, Loughborough, Leicestershire, LE11 3TU, UK.

Corresponding author: C.Potamialis@lboro.ac.uk , Tel: +44 (0)1509 635361

### Abstract

CdCl<sub>2</sub> treatment by evaporation has been optimised for CdTe solar devices without a copper annealing process. In this work, we show that the performance of CdTe devices follow a curvilinear trend by increasing the amount of chlorine used for the passivation treatment. It has been observed that the maximum of the curve represented the best performing devices. However, excessive CdCl<sub>2</sub> caused deleterious effect on electrical performances of the cells. The PL imaging analysis has been found to be a useful technique to assess the effectiveness of the activation treatment due to the presence of chlorine in CdS thin films. Electrical characterisation has been performed on each device and PL imaging analysis has been used to validate the performances of the CdTe solar cells. Results showed that the optimum performance corresponded to the highest PL image emission signal.

### Introduction

Among II-VI compounds, CdTe is an excellent material for photovoltaic applications because it has a nearly ideal optical band gap (1.45 eV) and a high absorption coefficient ( $>10^4\text{cm}^{-1}$ ). The cadmium chloride (CdCl<sub>2</sub>) treatment is an essential step for high efficiency CdTe/CdS solar cells, which significantly changes the structural and electrical properties of the film. After CdCl<sub>2</sub> activation, CdTe films undergo a change in surface morphology, with coalescence of grain boundaries, recrystallization and grain reorientation. Furthermore, the annealing treatment reduces optical losses due to the interdiffusion mechanism, where S diffuses into the CdTe, forming CdTe<sub>1-x</sub>S<sub>x</sub>, while Te diffuses in CdS as CdS<sub>1-y</sub>Tey. CdTe band gap is reduced, which results in higher absorption at long wavelengths; however built-in voltage can reduce and shunt issues can result as the CdS is consumed. Treated devices show higher p-type conductivity, passivation of

interface defects, reduction of planar defect density and change in concentration and distribution of trapping states. Additionally, CdCl<sub>2</sub> post-annealing enhances the charge separation, increasing hole depletion near the grain boundaries and improves carrier collection [1].

However, the process window that allows beneficial impact for the device output is small. Under-treatment can result in limited device current, while an over-treatment can result in excessive consumption of the CdS layer limiting the device voltage [2] and possibly causing blistering and delamination [3].

Electrical performances and material characterisation are generally carried out to assess the effect of CdCl<sub>2</sub> treatment. PL imaging is an advanced characterisation technique that can assist device optimisation, allowing each processing stage to be analysed.

In this paper, we report the optimisation of the CdCl<sub>2</sub> treatment for CdTe solar devices, assisted by PL imaging characterisation. The amount of CdCl<sub>2</sub> evaporated on CdTe surfaces was the investigated parameter in this study. CdCl<sub>2</sub> was varied in the range of 0 - 0.8 grams to evaluate the effect and the homogeneity of the treatment. Electrical output of the CdTe devices were measured and related to the amount of CdCl<sub>2</sub> used. Pixel counts of the PL images were also related to the electrical performances.

Here, the emission present in the PL imaging, is likely from chlorine containing defects as both sulphur (V<sub>s</sub>-Cl<sub>s</sub>) and cadmium vacancies (V<sub>cd</sub>-Cl<sub>s</sub>) in the CdS layer [4]. A low PL image signal indicates no chlorine presence in the films. In this case the image appears dark with low pixel counts (roughly estimated ~1,000). When a sample is CdCl<sub>2</sub> treated, the image appears brighter with higher pixel counts (estimated ~48,000) due to the presence of chlorine.

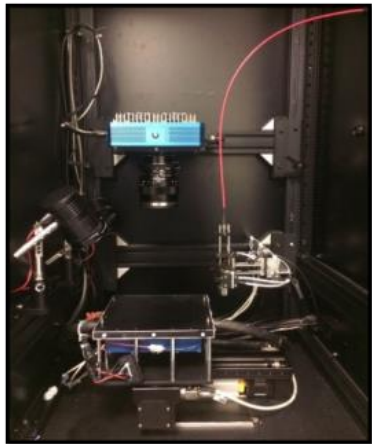


**Figure 1:** Bespoke PL imaging system used for this work with excitation wavelength of 405 nm and a 720 nm long-pass filter.

## Experimental Procedures

Prior to CdS deposition, 50x50mm<sup>2</sup> substrates (Pilkington TEC 10, FTO) were ultrasonically cleaned in a de-ionised (DI) water solution containing 10% acetone and 10% IPA, for 1 hour at 80°C, and subsequently received a 5-minute plasma clean in an argon/oxygen environment. CdS thin films were deposited by ultrasonically assisted chemical bath deposition (sono-CBD) [5], where an ultrasonic probe has been used instead of a conventional magnetic stirrer to agitate the bath. 0.01M Cd(CH<sub>3</sub>COO)<sub>2</sub>, 0.1M CH<sub>4</sub>N<sub>2</sub>S, 25% NH<sub>4</sub>OH were used as precursors in 200 mL DI water in a preheated vessel at 70° C, resulting in films of ~200 nm thickness [4]. After deposition, the substrates are rinsed with DI water and dried with dry compressed air.

The CdTe deposition was carried out in a homemade close-space sublimation system (CSS) [6]. The CdS substrate and source plate were loaded in the chamber and the sublimation procedure was initiated. Argon and oxygen were introduced in the chamber (6% O<sub>2</sub> in Ar); the deposition pressure during sublimation was 1 Torr. Sublimation is initiated when the substrate temperature and source temperature are 515° C and 630° C respectively. A 3 minute CdTe deposition results in 4-6 μm thick films.

The CdCl<sub>2</sub> treatment was carried out using thermal evaporation at various CdCl<sub>2</sub> concentrations. A quartz crucible was filled with 0.2, 0.4, 0.5, 0.6 and 0.8g of CdCl<sub>2</sub>, which was evaporated at ~3x10<sup>-7</sup> Torr,

until the crucible was empty. The samples were subsequently annealed on a hot plate using two-step ramping conditions 50°C / min up to 370°C and 5°C / min to the dwell temperature of 425°C, which was held for 1 minute. Devices were completed by depositing ~80 nm of gold using thermal evaporation, as the back contact.

PL imaging was carried out using a home-made system (Figure 1). An LED of 405 nm was used as the excitation source, with a Si CCD camera fitted with a 720 nm long-pass filter. Exposure time for all of the measured samples was kept to 10 seconds. All measurements were taken at room temperature, with the sample positioned with the glass side of the substrate facing the camera. Figure 2 shows a comparison of the PL emission detected for an untreated CdS film and a CdCl<sub>2</sub> treated CdS film, both on FTO. 0.2 g were evaporated on CdS film and annealed as for CdS/CdTe stacks. The intensity of the PL emission (pixel counts) is used as an indication of the effectiveness of the CdCl<sub>2</sub> treatment. The untreated CdS film has an average of 1,000 counts while the treated CdS film has an average of 58,000 counts. This is the range that the system can operate before the saturation limit of the detector is reached (~64,206 counts).

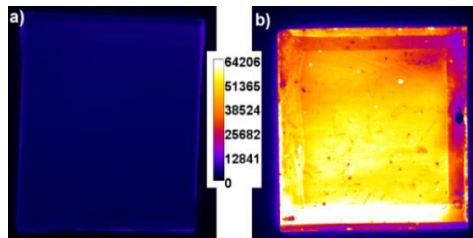


**Figure 2:** PL image of a) an as-deposited CdS layer and b) CdCl<sub>2</sub> treated CdS layer.

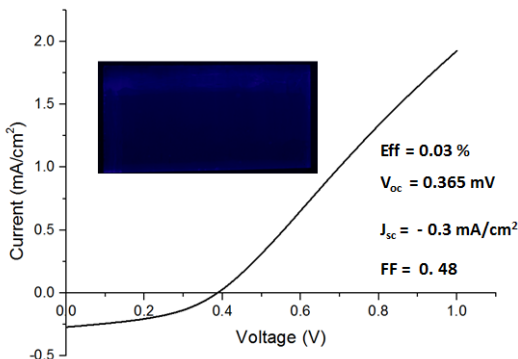
The electrical performance was studied using current density–voltage (J–V) curves, measured with the solar cell exposed under 1000 W/m<sup>2</sup> illumination and using an AM 1.5G filter.

## Results

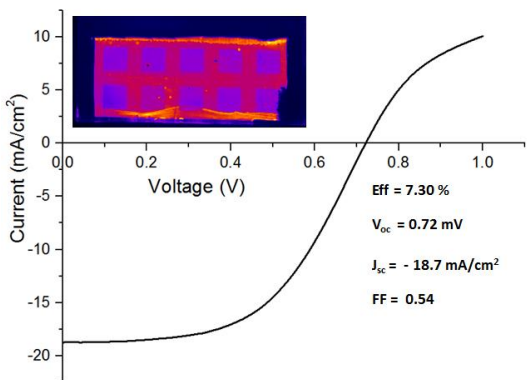
Figure 3 shows the J–V curve and the associated PL image of an as deposited device where no CdCl<sub>2</sub> treatment has been performed. The performance of this device is extremely poor, with an average V<sub>oc</sub> of 370mV and an average J<sub>sc</sub> of 0.3 mA/cm<sup>2</sup> and FF of 0.4. The average measurements were calculated using 10 cells across each CdS/CdTe device. PL

image analysis also confirmed that the post deposition annealing step performed without the presence of chlorine, had no effect on the device. In fact, low signal intensity was detected with an estimated average of ~1,000 counts.

The following experiments were carried out by varying the amount of CdCl<sub>2</sub>. 0.2 g (Figure 2) of evaporated CdCl<sub>2</sub> has been deposited on CdS/CdTe thin films and the electrical properties have been studied. The average efficiency increased from ~0.03% (when no CdCl<sub>2</sub> was added) to 7.2 %, with a V<sub>oc</sub>, J<sub>sc</sub> and FF of 727mV, 18.7mA/cm<sup>2</sup> and 0.5, respectively. These results were confirmed using PL imaging, which showed an average of ~13,700 counts contrary to the ~1,000 counts detected previously on the samples annealed with no CdCl<sub>2</sub>.



**Figure 3:** J-V Curve and PL image of an as-deposited CdTe device.



**Figure 4:** J-V Curve and PL image of a CdTe device with 0.2 g of evaporated CdCl<sub>2</sub>.

Increasing the amount of CdCl<sub>2</sub> further during evaporation to 0.4g results in higher performance devices. The average efficiency of the CdTe device was 7.9 %

and the counts detected by PL image were ~ 22,240. The average of PL counts was taken over the area (0.25 cm<sup>2</sup>) of 10 individual cells for each sample.

The optimum device performance was achieved when CdS/CdTe thin films were treated with 0.5 g of evaporated CdCl<sub>2</sub> with the device showing the highest average efficiency (8.40%) with 0.762 mV voltage 18.77 mA/cm<sup>2</sup> current density and 0.59 FF. Figure 3 shows the J-V curve with the associated PL image, with an average emission of 23,300 counts

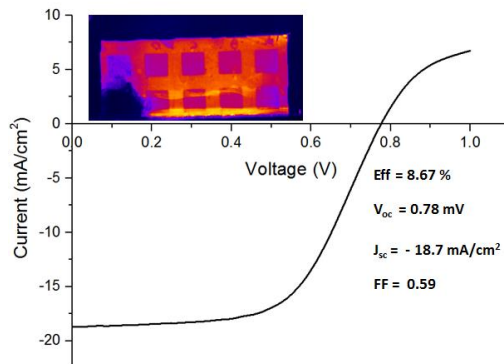
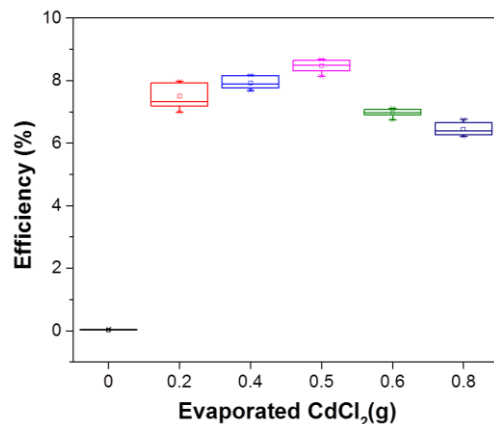


**Figure 5:** J-V Curve and PL image of a CdTe device with 0.5 g of evaporated CdCl<sub>2</sub>.

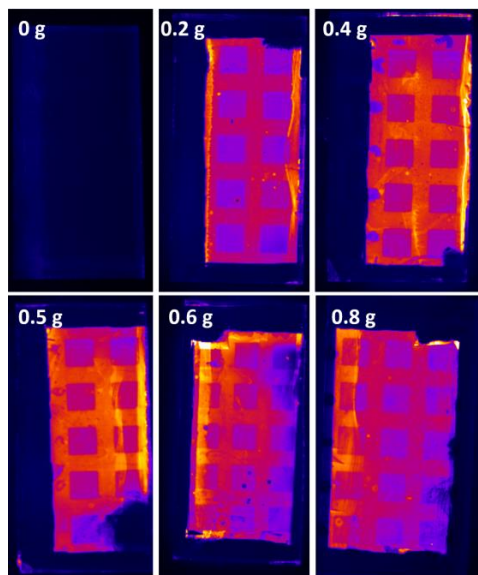
Further increase in the amount of CdCl<sub>2</sub> used in the deposition proved to have a deleterious effect on the performance of the devices. A dramatic drop in electrical performance has resulted when using 0.6 g CdC<sub>2</sub> on the CdTe device. The average V<sub>oc</sub> dramatically decreased to 662 mV while the J<sub>sc</sub> remained at approximately the same value (18.74 mA/cm<sup>2</sup>) and the FF decreased to 0.54. To conclude the study, 0.8 g of CdCl<sub>2</sub> was deposited on the CdTe, to identify an over-treated CdCl<sub>2</sub> treatment, performance of this sample was very similar with 0.6 g with average V<sub>oc</sub>, J<sub>sc</sub>, and FF to be 661 mV, -18.5 mA/cm<sup>2</sup>, and 0.51 respectively. The drop in voltage can be an indication of excessive consumption of sulphur from CdS due to the intermixing between the CdS and CdTe layers during the activation process.

Figure 6 shows the clear trend of efficiency against the increasing amount of evaporated CdCl<sub>2</sub>. The figure shows a curvilinear trend where the ascending part represents the progressive increase amount of the CdCl<sub>2</sub> used (starting from 0g), reaching the highest efficiency at 0.5 g. The descending part of the curve corresponds to the further increase of CdCl<sub>2</sub> used, where a deleterious effect has

been observed on the performances of the CdTe devices. A similar trend was observed in the PL imaging analysis (Figure 7) where the optimum performance corresponded to the highest intensity detected. This confirms the agreement between PL imaging analysis and electrical characterisation.



**Figure 6:** The efficiency trend versus the amount of evaporated CdCl<sub>2</sub>.



**Figure 7:** PL Images of CdTe devices treated with different amount of evaporated CdCl<sub>2</sub>.

## Conclusions

PL imaging and electrical characterisation were performed to investigate the effectiveness of CdCl<sub>2</sub> post-annealing treatment. Identical CdS/CdTe devices were fabricated and undergone different treatments by varying the amount of evaporated CdCl<sub>2</sub>. Results showed that the electrical performance is interlinked with the amounts of CdCl<sub>2</sub> used to treat CdTe thin films. As deposited CdS/CdTe

films resulted in poor device performance with no efficiency, while treated devices showed a progressive increase in performance. A clear trend was identified in the CdCl<sub>2</sub> treated devices where the electrical output improved with increasing quantity of evaporated CdCl<sub>2</sub>, up to an optimal amount (0.5 g) where the average efficiency was measured to be 8.40%. However, further increase of evaporated CdCl<sub>2</sub> caused a reduced performance of the CdTe devices, in particular for the V<sub>oc</sub>. This is believed to be caused from excessive consumption of the CdS layer during the CdCl<sub>2</sub> annealing process, leading to a weaker p-n junction. Additionally, PL imaging analysis of the devices confirmed the trend identified from the electrical characterisation, where optimum performance corresponded to the highest PL image emission signal. This indicates that advanced characterisation techniques such as PL imaging can provide useful information about the effectiveness and uniformity of the CdCl<sub>2</sub> post-annealing treatment.

## References

- [1] S. Girish Kumar and K. S. R. Koteswara Rao, "Physics and chemistry of CdTe/CdS thin film heterojunction photovoltaic devices: fundamental and critical aspects," *Energy Environ. Sci.*, vol. 7, pp. 45–102, 2014.
- [2] D. R. Hodges, "Development of CdTe thin film solar cells on flexible foil substrates," University of South Florida, 2015.
- [3] T. Trupke, B. Mitchell, J. W. Weber, W. McMillan, R. A. Bardos, and R. Kroeze, "Photoluminescence imaging for photovoltaic applications," *Energy Procedia*, vol. 15, no. 2011, pp. 135–146, 2012.
- [4] A. E. Abken, D. P. Halliday, and K. Durose, "Photoluminescence study of polycrystalline photovoltaic CdS thin film layers grown by close-spaced sublimation and chemical bath deposition," *J. Appl. Phys.*, vol. 105, no. 6, 2009.
- [5] F. Lisco, P. M. Kaminski, A. Abbas, K. Bass, J. W. Bowers, G. Claudio, M. Losurdo, and J. M. Walls, "The structural properties of CdS deposited by chemical bath deposition and pulsed direct current magnetron sputtering," *Thin Solid Films*, pp. 2–6, 2014.
- [6] Y. A. Salazar, R. Pati, and J. L. Peña, "Physical Properties of CdS / ITO Thin Films Growth by CBD Technique with Substrate Oscillating Agitation," *Brazilian J. Phys.*, vol. 36, no. 3, pp. 1058–1061, 2006.

## PVSAT-13

### AUTHOR INDEX

Afzaal M	149
Ahmed H	25, 129
Alrashidi H	145
Anthony R	49, 141
Arnou P	101
Aurang P	85
Baker J	1, 5
Barrioz V	21, 65, 85
Beattie N S	65
Begarney D	53
Betts T R	9, 61, 77, 97, 113, 125
Bliss M	61, 97, 125
Bowen L	85
Bowers J W	101, 153
Bristow N	117, 133
Carnie M J	1, 5, 13
Chandra S	25, 129
Charbonneau C M E	93
Clark A	53
Clayton A J	93
Cole I	77
Connell A	49, 141
Cooper C S	101
Crook J A	57
Crook R	57, 121
Dale S	137
Day J	109
De Brito Melo T	1
De Rossi F	1, 43
Dyer A	29
Ekins-Daukes N	53
Escalante R	1
Forbes I	137
Forster P M	57
Führer M	53
Furnell L	49, 141
Geatches D	49
Ghosh A	145
Ghosh S	105
Gómez D	105

## PVSAT-13

### AUTHOR INDEX

Gottschalg R	9, 61, 69, 77, 97, 113, 125
Gürlek A K	85
Hadibrata W	85
Hall J	29
Hall S R G	97
Haponow L	105
Hatton R A	89
Hobbs R	49
Hodgkinson J L	39
Hoffman Jr R	53
Holliman P J	49, 141
Hooper K	5, 43, 73
Irvine S J C	21, 29, 85, 93
Issa W	145
Jackson L S	57
Jewell E	1
Johnson A	53
Jones E W	49, 141
Kartopu G	85
Kershaw C	49, 141
Kettle J	105, 117, 133
Khanna S	17
Koubli E	69, 77
Koutsourakis G	61, 97, 125
Lakhiani H	13
Lamb D A	21, 29
Lisco F	153
Maiello P	85
Malkov A V	101
Mallick T K	17, 109, 145
Maniscalco B	153
Marshall K P	89
Martínez A L	105
Mazzamuto S	137
McCormack S J	25, 129
McGettrick J D	5, 43, 49
Meroni S. M. P.	1
Metz S	49
Mihaylov B V	61
Min G	133
Montiel-Chicharro D	113

## PVSAT-13

### AUTHOR INDEX

Mouhamad Y	1
Newman M	43
Ng C	113
Nicolay S	39
Oskam G	1
Osprey S M	57
Owen-Bellini M	9
Özcan C	85
Palmer D	69, 77
Pearce P	53, 81
Pearsall N M	137
Peter L M	137
Pockett A	1, 5, 13
Potamialis C	153
Qu Y	65, 85
Radeck R	53
Rafiee M	129
Ransome S	33
Reddy K S	17
Rolley M	133
Rowley P	69
Ryall N E	121
Sánchez P	105
Searle J	1
Sellami N	145
Senthilarasu S	109, 145
Sethi A	25
Siderfin P	93
Slade R	81
Smith C J	57
Stoichkov V	105, 117, 133
Stuart T	145
Sutterlueti J	33
Sweet T	117, 133
Togay M	153
Tokmoldin N	13
Tomos T	53
Troughton J	13, 43, 73
Tsai V	125
Turan R	85
Uličná S	101

## PVSAT-13

### AUTHOR INDEX

Ünalan H E	85
Underwood C I	21, 29
Walker M	89
Walls J M	101, 153
Walter A	39
Walton R I	89
Watson T	1, 5, 13, 43, 73
Weinstein J A	121
Wilson T	53
Wing Chung Tsoi	43
Wright L D	101
Xu X	65
Yates H M	39, 149
Yerci S	85
Zhantuarov S	13
Zhu J	9, 113
Zoppi G	65

## **Notes**

## **Notes**



# the SOLAR ENERGY Society (UK-ISES)

UK Section of the INTERNATIONAL SOLAR ENERGY SOCIETY

PO Box 489, Abingdon-on-Thames, Oxon OX14 4WY

Tel +44 (0)7760 163559, Fax +44 (0)1235 848684, Email [info@uk-isес.org](mailto:info@uk-isес.org), [www.uk-isес.org](http://www.uk-isес.org)

---

The Solar Energy Society, the UK national section of ISES, is a non-profit learned society which aims to further the use of all forms of renewable energy by encouraging research, promoting education and providing training. The Society provides a forum for all those interested in renewable energy technologies and its membership is drawn from industry, government, academic institutions, architectural and engineering practices and the general public. Through its meetings and publications, the Society aims to promote discussion and disseminate information on all aspects of renewable energy, including not only technical issues, but also political, institutional and economic barriers and opportunities for the development of solar energy industries, to serve the needs of developing as well as industrialised countries.

The Society was formed in 1974. Since that time it has organised some 100 conferences and published associated proceedings covering all major areas of renewable energy, including the ISES Solar World Forum in 1981, the UK-ISES Silver Jubilee conference in Brighton in 1999, EuroSun 2006 in Glasgow and the Photovoltaic Science, Applications and Technology series (PVSAT) held at different UK universities. The David Hall Memorial Lecture is held annually in London in December and past speakers include Government ministers and leading figures in the field.

The President of the Society is Dame Mary Archer, DBE.

The Acting Chair of the Society is Tony Book, Riomay Limited (retired).

Membership details available from the Secretariat or [www.uk-isес.org](http://www.uk-isес.org)

---

## PVSAT-14

14th Photovoltaic Science, Applications and Technology Conference, C100  
Imperial College London, UK, 18-20 April 2018

[www.pvsat.org.uk](http://www.pvsat.org.uk)

---



**INTERNATIONAL SOLAR ENERGY SOCIETY**  
ISES HQ: Villa Tannheim, Wiesentalstrasse 50, D-79115 Freiburg, Germany



The Solar Energy Society

[www.pvsat.org.uk](http://www.pvsat.org.uk)  
[www.uk-is-es.org](http://www.uk-is-es.org)

13th Photovoltaic Science, Applications and Technology Conference

## PVSAT-13

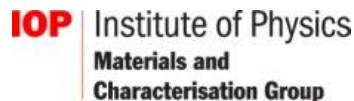
Bangor University  
Bangor, UK

Wednesday 5<sup>th</sup> –Friday 7<sup>th</sup> April 2017

*Sponsored and supported by*



EPSRC CENTRE FOR DOCTORAL TRAINING  
NEW AND SUSTAINABLE  
PHOTOVOLTAICS



*Date and Location of the 2018 PVSAT Conference:*

PVSAT-14  
Imperial College London  
Wednesday 18<sup>th</sup> –Friday 20<sup>th</sup> April 2018

*Further details at [www.pvsat.org.uk](http://www.pvsat.org.uk) ; [www.uk-is-es.org](http://www.uk-is-es.org)*